Superconducting quantum devices with germanium nanowires

Inauguraldissertation

zur
Erlangung der Würde eines Doktors der Philosophie
vorgelegt der
Philosophisch-Naturwissenschaftlichen Fakultät
der Universität Basel

von

Han Zheng

Basel, 2024

Genehmigt von der Philosophisch-Naturwissenschaftlichen Fakultät
auf Antrag von
Erstbetreuer: Prof. Dr. Christian Schönenberger
Zweitbetreuerin: Prof. Dr. Jelena Klinovaja
Externer Experte: Prof. Dr. Christian Andersen

Basel, den 27. Februar 2024

Prof. Dr. Marcel Mayor
Dekan

Contents

1 Introduction [1]

"The best way to predict the future is to invent it."
— Alan Kay

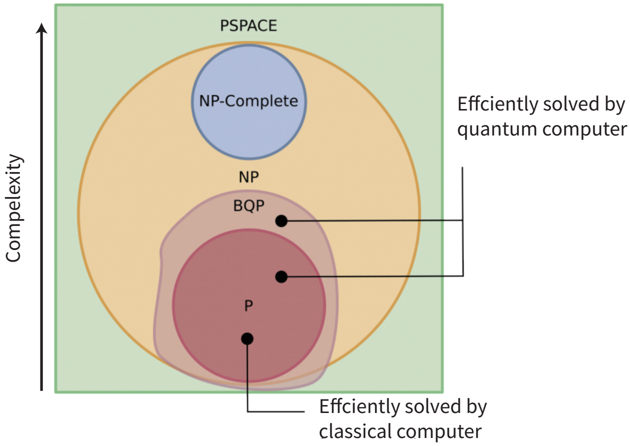

Looking back at human history, one could bet that nothing has shaped our lives more significantly than computers. From the colossal, room-sized machines of the past to the compact smartphones carried in our pocket today, the rapid evolution of computer technology has dramatically enhanced the efficiency and speed of data processing. The exponential increase in computational power, as forecasted by Moore's Law[2], has brought artificial intelligence (AI) from science fiction into reality, enabling the execution of complex algorithms like deep learning [2–4] and neural networks[5–7]. Behind inventions

---

[1] The title image shows classification of computation complexity. BQP stands for "Bounded-Error Quantum Polynomial Time", which represents the class of problems that can be solved efficiently with quantum computers, but beyond the reach of classical computation. Adapted from Ref. [1]

[2] Moore's Law predicts an exponential increase in transistor density, however it is also closely linked to computational power.

like self-driving cars, Boston Dynamics robots, AlphaGo, and large language models lies countless number of matrix computations performed on microchips. All in all, these advancements are revolutionizing numerous aspects of our life, including science, art, business, and entertainment, reshaping the world in ways that no one could have scarcely imagined.

This journey started with the simplest computational element: the transistor. In 1947, John Bardeen, William Shockley, and Walter Brattain invented the first transistor [8]. It had a simple structure consisting of a thin slice of germanium (Ge) with two closely spaced gold contacts on its surface. Shortly after, Jack Kilby created the first integrated circuit (IC) [9, 10], ingeniously combining various components—transistors, diodes, resistors, and capacitors—onto a single substrate. Meanwhile, the Ge-based transistor radio from Sony has achieved significant commercial success. However, devices based on Ge soon encountered significant issues. From an application point of view, these car radios manufactured on Ge stopped working due to thermal instability in summer time. From an industrial manufacturing perspective, the MOSFET (metal–oxide- semiconductor-field-effect transistor) technique, which leverages silicon oxide as the dielectric material, could not be applied to Ge[3]. Since then, silicon has become the core material, and has supported the development of the semiconductor industry for over fifty years.

Nowadays, the most advanced commercial microprocessor chips contain tens to hundreds of billions of transistors, a count on par with the number of stars in the Milky Way. However, as an old saying goes, all good things must come to an end. Some forecasters, including Gordon Moore himself, predict that Moore's law will end by around 2025 [11]. As the miniaturization of transistors continues, quantum effects begin to manifest, leading to current leakage in the transistor channels. On top of that, when the R&D cost for further miniaturization cannot be compensated by the profit, Moore's law is doomed to end.

However, is this the end for everything? Can we harness more computational power from nature? The answer is yes. In 1980s, Paul Benioff introduced the quantum Turing machine [12]. Then, Richard Feynman proposed physics can be more effectively simulated with a quantum computer [13]. The turning point happened when Peter Shor developed the famous Shor's algorithm [14, 15], a quantum algorithm enabling factorization into prime numbers at an exponentially faster rate than the best classical algorithms. Generally, the complexity of computational tasks can be classified as shown in the chapter title image. P represents a class of tasks solvable in polynomial time on a classical computer, whereas BQP (bounded-error quantum polynomial time)

---

[3] GeO_2 is less stable, susceptible to moisture and environmental impacts, and possesses numerous surface states that reduce gating efficiency. In contrast, SiO_2 is easily formed on silicon via economical thermal oxidation process, and SiO_2 is a great insulating material.

denotes the class of problems that a quantum computer can solve in polynomial time. The advent of quantum computing holds the promise for tackling a broader range of challenges previously unsolvable by any classical methods.

Over the past two decades, quantum computation has experienced a significant boost in multiple platforms. In fact, people start to think about whether Moore's law also works for qubits. Recently, IBM has released 1,000-qubit quantum chip based on superconducting circuit [16]. In the meantime, error-corrected logical quantum processor has been demonstrated with neutral atoms array up to 280 physical qubits [17]. In terms of spin qubits, a high fidelity gate passing the fault-tolerance threshold have been realized [18–20]. However, we have to admit that we are still in the very early era of quantum computing. Compared to the classical transistor, we have yet to invent the quantum equivalent of the first "car radio". In other words, a "killer app" in quantum computing has not appeared yet, and the debate over the roadmap for quantum computing is likely to continue for a while.

Amidst the frenzy of this quantum gold rush, Ge is resurging as a promising platform for quantum information processing [21]. First of all, Ge exhibits the highest hole mobility among any known semiconductor materials [22], featuring an ultra-clean material platform for quantum devices. Secondly, hyperfine interaction is strongly suppressed due to p-type valence band and low abundance of spinful isotopes, with further improvement achievable via isotopic purification. Absence of hyperfine interaction would contribute to an enhancement of qubit coherence time. Thirdly, the physics of holes in Ge's valence band results in a strong and tunable spin-orbit interaction (SOI), making it promising for all-electric control for spin qubit. Moreover, Ge nanowires harbor rich physics due to heavy-hole light-hole mixing. Fourthly, as a CMOS compatible material[4], Ge can be well integrated into existing semiconductor industry frameworks. Last but not the least, Ge facilitates transparent contacts to superconductors, showing great promise for semiconductor-superconductor hybrid devices.

Motivation of this thesis

This thesis investigates the potential of Ge-based nanowires as a platform for quantum information processing, particularly focusing on superconductor-Ge hybrid devices. One might wonder, why Ge hybrids? In the past five years, hole spin qubits in Ge quantum wells have seen rapid advancements [21, 23–26], propelled by the exceptional properties of Ge discussed above. Long coherence times, rapid operations and high gate fidelity have been achieved. Yet, chal-

---

[4] CMOS compatible means the material can be integrated with CMOS technology without causing harm or interference to the existing CMOS processes. Examples of CMOS-compatible materials include: Si, SiO_2, Si_3N_4, Ge, Si-Ge alloys, metals such as Al and Cu.

lenges remain in establishing long-distance interconnections for semiconductor spin qubits [27–31]. In the meantime, superconducting qubits [32, 33] stand out as another leading quantum computing platform. Their larger physical size and macroscopic quantum states facilitate remote coupling. Can we combine the advantages of both platforms? This is the central question that this thesis seeks to address. Our goal is to define and coherently manipulate qubits in Ge/Si core/shell NWs, leveraging Ge's unique properties and integrating Ge into circuit-QED architectures.

On the path of achieving this goal, several crucial steps must be undertaken. First and foremost, one need to establish reliable and reproducible recipes to making superconducting contact to Ge NWs, as detailed in Chapter 4. Next, it's essential to measure and comprehend the sub-gap states formed in Ge hybrid systems. To gain a deeper insight of the Andreev bound states (ABSs) in Ge/Si nanowire Josephson junctions (NW JJs), we conducted DC measurements. Our study included tunneling spectroscopy of ABSs, as elaborated in Chapter 5, and investigation of the current-phase relation of Ge/Si NW JJs using superconducting quantum interference device (SQUID), presented in Chapter 6.

To develop qubits in the Ge hybrids system, it is necessary to integrate Ge/Si NW JJs into microwave circuits. In this context, we explored two types of qubits: superconducting qubits, which utilize collective bosonic modes, and Andreev qubits, defined in fermionic quasiparticles of the ABSs spectrum. In Chapter 7, the NW JJ is shunted by a large capacitor, forming a gatemon qubit. In Chapter 8, we embedded the NW JJ in a RF SQUID loop, aiming for a Andeev qubit.

Outline of this thesis

Chapter 2 introduces the most relevant theoretical concepts for this thesis. We begin with a basic introduction to superconductivity, followed by Andreev bounds states and the Josephson effect. Then, we explore the concepts of quantum dots (QDs) and discuss QDs coupled to superconducting leads at various coupling strengths. Next, We introduce building block of transmon, and gate-tunable transmon using a semiconductor-superconductor hybrid JJ. Finally, we discuss physics of Andreev (spin) qubits.

Chapter 3 introduces the material platform of Ge. We start by discussing the physics of holes in Ge. Then, we focus on the 1D version of Ge nanostructures, specifically Ge/Si core-shell nanowires (NWs). We delve into concepts such as heavy-hole and light-hole mixing in the hole band of 1D NWs, as well as the direct Rashba spin-orbit interaction. Following that, we explore the growth of the NWs and discuss some fundamental properties of these nanowires.

Chapter 4 provides an overview of the experimental methods utilized in this thesis. It includes the fabrication processes of the devices, as well as a brief description of the measurement setups. Here, we elaborate our efforts in establishing superconducting contacts to Ge/Si core/shell NWs.

In **Chapter** 5, we study superconducting transport in Ge/Si NWs with standard surface contact methods. In the S-NW-S devices, unintentional quantum dots are observed due to the barrier at the S-NW interfaces. Despite this, we observe sub-gap states formed in proximitized QD in different coupling regimes and with various junction length. We also report sub-gap states formed in a double quantum dot configuration. Lastly, we revisit Al/Ge inter-diffusion devices, and highlight its high magnetic field compatibility.

In **Chapter** 6, we provide the first measurements of the current-phase relation (CPR) in Ge/Si NW JJ by integrating two JJs into an asymmetric DC SQUID. Our data reveals a skewed CPR, suggesting highly transparent JJs due to atomic-sharp alloyed Al/Ge interfaces. More interestingly, at specific gate voltages, we find an anomalous CPR where the dominant term is $\sin(2\phi)$ rather than the expected $\sin(\phi)$. Additionally, we report tunneling spectroscopy measurements of sub-gap states in each individual junction, when the junction is near pinch-off.

In **Chapter** 7, we integrate a Ge/Si NW JJ into a microwave circuit to demonstrate a gatemon qubit, revealing gate-tunable frequencies and analyzed its anharmonicity. We found the JJ is dominated by at most two quantum channels with high transparency. Moreover, we report the longest qubit coherence among group IV materials.

In **Chapter** 8, we embed the same NW JJ into an RF SQUID loop, aiming for an Andreev (spin) qubit. We report gate- and phase-tunable states with unique spectra and achieve coherent control over qubit states. The observed qubit coherence times significantly surpasses previous Andreev qubits. While the exact nature of these quantum states is still under investigation, our results highlight Ge's promising role in quantum information processing.

In **Chapter** 9, we provide a conclusion of this thesis and offer an outlook for future research.

2 Theoretical background [1]

> *"The most incomprehensible thing about the world is that it is comprehensible."*
> — Albert Einstein

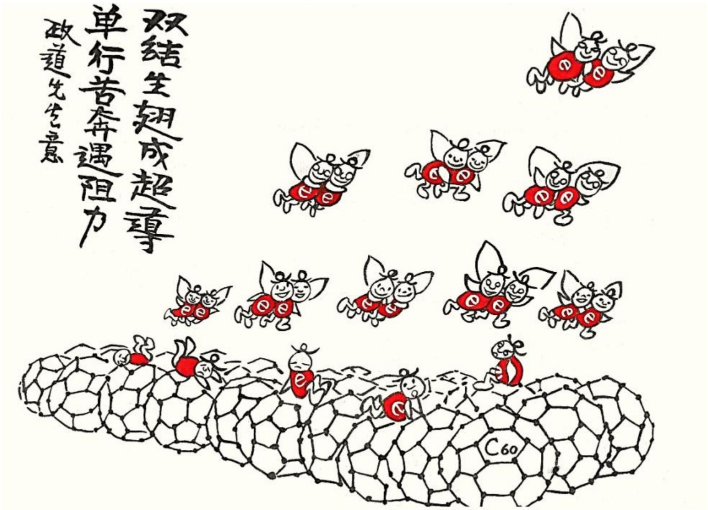

In this chapter, we will elucidate theoretical concepts essential for establishing a basic understanding of the research conducted in this thesis. We first give a brief introduction to superconductivity, transport through a normal-superconductor interface, and the basis of quantum dot physics. Then, we discuss the relevant transport mechanisms in a nanowire (NW) coupled with superconducting electrodes in different coupling regimes, from Andreev bound

---

[1] The title image is a comic depicting the mechanism of the Cooper pair, an idea proposed by Prof. Tsung-Dao Lee and created by the Chinese artist Junwu Hua. The accompanying poem translates as: "A lone journey faces resistance, while paired wings emerge as superconductivity."

states (ABSs) to Josephson junctions (JJs). Finally, we discuss how to implement NW JJ as a qubit, including the gatemon and Andreev (spin) qubit. This chapter follows Refs. [34–42].

2.1. Superconductivity

Superconductivity is one of the most important phenomenon in the realm of condensed matter physics. Since discovery, 5 Nobel Prizes have been awarded for works related to superconductivity. It is a state of matter in which certain materials, when cooled to sufficiently low temperatures, exhibit the extraordinary property of zero electrical resistance. In this state, electric currents can flow without energy dissipation. The implications of superconductivity extend far beyond its fundamental scientific interest, with profound applications across a wide spectrum of fields, including energy transmission and storage, medical diagnostics, and the development of quantum technologies.

The discovery of superconductivity dates back to 1911 when Heike Kamerlingh Onnes first observed the abrupt disappearance of electrical resistance in mercury at liquid helium temperature [43]. This groundbreaking work initiated a fascinating journey into the world of superconductors. The transition to the superconducting state happens when the material is cooled down to a critical temperature, often denoted as T_c. It is worth noting that T_c varies among materials and serves as a characteristic of superconductors.

Another key phenomena of superconductivity, which appears along with the zero resistivity, is found by Meissner [44]. The superconductors perfectly expel magnetic fields from their interior. The London theory [45] was the initial theoretical framework to provide a phenomenological explanation for these two key characteristics: dissipationless transport and perfect diamagnetism. The theory considers a phenomenological constant associated with a number density of superconducting carriers n_s. From the theory, a London penetration depth λ_s is derived, which defines the characteristic length scale over which external magnetic fields experience an exponential suppression inside the superconductor.

2.1.1. Cooper pairs and superconducting gap

Despite the success of the London theory, it does not touch the microscopic origin of superconductivity. The understanding of superconductivity took a significant step with the development of the BCS theory, named after its creators John Bardeen, Leon Cooper, and Robert Schrieffer [47, 48]. In 1957, they proposed a microscopic theory for superconductivity based on phonon-mediated electron-electron interaction. As shown in Fig. 2.1 (a), a moving electron which attracts the lattice, causing a lattice displacement along its path.

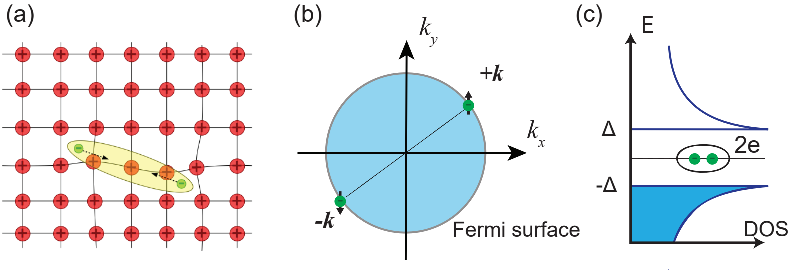

Figure 2.1. BCS theory and Cooper pair formation. (a) Two electrons (small green circles) in an ionic lattice (large red circles) interact with phonons, forming Cooper pairs (yellowish ovals) with opposite spins. (b) Cooper pair formation in momentum space, two electrons at opposite side of the Fermi sphere have opposite spins and momenta. (c) Quasiparticle density of states (DOS) near the Fermi energy. Cooper pairs condensed to a collective quantum ground state at Fermi energy, and a superconducting gap Δ is opened. Figure adapted from Ref. [46].

Another electron passing in the opposite direction is attracted to that displacement. This interaction is shown in momentum space in Fig. 2.1 (b), resulting in these two electrons forming a Cooper pair. Despite the fact that negatively charged electrons are pushed apart by the Coulomb force, this interaction gives rise to an attractive force. Two electrons with opposite spins/momenta now behave like a boson, and condense into a collective ground state at Fermi energy, called the BCS ground state. This states is a macroscopic quantum state, meaning all Cooper pairs share the same wave-function. The formation of Cooper pairs leads to an energy gap in the energy spectrum. This gap, known as the superconducting gap, represents the energy required to break a Cooper pair and create two individual electrons (quasiparticles). In BCS theory, the quasiparticle density of states is described by [49]

$$\mathcal{D}_{\mathrm{S}}(E) = \mathcal{D}_{\mathrm{N}}\left(E_{\mathrm{F}}\right) \frac{|E|}{\sqrt{E^2 - \Delta^2}} \Theta(E - \Delta) \tag{2.1}$$

where Θ is the Heaviside step function, $\mathcal{D}_{\mathrm{N}}$ is the normal density of states and Δ is the superconducting gap. The density of state (DOS) near the Fermi energy is plotted in Fig. 2.1 (c). Below the energy gap, $|E| < \Delta$, the DOS is zero, signifying the absence of quasiparticles. As energy surpasses $|E| \approx \Delta$, the DOS sharply increases, manifesting as a BCS DOS peak. Subsequently, it decreases for higher energies until it converges with the DOS of the normal state for $|E| \gg \Delta$.

2.2. Andreev reflection and proximity effect

To study semiconductor-superconductor (Sm-S) hybrid systems [50], it is important to understand the electron (hole) transport at Sm-S interfaces. Here, the semiconductor can be generalized as a normal conductor (N). Two different scenarios are shown in Fig. 2.2 (a). When an electron comes from N to the N-S interface with energy $|\epsilon| < \Delta$ relative to Fermi energy E_F, it cannot enter S due to absence of quasiparticle DOS.

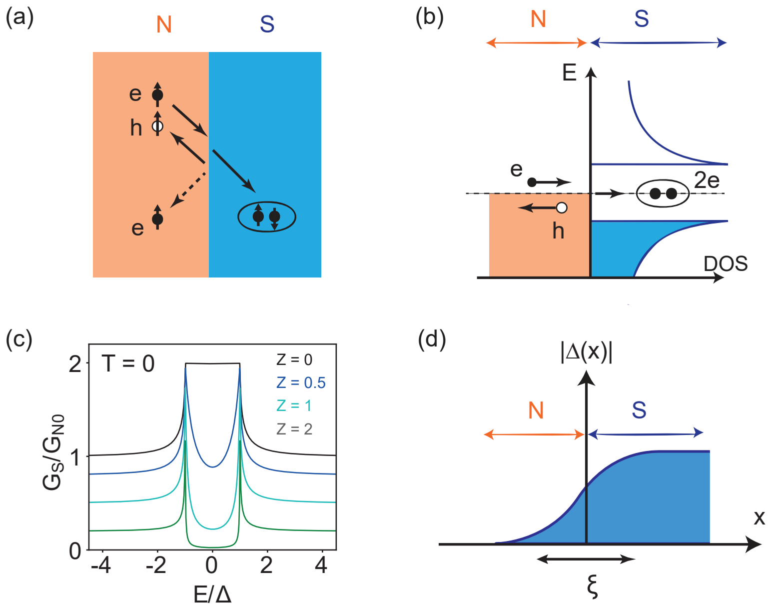

Figure 2.2. Andreev Reflection. (a) a Schematic illustration of Andreev reflection (solid line) and normal reflection (dashed line) of electron at normal-superconductor (N-S) interface. (b) Andreev reflection depicted in energy diagram. (c) Differential conductance $G_S(E)$ for an N-S junction according to the BTK model at $T = 0$, plotted for cases with different barrier strengths Z. (d) A schematic illustration of superconducting order parameter $|\Delta(x)|$ at N-S interface. The superconducting state leaks from S to N due to the proximity effect, with a characteristic coherence length ξ. Figure adapted from Ref. [35, 38, 51].

However, Alexander Andreev found in 1964 that the electron transport through N-S interface below the gap Δ is possible via a so-called Andreev reflection (AR) process [52]. This is shown in Figs. 2.2 (a) and (b). The incoming electron with energy ϵ above E_{F} can be retro-reflected as a hole with energy $-\epsilon$. The hole travels backwards along the trajectory of the incident electron. As a consequence, a Cooper pair can be transferred to the S. This process conserves energy, momentum and spin [53]. The conservation of momentum is an approximation, valid if the superconducting excitation gap Δ is much smaller than the Fermi energy E_{F} of the normal metal. Charge will also be conserved when taking into account the 2e charge of the Cooper pair. The spin of retro-reflected hole, defined as angular momentum, should have the same sign as the electron.

In reality, the probability of AR will be affected by elastic scattering. This process is well described by the BTK model [54], named after Blonder, Tinkham and Klapwijk. Here, the scattering potential at the N-S interface is modeled as a delta-function $V(x) = Z\hbar v_{\mathrm{F}}\delta(x)$ with a dimensionless barrier strength Z. Solving the Bogoliubov-de-Gennes equations with appropriately matching boundary conditions enables the derivation of an expression for the differential conductance, G_S, as a function of energy E and the strength of the barrier Z. This is plotted in Fig. 2.2 (c) for different Z. When $Z = 0$, we have perfect transmission and AR dominates, resulting in a doubling of G below the gap Δ. When Z increases, the AR is suppressed due to a non-perfect interface, and the conductance below the gap decreases correspondingly. In large Z case, the model describes tunneling spectroscopy measured in a N-insulator-S structure.

The AR process also induces a superconducting proximity effect, as dipicted in Fig. 2.2 (d). Considering the time-reversed process of AR, when a Cooper pair is extracted from the S, it results in the creation of an electron-hole pair in the N. This electron-hole pair remains phase coherent over a finite distance. Alternatively viewed, this phenomenon can be described as the leakage of the superconducting wavefunction into the N. Consequently, the N begins to acquire certain superconducting properties, such as an energy gap and paired electron states, over a characteristic length ξ_0. The coherence length ξ_0 depends on several factors, including the coherence length of the superconductor, the properties of the normal material, and the quality of the interface. In a simplified case, we can obtain the coherence length ξ_0 in clean (ballistic) and dirty (diffusive) limit [49, 55]:

$$\xi_0^{\mathrm{clean}} = \hbar v_{\mathrm{F}}/\pi\Delta, \tag{2.2}$$

$$\xi_0^{\mathrm{dirty}} = \sqrt{\hbar v_{\mathrm{F}} l_{\mathrm{e}}/(\pi\Delta)} = \sqrt{\xi_{\mathrm{clean}} l_{\mathrm{e}}}, \tag{2.3}$$

where v_{F} is Fermi velocity, and l_{e} is electron (hole) mean free path. In the case of $l_e < \xi_{\text{clean}}$, the coherence length will be reduced due to scattering. Moreover, it can be observed that a longer coherence length ξ is expected in a normal material with a larger v_F, when combined with a superconductor with a smaller superconducting gap Δ.

2.3. Andreev bound states

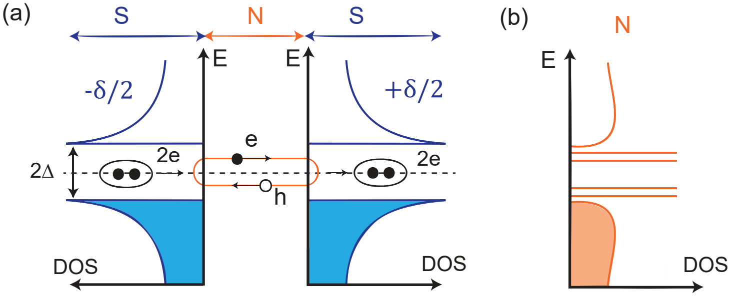

Figure 2.3. Andreev bound states. (a) Schematic illustration of Andreev bound states formed in a S-N-S junction. (b) Energy diagram of DOS in the normal section. The peaks in the gap represent ABSs. Adapted from [51].

Now, let us consider an S-N-S junction where AR can occur at both N-S interfaces, see Fig. 2.3 (a). Intuitively, one can imagine the electron-hole pair as being "trapped" within the N section. This confinement leads to the formation of bound states, analogous to the scenario of a particle-in-a-box problem in quantum mechanics. These bound states serve as the fundamental basis for superconducting transport in S-N-S junctions. To have a better understanding, we derive the energy spectrum of ABSs for different channel length. Here, we only consider the clean (ballistic) limit[2].

Short junction limit

We start with the simple case where the junction length L of the normal region is sufficiently small ($L \ll \xi$), such that the dynamic phase accumulated by an electron (or hole) when traveling through the normal region can be neglected. We assume that the left (L) and right (R) electrodes exhibit distinct superconducting phases of $\phi_L = -\delta/2$ and $\phi_R = +\delta/2$, respectively. The

---

[2] The mean-free path l_e of the Ge/Si NWs is $\sim 500\,\text{nm}$ [56], while the typical junction length of our devices is smaller than this value.

phases acquired in an AR process of an electron into a hole (φ_{eh}) and of a hole into an electron (φ_{he}) are [49, 55],

$$\varphi_{eh} = -\arccos\left(\frac{E_{\mathrm{A}}}{\Delta}\right) + \phi_{\mathrm{R}}, \quad \varphi_{he} = -\arccos\left(\frac{E_{\mathrm{A}}}{\Delta}\right) - \phi_{\mathrm{L}}, \tag{2.4}$$

In total, the phase acquired in the round trip is determined by the AR processes from both sides,

$$\begin{aligned} \phi_{\mathrm{tot}}^{+} &= \varphi_{eh} + \varphi_{he} \\ &= \left(-\arccos\left(\frac{E_{\mathrm{A}}}{\Delta}\right) + \delta/2\right) + \left(-\arccos\left(\frac{E_{\mathrm{A}}}{\Delta}\right) - (-\delta/2)\right) \\ &= -2\arccos\left(\frac{E_{\mathrm{A}}}{\Delta}\right) + \delta, \end{aligned} \tag{2.5}$$

where the + sign corresponds to the case of right moving electrons, as depicted in Fig. 2.3 (a). We note there is also the opposite process for a left moving electrons, this yields for a total phase

$$\phi_{\mathrm{tot}}^{-} = -2\arccos\left(\frac{E_{\mathrm{A}}}{\Delta}\right) - \delta. \tag{2.6}$$

If the total phase acquired within a full cycle is a multiple of 2π, $\phi_{\mathrm{tot}}^{\pm} = 0[2\pi]$, this results in a bound state in the weak link. The energy of the bound state is given by,

$$E_{\mathrm{A}}^{\pm}(\delta) = \pm\Delta\cos\left(\frac{\delta}{2}\right). \tag{2.7}$$

However, in a real device, a non-perfect interface could reduce the probability of AR process, and a normal refection where the electron is reflected back as an electron could also happen. In this case, Equation 2.7 can be rewritten by taking the junction transparency τ into account:

$$E_{\mathrm{A}}^{\pm}(\delta) = \pm|\Delta|\sqrt{1 - \tau\sin^2\left(\frac{\delta}{2}\right)}. \tag{2.8}$$

Long junction limit

Next, we consider the case where the junction length L is finite. In this case, the dynamical phase accumulated when the electron (hole) travels in the normal region needs to be considered [49, 55],

$$(k_h + k_e)L = 2EL/v_F = 2\lambda\epsilon. \tag{2.9}$$

where $\epsilon = E_{\mathrm{A}}/\Delta$ is the reduced energy, and $\lambda = L/(\hbar v_F/\Delta) = L/\xi$ is a dimensionless parameter that determines the effective length of the junction.

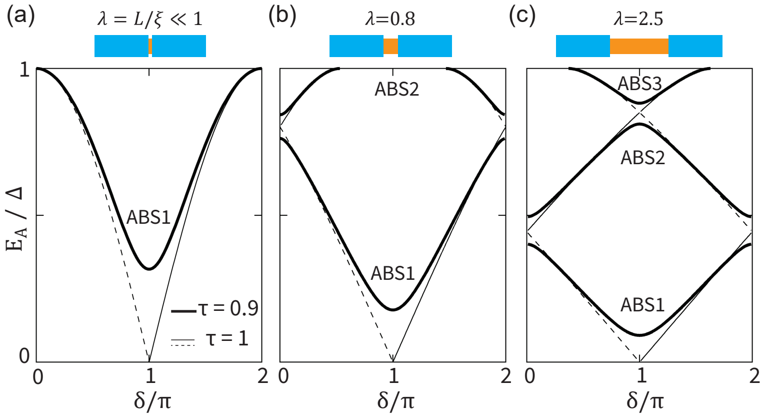

Figure 2.4. Andreev spectrum in different channel lengths. The positive branch of ABSs is shown for different parameter $\lambda = L/\xi$. The thin lines depicts energy dispersion for right-moving (solid) and left-moving-electrons with $\tau = 1$. The solid thick lines consider the case of finite transparency where $\tau = 0.9$. Adapted from [42, 57]

Here, $\xi = \hbar v_F/\Delta$ is the superconducting coherence length in the weak link. Now, we can take this dynamical phase into Equation 2.5, and derive the new resonant condition as

$$\pm\delta - 2\arccos(\epsilon) + 2\lambda\epsilon = 0[2\pi]. \tag{2.10}$$

An analytical solution to Equation 2.10 does not exist. Figure 2.4 presents the numerically calculated Andreev bound states (ABS) within the positive energy spectrum for three distinct junction lengths: $L \ll \xi$, $L = 0.8\xi$ and $L = 2.5\xi$. It is noteworthy that for each positive branch of the ABS, there exists a corresponding state with negative energy, attributable to the electron-hole symmetry inherent in ABS. In zero length limit ($\lambda = L/\xi \ll 1$), we recover the same result as in Equation 2.8. At phase of π, the positive branch and negative branch is separated by a gap of $2\Delta\sqrt{1-\tau}$.

For a junction with a finite length, more than one branch of ABSs emerges, as shown in Figs. 2.4 (b) and (c). The number of ABSs increases with λ, with a quantitatively estimation of $1 + \lfloor 2\lambda/\pi \rfloor$ to $2 + \lfloor 2\lambda/\pi \rfloor$ depending on δ ($\lfloor x \rfloor$ means the integer part of x) [42]. In addition, for finite τ, different branches of ABS are also separated by a gap [58].

However, it's worth to note that the spin degree of freedom has not been considered yet. This means all the spectra shown in Fig. 2.4 have a degeneracy of 2, representing spin ↑ and spin ↓. The spin degeneracy can be lifted in the presence of an external magnetic field, or spin-orbit interaction. The latter case will be discussed in the Section 2.7.

Terminology

We note that ABSs can be generalized to refer to bound states formed in an inhomogeneous superconductor [59], where $\Delta(x)$ varies with position x. In different systems, these bound states are given different names, reflecting the specific interactions they involve. For example, there are Caroli–Matricon–De Gennes states in superconducting vortices [60], Yu-Shiba-Rusinov (YSR) states in magnetic impurities of superconductor [61–63] and ABSs in SNS junctions as discussed above [64]. However, it is important to use the correct terminology when discussing different physics scenario.

For clarity, the ABS refers to the hybridization of empty (0) and doubly occupied (2) states. In contrast, the YSR state refers to the hybridization of [↑ + Cooper pair] and [↑↓+ Quasiparticle] states, with the energy difference given by $\Delta E = -E_{exchange} + 2\Delta$.

2.4. Josephson junction

While ABS provide a microscopic description of the states formed within a superconducting weak link, the Josephson effect is a macroscopic manifestation of these coherent states. Specifically, the ABSs facilitate the coherent transport of Cooper pairs between two superconducting leads, resulting in a dissipationless supercurrent that flows between the leads [51, 58, 65–68]. In 1962, Brian Josephson theoretically predicted this phenomenon in an S-I-S junction [69], where I stands for an insulator. In fact, the Josephson effect can be extended to scenarios where the weak link exhibits various forms, as depicted in Fig. 2.5.

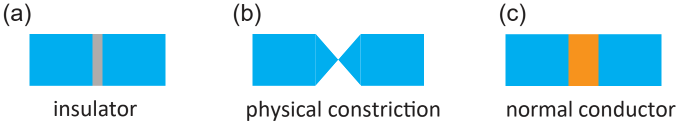

Figure 2.5. Types of Josephson junction. Different types of weak links connecting two superconductors: (a) an insultor, (b) a constriction or (c) a conductor. Adapted from Ref. [41].

The flow of supercurrent is driven by the phase difference between the superconducting leads. The fundamental equations governing the DC Josephson effect for a SIS junction is given by:

$$I(\varphi) = I_c \sin(\varphi) \tag{2.11}$$

where I_c is the critical current, and φ is the phase difference $\varphi = \phi_1 - \phi_2$. Equation 2.11 describe the relation between the current flowing through the weak link $I(\phi)$ and the phase drop ϕ, and therefore referred as current-phase relation (CPR). The maximum I_c depends on specific device parameters like size of the junction. We note that Equation 2.11 is only applicable to the case where the channel transparency is close to zero. The Al-Al$_x$O$_y$-Al tunneling junction is a classic example, where a thin layer of Al$_x$O$_y$ acts as the insulating barrier. This type of junction have been widely used in superconducting electronics, including in Superconducting Quantum Interference Devices (SQUIDs) and superconducting qubits. However, for other Josephson junction variants, the CPR deviates from a simple sinusoidal form, a topic will be discussed in the subsequent section.

2.4.1. Current-phase relation

In fact, there is a close link between ABSs $E_{\mathrm{ABS}}(\phi)$ and CPR $I_S(\phi)$ [55]:

$$I_S = \frac{2e}{\hbar} \sum_{\pm} \frac{\partial E_{\pm}^{\mathrm{ABS}}(\phi)}{\partial \phi} \tanh \left[\frac{E_{\pm}^{\mathrm{ABS}}}{2k_B T} \right] \tag{2.12}$$

In low transmission cases, ABSs would stick to the gap edge $E_{+}^{\mathrm{ABS}} \approx \Delta$. Summing over the transmission probabilities for all the channels, we obtain the Ambegaokar-Baratoff relation [70] for a tunneling junction:

$$I_S = \frac{\pi \Delta \sin(\phi)}{2eR_N} \tanh \left(\frac{\Delta}{2k_B T} \right) \tag{2.13}$$

Here, $R_N^{-1} = 2e^2/h \sum_p \tau_p$ represents the normal-state resistance of the junction, yielding a similar form as in Equation 2.11.

In the case of finite transmission ($0<\tau<1$), the CPR would deviate from standard sinusoidal form. For simplification, we plotted the ABSs spectra and the corresponding CPRs in the short junction limit, as shown in Fig. 2.6. When τ increases, the CPR exhibits a forward skewness. This skewed CPR have been reported in various experiments, like atomic point contact [71], nanowires [72], graphene [73, 74].

We note that the current studies mainly focus on CPR in the short junction limit. However, the CPR in long junction limit is less explored due to its complexity [58, 75–77]. In this limit, CPR could exhibits distinct patterns compared to Fig. 2.6 (b). In addition, spin-orbit interaction [78–83] and charging energy [84, 85] would also affect the ABS spectrum, resulting in an anomalous CPR, as shown in Fig. 2.7.

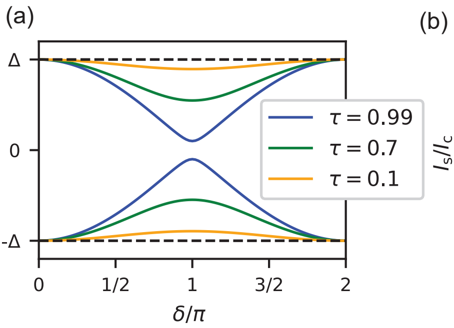

Figure 2.6. Current phase relation in the short junction limit. (a) The ABSs spetrum in a short junction limit for different transmission τ, plotted with Equation 2.8. (b) Current phase relation, calculated from the ABSs spetrum in (a), $I_S(\phi) = 2e/\hbar \frac{d}{d\phi} E_{\mathrm{ABS}}(\phi)$.

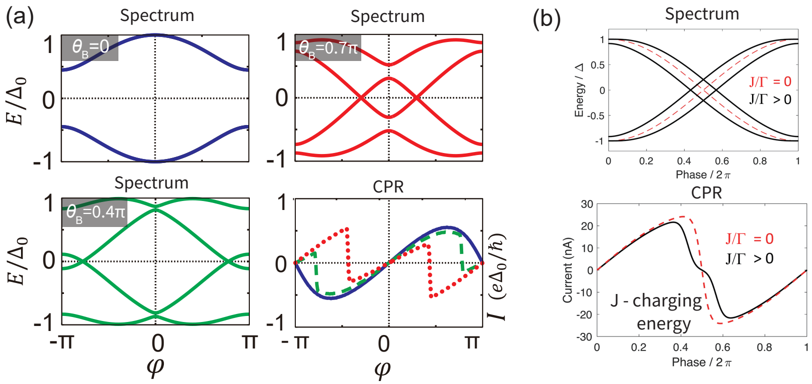

Figure 2.7. Anomalous CPR. (a) Effect of spin-orbit interaction on the ABSs spectrum and the CPR with a finite magnetic field. The magnetic field is defined as $\theta_B = 2E_Z/E_T$, where E_Z is the Zeeman energy and $E_T = \hbar v_F/L$ is the Thouless energy. **(b)** Effect of the charging energy on the ABSs spectrum and the CPR. The charging energy is modeled as an exchange energy J in this model, and Γ is the coupling strength to the superconducting lead. Adapted from Ref. [85, 86]

General properties of current-phase relation

Several characteristics of the CPR are notably universal, independent of the junction's materials, geometry, or the theoretical model employed to characterize the processes within the junction [87]. Here, we will briefly discuss these general properties.

(a) Phase change of 2π should not change physical state[3]: $I_S(\phi) = I_S(\phi+2\pi)$

(b) In the absence of an external magnetic field, time reversal symmetry should be preserved: $I_S(\phi) = -I_S(-\phi)$

(c) Supercurrent flows only with phase difference: $I_S(2\pi n) = 0$, $n = 0, \pm 1, \pm 2, ...$

(d) Following 1st and 2nd rules, supercurrent should be zero when $\phi = n\pi$: $I_S(\pi n) = 0$, $n = 0, \pm 1, \pm 2, ...$

With these general properties, $I_S(\phi)$ can be written as a Fourier series:

$$I_S(\phi) = \sum_{n\geqslant 1} \{I_n \sin(n\phi)\}\,, \tag{2.14}$$

where, I_n are coefficients determined from the specific junction. When time-reversal symmetry is broken, cos terms with coefficients J_n may appears in the CPR, as expressed by:

$$I_S(\phi) = \sum_{n\geqslant 1} \{I_n \sin(n\phi) + J_n \cos(n\phi)\}\,. \tag{2.15}$$

π junction and ϕ_0 junction

A particularly intriguing type of JJ is known as the π junction [88], in contrast to the standard 0 junction. In this case, the ground state of the junction is at $\phi = \pi$, and the supercurrent will be reversed in direction. A π junction can arise in quantum dots JJ [89, 90], ferromagnetic JJ [91], p-wave superconductors JJ [92], high temperature superconductor [93], non-equilibrium SNS junction [94].

Another interesting type of JJ is referred to as ϕ_0 junction [95], where the ground state is at phase $\phi = \phi_0$. The first ϕ_0 junction was reported in a superconducting-insulator-ferromagnetic-superconductor hybrid device [96]. Later, the ϕ_0 junction have been achieved in InSb NWs with strong spin-orbit interaction and external magnetic field [97].

Although Josephson effect is a long-established research area, novel phenomena and mechanisms continually emerge. In the context of quantum computing, a rapidly advancing field, the emergence of new types of JJs offers promising avenues for the development of novel qubit architectures [98–100].

---

[3] This rule may be not valid for a topological junction with 4π periodic CPR.

2.5. Quantum dots

Quantum dots (QDs) commonly appear in the measurements of semiconductor nanostructures, including NWs and gate-defined structures within two-dimensional electron gases (2DEGs). Therefore, understanding the underlying mechanisms is crucial. In these nanostructures, the three-dimensional confinement of charge carriers (electrons and holes) leads to quantized energy levels. Consequently, quantum dots emerge, exhibiting interesting effects like Coulomb blockade, single-electron tunneling, etc.

Quantum dot model & Coulomb blockade diamonds

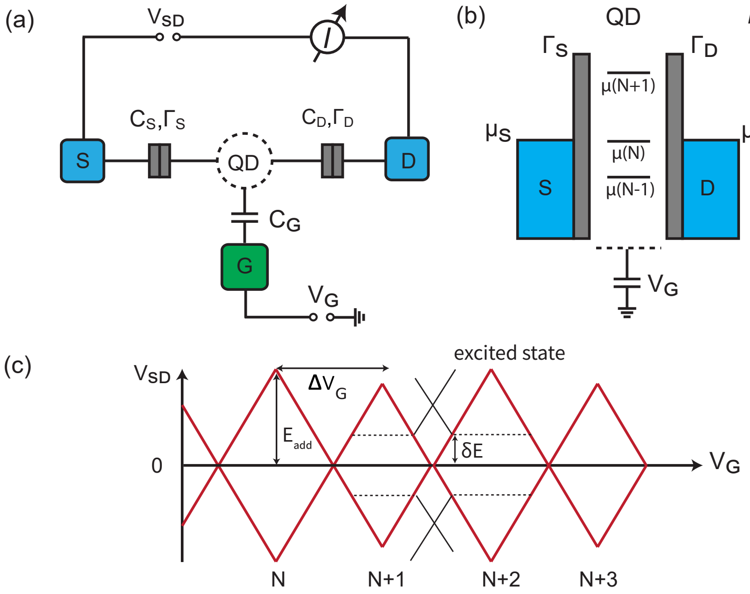

Figure 2.8. Quantum dot model.(a) Capacitance model and typical circuit measurement diagram. A quantum dot (QD) is tunnel coupled to a source-drain leads with capacitances $C_{S/D}$ and tunnel coupling $\Gamma_{S/D}$. A purely capacitive coupling C_G to the gate (G) allows to tune the electrochemical potential of the QD. **(b)** Schematic of the energy level diagram of a QD with N electrons and electrochemical potential μ_N. **(c)** Coulomb blockade diamonds. Current can flow in the outside the diamonds. Adapted from [35, 38, 101, 102].

We first discuss simple case for a N-QD-N. In this case, a QD is tunnel-coupled to two electrodes, a source and a drain, as depicted in Fig. 2.8 (a). A gate is capacitively coupled to the QD, allowing for tuning the electrochemical potential of the QD, see Fig. 2.8 (b). During the measurements, a source-drain bias voltage V_{SD} is applied to the QD, which establishes a difference between the electrochemical potentials μ_{S} and μ_{D}.

The characteristic energy scale defining a QD is the charging energy, $E_C = e^2/C$, where C is the self-capacitance of the QD. In large structures, E_C is typically negligible. However, as the size diminishes to the order of a few hundred nanometers, C decreases significantly, making E_C the dominant energy term within the system. Essentially, E_C can be interpreted as the energy required to overcome the Coulomb interaction when adding an additional electron to the QD.

To observe the QD effect, certain requirements must be met [34]:

- The charging energy should be greater than the thermal energy, $E_C \gg k_B T$, with k_B being the Boltzmann constant and T the temperature. This necessitates that the dot be sufficiently small, and the temperature be kept suitably low.

- The quantum dot should be sufficiently isolated, which means the tunnel coupling Γ should be much lower than the charging energy $E_C \gg h\Gamma$, where h is Planck's constant. Alternatively viewed, the tunnel resistance being substantially greater than the resistance quantum $R_t \gg h/e^2 = 25.813\,\mathrm{k\Omega}$.

In measurements, QD are characterized by Coulomb blockade (CB) diamonds, as illustrated in Fig 2.8 (c). Single-electron transport typically occurs when $\mu_S \geq \mu_N \geq \mu_D$, meaning that a QD energy level must lie within the bias window. Consequently, transport is blocked inside these diamond-shaped regions, an effect known as Coulomb blockade.

The situation, however, is more complex in reality. The QD can exhibit quantized energy levels E_{orb}, akin to real atoms and therefore named as "artificial atoms" [103]. As a consequence, the vertical extent of CB diamonds is determined by $E_{\mathrm{add}} = E_C + E_{\mathrm{orb}}$. In many systems, an odd-even occupancy pattern of the QD is expected. Nonetheless, in materials like graphene [104–106] or carbon nanotubes [107–109], a fourfold degeneracy is often observed. Moreover, the excited states of QD's level could also be involved in transport, featuring as co-tunneling line inside the CB diamonds as indicated by the dashed lines in Fig. 2.8 (c). Another important concepts for QDs is the lever arm α of the gate, which determines the efficiency of changing μ_N with the gate voltage V_G. The lever arm can be directly deduced from the Coulomb blockade diamond, calculated as $\alpha_G = V_{SD}/\Delta V_G$.

Double quantum dot model & charge stability diagram

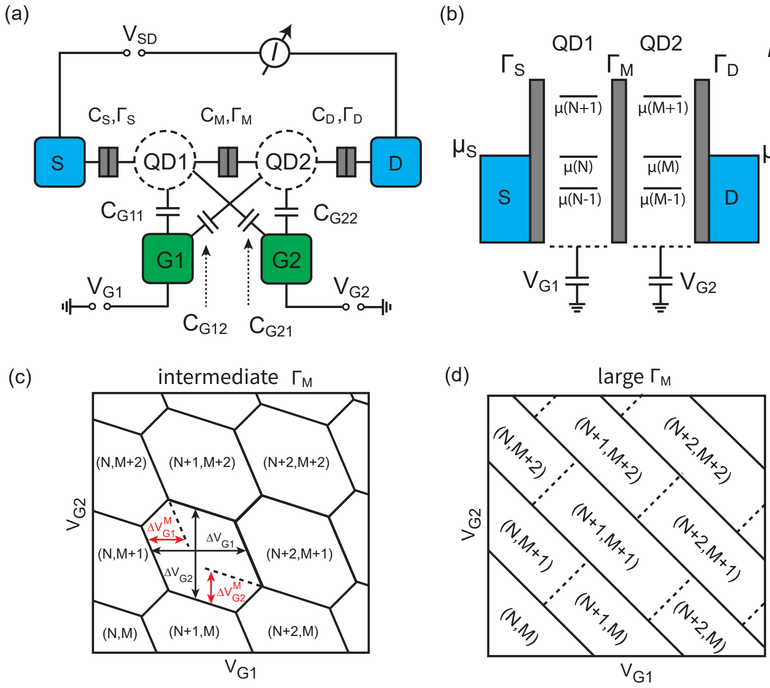

Figure 2.9. Double Quantum dot (DQD) model. (a) Capacitance model and typical circuit measurement diagram for a DQD. QD1 and QD2 are tunnel coupled to source (S) and drain (D), and they are also tunnel coupled to each other. The corresponding coupling strengths $\Gamma_{S/M/D}$ are indicated in the figure. The gates ($G_{1/2}$) are used to tune electrochemical potentials for each QD, typically with cross-talks involved. **(b)** Schematic of the energy level diagram of a DQD. **(c)** Charge stability diagram with an intermediate inter-dot coupling Γ_M. **(d)** Charge stability diagram with a large inter-dot coupling Γ_M, featuring an effective single dot. Adapted from [35, 38, 40, 101, 102].

Next, we consider two QDs connected in series as shown in Fig. 2.9 (a) and (b). Two QD have occupancy N and M with electrochemical potentials μ_N and μ_M. Similarly, the charge transport require $\mu_S \geq \mu_N \geq \mu_M \geq \mu_D$. When the inter-dot coupling strength Γ_M is large enough, the middle barrier does not effectively separate the charges in two QDs. In this case, we restore the case of single quantum dot, and the charge stability diagram is shown in Fig. 2.9 (d).

The interesting case would be Γ_{M} is comparable $\Gamma_{\mathrm{S/D}}$. Then charge can be individually filled into both QD. The occupancy configuration (N,M) of DQD is depicted by a honeycomb pattern, as shown in Fig. 2.9 (c). Considering the spin degree of freedom introduces additional phenomena, such as the Pauli spin blockade [110]. This concept is particularly relevant in the spin qubit community, as it represents the simplest method for spin readout [111].

2.5.1. Quantum dot coupled to superconducting leads

In this section, we will explore a quantum dot coupled to superconducting leads. In this hybrid device [112], the interplay between the superconducting pairing mechanism and the physics of QD creates intriguing conditions that facilitate single-electron tunneling. Moreover, the strength of coupling between the superconducting electrodes and the quantum dots can be tuned, and different regimes of coupling exist, such as weak, intermediate, and strong coupling. These three regimes can be classified as following:

- Weak coupling: $\Gamma \ll \Delta, E_{\mathrm{add}}$
- Strong coupling: $\Gamma \gg \Delta$
- Intermediate coupling: $\Gamma \sim \Delta \sim E_{\mathrm{add}}$

where Γ is coupling strength to the superconducting lead, Δ is the superconducting gap, E_{add} is the addition energy of QD. Next, we will discuss these three regimes. This part follows Ref. [37, 38].

Weak coupling regime

In the weak coupling regime, the transport behavior is characterized by the suppression of Cooper pair tunneling and the dominance of quasiparticle tunneling. This means that the transport of individual quasiparticles with charge 1e across the quantum dot is possible, and the supercurrent is absent. Additionally, the onset of quasiparticle tunneling ($|eV_{SD}| > 2\Delta$) is accompanied with a sharp increase in the current due to the BCS density of state (DOS) peak in the leads. The emergence of negative differential resistance is also anticipated, resulting from the BCS peaks in the superconducting leads on both sides.

Strong coupling regime

In the strong-coupling regime, transport behavior is marked by the near-absence of Coulomb blockade, owing to the fast tunneling rates (Γ) to the superconducting leads. Consequently, the transport of Cooper pairs becomes feasible, leading to the emergence of a supercurrent. For a single non-interacting quantum dot situated between two superconductors with equal tunnel barriers, the maximum value of the resonant supercurrent can be expressed as $I_C = (\pi e/h)\Gamma\Delta/(\Delta + \Gamma/2)$ [113].

Intermediate coupling regime

In the intermediate-coupling regime, the energy scales Γ, Δ, and U are comparable. This makes it the most complex and intriguing regime. In this regime, Cooper pairs can split into quasiparticles with a charge of 1e, which can tunnel individually across the quantum dot. If the time it takes the quasiparticles to tunnel across the dot is shorter than the characteristic coherence time of the Cooper pairs, it is possible for the Cooper pairs to reform in the second electrode. The transport behavior in this regime is highly dependent on the electronic state of the quantum dot, with the precise nature of the supercurrent being influenced by this electronic state.

Andreev bound states formed in QD

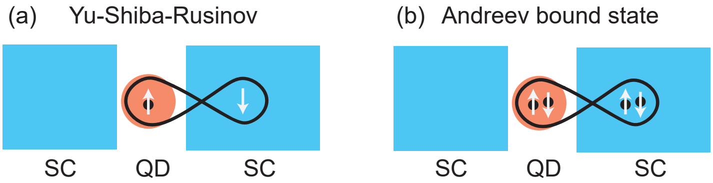

Figure 2.10. Schematic of states formed in proximitized QD. (a) Yu-Shiba-Rusinov states (b) Andreev bound states.

When coupled to SC lead, ABSs [4] could formed in QD. The formation of ABSs can be understood by considering a single QD level proximitized by the SC lead, forming new subgap eigenstates.

In the case of even charge states, Cooper pairs could enter or leave the QD, manifesting as a BCS-like superposition of an empty and a doubly occupied QD levels [116–118]. The system has a singlet ground state. When the QD is oddly occupied, it holds an unpaired spin. This situation is conceptually similar to the presence of an isolated magnetic impurity within a superconductor, as shown in Fig. 2.10. The magnetic impurity gives rise to localized bound states within the superconducting gap, as proposed by Luh Yu [61], Hiroyuki Shiba

---

[4] In some references, this is call Andreev level[114], or Andreev resonances [115]

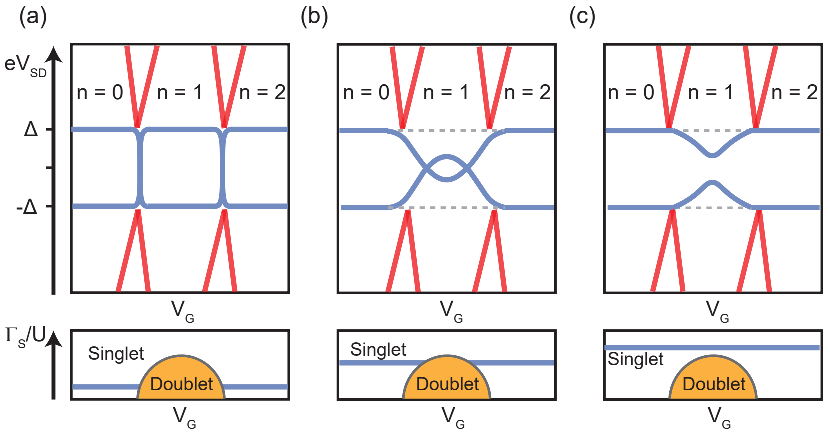

Figure 2.11. Andreev bound states as a function of gate. (a)-(c) Qualitative schematic of gate dispersion of ABS resonances (blue) in charge stability diagram of QD (red). The coupling strength to the superconductor Γ_S increases from (a) to (c). The corresponding bottom panels illustrate the predicted phase diagram with respective ground state as a function of Γ_S/U and gate voltage V_G. Adapted from [35, 36, 38, 51].

[62], and Anatole Rusinov [63]. In this case, a doublet ground state is expected. However, if the coupling strength (Γ_S/U) reaches a critical threshold, the system undergoes a quantum phase transition, resulting in a magnetically screened, spin-singlet ground state, as shown in bottom panel of Fig. 2.11 (c). Figure 2.11 shows a schematic of ABS dispersing with gate, in different coupling strengths [119].

The ABSs in QD have been experimentally reported in various systems, like carbon nanotube [51, 120, 121], InAs NWs [114, 122–124].

2.6. Transmon

Now, we discuss an important application of JJ in the field of quantum computing. Superconducting qubits are the most popular quantum computing platforms [33, 126]. Leveraging Josephson junctions as a basic element, qubits can be engineered in different degrees of freedom, such as charge [127, 128], flux [129, 130] and phase [131]. Figure 2.12 presents a classification of superconducting qubits based on the ratios E_J/E_C and E_J/E_L [125], where E_J is Josephson energy, E_C is charging energy and E_L is inductive energy. De-

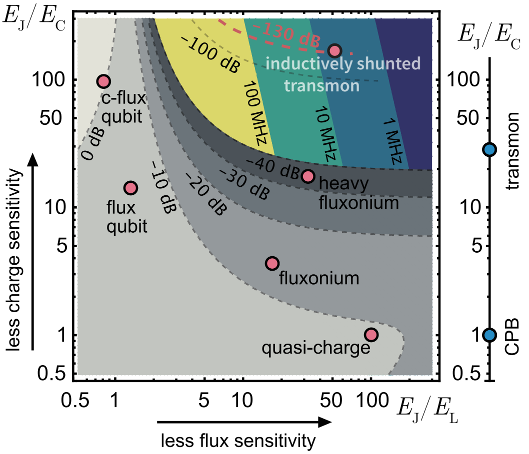

Figure 2.12. Types of superconducting qubits. Classified according to E_J/E_C and E_J/E_L ratio. Adapted from Ref.[125].

tailed discussions about the advantages and disadvantages of different types are available in Ref. [132–134].

In this section, our focus will be on the transmon qubit, short for "transmission line shunted plasma oscillation qubit", a particular type of superconducting qubit [135]. Transmon is an extension of the "Cooper pair box" qubit [127], where the charge sensitivity is significantly reduced by the use of a large shunt capacitor, as shown in Fig. 2.13 (b).

To understand the transmon quantum levels, we can simply compare it to a classical harmonic oscillator, as shown in Fig. 2.13 (a). With quantum-mechanical quantization of this LC oscillator, one would obtain equally spaced energy levels $\hbar\omega_r$, due to the linear characteristics of L_r and C_r. To have a well-define two-level state as a qubit, a non-linear element is required. To this ends, a SIS JJ can serve as an non-linear inductor with:

$$V_J = \frac{\Phi_0}{2\pi I_C \cos\delta}\frac{dI}{dt}, \tag{2.16}$$

where the Josephson inductance reads

$$L_J = \frac{\Phi_0}{2\pi I_C}\frac{1}{\cos\delta}. \tag{2.17}$$

The non-linearity in the system arises from the $\cos\delta$ terms, leading to the formation of energy levels that are not equally spaced, as illustrated in Fig. 2.13

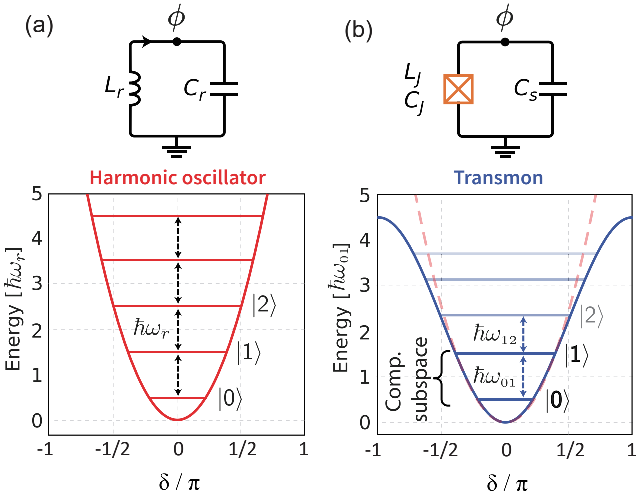

Figure 2.13. From harmonic oscillator to transmon. Adapted from Ref.[32].

(b). The lowest two energy levels of this configuration can serve as the computational subspace for the qubit, representing the $|0\rangle$ and $|1\rangle$ states. In the meantime, the shunt capacitor could minimize the effect of charge fluctuation on the qubit energy level.

An important parameter is E_J/E_C ratio. As shown in Fig. 2.14, for large ratio, the energy dispersion with charge offset n_g is negligible, and the qubit frequency is given by $\hbar f_q \approx \sqrt{8E_C E_J}$. The anharmonicity is another important parameter for transmon, defined as the energy difference $\hbar\alpha = E_{12} - E_{01}$. In the transmon limit, the anharmonicity is determined by the charging energy $\alpha \approx E_C$.

However, when replacing the SIS JJ with SNS JJ with finite transparency T_i, the Josephson potential will be different. This will modify the f_q and α accordingly [136]. In this case, the Hamiltonian can be written as

$$\hat{H} = 4E_C\hat{n}^2 + V(\hat{\phi}) = 4E_C\hat{n}^2 - \Delta\sum_i \sqrt{1 - T_i \sin^2(\hat{\phi}/2)}, \tag{2.18}$$

where Δ, T_i, and $\hat{\phi}$ are the superconducting gap, the individual channel transparencies, and the phase difference between SC leads. The Hamiltonian can be expanded to fourth order in $\hat{\phi}$ around the potential minimum at $\hat{\phi} = 0$,

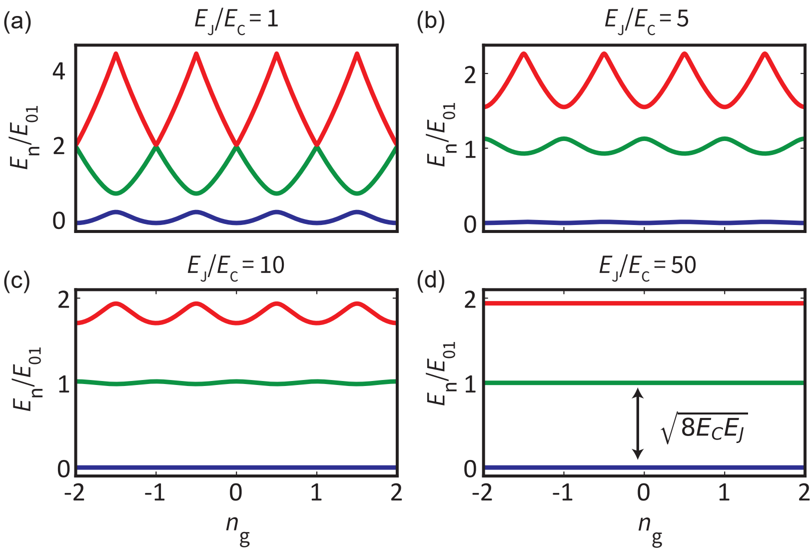

Figure 2.14. Transmon energy level. Eigenenergies E_n of transmon as a function of effective charge offset n_g, at different E_J/E_C ratio. For large E_J/E_C ratio, the transmon energy become insensitivity to charge fluctuation. Adapted from Ref.[135].

$$\begin{aligned} V(\hat{\phi}) &\approx \frac{\Delta}{4}\sum_i \left[\frac{T_i}{2}\hat{\phi}^2 - \frac{T_i}{24}\left(1-\frac{3}{4}T_i\right)\hat{\phi}^4\right] \\ &= E_J\frac{\hat{\phi}^2}{2} - E_J\left(1-\frac{3\sum T_i^2}{4\sum T_i}\right)\frac{\hat{\phi}^4}{24}. \end{aligned} \tag{2.19}$$

Treating the non-harmonic terms as a perturbation [136], we can obtain the qubit frequency and anharmonicity as,

$$hf_{01} = \sqrt{8E_\mathrm{c}E_\mathrm{J}} - E_\mathrm{c}\left(1-\frac{3\sum_i T_i^2}{4\sum_i T_i}\right) \tag{2.20}$$

and

$$\alpha = -E_\mathrm{c}\left(1-\frac{3\sum_i T_i^2}{4\sum_i T_i}\right). \tag{2.21}$$

Inspecting Equations 2.20 and 2.21, we see that the f_q will only be slightly modified with a small correction term. However, α could be significantly reduced, up to a factor of 4, when T_i is approaching unity.

2.7. Andreev qubit

Recently, the Andreev qubit has emerged as a novel platform for quantum computing. This approach leverages fermionic excitations in individual Andreev levels to define a qubit, a concept proposed over two decades ago [137, 138]. Additionally, spin-orbit interactions (SOI) play a crucial role in lifting the spin degeneracy of ABSs, facilitating the encoding of quantum information within the pseudospin states of the JJ [139–141].

To implement Andreev qubits, it is essential to have a superconducting weak link with few channels and high transparency. This combination minimizes the number of ABSs in the spectrum and ensures the transition frequencies of these fermionic excitations are within the accessible range for circuit-QED techniques. For Andreev spin qubits, the presence of SOI is also required. Hybrid nanowires, with their inherently strong SOI and high-quality interfaces, offer a feasible platform for Andreev (spin) qubits [142–144].

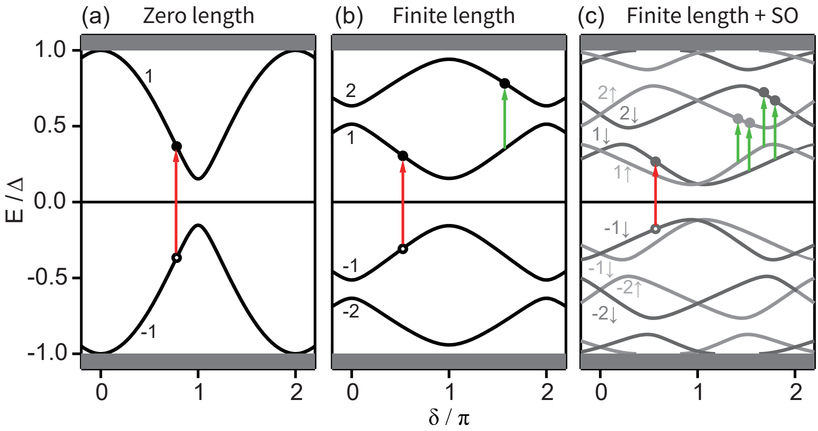

Figure 2.15. Andreev bound states with spin-orbit interaction. (a) ABSs in short junction limit. (b) ABSs with finite junction length. (c) ABSs with finite junction length and Rashba SOI. The arrows indicated quasiparticle excitations that can occurs. The red arrows represent pair transitions (PT), while the green arrows indicate single-quasiparticle transitions (SQPT). Adapted from Ref.[42].

In the following discussion, we delve into the physics of spin-split ABSs resulting from SOI, and the Andreev spectrum as observed under microwave excitation. In Section 2.3, we have discussed the ABSs in the short and long junction limit, the corresponding spectrum is schematically shown again in

Figs. 2.15 (a) and (b). To account for the SOI, we model a nanowire oriented along the $\hat{x}$ direction, and consider an electric field arising from bulk or structural asymmetry in the $\hat{z}$ direction. This leads to the following Hamiltonian [42]:

$$H = H_0 + H_{SO} = \frac{\hbar^2 \vec{k}^2}{2m^*} + U(y,z) - \alpha \hat{z} \cdot (\vec{k} \times \vec{\sigma}), \tag{2.22}$$

where m^* represents the effective mass of the electron, $U(y,z)$ denotes the confining potential in the transverse direction, α is the SO coupling strength, and $\vec{\sigma}$ is the vector of Pauli matrices.

In a 1D nanowire, confinement in transverse direction leads to a quantized mode. Under a quantum harmonic oscillator assumption, one obtain $\hbar^2 \left(k_y^2 + k_z^2\right)/2m^* + U(y,z) = \hbar\omega_0(n+1/2)$, where n represent transverse mode number. Equation 2.22 can be simplified as,

$$H = \frac{\hbar^2 \left(k_x - k_\alpha \sigma_y\right)^2}{2m^*} + \alpha k_y \sigma_x + \hbar\omega_0 \left(n + \frac{1}{2}\right) - \frac{m^* \alpha^2}{2\hbar^2}. \tag{2.23}$$

In this case, each transverse band will spin-split in two subbands. In addition, $\alpha k_y \sigma_x$ could couple different transverse sub-bands with opposite spin, leading to hybridized bands. In this context, spin is not a conserved quantity. However, it is still possible to assign a pseudospin for each subbands. The resulted ABSs spectrum with SOI is depicted in Fig. 2.15 (c).

Two kinds of qubits can be realized using the Andreev spectrum. The first type is known as the *Andreev level qubit*. In this case, under microwave excitation, a quasiparticle transitions from the lower branch ($E < 0$) to the upper branch ($E > 0$) of the ABSs, as indicated by the red arrows in Fig. 2.15. This process, called pair transition (PT), is characterized by the system occupying even states. The second type, referred to as the *Andreev spin qubit*, occurs when a quasiparticle trapped in the upper branch of ABSs being excited by a microwave photon to a higher branch, as indicated by the green arrows. This process is known as a single-quasiparticle transition (SQPT), and happens when the system is in the odd states.

Figure 2.16 shows the simulated and measured excitation spectrum of ABSs with a InAs/Al NW JJ. We note that the electron-electron interaction could also play a role, as shown in Fig. 2.16 (b). The odd states (SQPT), as indicated by the green lines, have a "spider" pattern. The even states (PT), often have a parabolic-like dispersion in phase.

Last but not the least, the discussion and theoretical model, as in Equations 2.22 and 2.23, are based on electron band with standard Rashba SOI. However, in our experiments with Ge NWs, the conduction occurs through a hole-band, and the SOI arises primarily from significant heavy-hole light-hole mixing, instead of the standard Rashba SOI. To our knowledge, there is no existing theoretical work that has explored the Andreev spectrum in this context.

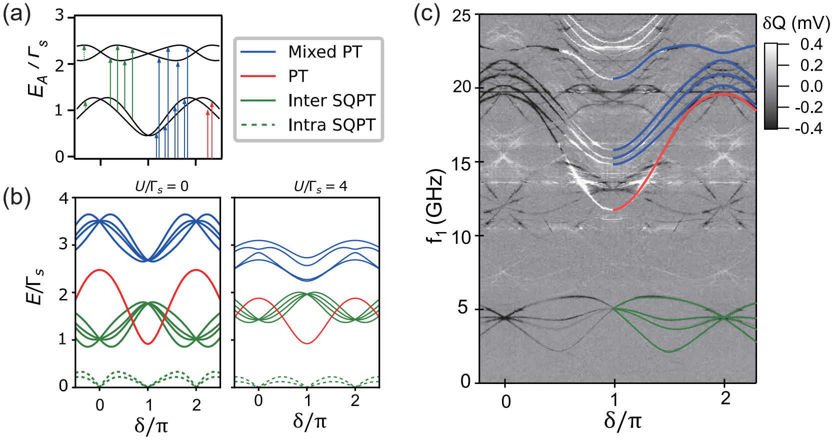

Figure 2.16. Andreev excitation spectrum. (a) Transitions involved in the excitation spectrum. (b) Excitation spectra with and without electron-electron interaction. (c) Andreev excitation spectrum measured in two-tone spectroscopy. Adapted from Ref.[42].

3 Material Platform [1]

"Not to be confused with geranium."
— Wikipedia page of Germanium

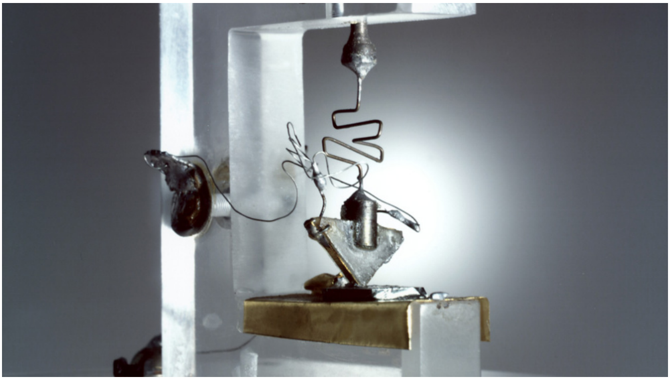

In this chapter, we will discuss the material platform forming the basis of this thesis: Germanium (Ge). We will start with the fundamental properties of Ge and its historical applications in transistors. Following that, we will discuss the Ge hole band within confined structures, with a focus on heavy-hole (HH) and light-hole (LH) states in lower dimensions. Finally, we will address the growth of Ge/Si core/shell nanowires (NWs) and discuss their transport properties.

3.1. Germanium

Germanium, first discovered in the late 19th century, has played a pivotal role in the development of semiconductor technology. Although less abundant than silicon, Ge is found in various minerals and is commercially obtained as a

---

[1] The title image is the very first germanium transistor, which was created in Bell Labs in 1947.

byproduct of sphalerite zinc ores [145]. Its crystal structure is similar to that of silicon, with a diamond cubic crystal structure.

Ge was the material used in the first transistors, which were developed in the Bell Labs in 1948. Its use in early transistors marked the beginning of the semiconductor revolution. In fact, the first 20 years of semiconductor industry exclusively relied on the Ge diode and the bipolar-junction-transistor [22]. The advantages of Ge transistors include higher carrier mobility compared to Si. Despite this, they were eventually surpassed by Si transistors due to Si's better thermal stability and the excellent quality of SiO_2.

Recently, advances in materials science, such as the integration of Ge on a Si wafer with a Si_xGe_{1-x} buffered layer [146–148], and the development of high-quality gate dielectrics for Ge [149–151], have significantly mitigated the shortcomings of Ge. Consequently, Ge is experiencing a revival as a material that enables high-speed and low-power-consumption transistors [22, 152, 153].

In the realm of quantum information processing, Ge also emerges as a promising material [21]. Ge's properties, like high hole mobility and strong spin-orbit coupling, make it a strong candidate for quantum information applications. The strong spin-orbit coupling in Ge facilitates fast-electric-control over qubit states, and the reduced hyperfine interaction boost the coherence time in Ge based qubits.

From a fabrication perspective, Ge offers several advantages. Most metal contacts to Ge exhibit a Fermi level pinned near the valence band, including superconductors. This simplifies the establishment of Ohmic contacts with confined holes in Ge, eliminating the need for local doping or implantation. Additionally, the low Schottky barrier at the metal-semiconductor interface facilitates the creation of transparent contacts to superconductors, a crucial element in semiconductor-superconductor hybrids. In the case of Ge quantum wells, the small effective mass of heavy-hole (HH) states simplifies fabrication, allowing for relatively large planar Ge quantum dots. Furthermore, Ge is a foundry-compatible material, supporting advanced device manufacturing and integration. This is pivotal for the development of large-scale quantum systems.

3.2. Physics of holes in Germanium

A hole can be understood as an unfilled valence-band state. The interest in Ge for quantum information primarily arises from its unique properties in the valence band. Therefore, we will focus on the physics of holes in Ge in the following section.

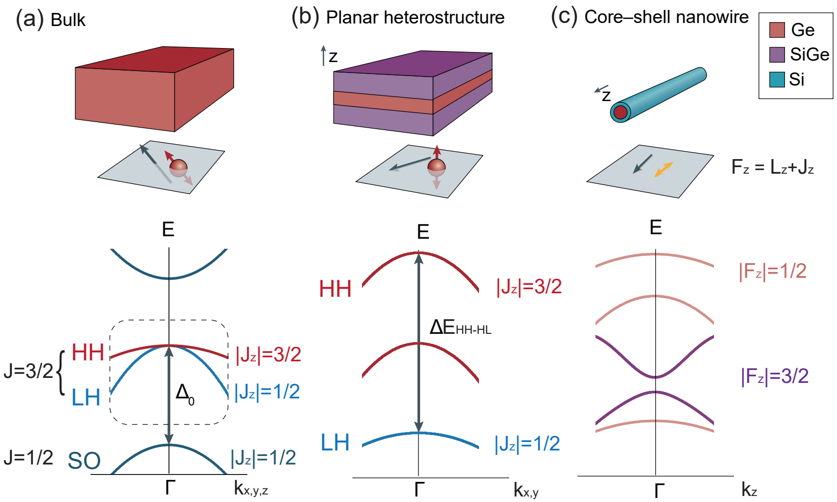

Figure 3.1. Germanium hole band in confined structures. **(a)** Bulk Ge and the band structure (bottom). The topmost hole band consists of heavy-hole (HH) and light-hole (LH) bands. **(b)** Planar heterostucture. The HH and LH bands are split by $\Delta E_{\text{HH-LH}}$ due to strong confinement along the z axis. The ground state is the HH state. **(c)** In Ge/Si core-shell nanowires, the HH and LH states are heavily mixed due to strong confinement in two axes. The new eigenstates are grouped via the total angular momentum F_z along the NW. Adapted from Ref. [21].

Bulk Ge

Let us begin with bulk Ge. In Ge, the electrons in the conduction band possess s-like orbitals, whereas the holes in the topmost valence band exhibit p-like orbitals. This means that, in the Ge valence band, the orbital angular momentum quantum number is l=1. Next, taking spin into account, the valence band states are characterized by a total angular momentum quantum number j of 3/2 and 1/2, with a spin-orbit gap denoted as Δ_0 separating them, as shown in Fig. 3.1 (a). Notably, for Ge, this spin-orbit gap is relatively large, approximately 0.3 eV. Consequently, in most cases, we only consider the properties of holes in the topmost valence band.

Near the gamma point, the states in the topmost valence band of Ge are well described by the Luttinger-Kohn Hamiltonian in the spherical approximation:

$$H_{\mathrm{LK}} = -\frac{\hbar^2}{2m_0}\left[\left(\gamma_1 + \frac{5}{2}\gamma_s\right)k^2 - 2\gamma_s(\boldsymbol{k}\cdot\boldsymbol{J})^2\right], \tag{3.1}$$

where m_0 is free electron mass, $k^2 = \boldsymbol{k}\cdot\boldsymbol{k} = k_x^2 + k_y^2 + k_z^2$, $\hbar\boldsymbol{J}$ is the operator for an effective 3/2 spin, γ_1 and γ_s are material-dependent parameters. When solving this equation, the eigenstates of H_{LK} can be grouped into heavy-hole (HH) and light-hole (LH) states. For HH states, the effective spin 3/2 is parallel or antiparallel to the hole's direction of motion, with an effective HH mass $m_{\mathrm{HH}} = m_0/(\gamma_1 - 2\gamma_s)$. For LH states, the 1/2 spin is projected along the direction of motion, with a LH mass $m_{\mathrm{HH}} = m_0/(\gamma_1 + 2\gamma_s)$. It is noteworthy that the $\boldsymbol{k}\cdot\boldsymbol{J}$ term in the Hamiltonian highlights a crucial feature of hole states: the close interrelation between crystal momentum and effective spin.

Ge Planar heterostructure

We now consider the case of strong confinement in one axis (out-of-plane), such as a Ge/SiGe planar heterostrucure as shown in Fig. 3.1 (b). Now, the hole gas is confined to the strained Ge layer because of the valence-band offsets between Ge and SiGe. Specifically, the type of band offset (type-I or type-II) depend on both the strain and the heterostructure stack composition [154].

Due to the strong confinement in the z axis, the holes in Ge quantum well can only propagate in-plane. In this case, the hole states in the topmost valence bands can be classified by the out-of-plane component of the effective spin. States with $J_z = |3/2|$ and $J_z = |1/2|$ are denoted as HH and LH states, respectively. However, it is important to note that HH and LH states are not identical to the bulk, since the effective spin is defined along a different direction. As a result, the HH states in the Ge quantum well, surprisingly, have a smaller effective mass, and vice versa for LH states.

Moreover, confinement and strain also induce a significant splitting of more than 100 meV between HH and LH states, with HH states being energetically favored. It turns out that HH states have a very small in-plane effective mass of $\sim 0.05m_0$ at the topmost of the valence band. The small effective mass means quantum effects can be observed in a relatively large size. This is also the reason why research in hole spin qubits in Ge quantum wells has witnessed rapid progress, advancing from single quantum dots to a four-qubit processor [25] in a very short time.

Ge/Si core/shell NW

Now, we discuss the one-dimensional version of Ge nanostructures, specifically the Ge/Si core/shell NW as shown in Fig. 3.1 (c). Si and Ge have different band gap energies, which are 1.14 eV for Si and 0.67 eV for Ge. This leads to

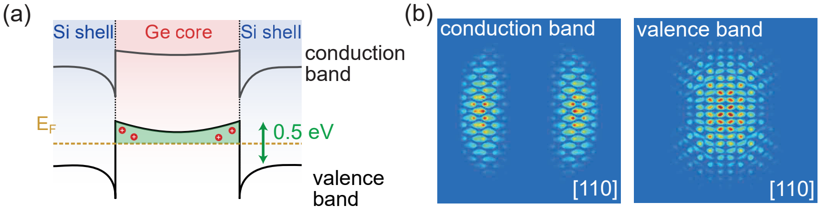

Figure 3.2. Ge/Si core/shell NW. (a) The schematic band structure alignment of a Ge/Si core/shell nanowire results from a combination of band offsets and interface states, leading to the formation of a hole gas within the Ge core. (b) The charge distribution in the conduction band and in the valence band of a [110] Ge/Si core/shell nanowire. Due to the type-II band alignment, electron and hole states are localized in distinct regions: conduction band states primarily within the Si shell, and valence band states concentrated within the Ge core. Adapted from Ref. [155–157].

a valence band offset of about 0.5 eV at the Ge/Si interface, confining holes in the Ge core, as illustrated in Fig. 3.2 (a).

Moreover, from numerical simulations in Ref. [155, 158], the valence band states of a Ge/Si core/shell nanowire are concentrated within the Ge core, with a notable spatial separation from the surface. This is shown in the simulated charge distribution as illustrated in Fig. 3.2 (b). Due to this mechanism, the holes in Ge are less susceptible to scatters/defects in the Si shell and Ge/Si interface, resulting in a very high carrier mobility in transport. It's noteworthy that the charge distribution of Ge valence band states also strongly depends on the growth direction [155, 158]. This is in good agreement with the reported high mobility in [110] direction NWs, comparing to a lower mobility that it is found in [111] direction [159].

Furthermore, the presence of strain in Ge/Si core/shell nanowires can have a profound impact on the band structure, consequently influencing some important properties. Ge has a lattice constant of 5.66 Å, whereas Si has a lattice constant of 5.43 Å. This yields a 4% lattice mismatch. As a result, the Si shell will compressively strain the Ge core. Moreover, the effective mass m_{eff} in the Ge/Si core/shell nanowires exhibits a strong dependence on strain [160, 161]. Specifically, m_{eff} is found to be influenced by the thickness of the Si shell. Calculations have indicated that m_{eff} can vary widely, ranging from small values ($<0.1m_0$) to infinity, and it can even undergo a change in sign. Larger effective mass have the effect of reducing the kinetic energy term, thereby enhancing the hole–hole interactions. This is primarily interesting for the exploration of Majorana physics.

More intriguingly, due to the strong confinement of holes in two axes, the

HH and LH states are largely mixed. Consequently, this gives rise to a strong and electrically tunable direct Rashba spin-orbit interaction (SOI) on the order of meV. We will delve into this topic in detail in the next section.

3.3. Direct Rashba spin-orbit interaction

In Ge/Si nanowires, the effective spin states related to J are closely linked to the orbital parts of the envelope wave functions. We discuss the derivation of direct Rashba spin-orbit interaction by solving the Hamiltonian in the 1D case. The following section follows Ref. [160, 161] closely. Due to the large valence band offset, the radial confinement can be treated as a hard wall potential,

$$V(x,y) = \begin{cases} 0, & \sqrt{x^2+y^2} < R \\ \infty, & \text{otherwise.} \end{cases} \tag{3.2}$$

where the R is the radius of the NW. The total Hamiltonian can be written as,

$$H^{\text{tot}} = H_{\text{LK}} + V(x,y) - eE_x x, \tag{3.3}$$

the last term is coming from an external electric field, where x is a direction perpendicular to the NW. In this case, J_z is not a good quantum number anymore. Since H^{tot} commutes with the operator $F_z = L_z + J_z$, where $L_z = -i\partial_\phi$ is the orbital angular momentum along the wire axis, F_z is a good quantum number and the states can be grouped accordingly. To obtain the effective 1D Hamiltonian that describes the low energy hole spectrum, one can treat k_z in perturbation theory and write the effective Hamilton as,

$$H^{\text{eff}}_{4\text{x}4} = \begin{pmatrix} \frac{\hbar^2 k_z^2}{2m_g} & 0 & eUE_x & -iCk_z \\ 0 & \frac{\hbar^2 k_z^2}{2m_g} & -iCk_z & -eUE_x \\ eUE_x & iCk_z & \frac{\hbar^2 k_z^2}{2m_e} + \Delta & 0 \\ iCk_z & -eUE_x & 0 & \frac{\hbar^2 k_z^2}{2m_e} + \Delta \end{pmatrix} \tag{3.4}$$

where $m_g = 0.043m$ and $m_e = 0.054m$ are effective masses, $C = 7.26\hbar^2/(mR)$ and $U = 0.15R$, and Δ is the gap between ground and excited state. The new eigenstates are now $|g_+\rangle$, $|g_-\rangle$, $|e_+\rangle$ and $|e_-\rangle$. They denote the ground states and first excited states. The subscript "+" ("-") stands for a spin block, signifying that each new eigenstate comprises the two spin states $|3/2\rangle$ and $|-1/2\rangle$ ($|-3/2\rangle$ and $|1/2\rangle$). The schmatic of basic states and their coupling is shown in Fig. 3.3 (a).

Strain will modify the gap $\Delta = \Delta_{BP} + 0.73\hbar^2/(mR^2)$ via the Bir-Pikus (BP) Hamiltonian. In Fig. 3.3 (c), the hole spectra of a Ge/Si core/shell NW is shown for different strains. As strain increases, so does the gap between the

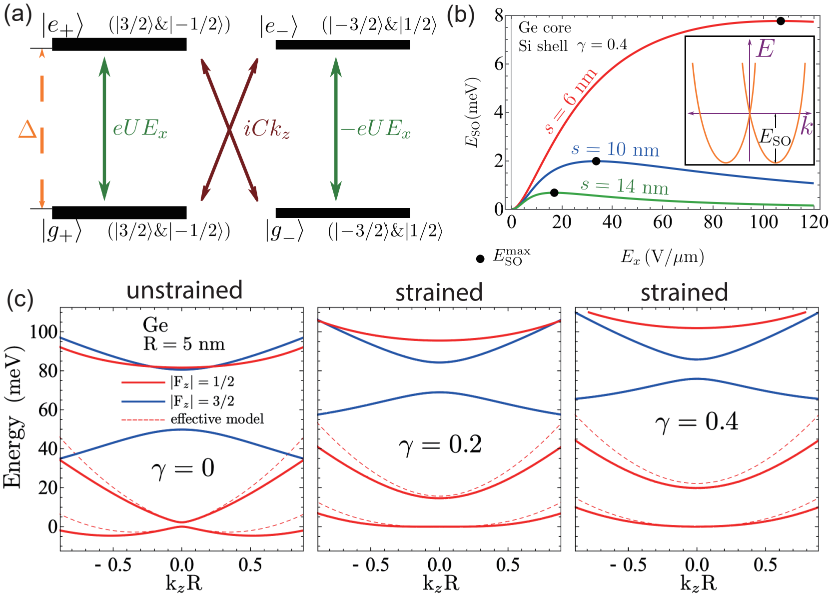

Figure 3.3. Direct Rashba spin-orbit interaction. (a) Strong confinement results in new sets of eigenstates with ground states $|g_\pm\rangle$ and first excited states $|e_\pm\rangle$. The subscript "+" ("-") denotes a spin block, meaning that the each new eigenstate contains the two spin states $|3/2\rangle$ and $|-1/2\rangle$ ($|-3/2\rangle$ and $|1/2\rangle$). The $|g_\pm\rangle$ and $|e_\pm\rangle$ are separated by a gap Δ. The green arrows indicate coupling between $|g\rangle$ and $|e\rangle$ within the same spin block. The coupling is coming from electric-field-induced shift $-eE_x x$ of potential energy, featuring spin-conserving. The cross couplings iCk_z terms (brown arrows) results from the LK Hamiltonian. Direct Rashba SOI is a combined effect from these two coupling mechanism. **(b)** Spin-orbit energy E_{SO} as a function of external electric field E_x for different NW diameter s. **(c)** Hole spectra of a Ge/Si core/shell NW with a fixed core radius $R = 5\,\text{nm}$ and varying Si shell thickness. The relative Si shell thickness γ effectively characterize the strain applied to the Ge core. Due to the cylindrical symmetry, the subbands can be grouped via the total angular momentum F_z along the NW axis. As strain increases, the band structure significantly modifies. Adapted from Ref. [160, 161].

ground and first excited state. Notably, at $k_z = 0$, the ground state curvature goes through a sign change from negative to positive.

Most importantly, it turns out that a very strong Rashba SOI arises from the effective Hamiltonian. When treating $|eUE_x/\Delta|$ and $|Ck_z/\Delta|$ as small perturbation, one can simplify the above-mentioned Hamiltonian via a Schrieffer-Wolff transformation,

$$H^{\text{eff}}_{2\text{x}2} = \left(\frac{\hbar^2}{2m_g} - \frac{C^2}{\Delta}\right) k_z^2 + \frac{2eCU}{\Delta} E_x \sigma_y k_z \tag{3.5}$$

for the two subbands of lowest energy, where σ_y corresponds to a Pauli matrix. Notably, the $\frac{2eCU}{\Delta} E_x \sigma_y k_z$ term is very similar to the standard Rashba-type SOI term $\alpha_{el} E_x \sigma_y k_z$ for electrons. Consequently, it is named Direct Rashba SOI (DRSOI) [160]. Figure 3.3 (b) shows the calculated spin-orbit energy E_{SO} as a function of the applied electric field E_x for the three wire diameters s = 6, 10, and 14 nm. With moderate E_x, a spin-orbit energy up to meV can be obtained.

Indeed, the strong DRSOI has been reported in various experiments [162–165]. For example, a very short spin-orbit length l_{SO} ranging from 20–65 nm in different devices, and spin-orbit energy ranging from 1-6 meV were reported [166]. More recently, an extremely short l_{SO} of 3 nm has been reported in a hole spin qubit device from analysis of the ultrafast f_{Rabi} [165]. It is noteworthy to say that the DRSOI is one order of magnitude stronger than the conventional Rashba SOI, which is reported in InSb or InAs NWs [167–171]. The unique properties of Ge/Si core/shell NWs make them excellent candidates for developing hole spin qubits, Andreev spin qubits, or Majorana bound states.

3.4. Nanowire growth

In this section, we discuss the growth of Ge/Si core/shell nanowires (NWs). The description of the NW growth follows closely to Ref. [37, 159]. Pioneering work on core/shell NW growth was conducted in 2002 [172]. Since then, numerous research efforts have been devoted to optimizing the growth of Ge/Si core/shell NWs [56, 173–177]. Using these NWs, various devices such as NW transistors [178–181], quantum dots [162, 182–188], Josephson junctions [189–192], and spin qubits [165, 193, 194] have been fabricated and studied.

VLS growth of Ge/Si core/shell NWs

The Ge/Si core/shell NWs used in this thesis were grown by Prof. Erik Bakker's group at Eindhoven Technical University [159]. These NWs were

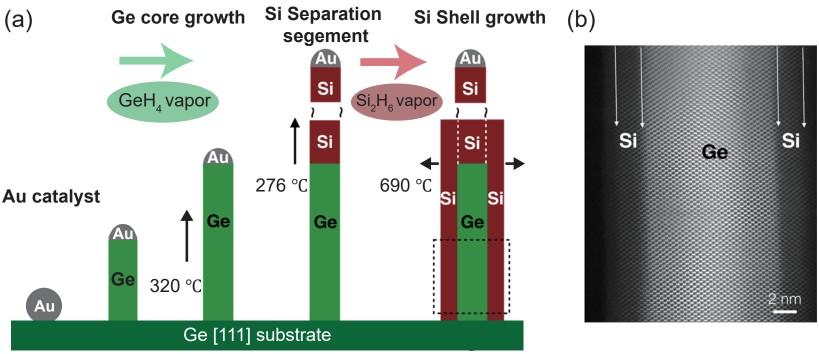

Figure 3.4. NW growth. (a) Schematic illustrating the stages of Ge/Si core/shell NW growth. (b) High-angle annular dark-field (HAADF-STEM) image of a representative Ge-Si core-shell NW. Adapted from Ref. [159].

vertically grown using the vapor-liquid-solid (VLS) method [195]. The important steps of the NW growth are shown schematically in Fig. 3.4 (a). The NW growth process begins on a Ge [111] substrate. Commercially available 10 nm Au colloid solution was deposited on the substrate to serve as a catalyst for the subsequent NW growth. After cleaning with oxygen plasma and an HF solution, the samples were loaded into a N_2-filled glove box in preparation for transfer to the growth system.

The growth of Ge/Si core/shell NWs was performed in a Metal-Organic Vapor Phase Epitaxy (MOVPE) system. The precursor gases used are GeH_4 and Si_2H_6 diluted with H_2. The precursor, Germane (GeH_4), dissociates at high temperatures on the Au droplet surface, leading to the formation of Ge and H_2. Ge is adsorbed by the Au droplet until it becomes supersaturated, causing the deposition of Ge onto the substrate and pushing the droplet upward. This epitaxial process produces a monocrystalline wire with a length of several micrometers with the wire's diameter determined by the size of the initial droplet.

Subsequently, the precursor gas was switched to Si_2H_6 to enable Si growth. Initially, a Si separation segment was grown at 275 °C. This step served to create a separation between the Ge NW and the Au droplet, preventing Au from diffusing into the NW during subsequent high-temperature processes. Following that, the temperature was adjusted to 690 °C to promote radial growth, resulting in the formation of a Si shell around the Ge NW. Figure 3.4 (b) shows a TEM image of the NW after growth, where the Si shell and Ge core is clearly visible.

Hole Mobility vs NW crystal direction

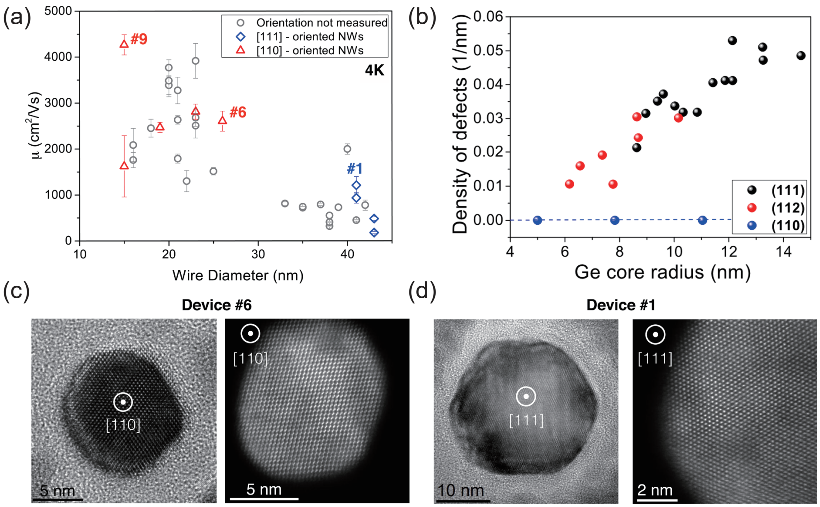

Figure 3.5. NW mobility is strongly correlated with crystal direction. (a) Hole mobility (μ_H) versus wire diameter for 33 different nanowires from the same growth batch. The outer diameter was measured using atomic force microscopy. The red diamonds and green circles correspond to the specific devices that were analyzed by high-resolution transmission electron microscopy (HR-TEM). **(b)** Defect density as a function of Ge core radius. **(c)** and **(d)** Left panels show HR-TEM images, while right panels show HR-STEM images of the cross-sections of two representative NWs with small and large Ge core radius, respectively. The atomic arrangement further confirms their growth direction as [110] and [111]. Adapted from Ref. [159].

The Ge/Si core/shell NWs have 3 different growth directions, namely [111], [110], and [112]. The orientation of the NWs exhibits a pronounced correlation with the radius r of the Ge core. For $r < 10\,\mathrm{nm}$, NWs grow along [110] direction. For $r > 10\,\mathrm{nm}$, the [111] and [112] growth directions are preferred. More importantly, the NW's electronic properties, for example the hole mobility, are closed related to the NW crystal direction. This has been studied in Ref. [159] and Ref. [196].

The strain-induced defect formation turns out to be the main limiting factor for high hole mobility. As discussed before, the Si shell will compressively strained Ge core due to a 4% lattice mismatch. In thin NWs of [110] growth direction, the strain is homogeneous, therefore a coherent strain relaxation in the Ge core is expected. On the contrary, the thick NWs are not able to accommodate strain coherently, resulting in nucleating defects. In Fig. 3.5 (a), the hole mobility of NWs is shown as a function of wire diameter. The mobility is extracted by fitting the linear regime of $I - V_g$ curve. The NWs with thinner diameter exhibit higher mobility up to 4200 $\mathrm{cm}^2/(\mathrm{Vs})$. The thicker NWs tend to have a lower mobility around 500 $\mathrm{cm}^2/(\mathrm{Vs})$.

In a study conducted by Nguyen et al. [196], the hole mobility in Ge NWs with and without the Si shell was investigated. It was found that in the absence of the Si shell (homogeneous Ge NWs), the mobility was only in the range of 40–50 $\mathrm{cm}^2/(\mathrm{Vs})$. The presence of the Si shell significantly enhanced the mobility, increasing it by a factor of 4–5. The mobility enhancement can be attributed to the confinement of accumulated holes within the Ge core. This confinement effectively separates the carriers from the semiconductor/dielectric interface, leading to a reduction in interface scattering.

Furthermore, the density of misfit dislocations has been analyzed for NWs with 3 different crystal direction, as shown in Fig. 3.5 (b). Remarkably, no strain-induced nucleating defects have been observed in [110] NWs. As for [112] and [111] NWs, the density of defects increase with the Ge core radius, indicating a non-ideal stain relaxation in thicker NWs. The crystal orientation of the NWs was determined using TEM images, see Fig. 3.5 (c) and (d), and the data points in Fig. 3.5 (a) were marked in red and blue accordingly.

4 Experimental Methods

> *"Science is about knowing; engineering is about doing."*
> — Henry Petroski

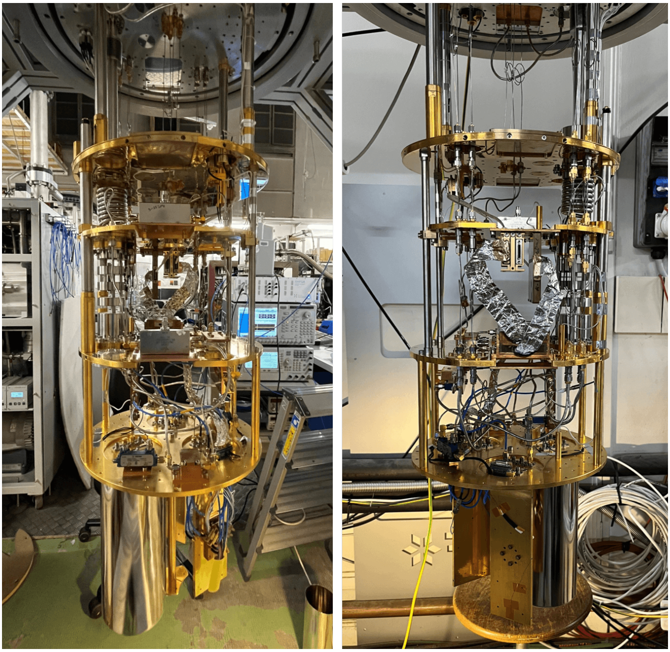

In this chapter, we will first introduce the nano-fabrication of the devices, which are investigated in this thesis. We will cover the most important fabrication methods. Details about recipes can be found in Appendix. A. Next, we discuss how to integrate the fabricated samples in a DC or a RF sample holder. In the end, we introduce the cryostat setup for for DC and RF measurement.

4.1. Device fabrication

The fabrication of our devices commences with a silicon (Si) wafer, either doped or undoped depending on the type of experiments. To create micro- and nano-structures, we employ standard lithography techniques such as laser writing (Heidelberg instrument μMLA) and electron beam lithography (EBL). Following the spin-coating of photoresist (electron-beam resist), we pattern the designed structures onto the wafer. Next, fabrication processes like wet/dry etching, deposition, lift-off can be performed. The laser writer is practical for making larger structures, but its resolution is limited to $\sim \mu$m. For nanometer scale structures like side gates or contacts to nanowires (NWs), we use EBL.

Base structure for DC measurements

For DC measurement, we choose a highly p-doped silicon (Si) wafer as a substrate. The doped Si can be used as a global backgate (BG) with a 100 nm thick thermally grown silicon oxide (SiO_2) as a dielectric layer. Before fabricating NW devices, we need to fabricate a base structure. The base structure contains large bond pads and small alignment markers, as shown in Fig. 4.1. The alignment marker is crucial for localizing the nanowires with high precision and to align the following EBL steps.

After cleaning, we dive the wafer into 2.5 cm x 2.5 cm pieces. The base structure, as illustrated in Fig. 4.1 (a), have a size of 5 mm x 5 mm. With the laser writer, we normally pattern 25 such base structures. Next, we deposit 1 nm/20 nm titanium/palladium (Ti/Pd) with electron beam evaporation, followed by a lift-off process in warm acetone at 50°C. The alignment markers, seen in Figure 4.1 (b), are patterned with EBL, followed by a similar metal deposition procedure. Now, the base structures are ready for further NW device fabrication. Figure 4.1 (c) shows a dark field optical microscope image of a single block from a marker area. Here, one can see the deposited NWs. Details about NW deposition will be discussed in the following section.

NbTiN resonators

For RF measurements, the microwave circuits are fabricated on an un-doped Si wafer with 170 nm thermal SiO_2 on top. The thermal SiO_2 layer is crucial here. Since the fabrication of Ge/Si NW JJ involves a buffed-hydrofluoric acid (BHF) etching process which could etches the native SiO_2, one would have a gate leakage problem if fabricating on a pure Si wafer. The microwave circuits are defined on a sputtered NbTiN film, while the NbTiN film sputtering and patterning was based on a well-established recipe from our group, which have been developed over generations of group members. Here, we will discuss the main steps. Detailed recipes can be found in Ref. [57, 197].

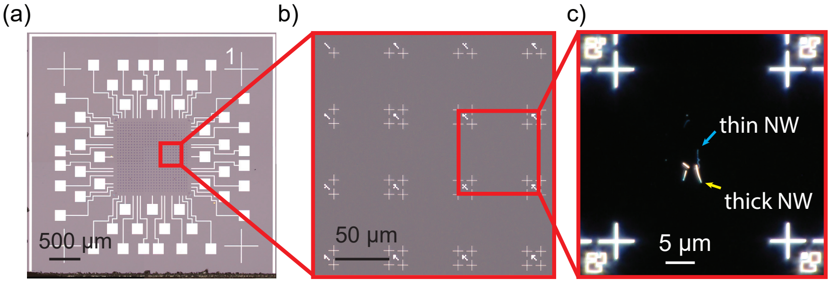

Figure 4.1. Base structure. Optical microscope images of a DC measurement base structure (a) and marker area (b) for NW deposition and alignment. (c) Dark field optical microscope image of a block of the marker area where NWs were deposited. The brightness is related to the NW thickness, the barely visible NWs are typically the ones with [110] growth direction.

First, a wafer (typical a quarter of 4 inch wafer) is thoroughly cleaned with sonication using (1) Deconex® 12 BASIC/ DI water solution (1:100), (2) DI water, (3) acetone, (4) IPA, and finally completed with an UV-ozone clean. The cleaned wafer is immediately loaded into the AJA ATC Orion 8 sputtering machine. After conditioning the chamber, the wafer is transferred from the load-lock to the sputtering chamber. The base pressure in the chamber is around $\sim 8 \times 10^{-9}$ Torr. The sputtering is done using a NbTi-target (70%/30%, 99.995% purity), while N_2 gas is added to the Ar sputtering gas.

The quality of the film is examined by measuring a test resonator structure in a 4 K liquid He dipstick measurement, where parameters like critical temperature T_c and kinetic inductance L_k can be extracted. For the final microwave circuit fabrication, we use either EBL or a Laser writer to pattern the designed structures. After development, an oxygen plasma was performed to remove the resist residue in the patterned region. Then, the chip is loaded in an inductively coupled reactive-ion etching (ICP-RIE) machine, where the exposed NbTiN region was etched using Ar/Cl_2 gases. In a final step, the PMMA or photo-resist was lifted-off in a warm acetone bath at 50 °C with sonication.

Furthermore, the resonator chip design was developed in collaboration with Dr. Luk Yi Cheung. The design for the Andreev qubit chip was based on ideas from the Quantronics group. Further details on this can be found in Ref. [42, 57].

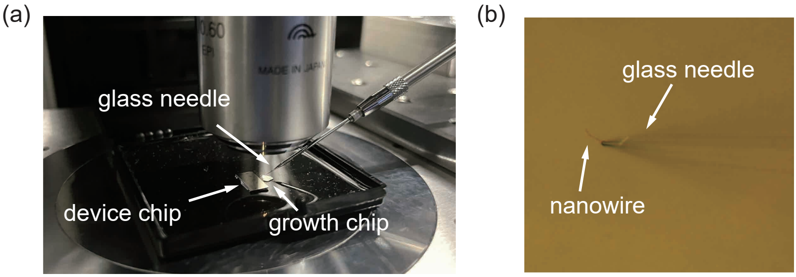

Figure 4.2. NW deposition. (a) Setup of the micro-manipulator. (b) Optical image of the glass needle with a NW attached to the tip.

Nanowire deposition

The Ge/Si core/shell NWs were growth by Erik Bakker's group [159]. To precisely transfer the NW from the growth chip to a substrate with alignment markers, we used a micro-manipulator, as shown in Fig. 4.2(a), which was set up by Deepankar Sarmah in our group. The micro-manipulator comprises glass needle with shaped end, which is controlled by a hydraulic system. The glass needle is produced with a dual-stage glass micropipette puller (Narishige's PC-100).

This system enables accurate picking up and positioning of nanowires onto the device chip, with a precision on the order of sub-10 μm. During the operation, the NW is first broken off from the growth chip by the glass needle, it then attaches to the needle due to van der Waals force, as shown in Fig. 4.2 (b). Subsequently, the NWs are transferred onto the device chip and delicately positioned at the desired location.

We note the Ge/Si core/shell NWs have 3 different growth directions, where NWs that grow along [110] direction have the thinnest wire diameter and highest hole mobility. A detailed discussion of NWs growth direction can be found in section. 3.4. Aiming for the best device quality, we intentionally pick the thinnest NWs for further device fabrication. A dark field optical microscope image is shown in Fig. 4.1 (c). In the image, one can see 3 NWs with brighter contrast, indicated by the yellow arrow. These are the thick NWs which have a typical diameter of 35 to 50 nm, as measured in SEM image. The thin NWs are barely visible in the optical microscope, where a blue arrow indicates such a NW in the image.

Nanowire metallization

For both DC and RF experiments, the NWs need to be contacted either to bonding pads or to the RF circuit. Before contact, the positioning of nanowires (NWs) relative to alignment markers was determined using SEM images. Subsequently, the contacts were designed and patterned through standard EBL lithography.

The key to make Ohmic contacts to NWs is the metal/NW interface treatment. The Ge/Si core/shell NW have a Si shell of $\sim 2\,\mathrm{nm}$, followed by a native SiO_2 of $\sim 2.5\,\mathrm{nm}$. Before depositing the contact, the native oxide must be removed through wet etching with buffered HF. It is noteworthy that we often fabricate etching windows using a cold development recipe, resulting in smaller undercuts and preventing buffered HF from creeping under the resist and over-etching the Si Oxides on the substrate. For the lift-off process, we use a stronger remover AR 300-76 (ALLRESIST) at a temperature of 70 °C. In the following, we will discuss different contact methods for the NWs, including standard surface contacts, and the Al/Ge inter-diffusion contacts.

Surface contact

For a surface contact, the contact metal is directly deposited on the surface of NWs. To make superconducting contacts, we choose aluminum (Al) as contact material due to its long Cooper pair coherence length ξ_0. However, depositing Al directly onto Ge/Si nanowires will lead to a Schottky contact, resulting in contact resistances ranging from tens to hundreds of MΩ, even with the native SiO_2 being removed.

Therefore, I invested considerable effort in conducting systematic tests on various contact methods and measuring the two-terminal resistance. This allowed us to determine whether Ohmic contact was achieved. The results are summarized in Table. 4.1

From it, we are able to target two methods that enable reproducible Ohmic contacts to the Ge/Si NWs: TMAH etching and multi-layer contacts with Pd/Al. The results of the low-temperature transport measurements obtained through these two distinct contact methods are discussed in **Chapter** 5.

Al/Ge inter-diffusion contact

Apart from the conventional surface contact, it has been demonstrated that there exists an "magic" recipe to make superconducting contacts with atomically sharp N-S interface [190, 198], which is unique for Ge NW. This is so-called Al/Ge inter-diffusion contact. In the following section, we will introduce the discovery of this contact recipe in a chronological order.

First Ge/Si core-shell NW JJ was demonstrated by Charles M. Lieber's group in 2006 [191], where critical supercurrents up to 100 nA and high order

Device No.	Type	Description	Metal	Two-termial resistance	Results
03	Normal contact	Used as a control group	Ti/Pd (1 nm/45 nm)	10 kΩ	Good ohimc contacts. Gate tunable NW transistor
05	TMAH etching	15 s TMAH etching	Al 45 nm	10 - 500 kΩ	Ohmic contact. ABSs measured
07	TMAH etching	15 s TMAH etching	Al 45 nm	20 - 250 kΩ	Ohmic contact. Supercurrent measured
10	TMAH etching	4 mins TMAH etching	Al 45 nm	100 - 1,500 kΩ	Ohmic contact. not measured in dilution fridge.
12	TMAH etching	2 mins TMAH etching	Al 45 nm	20 - 500 kΩ	Ohmic contact. not measured in dilution fridge.
13	TMAH etching + Ar milling	2 min TMAH etching + 15 s Ar milling	Al 45 nm	not applicable	NWs being etched away by Ar milling
14	TMAH etching + Ar milling	2 min TMAH etching + 3 s Ar milling	Al 45 nm	not applicable	NWs being etched away by Ar milling
15	SF_6 plasma	RIE with SF_6 plasma (10W) for 7s	Al 45 nm	not applicable	No tranport signal in needle prober, although devices looks good in SEM.
16	Pd interlayer	no extra etching steps	Pd/Al (7 nm/ 45 nm)	15 kΩ (one device)	Ohimc contacts, ABSs measured, induced gap $\Delta^* \approx 50\mu ev$
17	Pd interlayer	no extra etching steps	Pd/Al (2.5 nm/ 45 nm)	10 - 60 kΩ	Ohimc contacts, ABSs measured, induced gap $\Delta^* \approx 150\mu ev$
21	Pd interlayer	no extra etching steps	Pd/Al (2.5 nm/ 45 nm)	10 - 200 kΩ (long junction)	Ohimc contacts. ABSs measured in double quanutm dot.
08, 09	N-NW-S devices	TMAH etching for S contact	N: Ti/Pd S: Ti/Al	not applicable	Failed attemps, NWs being etched away during the BHF ecthing for 2nd contact.
18, 19, 20	N-NW-S devices	Pd interlayer for S contact	N: Ti/Pd S: Pd/Al	not applicable	Failed attemps, NWs being etched away during the BHF ecthing for 2nd contact.

Table 4.1. A general overview of the various contacting approaches In the last two column, the green color stands for successful samples, where good Ohmic contacts were established. The red color stands for failed samples, either no Ohmic contacts or the NWs were damaged during the processes.

(n=25) multiple Andreev reflections were reported. These findings indicates a highly coherent charge transport. In Ref. [191], the authors used Al as the contact material and fabricated the devices with a top-gated structure. Although the device is not intentionally annealed, fabrication processes such as resist bake-out or oxide growth with atomic layer deposition (ALD), inadvertently led to a contact annealing. Authors mention that this unintended annealing process may have contributed to the development of ohmic contacts to the Ge hole gas at low temperature. But no further studies had been carried out to investigate the underlying mechanism.

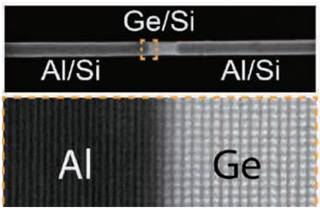

Figure 4.3. Al/Ge inter-diffusion contact. Top panel: SEM image of the Al-Ge-Al junction formed during annealing. Bottom panel: TEM image of the Al/Ge interface. Adapted from Ref. [190].

It was not until 2015, that Kral et al. [199] demonstrated the formation of abrupt interfaces between Al and Ge during a annealing process. It is not simply a silicide/Si and germanide/Ge intermetallic alloy formation [180, 200], but a formation of single crystal metal/semiconductor interface.

The formation mechanism can be explained by the unique Ge-Al phase diagram and different diffusion behaviors of Ge in Al and vice versa [199]. Firstly, the Ge-Al phase diagram exhibits a straightforward eutectic nature, devoid of the formation of any intermetallic phases. Secondly, the diffusion constants of both Ge and Al in Al are much higher than the diffusion constants of Ge and Al in Ge. Thus, Ge can effectively diffuse into the Al contact pad, where the empty sites from Ge are effectively filled by Al atoms through a fast self-diffusion process. Furthermore, it has been observed that the Al segment expands in a stepwise manner along the axial direction. This is due to its propagation velocity being significantly higher in the radial direction. As a result, ultra-clean and atomically-sharp Ge/Al interfaces are formed.

Using in-situ transmission electron microscopy (TEM), kinetic analysis of this diffusion process was studied in Ref. [201]. Their findings can be summarized as the following: (1) The reaction initiates at multiple nucleation points beneath the Al contact. Plus, the nucleation require an activation energy which may depend on the initial interface condition. (2) Diffusion Al length

L has a parabolic dependence as a function of time, $L = \sqrt{2Dt}$, where D is metal diffusion constant and t is the annealing time after inter-diffusion starts. D varies with NW diameter and annealing temperature. (3) In the remaining Ge NW segment, no Al contamination can be identified, which is ascribed to the exceedingly low diffusion coefficient of Al in Ge.

The first point explains an often-observed asymmetry of Al segment's length on two different sides after annealing. At the same time, it suggest that the inter-diffusion could happen in a more reproducible manner with elevated temperature. The second point suggests that the propagation of Al in NW decelerates as the length (L) increases. This offers the opportunity for precise control over the final Ge segment length at a nanometer scale.

According to these findings, we optimized the yield of the annealing recipe [1] by fabricating longer junction, as well as increasing the annealing temperature. This results in a significant increase in device yield, reaching up to 90%, where yield is defined as the observation of Al annealing fronts from both sides of the contact. Additionally, we conducted needle probing at room temperature to measure the two-terminal resistance. In this context, we observed that junctions exhibiting clear Al annealing fronts in SEM images typically corresponded to good Ohmic contacts, allowing for resistance tuning to a few tens of kΩ with gate voltage. This establishes a strong correlation between SEM results and transport characteristics. We note that the Ge segment length still varies from device to device. Nevertheless, this is not a limiting factor for us, since the annealing can be iterated for multiple times to obtain the targeted channel length.

Last but not least, considering that inter-diffusion could occur at temperatures as low as 180 °C, which coincides with the typical baking temperature for common E-beam resist [192], precautionary measures are necessary. To prevent inadvertent annealing, we opt for a lower resist bake-out temperature of 150 °C for fabrication steps subsequent to obtaining the Al/Ge inter-diffusion contact. At this reduced temperature, no unintentional propagation of Al is observed.

4.2. Sample holder

In the final stage of device fabrication, we integrate the nano-fabricated chip into a sample holder, which will be incorporated into a dilution refrigerator later. Depending on whether it is a DC or RF experiment, we choose different sample holders.

---

[1] The optimization study was conducted together with Tom Jenniskens, a semester project student from Eindhoven University of Technology.

DC chip carrier

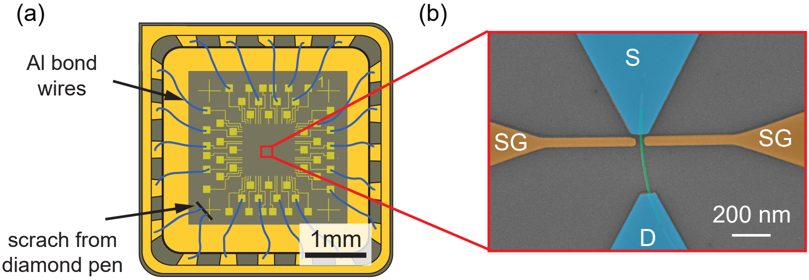

Figure 4.4. Chip carrier with bonded sample. (a) Schematic of a sample after bonding. The sample is glued into the chip carrier with PMMA. The contacts pads are bonded to the chip carrier with aluminum wire. (b) False-colored SEM image of a finished Ge/Si NW device with superconducting contact (blue), two side-gates (orange). Adapted from refs. [40, 102].

For the DC samples, we choose a commercially available non-magnetic chip-carrier. A schematic of such a sample holder is shown in Fig. 4.4 (a). To achieve electric contacts to the nano-device, specifically speaking the gates and contacts, we employ standard wire bonding techniques. The aluminum bonding wires are illustrated by the blue wires drawn in Fig. 4.4 (a).

The electric contact to the doped Si substrate can be realized in two different ways: (1) Gluing the sample on the chip carrier with conductive silver paste, and extend the silver paste to contact pads of the chip carrier. (2) Remove the thermal oxide layer by gently scratching the chip with a diamond pen, and then perform wire bonding on the exposed scratches. We choose the second way due to its elegance, preventing contamination of the sample with sliver paste. It's noteworthy that both the sample and bonder need to be properly grounded during the bonding. The nano-scale devices like NWs are vulnerable to electrostatic discharge (ESD) and could easily blow off if not handled properly. After successful bonding, the chip carrier can be integrated into the cryogenic measurement setup.

RF sample holder

For the RF samples, we use a double-layer printed circuit board (PCB) designed by Luk Yi Cheung, as shown in Fig. 4.5 (a). The PCB integrates both DC lines and RF connections. The sample can be glued by either sliver paste or PMMA in the device area (black box). DC lines are connected via an Omnetics double row nano-D connector to the PCB (green box).

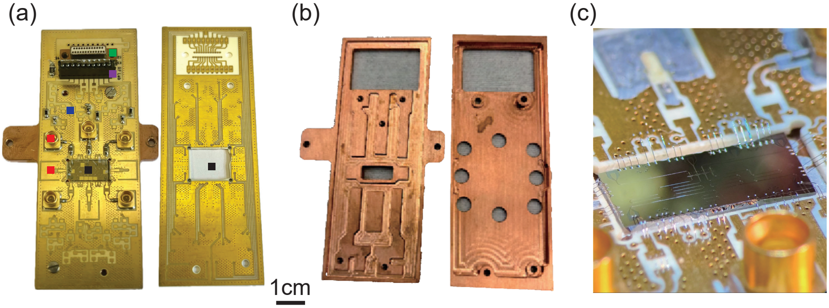

Figure 4.5. RF sample holder (a) A PCB that is used for integrating the device chip with DC and RF lines. (b) Copper plates that are utilized to encase both the PCB and the device chip. (c) A gatemon chip during wire-bonding on PCB. Adapted from Refs. [57]

To prevent devices from destroyed by ESD, a home-made connectors (purple box) is used to short all the DC lines to the PCB's ground. It's noteworthy that a 1 MΩ resistor is soldered in between to create a "soft-grounding". During wire-bonding and sample-transferring, this grounding strategy can protected the device. On top of that, after wire-bonding the sample is transferred to the dilution refrigerator using a conducting box. This reduces the chance of charge accumulation on the chip and therefore ESD. In the last stage, we build the sample into the dilution refrigerator and plug in the nano-D connector. From then, the device grounding is given by the break-out box's ground, and we can remove the customized connector.

The RF connectors could be integrated on the PCB. In the experiments, we use Rosenberger surface mount mini-SMP 18S102-40ML5. This RF connectors can be soldered on the PCB with a position indicated by the red dot. Furthermore, some standard electronic elements, such as low- or high-pass filters and bias-tees, can be constructed using surface mount components (SMC) on the PCB (blue box) at the mixing chamber temperature.

After wire-bonding and SMC component soldering, the sample is almost ready to be measured. In the final stage, the PCB is enclosed between a pair of copper plates, as illustrated in Fig.4.5 (b), and is then build in the dilution fridge for the cool-down process. Fig.4.5 (c) shows a gatemon sample on the PCB during wire-bonding. To reduce the impact of spurious resonance modes, we employ a considerable number of bonding wires to connect separated sections on the NbTiN grounding plates. Furthermore, we make connections from the NbTiN ground to the PCB ground using additional bonding wires.

4.3. Cryostat setup

Since quantum phenomena involve a small energy scale, they can easily be destroyed by thermal fluctuations at ambient temperature. Therefore, we conduct the measurements in a dilution refrigerator [202, 203]. The dilution refrigerator is a type of cryogenic system used to reach extremely low temperatures, where the base temperature could be as low as 15 mK. The dilution refrigerator operates based on the principle of dilution of ^{3}He in a mixture of ^{3}He and ^{4}He isotopes. When ^{3}He is diluted in ^{4}He, it undergoes a phase separation at low temperatures, and this process extracts heat from the system.

The dilution cooling process commences with a liquid-state mixture of ^{3}He and ^{4}He. This mixture goes through a multi-stage progression, with each stage featuring a heat exchanger. The heat exchangers play a pivotal role in achieving distinct temperature levels at various stages, typically reaching values such as 50 K, 4 K, 100 mK, and 20 mK. At the lowest stage, characterized by the base temperature, the experimental sample is mounted and further cooled for subsequent measurements.

The DC measurements within this thesis works are carried out in either a Leiden wet dilution refrigerator or a Bluefors dry dilution refrigerator. All the RF measurements are performed using the Bluefors refrigerator.

Cryostat setup for DC Measurement

The cryostat setup for DC measurement is shown in Fig. 4.6. The chip carrier is mounted to the cryostat using a commercially available chip socket, with both the sample and chip socket shielded within a Faraday cage. For connecting our measurement instruments at room temperature, a home-made breakout box equipped with BNC connectors and grounding switches is employed. To eliminate high-frequency noise and minimize electron temperature, the measurement lines are fitted with various filters. A self-constructed tapeworm filter, mounted on the cold-finger with a cutoff frequency of 10 MHz, is utilized, and additional π filters are used directly on the breakout box.

We employ standard low-frequency lock-in techniques to measure differential conductance. Figure 4.6 illustrates a fundamental schematic of the measurement setup for a two-terminal measurement. An AC bias at frequency $f = 77.7\,\mathrm{Hz}$ is applied to the source contact using an SR830 lock-in amplifier. The resulting drain current is amplified by an in-house, low-noise I-V converter from the Electronics Lab, and the output voltage is measured by the lock-in, providing the differential conductance, $\mathrm{G} = \mathrm{dI/dV}$. The DC voltage is provided by an in-house low-noise, high-resolution digital-to-analog converter (DAC). A standard 4:1 transformer is utilized to superimpose the AC voltage onto the DC voltage. A 1:1000 voltage divider is used to further reduces the

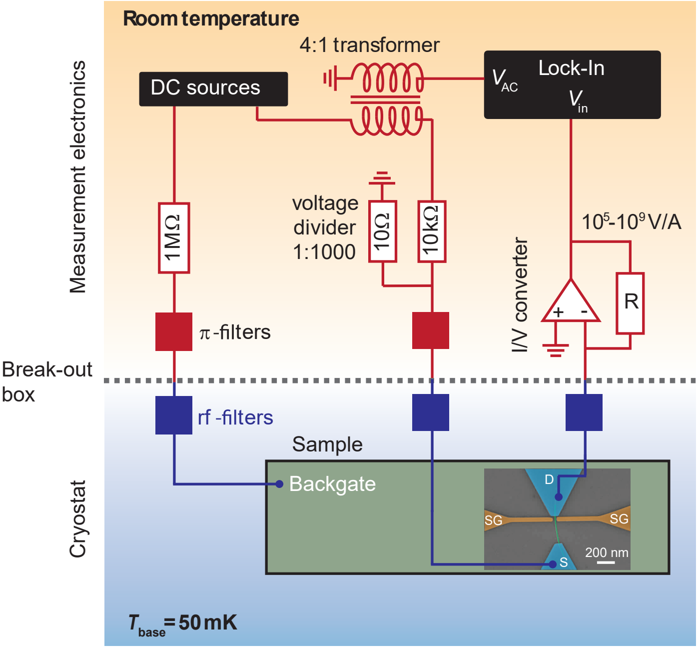

Figure 4.6. Schematic of DC measurement setup. A conventional measurement setup, where voltage-biased differential conductance measurements of a nanowire (NW) are performed within a dilution refrigerator, with a base temperature of 50 mK. Adapted from Refs. [35, 38, 40, 101, 102].

voltage amplitude. Additional DC voltages for the gates are also provided by the DAC.

For current-bias measurements, the current-bias is generated by the DAC voltage in conjunction with a pre-resistor (either 1 MΩ or 10 MΩ). The application of AC current-bias follows a similar transformer approach, resulting in an AC current-bias amplitude in the order of 0.1 nA.

Cryostat setup for RF measurement

The RF measurements were performed either using a Rohde&Schwarz ZNB-8 vector network analyzer or a Zurich Instrument SHFQA Quantum Analyzer. The drive and probe signals were heavily attenuated by 66 dB and filtered with home-made Ecosorb filters at low temperature. The output signals were amplified in an amplification chain consisting of a Josephson parametric amplifier (JPA), several circulators, an Ecosorb filter and dual junction isolators, followed by a HEMT amplifier. All components are shown in detail in Fig. 4.7.

The qubit drive tone is generated by a vector signal generator (Agilent E8267D) modulated by an envelope signal from an arbitrary waveform generator (AWG, Tektronix 5014C). The DC flux and gate lines are filtered using Ag epoxy filters at the coldplate and a 3-stage LC-filter with the cutoff frequencies 80 MHz, 225 MHz and 400 MHz. The qubit drive via the gate is achieved by combining a DC and an RF line on the PCB with a RC bias tee using a 1 kΩ resistor and a 15 nF capacitor.

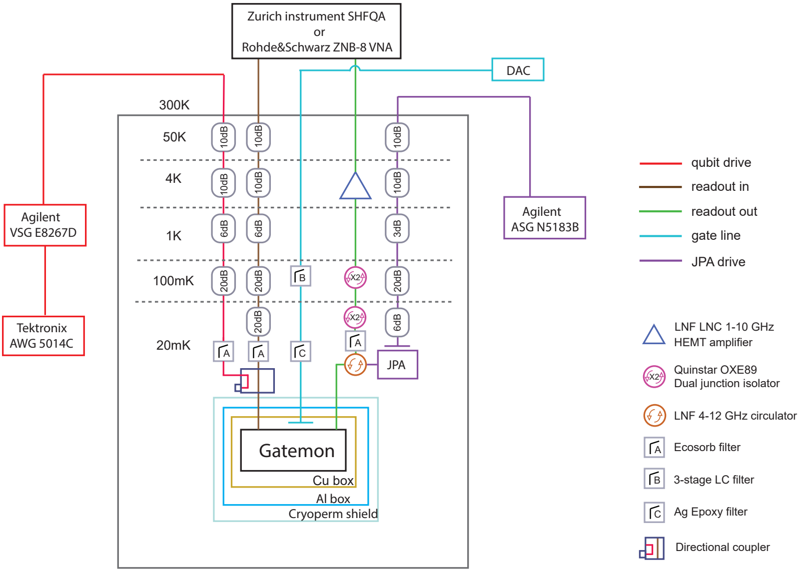

Figure 4.7. Schematic of the dilution refrigerator and measurement setup.

5 Superconducting transport in Ge/Si core/shell nanowires [1] [2]

"I have not failed. I've just found 10,000 ways that won't work."
— Thomas Edison

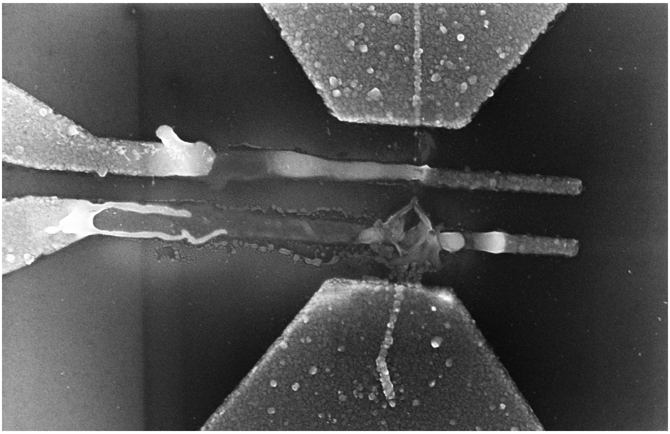

In this chapter, we discuss superconducting transport experiments on Ge/Si core/shell NWs. We first motivate our interest in sub-gap states, particular in Ge/Si core/shell NWs. Next, we discuss measurements in S-NW-S devices. We find sub-gap features that arise from the interplay between Coulomb interactions and the superconducting proximity effect for two types of devices: Al surface contacts with a Pd interlayer and TMAH etching. With the Pd interlayer contact, we employ finger gates to locally pinch off the NW, and demonstrate ABSs that can be probed in tunneling spectroscopy via a second

---

[1] The title image shows a broken device, consisting of a Ge/Si nanowire with Al contacts. An electrostatic discharge (ESD) occurred during the fabrication process, causing the damage.

[2] Parts of this chapter is under preparation for a publication.

QD [204]. Finally, we discuss devices with Al inter-diffusion into the NW core. This type of contacts was used in all the following chapter, so that we only show some very basic results in this chapter.

5.1. Introduction

Sub-gap states in a superconductor refer to electronic excitations that occur below the energy gap of the superconducting state. These states are known as Andreev bound states (ABSs) and can arise in inhomogeneous superconductors [60–63] or hybrid systems involving normal metal-superconductor interfaces [112, 205–207, 207–210, 210]. ABSs are based on a scattering process called Andreev reflection [52], where an incoming electron-like excitation converts into an outgoing hole-like excitation and vice versa. The formation of ABSs is affected by spatial variations in the pair potential of the system, as well as by the spin-orbit coupling in the material comprising the Josephson junction (JJ) [211–213], details can be found in Section. 2.3. Understanding the physics of ABSs is crucial for applications in quantum computing, including superconducting qubits [32, 33] and Andreev qubits [142, 143]. More intriguingly, the discovery of topological superconductivity has introduced a new kind of sub-gap state called Majorana bound states (MBSs) [214–217]. MBSs have unique properties, including zero energy and non-locality, which make them promising for realization of topological quantum computation [59, 218].

To date, sub-gap states in hybrid systems have been extensively investigated using carbon nanotubes, and III/V materials such as InAs nanowires, InAs 2DEG, and InSb nanowires In this project, we chose Ge/Si core/shell nanowires (NWs) as our research platform. These NWs offer attractive characteristics, including strong and electrically tunable spin-orbit interactions (SOI), as well as the potential for compatibility with semiconductor industry CMOS processes. Moreover, it has been predicted that MBSs could be realized in this platform [219].

Sub-gap states in Ge/Si core/shell NWs have been reported in a handful of studies [190, 191, 198, 220], in all of which superconducting proximity is introduced by alloying Al into the Ge core. However, in the context of MBSs, this alloyed structure is not suitable for hosting MBSs. In a 1D system, MBSs are predicted to emerge at both ends of a semiconductor/superconductor hybrid structure, where the SOI from the semiconductor and the superconducting pairing from the superconductor are two fundamental elements essential for establishing a topological phase.

To this end, we need to establish a surface superconducting contact to Ge/Si core/shell NW. For this, various strategies have been attempted, as discussed in **Section** 4.1. Introducing proximity paring via surface contact is problematic for these NWs. First of all, the wave-function is concentrated in Ge core.

Secondly, the Si shell can easily result in a Schottky barrier due to strong Fermi level pinning, and the SiO_2 itself acts as a barrier. Here, we report data of two successful approaches: depositing Pd interlayer to minimize the Schottky barrier, or (partially) etching away the Si shell and directly contacting the Ge core.

Specifically, in this work, we report superconducting transport measurements with Ge/Si core/shell NWs. In both single and double quantum dot (QD) structure, we observed sub-gap states. In the double QD, we find replicas of ABSs due to co-tunneling through one QDs into ABSs. Within the study, we have not been able to find any signatures of MBSs, featuring as close and reopen of induced gap and zero-bias anomalies. We conclude that the currently-available NWs are not suitable for exploring topological superconductivity, due to the small g-factor and a lower critical field from evaporated superconductor. Nevertheless, our experiments demonstrate a very good material quality of hybrid structures, which we exploit in later chapter for various qubits such as gate-tunable superconducting qubit (gatemon), and Andreev qubit.

5.2. S-NW-S devices

In this section, we discuss measurements on S-NW-S devices. The aim is to test whether superconducting proximity can be introduced to the NWs via surface contacts. We begin by presenting the results of devices with Pd interlayer contacts, followed by a discussion of the results from devices fabricated with TMAH wet etching of the Si shell. Our findings indicate that superconducting proximity was successfully introduced with both contact methods, proven by the observation of sub-gap states.

Pd-interlayer contact

As mentioned above, directly depositing superconductor (for example Al) onto NWs can lead to the formation of a Schottky barrier. In a simplified model, the Schottky barrier height for holes can be approximated as $\Phi_{\mathrm{B}} = E_{\mathrm{gap}} - \Phi_{\mathrm{m}}$, where Φ_{m} is the metal work function and E_{gap} is the energy gap of the semiconductor [221, 222]. In reality, factors like surface charge states at the metal-semiconductor interface can significantly alter the band bending, adding complexity to the issue.

To minimize the barrier, we opted for an interlayer metal with a high work function. This strategy allows for a deeper penetration into the Si's band gap, effectively creating a hole-accumulated interface. Previously, a reproducible normal-contact recipe, using Pd or Pt, have been established for Ge/Si core/shell NW [184, 186], and Ge hut wire (with Si cap) [223]. Hence, we followed this approach and deposited a thin layer of 2.5 nm of Pd between the

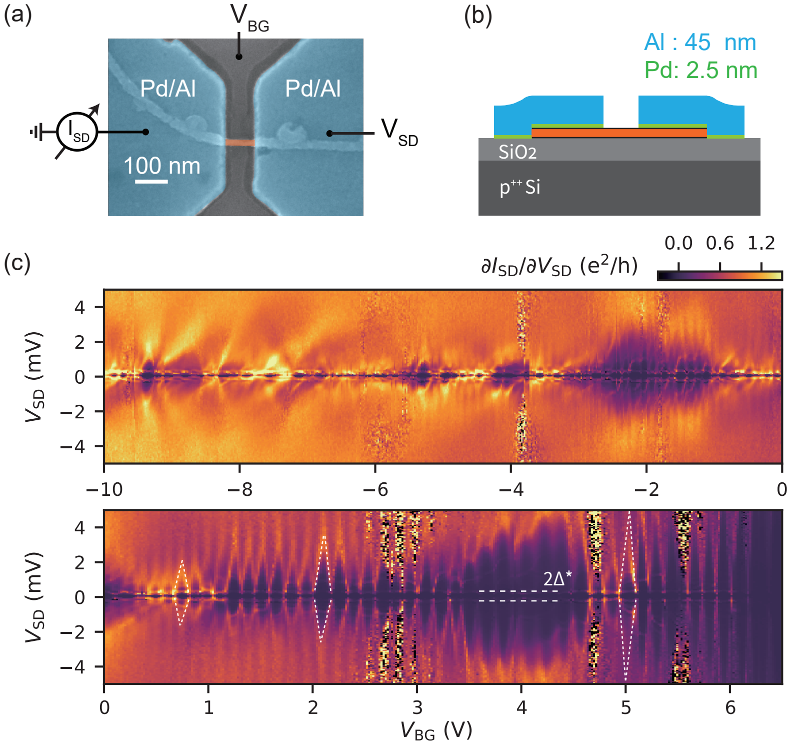

Figure 5.1. Device and voltage-bias spectroscopy (a) False-color SEM image of a S-NW-S device. (b) The schematic of the contact strategy. (c) Differential conductance $\partial I_{SD}/\partial V_{SD}$ as a function of back-gate voltage V_{BG} and source-drain bias V_{SD}. The presence of Coulomb diamonds is outlined by the white dashed lines forming diamond shapes.

Al and NWs. Figure 5.1 (a) presents the SEM image of the completed device, with the schematic illustration shown in Fig. 5.1 (b). The S-NW-S device is characterized by a source/drain contact spacing of 100 nm. A back-gate is realized by a p-doped Si wafer, which is covered with a thermal Si-oxide layer of 100 nm in thickness.

We performed standard lock-in measurements in a dilution refrigerator at a temperature of 60 mK. Figure 5.1 (c) shows the measured differential conductance $\partial I_{SD}/\partial V_{SD}$ as a function of back-gate voltage V_{BG} and source-drain bias V_{SD}. The measurements exhibit characteristic of hole conduction feature of the NWs. At higher gate voltageS ($V_{\mathrm{BG}} > 6\,\mathrm{V}$), the NW is near depletion. We observed Coulomb-blockade (CB) diamonds, indicating a quantum dot (QD) is formed between two superconducting (SC) leads. The size of the CB diamonds varies, reflecting a decrease in the charging energy of the QD from 5 meV to 2 meV, when an increase in hole density is achieved through gating. In addition, we observed the CB diamonds are opened by a gap 2Δ, suggesting the proximity effect is induced by the SC contacts. When the gate voltage is further decreased to a more negative value, the conductance increases to a typical value of $\sim e^2/h$, and the CB features smeared out due to a stronger coupling to the lead. We note that in this highly doped regime, a gap feature is still visible for low biases.

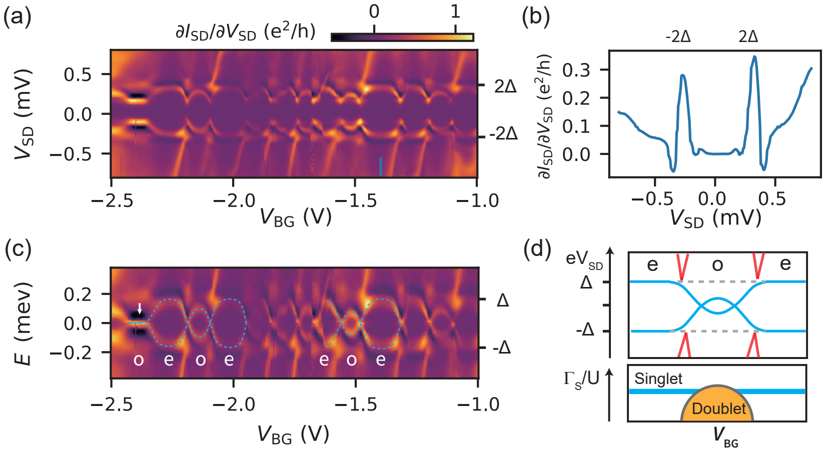

Figure 5.2. Sub-gap states. **(a)** Differential conductance $\partial I_{\mathrm{SD}}/\partial V_{\mathrm{SD}}$ measured with higher-resolution in small V_{SD} range. **(b)** a cross section at $V_{\mathrm{BG}} = 1.4\,\mathrm{V}$, a negative conductance is observed. **(c)** Density of states in the NW obtain from the data in (a), here we simply cut the data between Δ and $-\Delta$ ($\Delta \approx 150\,,\mu\mathrm{eV}$) get rid of the BCS gap from the probe lead. **(d)** Schematic of gate dispersion of the ABS resonances (blue) below the Coulomb diamond of QD (red).

Now, we shift our focus to lower bias voltages V_{SD}, as shown in Fig. 5.2 (a). We identify an induced gap of 2Δ, originating from the superconducting proximity effect. In addition, a pronounced negative differential conductance is observed at the dark region of the figure. Figure 5.2 (b) shows a cross section at $V_{\mathrm{BG}} = -1.4\,\mathrm{V}$, where a negative differential conductance is clearly visible. This, we attributed to the convolution of the coherence peaks on both sides of the SC leads, which is often observed in S-N-S devices like this [204, 224]. Moreover, an induced gap of $\Delta = 150\mu\text{eV}$ is obtained, smaller than the typical SC gap of Al $\Delta \approx 180\mu\text{eV}$.

Assuming that the observed sub-gap states are pinned to one contact, while the other contact serves as a "spectrometer" with a standard BCS gap, the density of states (DOS) in the NW can be inferred qualitatively. In Fig. 5.2 (c), we attempt to extract the DOS in the NW by excised the data between Δ and $-\Delta$. We note that a more appropriate approach would involve a deconvolution procedure of the raw data with the BCS gap of the spectrometer lead [51]. Nonetheless, this simplified approach should still provide a qualitative representation of the DOS. At $V_{\mathrm{BG}} \approx -1.5\,\mathrm{V}$, a pair of sub-gap states evolve as a function of V_{BG}, as indicated by the blue dashed lines. This can be explained by ABSs in a regime where Coulomb interaction competes with the superconducting pairing [224], as shown schematically in Fig. 5.2 (d). In the case of even QD occupancy, the ABS is pinned to the gap edge, wit a spin singlet ground state. However, in the odd occupancy, a single hole is trapped in the QD, resulting in a doublet ground state when the SC pairing energy is not enough to overcome the charging energy, see details in Section 2.5.1. Another example of such a singlet-doublet transition is visible in $V_{\mathrm{BG}} \approx -2.2\,\mathrm{V}$. Notably, we find a flat resonance at $V_{\mathrm{BG}} \approx -2.4\,\mathrm{V}$ as indicated by the white arrow in Fig. 5.2 (c). This could be an ABS pinned to zero energy, which we do not fully understood yet. We note that with a more negative V_{BG}, we also observe singlet ground states for odd QD occupancy due to the increasing coupling Γ_{S}. The data can be found in Fig. S5.1. In addition, with an external magnetic filed, we can quench the superconductivity in the SC lead, leading to a vanishing of the induced gap, see in Fig. S5.2.

TMAH etched contacts

In this section, we discuss the measurements of devices employing TMAH (Tetramethylammonium Hydroxide) etching for contact formation. TMAH is an etchant that has been extensively used in the industry for the anisotropic etching of Si [225]. Its widespread use is attributed to the absence of alkali metal ions, making it compatible with CMOS technology. Furthermore, the etch rate of TMAH is significantly slower for Ge compared to Si, with a rate difference exceeding a few orders of magnitude [226, 227]. This selectivity enables the removal of the Si shell without damaging the Ge core. Most importantly, almost every metal-Ge interface shows Fermi level pinning near the valence band, thus facilitating the formation of Ohmic contacts [21].

Figure 5.3 (a) shows the differential conductance $\partial I_{\mathrm{SD}}/\partial V_{\mathrm{SD}}$ measured at low bias voltages V_{SD}, and the schematic of measured device is shown in Fig. 5.3 (c). The contacts are made of evaporated Al, deposited after the

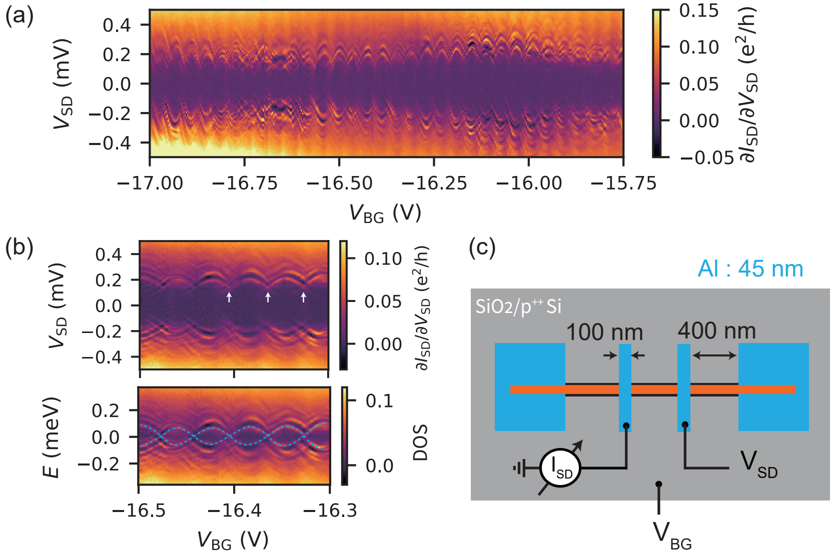

Figure 5.3. Sub-gap states in NW with TMAH etching contact. (a) Differential conductance $\partial I_{SD}/\partial V_{SD}$ as a function of back-gate voltage V_{BG} and source-drain bias V_{SD}. (b) Top panel: A zoom-in view of (a). Bottom panel: the extracted DOS by excising the data between Δ and -Δ. (c) Schematic of the measured device, Al contacts are separated by 400 nm. The thermal SiO_2 have a thickness of 300 nm. This data set is measured between the middle two contacts. We note sub-gap states are also observed when measuring other two nearby contacts.

etching of the Si shell with TMAH [3]. The SC contacts have a spacing of 400 nm, featuring a longer NW channel length compared to the devices discussed in the previous section.

In Fig. 5.3 (a), we observe a periodic pattern in conductance as a function of V_{BG}, which we attribute to CB oscillations. Since the length of the NW is relatively long of 400 nm, we expect to be in the long junction limit where the junction length L is longer than the superconducting coherence length ξ_0. This is supported by the fact, that we always see a set of multiple lines from

---

[3] Native SiO_2 was first removed by a BHF etching, followed by a 15 s etching in TMAH, then another 3 s dip in BHF solution for surface passivation. The TMAH etching time should be enough to remove Si shell completely with etching rate ∼ 10 nm/min. However, we found TMAH have a etching start time which depends on the surface condition. It is possible that the Si shell is only partially removed.

2 up to 5 resonances at a roughly equal bias intervals, as shown in a higher resolution map in Fig. 5.3 (b). Again, we tentatively excise the data between Δ and -Δ ($\Delta \approx 150\mu$eV) to get rid of the BCS gap of spectrometer lead, see the bottom panel in Fig. 5.3 (b). We found that the nearby resonance crosses each other without level anti-crossing, as indicated by the white arrow. This suggests that they belong to different parities. We note that, with the same etching recipe, supercurrent has been measured in another device with a shorter junction length of 200 nm, see Fig. S5.3.

Comparison between the two different contact methods

In summary, we were able to induce superconducting pairing with both contacting methods, and have measured sub-gap states in different limits. However, we found that the devices fabricated with TMAH etching often have a large device-to-device variation. Some devices show good proximity effect, while others not. This could be attributed to the variation in the process of TMAH etching. From the etch tests on a pure Si wafer, we found that the TMAH etching of Si can have a starting time, depending on the interface condition. This makes the recipe less reproducible. We also tried to vary the TMAH etching time, as well as performed an in-situ Ar miling after the TMAH etching. No significant improvement is observed.

As for the Pd interlayer devices, the device yield is higher. Moreover, this contact method preserves the integrity of the Si shell. The strain induced by the Si shell is crucial for the DRSOI physics. Hence, we used this contact method in the experiments that will be discussed in the next section.

5.3. ABS in double quantum dot configuration

In the previous section, the spectroscopic data is obtained relying on tunneling barriers located at the NW/metal interface, or disorders nearby the NW. However, to effectively probe the DOS at the end of hybrid section, a more precise control over the tunnel barrier is required. To this ends, we implemented two local side gates as shown in Fig. 5.4 (a), so that a tunneling barrier can be created by depleting the NW locally. The side gates have a width of 80 nm, placed at the end of the source contact, and with a spacing ~50 nm to the NW. The total NW junction length is around 500 nm. In the experiment, we always apply the same gate voltage V_{SG} to both side gates.

To test whether the side gates can pinch off the NW, we measured the differential conductance as a function of V_{SG} and V_{BG}, as shown in Fig. 5.4 (b). The pinch off of the NW is found at $V_{\mathrm{SG}} \approx 2\,\mathrm{V}$, varying linearly with V_{BG}. We observe two different features with different slopes in the gate-gate map, as indicated by the blue and green dashed lines. This can be explained

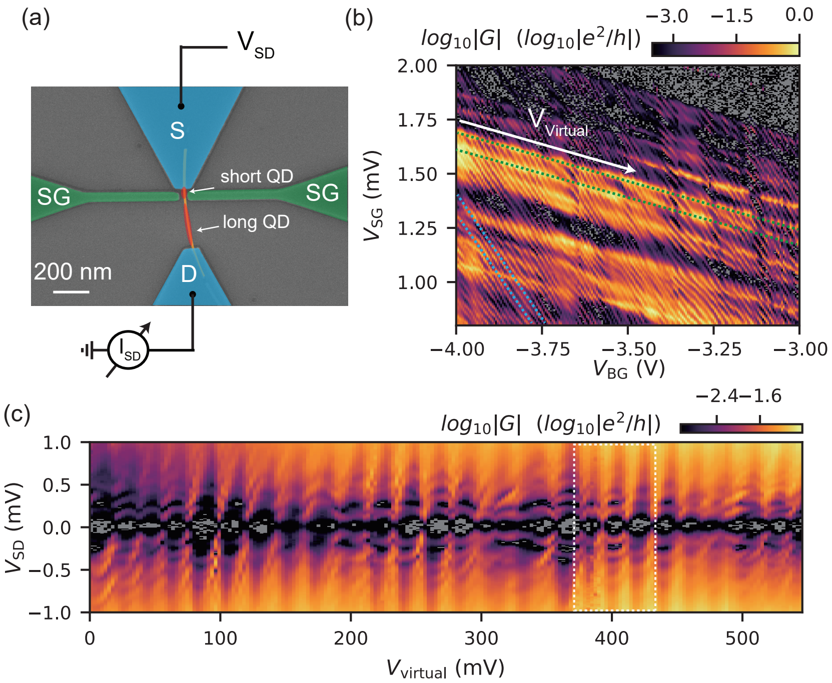

Figure 5.4. Tunneling spectroscopy with local side gates. **(a)** False-colored SEM of the device. **(b)** Differential conductance measured as a function of side gate voltage V_{SG} and global back gate voltage V_{BG}, measured with $V_{SD} = 80\,\mu V$. Two different slopes are observed, indicated by the blue and green dashed line. **(c)** Voltage bias spectroscopy measured as a function of virtual gate voltage $V_{virtual}$ as indicated by the white arrows in (a). White dashed lines show a gate range which is studied in detail in Fig. 5.5.

by the presence of a double quantum dot (DQD) in the NW[4]. The blue dashed lines show a stronger coupling to V_{SG}, and therefore can be attributed to a short QD in the vicinity of the source contact. In contrast, the green dashed lines show a stronger coupling to V_{BG}. We conclude it is originated from a long QD, as indicated in Fig. 5.4 (a).

Next, we performed tunneling spectroscopy on in this double quantum dot configuration. Since both the long and short QD are coupled to V_{BG} and

---

[4] Under certain gate configuration, a clear DQD honeycomb pattern is found as shown in SI Fig. S5.6.

V_{SG}, to simplify the problem, we measured the voltage bias spectroscopy as a function of virtual gate $V_{\mathrm{virtual}} = aV_{\mathrm{SG}} + bV_{\mathrm{BG}}$, where a and b is determined from the slope in gate-gate map. This keeps potential constant in short NW segment, which allows us to use the short QD as a constant barrier and do spectroscopy on the long section [204]. Figure 5.4 (c) shows the voltage bias spectroscopy as a function of V_{virtual}, where the virtual gate axis is shown by the white arrow in Fig. 5.4 (b). Again, we observed periodic CB diamonds in gate voltage. With this virtual gate axis, the state in the short QD should be constant, and we are changing the states in the long QD.

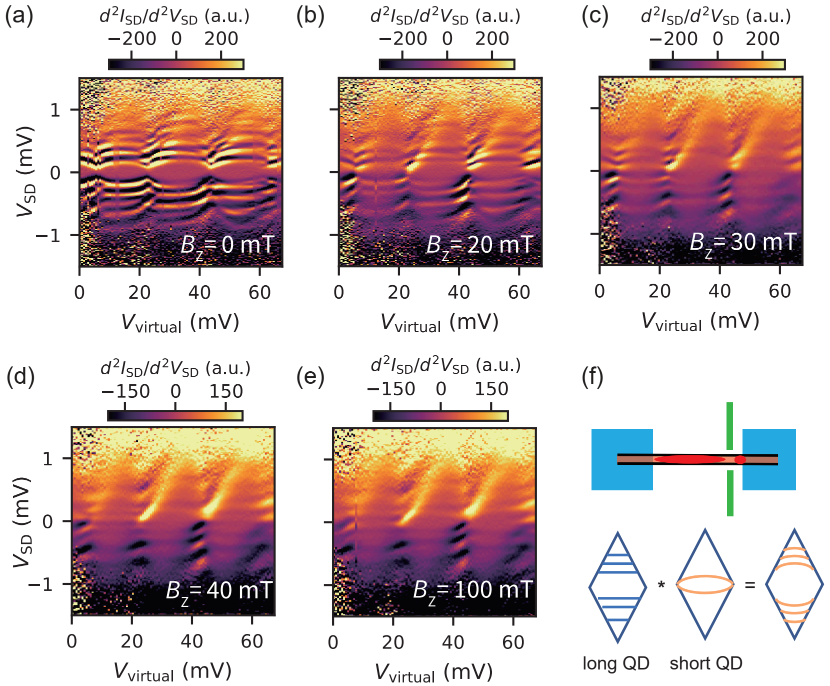

Figure 5.5. Replicas of ABS (a)-(e) Voltage bias spectroscopy measured at different external magnetic field B_z. For better visibility, we plotted the numerical derivative $d^2I_{\mathrm{SD}}/d^2V_{\mathrm{SD}}$. At low field, we observed multiple curved states. As B_z increasing, these states become flat, manifesting themselves as co-tunneling lines as shown in (e). (f) A conceptual schematic illustrating the states involved in the spectroscopy measurement.

We observe many states inside CB diamonds of the long NW segment, which we study as a function of magnetic field, as shown in Fig. 5.5. At zero field, we find at least 5 discrete states, some with energies clearly exceeding 2Δ. This suggests that they cannot all the be sub-gap states. In fact, we are able to explain these states using the schematic shown in Fig. 5.5 (f). The short QD is well proximitized by the SC lead, and exhibits sub-gap ABS. The long QD, measuring more than 450 nm in length, results in multiple co-tunneling lines. This can be seen in Fig. 5.5 (e), while superconductivity is quenched by an external magnetic field. As a result, in our spectroscopy measurements, we observe the convolution of the ABS in the short QD with the co-tunneling states in the long QD.

In addition, we measured the similar spectroscopy data at $V_{\mathrm{BG}} \approx -7.5\,\mathrm{V}$, where the short QD coupling to the SC lead Γ_{S} is large. The result is shown in Fig. S5.4. Last but not the least, it's worth to emphasis the high quality of the NW. The long QD have a size as long as 450 nm , without being interrupted by scatters/defects in the NW. Indeed, the mean free path l_e of similar Ge/Si core/shell NWs have been reported up to 500 nm [56].

In the last, We investigated the states' evolution in magnetic field. From the Zeeman splinting of a Kondo peak, we extracted a g-factor of 2.2 with the field direction perpendicular to the NW axis, as shown in Fig. S5.5. This value is in good agreement with the value reported in Ref. [184]. The comparatively small g-factor makes it difficult for us to explore the predicated topological regime: $E_{\mathrm{z}} > \sqrt{\Delta^2 + \mu^2}$.

5.4. Annealing device

In this section, we will shift our focus to the annealing device. Specifically, we will discuss the measurements of a fully metalized NW, meaning the Al fully replaced the Ge in the core. The aim is to characterize the properties of the alloyed Al. This measurement will help us understand the unique features of this alloyed Al NW.

The schematic of the device is shown in Fig. 5.6 (a). The NW was contacted by thermal evaporated Al, then annealing at 200°C induces the Al-Ge interdiffusion. When the annealing time is long enough, we would obtain a Al - alloyed Al - Al junction. The typical two-terminal resistance of such a device is below 1 kΩ, showing no response when sweeping V_{BG}.

We cooled down the device in a self-evaporated He3 refrigerator at temperature of 300 mK. The differential resistance R is measured with standard lock-in technique in a two-terminal probe. To determine the critical current I_{C} and critical field B_{C}, we conducted current-bias spectroscopy under varying external magnetic fields. The results are depicted in Fig. 5.6 (b) for the out-of-plane field B_{z} and in Fig. 5.6 (c) for the in-plane field B_{y}. First of all, we observed a switching of resistance value along horizontal axis, as indicated

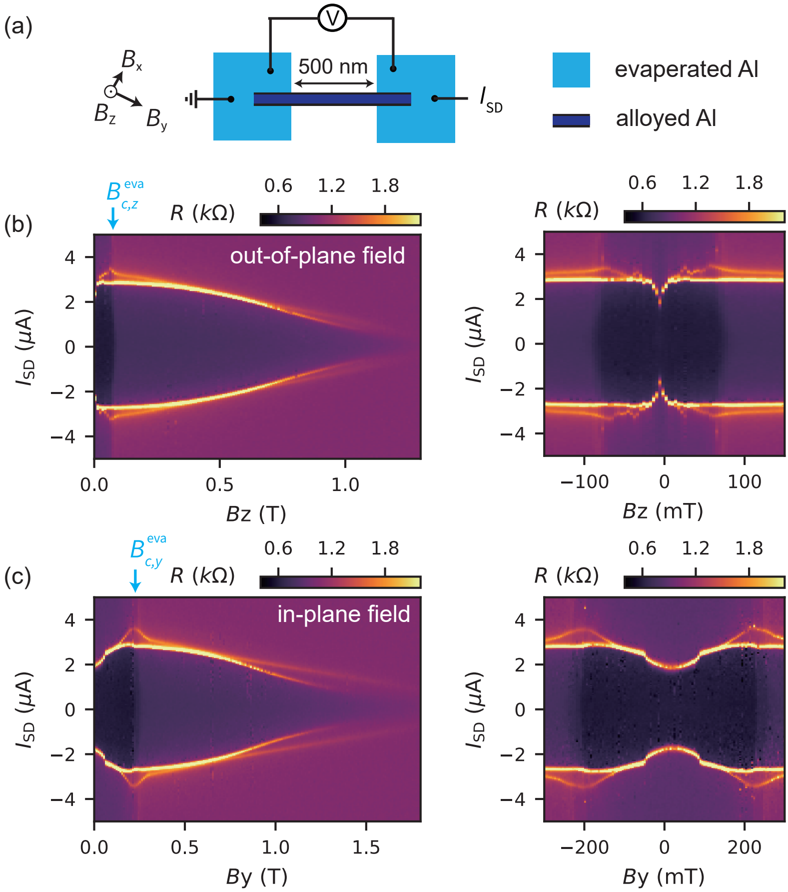

Figure 5.6. Measurements of a fully metallized NW. (a) Schematic of the measured device. (b) Differential resistance R measured as a function of out-of-plane magnetic field B_z and current bias I_{SD}. Right panel shows a zoom-in near zero field. (c) Differential resistance R measured as a function of in-plane magnetic field B_y and current bias I_{SD}. Right panel shows a zoom-in near zero field.

by the blue arrows in Fig. 5.6 (b) and (c). This occurs because the evaporated Al contacts switch to a normal state. From this, we obtained the critical field for evaporated Al, $B_{c,z}^{eva} = 60\,\mathrm{mT}$ for out-of-plane field, and $B_{c,y}^{eva} = 220\,\mathrm{mT}$ for in-plane field.

Next, we observed the supercurrent switching, characterized by a peak in differential resistance R, at a finite current bias I_{SD}. The switching current I_{sw} is on the order of a few μA and varies with the external magnetic field. Notably, a second resistance peak was found outside the main switching peak. The physics underlying this second peak remains unclear to us. This feature was not observed in a second fully metallized NW, and we have not yet invested more time in fabricating and testing more samples.

Now, we discuss the behavior of I_{sw} as a function of external magnetic field. As shown in Fig. 5.6 (b), the I_{sw} =1.5 μA at zero field. As B_{z} increases, I_{sw} also witnesses a significant increase, rising to approximately 3 μA. The increasing I_{sw} is accompanied by the quenching of the evaporated Al lead. Based on this, we can explain the increase in I_{sw} by quasi-particle trapping effect from the evaporated Al lead [228]. When turning normal, the evaporated Al lead traps the quasi-particles generated in the alloyed Al, thereby enhancing I_{sw}. This feature is also observed in Fig. 5.6 (c), as well as in a second fully metallized NW. This finding encourages us that by gap engineering, one can significantly reduce the quasi-particle poisoning, which is detrimental to superconductor-semiconductor hybrid devices.

We note that the critical magnetic field for the alloyed Al $B_{\mathrm{c}}^{\mathrm{alloyed}}$ can be remarkably high, exceeding 1 T for both in-plane and out-of-plane directions. This value is in good agreement with what has been reported in Ref. [198] in the same NWs. More importantly, it enables us to investigate the physics of hybrid devices under high magnetic fields, similar to studies conducted with InAs with epitaxial Al.

5.5. Discussion and outlook

In conclusion, we have successfully induced superconductivity in Ge/Si core/shell NW with surface contact, and investigated the sub-gap states using naturally occurring (surface barrier) or electrically induced (local finger gate) barriers for tunneling spectroscopy.

In device with Pd interlayer contacts, we observed discrete sub-gap states in a regime where Coulomb interactions compete with proximity-induced pairing, leading to a singlet/doublet ground state transition. In the device with TMAH etched contacts, we observed multiple branches of sub-gap states, which we attribute to ABSs in the long junction limit.

In addition, we have investigated devices with local side gates. The origin aim is to probe the sub-gap states in the hybrid section. However, we found a double quantum dot is formed in this configuration. Moreover, we observed replicas of ABS, which can be explained by the convolution of co-tunneling states in the long QD and ABS in the short QD. In this study, we were not able to observe signature of topological states. This is likely due to the small g-factor of the NW, and the low critical field of the superconductor. A possible direction for the future exploration includes modify the NW structure to boost the g-factor [229], and enhance the critical field of superconductor with a thin layer of Pt [230–232].

In the final part, we investigated devices where the Ge core was fully replaced by alloyed Al. Our findings revealed that the alloyed Al demonstrates a high critical magnetic field, which is promising for exploring hybrid physics in high magnetic field.

Supplemental to Superconducting transport in Ge/Si core/shell nanowires

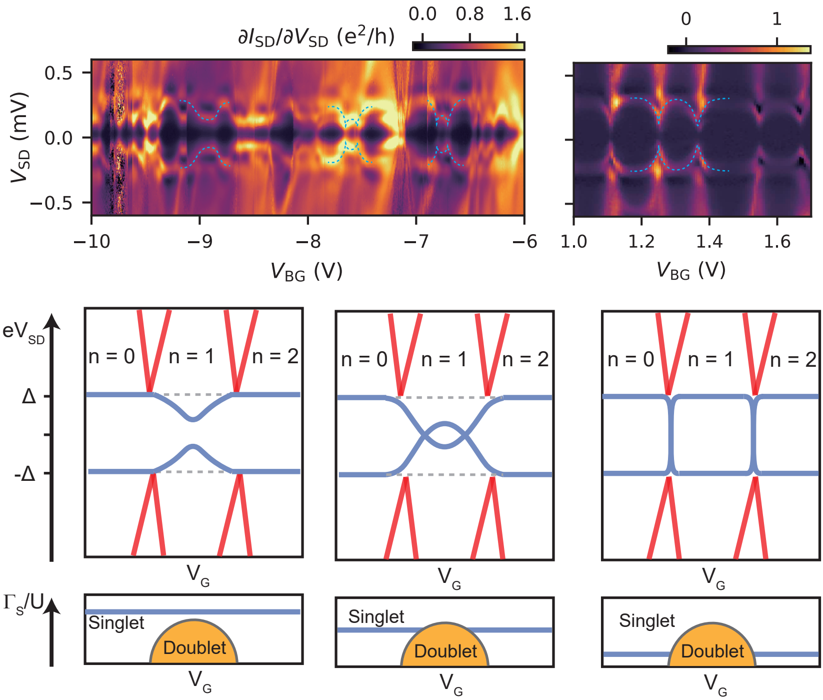

Figure S5.1. ABSs in different regimes From positive to negative gate voltage, the Γ_S increases. The gound state at odd QD occupancy can also have a singlet ground state. We note for the data present here, the BCS gap of the spectrometer lead has not been removed. Therefore, the data and the schematic shown below have a energy offset $\pm\Delta$.

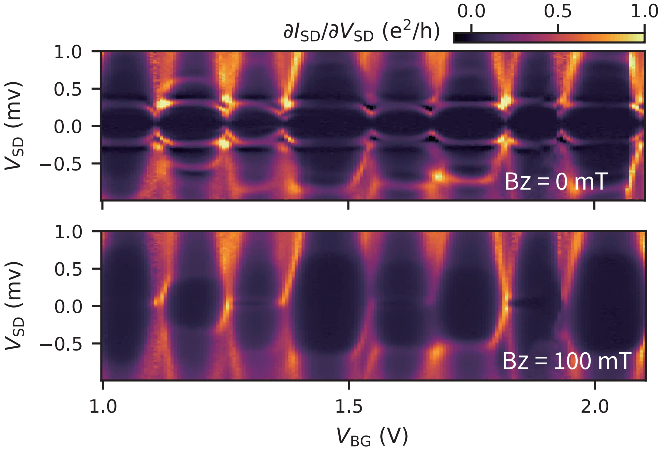

Figure S5.2. Superconducting states and normal state transport. An external magnetic field $B_Z = 100\,\mathrm{mT}$ could quench the superconductivity in the Al lead. When this happens, the induced gap vanished. In the meantime, co-tunneling lines, which is clearly visible at zero field, also boarded. This suggests the sharp BCS peak in the SC lead could enhance the resolution in spectroscopy.

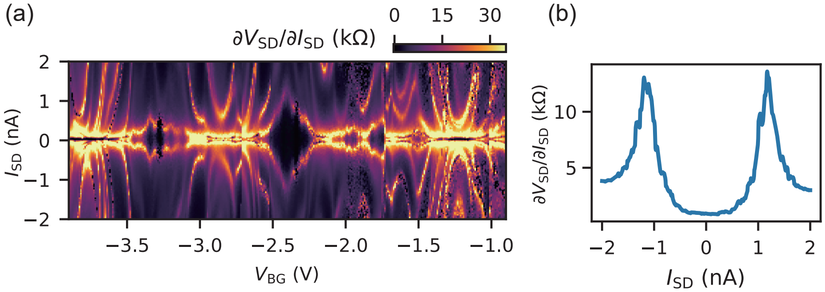

Figure S5.3. Supercurrent measured in a 200 nm long junction with TMAH echtching contact (a) Differential resistance $\partial V_{\mathrm{SD}}/\partial I_{\mathrm{SD}}$ as a function of back-gate voltage V_{BG} and current bias I_{SD}. (b) a cross section from (a) at $V_{\mathrm{BG}} = -2.4\,\mathrm{V}$.

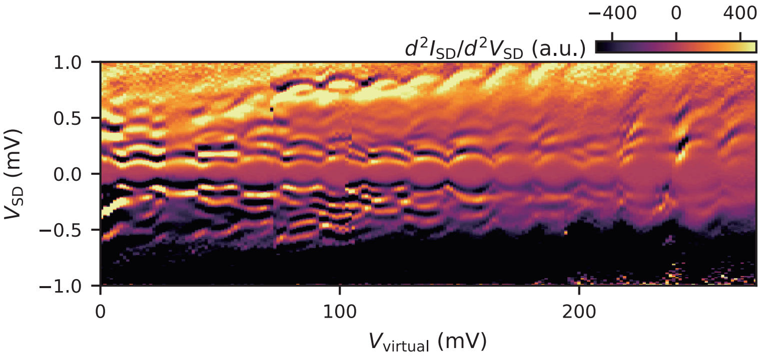

Figure S5.4. Replicas of ABS. Measured at more negative voltage with $V_{BG} = -7.5\,\mathrm{V}$ for $V_{virtual} = 0\,\mathrm{V}$. The virtual gate axis follows the same slope as in Fig. 5.4.

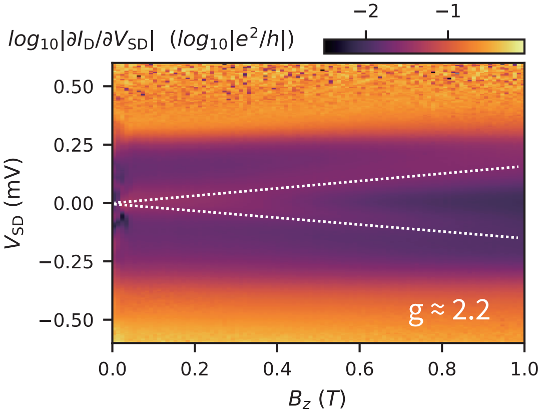

Figure S5.5. Kondo peak splitting in a odd QD. From which, we estimated a g-factor of 2.2 in the direction perpendicular to the NW.

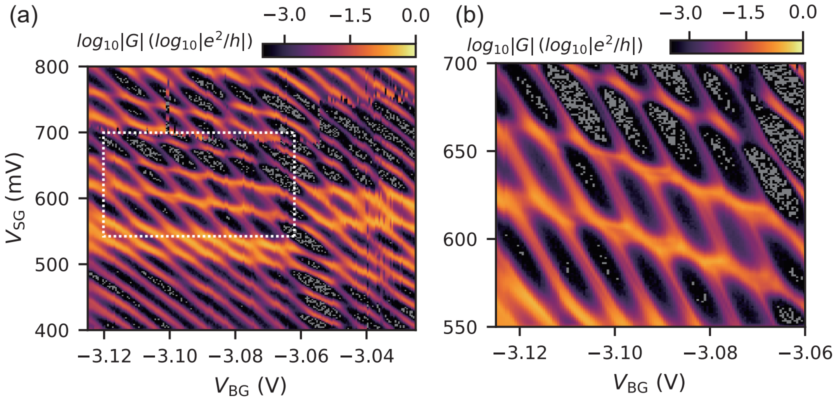

Figure S5.6. Charge stability diagram for DQD. In a certain gate range, a typical DQD feature is clearly visible. When sweeping gates, the inter-dot coupling strength Γ_M could change accordingly, result in different patterns as discussed in Fig. 2.9.

6 Current-Phase Relation of a Ge/Si Nanowire Josephson Junction [1] [2]

Wir müssen wissen. Wir werden wissen.
— David Hilbert

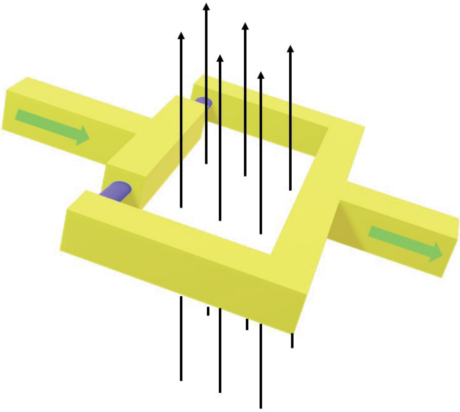

In the previous chapter, we have discussed the fabrication and electrical measurements of the Ge/Si core/shell NWs coupled to superconducting leads. Next, we embed two NW Josephson junctions (JJ) into a superconducting quantum interference device (SQUID) geometry. To obtain high quality superconducting contacts to the NW, we fabricated the NW JJ with an annealing method. The SQUID is designed in an asymmetrical configuration, with two JJs of different channel lengths. The short junction has a higher critical current and is therefore used as a reference junction. This allows us to measure the current phase relation (CPR) of the long junction. In the measurement, we observe an non-sinusoidal critical current, indicating highly transmitting modes. More intriguingly, we find an anomalous CPR with a dominating $\sin(2\phi)$ terms

---

[1] The content of this chapter is under preparation for a publication.

[2] This experiment was conducted together with Tom Jenniskens, a semester project student from Eindhoven University of Technology. The title image was generated by him.

at few specific gate voltages. We tentatively attribute this anomalous CPR to the interference of ABSs in the long-junction limit.

6.1. Introduction

Interest in group IV materials for quantum information technologies is continuously increasing, in particular for CMOS compatible germanium(Ge)-based systems [21]. Holes in germanium hold excellent properties like reduced hyperfine interaction and strong and electrically tunable "direct" Rashba spin-orbit interaction (SOI) [161].

The current-phase relations (CPR), as one of the most fundamental properties of a Josephson junction, contains information about the Andreev bound state (ABS) spectrum in the weak link [87] and can serve as a powerful tool to explore the physical phenomena like superconducting pairing[233], electron-electron interactions [97], band topology [234], or SOI [78]. CPR measurements have been reported in various material platforms, like InAs nanowires with epitaxial aluminum shells [85], carbon nanotubes [90, 235–237], ballistic graphene [74], high T_C superconductors [233], magnetic junctions [238, 239], superconducting atomic contacts[71], or topological materials [240, 241]. Despite the growing attention on Ge-based platforms, corresponding CPR measurements are largely missing, with a few notable exceptions on Ge based 2D platforms [242, 243].

Here we report the first CPR measurements for a Josephson junction based on Ge/Si core/shell nanowires, embed in a superconducting quantum interference device (SQUID) geometry. The DC SQUID consists of two JJs, both formed in the same NW. They have largely different critical currents, thus resulting into an asymmetric SQUID. The JJs are fabricated by annealing Al into the Ge core [198]. With electrical side gates, we can individually tune the critical current in each arm. In the measurements, we find a non-sinusoidal CPR, indicates the presence of higher harmonics due to highly transparent channels. Most importantly, we find an anomalous CPR with a dominating $sin(2\phi)$ terms. After discussing different possible origins of the anomalous CPR, we conclude that our device is most likely due to the interplay of ABS spectrum in the long junction limit.

6.2. Ge/Si NW SQUID device

Figure 6.1 (a) shows an electron micrograph of the device under investigation. It consists of a DC SQUID that incorporates two Ge/Si NW JJs in a superconducting Al loop, with a loop area $A \approx 12\ \mu\text{m}^2$. A schematic of the NW SQUID is shown in Fig. 6.1 (b). The JJs are fabricated on a single $5\,\mu$m long NW, which was transferred with the aid of a micro-manipulator to the device

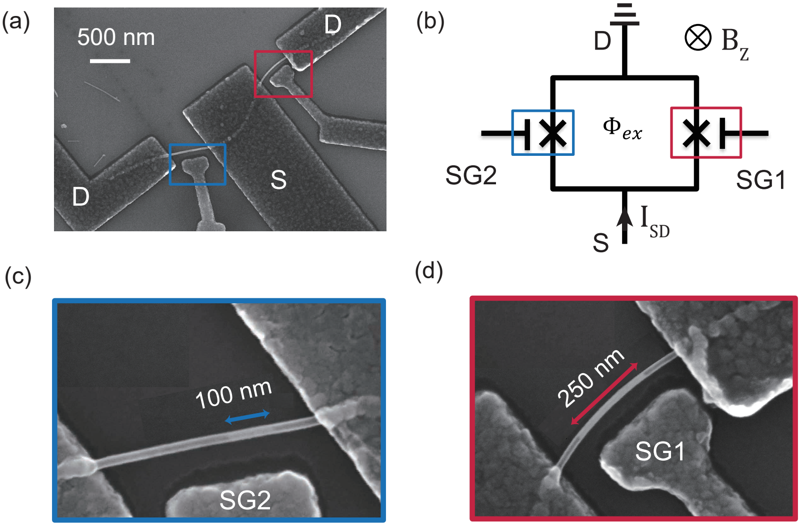

Figure 6.1. Ge/Si NW SQUID. (a) SEM image of the Ge/Si NW SQUID device. (b) Schematic illustration of the SQUID. (c) and (d) Zoomed-in SEM images of (a) as indicated by the blue and red squire. Two NW JJs feature different junction lengths, with a long junction of 250 nm and a short junction of 100 nm.

chip, and contacted by thermally evaporated Al using standard lift-off processes. Then, an thermal annealing step at 200 °C induces an inter-diffusion of Al atoms from the contact into the Ge core [189, 190]. This results in atomically sharp Al/Ge interfaces, while the Si shell remains intact. Details about mechanism of the inter-diffusion process can be found in Section 4.1.

Due to variations in the initial interface conditions, the start of inter-diffusion at individual contacts does not occur simultaneously. Consequently, an inherent asymmetry in the contacts is anticipated. As illustrated in Fig. 6.1 (c) and (d), the Al segments are of unequal length. The long junction features a Ge segment measuring approximately 250 nm, while the shorter junction has a length of ∼ 100 nm. The short junction possesses a higher critical current, making it suitable as a reference junction for the longer junction with a lower critical current, allowing for the measurement of the CPR of the long junction. In addition, two side gates allows us to individually tune the critical current in each JJ. A global back gate can tune the hole density in both NW junctions simultaneously with a much larger lever arm compared to the side gates.

6.3. Josephson current in each individual junction

To confirm both JJs could carry supercurrent, we first performed current-bias measurements of each JJ individually using a standard low-frequency lock-in technique. A current I_{SD} is applied to the source contact, and the differential resistance $\partial V_{\mathrm{SD}}/\partial I_{\mathrm{SD}}$ is measured. As shown in Fig. 6.2 (a), the differential resistance of the long junction is measured, while the short junction is pinched off with $V_{\mathrm{SG2}} = 4\,\mathrm{V}$ and back gate voltage $V_{\mathrm{BG}} = 0\,\mathrm{V}$. The supercurrent manifest itself as a resistance dip around zero current bias[3]. At $V_{\mathrm{SG1}} < -4\,\mathrm{V}$, a critical supercurrent $I_{\mathrm{c},1}$ varying from (almost) 0 to 3 nA is observed. The vanishing supercurrent at some gate voltages could be due to the finite step size in I_{SD} when sweeping the current and a varying contact transparency in gate voltage. The normal state resistance $R_{\mathrm{n},1}$ varies from 10 kΩ to 16 kΩ in this gate range, yielding a maximum $I_{\mathrm{c}}R_{\mathrm{n}}$ product $\sim 35\,\mu\mathrm{V}$.

We also measured the differential resistance of the short junction in a similar configuration, specifically at $V_{\mathrm{SG1}} = 6.5\,\mathrm{V}$ and $V_{\mathrm{BG}} = 0\,\mathrm{V}$. It is shown as a function of V_{SG2} in Fig. 6.2 (b). The appearance of Josephson current happens at a more negative gate voltage ($V_{\mathrm{SG2}} \approx -8\,\mathrm{V}$) compared to the long junction. This could be attributed to different pinch-off voltages for these two junctions, and a different lever arm of each respective side gate. Within this gate voltage range, the maximum critical supercurrent $I_{\mathrm{cmax},2}$ is observed at $V_{\mathrm{SG2}} \approx -9.5\,\mathrm{V}$. The normal state resistance $R_{\mathrm{n},2}$ varies from 12 kΩ to 19 kΩ in this gate range. In the short junction limit, maximum $I_{\mathrm{c}}R_{\mathrm{n}}$ reaches $250\,\mu\mathrm{V}$. This value closely aligns with previously reported values for Al-alloyed Ge/Si Josephson junctions [189, 191].

For both maps, a pronounced feature is observed at higher current bias: multiple enhanced conductance lines manifest as a wavy pattern with respect to gate voltage. These lines is consistent with multiple Andreev reflections (MAR), as analyzed in SI Fig. S6.1 and SI Fig. S6.2 in the supplementary information. Integrating the $\partial V/\partial I$ data to obtain V_{SD}, these wavy lines appear at a finite source-drain voltage, with peak positions given by $2\Delta/(n \cdot e)$. By fitting the MAR peak positions, as depicted in Fig. S6.1 (b), we extract a superconducting gap $\Delta_1 = 200\,\mu\mathrm{V}$ for the long junction. We observed that the peak positions correspond to $n = 1, 2, 3, 4, 5$ and 7[4]. A similar analysis is performed for the short junction, see Fig. S6.2 (b). Here, the MAR is observed up to order of 6, with $\Delta_2 = 210\,\mu\mathrm{V}$. Observing higher order MAR requires a coherent transport in the NW and homogeneous interfaces between superconductor and nanowire. Again, our measurements are in good agreement with MARs reported in Ge/Si NW JJ with similar annealing contacts [189, 191].

---

[3] The measurements were performed in a two-terminal configuration, where a line resistance of $\sim 100\,\Omega$ still exist.

[4] Even higher order MAR exists, but not labeled accordingly due to the limited measurement resolution

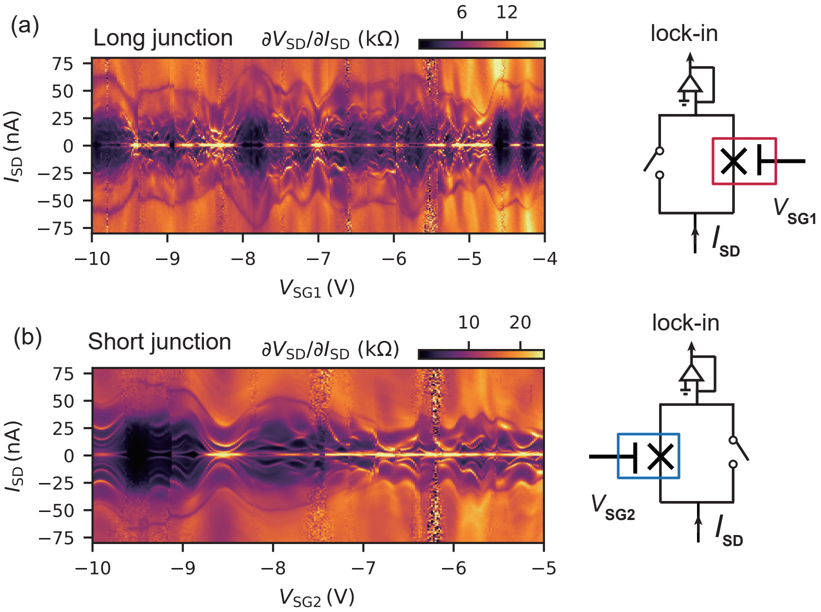

Figure 6.2. Current bias spectroscopy of each individual junction. (a) The differential resistance, $\partial V_{\mathrm{SD}}/\partial I_{\mathrm{SD}}$, is measured as a function of the current bias I_{SD} and side gate voltage V_{SG1} for the long junction (250 nm). In this configuration, the short junction is pinched off ($V_{\mathrm{SG2}} = 4\,\mathrm{V}$), and the back gate voltage is set to $V_{\mathrm{BG}} = 0\,\mathrm{V}$. (b) The differential resistance, $\partial V_{\mathrm{SD}}/\partial I_{\mathrm{SD}}$, is shown for the short junction (100 nm). Similarly, the long junction is pinched off ($V_{\mathrm{SG1}} = 6.5\,\mathrm{V}$), and the back gate voltage is set to $V_{\mathrm{BG}} = 0\,\mathrm{V}$.

Together with the TEM studies reported in Ref. [190, 199, 201], we conclude that the Al/Ge inter-diffusion process result in atomic-sharp and homogeneous interfaces.

We note that the above-mentioned current bias spectroscopy are both measured at $V_{\mathrm{BG}} = 0\,\mathrm{V}$. We cannot pinch off the other junction with the corresponding side gate once a more negative V_{BG} is applied. This is attributed to the large lever arm of the back gate compared to the side gate, with a ratio exceeding 5:1. However, in the following SQUID measuremnts, we heavily doped both NW JJs with the global back gate to ensure large Josephson currents.

6.4. Voltage bias spectroscopy

To complete the basic characterization of the same device, we performed the voltage bias spectroscopy of each individual junction. Although the atomically sharp interfaces yields transparent contacts in the open regime, a quantum dot is expected near pinch off of the NW. This is due to the Fermi velocity mismatch between superconducting Al and semiconducting Ge, leading to a reduced transmission, similar to an energy barrier at the interfaces. This allows us to perform tunneling spectroscopy of Andreev bound states in the NWs.

Long junction

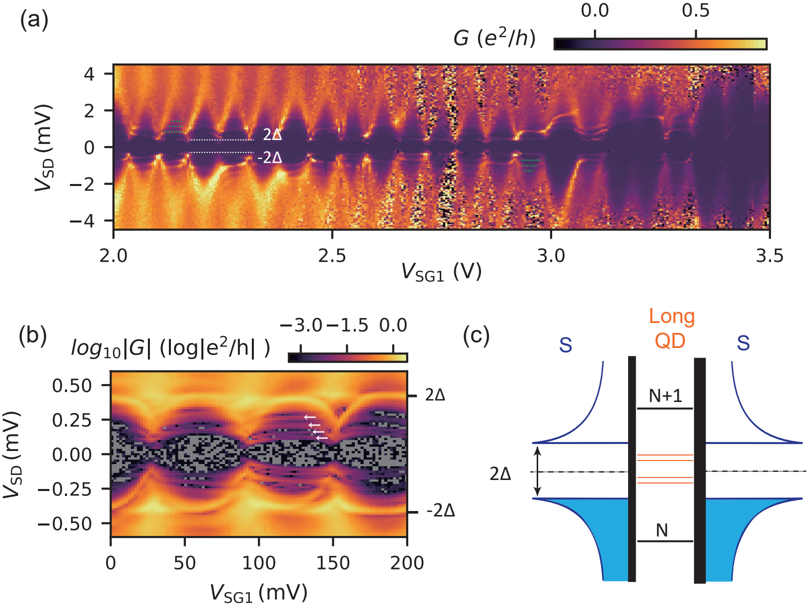

Figure 6.3. Voltage bias spectroscopy of the long junction near depletion. (a) Differential conductance measured as a function of V_{SD} and V_{SG1}. ($V_{\mathrm{BG}} = 0\,\mathrm{V}$). (b) Sub-gap states measured at a smaller V_{SD}, with a slightly different $V_{\mathrm{BG}} = 0.31\,\mathrm{V}$. (c) Energy diagram of S-QD-S system.

We perform spectroscopy measurements of the long junction while the short one is pinched off ($V_{\mathrm{SG2}} = 5\,\mathrm{V}$, $V_{\mathrm{BG}} = 0\,\mathrm{V}$). As shown in Fig. 6.3 (a), the differential conductance $G = \partial I_{\mathrm{SD}}/\partial V_{\mathrm{SD}}$ is measured as a function of the source-drain bias voltage V_{SD} and side gate voltage V_{SG1} for the long junction.

Close to depletion, we observe well-defined Coulomb blockade (CB) diamonds with a charging energy $E_{\mathrm{c}} \approx 3\,\mathrm{mV}$. The CB diamonds are very regular over a large gate voltage range, demonstrating the absence of strong scatter in the Ge section (250 nm). This is consistent with hole mean free paths up to 500 nm in Ref. [56]. Cotunneling lines are also observed as indicated by the green dashed line in Fig. 6.3 (a), originating from the higher-order transport via excited states of the QD. In addition, we point out that the CB diamonds are shifted by a gap of 2Δ around zero bias, a standard S-QD-S transport characteristic [224]. The corresponding energy diagram of the system is illustrated in Fig. 6.3 (c).

Now we focus on smaller V_{SD} to study the sub-gap Andreev bound states, as shown in Fig. 6.3 (b). We note that $V_{\mathrm{BG}} = 0.31\,\mathrm{V}$ is applied here, hence we are looking at a gate regime $V_{\mathrm{SG1}} \approx 1\,\mathrm{V}$ in (a)[5]. To resolve fine features, the condutance is plotted on a logarithmic scale. In the map, we identify at least 4 branches of ABSs, as indicated by the white arrows. The states disperse very little with gate voltage. Since the NW is close to depletion, we expect only one or two transverse modes [220]. This means each mode could make 2 branches of ABS, due to the finite channel length of the long junction.

Furthermore, the above-mentioned $I_{\mathrm{c}}R_{\mathrm{n}}$ product also serves as a measure of the limit the JJ is in. In the short ballistic regime, the $I_{\mathrm{c}}R_{\mathrm{n}}$ could reach the ideal value of $\pi\Delta/e$ [244]. In contrast, the $I_c R_n$ product of the long juncion has a maximum value $\sim 35\mu\mathrm{eV}$, significantly smaller than Δ. Given the existence of multiple branches of ABSs as well as a small $I_{\mathrm{c}}R_{\mathrm{n}}$ product, we conclude that the longer junction is in the long ballistic limit.

Short junction

Now we discuss the voltage bias tunnel spectroscopy of the short junction, with data shown in Fig. 6.4. Surprisingly, we find a completely different pattern. A branch of ABS, denoted by the black dashed line in Fig. 6.4 (a), disperses over a wide range from Δ to 2Δ. We also found a mirrored copy of this state between 0 and Δ, as denoted by the white dashed line. Another interesting regime is shown on the right panel. Within this region, we have identified states crossing, which appears between $-\Delta$ and -2Δ as indicated by the white arrows, now also appears between 0 and Δ.

As gate voltage decreases, more sub-gap states emerge, giving rise to a rich spectrum as shown in Fig. 6.4 (b). The mirrored pair of states from (a) continues, as indicated by the black and white dashed lines. However, we have also identified states between $-\Delta$ and Δ do not have a mirrored partner states between Δ and 2Δ, marked by the green dashed line in Fig. 6.4 (b).

---

[5] Judging by counting the CB diamonds

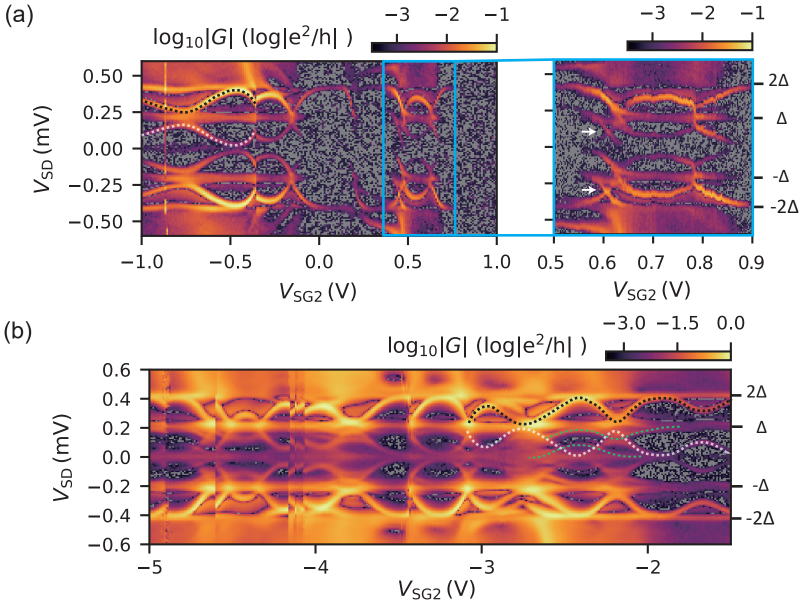

Figure 6.4. Voltage bias spectroscopy of the short junction near depletion. (a) Differential conductance measured as a function of V_{SD} and V_{SG2} ($V_{\mathrm{BG}} = 0\,\mathrm{V}$). The right panel shows a zoom-in in the gate range $V_{\mathrm{SG2}} \approx 0.6\,\mathrm{V}$. (b) Differential conductance measured in more negative gate voltage. More states emerges, as indicated by the green dashed line.

We note that such a rich spectrum spanning from $-\Delta$ to Δ, along with the presence of mirrored-states, has not been reported in other systems like carbon nanotube (CNT) [51, 208, 224], InAs nanowire [59, 122, 245] and 2DEG [68, 246].

We tentatively explain the mirrored-states as follow: A pair of ABS formed in the vicinity of one contact with energy ξ and $-\xi$, while the other contact serve as a "spectrometer" lead. When the BCS density of state of this "spectrometer" lead is aligned with the ABS, we obtain resonance at energy $\Delta+\xi$, $\Delta-\xi$, as well as at $-\Delta+\xi$ and $-\Delta-\xi$. As for the states marked by the green lines, they could extent over the whole JJ (see theory Section 2.3), and therefore cannot be explained with this simple picture. However, we find that the magnitude of resonance between Δ and $-\Delta$ is much weaker than the resonance above $|\Delta|$. The exact explanation for this remains unclear and falls beyond the scope of our study. Nevertheless, we highlight that the well-defined and homogeneous Al/Ge interfaces can serve as a valuable platform for investigating sub-gap states with high resolution, akin to NW with crystal-defined barriers [123, 247].

In summary, we conclude that the short junction operates within the short ballistic limit. This conclusion is drawn from the significant dispersion of ABS and the large $I_c R_n$ product measured, which extends up to 250μeV.

6.5. Current-phase relation measurements

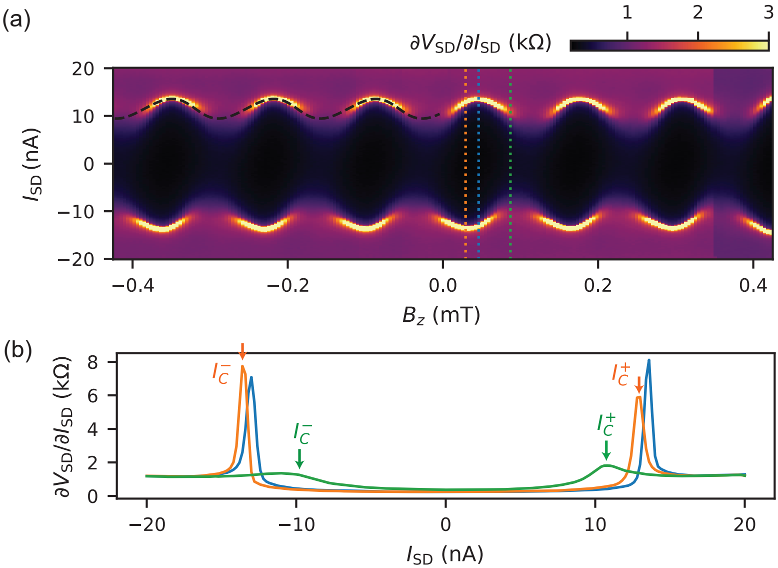

Figure 6.5. Current-phase relation measurement of the SQUID. (a) The differential resistance of the SQUID device as a function of the current bias I_{SD} and the external magnetic field B_Z in an asymmetric configuration with $I_{c1} \approx 2\,\text{nA}$ and $I_{c2} \approx 11.5\,\text{nA}$. The gate voltages are set to $V_{SG1} = -9.3\,\text{V}$, $V_{SG2} = -9.9\,\text{V}$, and $V_{BG} = -4.65\,\text{V}$. The black dashed line represents the fit for a forward-skewed CPR (see main text). (b) Three cross sections are taken at fixed magnetic fields, namely 0.029 mT (orange), 0.046 mT (blue), and 0.087 mT (green). The orange and blue traces are taken at the maximum critical supercurrent $I_{C,\text{max}}$ for negative and positive current-bias branches. The green traces are taken close to the π phase, where the supercurrent transition is smeared out.

The main results of this chapter are CPR measurement for the long junction, as will be discussed now. We measured the SQUID in an asymmetric configuration. The short junction has a $I_{\mathrm{c}2}$ of approximately 11.5 nA, significantly larger than $I_{\mathrm{c}1}$, which is $\approx 2\,\mathrm{nA}$. Consequently, the superconducting phase ϕ across the short junction remains approximately constant [87], and the critical current of the SQUID captures the current-phase relation of the long junction. As shown in Fig. 6.5 (a), the critical current of the SQUID is measured as the peak of the differential resistance as a function of the external magnetic field B_z and the current-bias I_{SD}. The measurement reveals a distinct SQUID oscillation pattern with a period that aligns well with one flux quantum threading the loop area $A \approx 12\,\mu m^2$. We notice that the critical current transition is smeared out at phase close to odd multiples of π, as shown by the cross section (green) in Fig. 6.5 (b). An exact explanation for this is not yet clear. We speculate that the thermal broadening in a capacitively and resistively shunted JJ could lead to a switching characteristic like this.

Skewness and non-reciprocal critical current

The positive (negative) branch of the critical current exhibits a distinct non-sinusoidal pattern with a forward skewness. These characteristics imply the presence of highly transparent channels in the JJ. As indicated by the black dashed line, we tentatively fit the SQUID oscillation with the expression in the short junction limit,

$$I(\phi) = I_c \frac{\sin(\phi)}{\sqrt{1 - t\sin^2(\phi/2)}} \tag{6.1}$$

where ϕ is the phase drop across the junction, t is an effective junctions transparency. The fit qualitatively explains the skewness with $t = 0.45$. However, it is important to note that the fits do not fully capture the data, from which we conclude that either there are many channels or the JJ is in the long junction limit. As discussed above, multiple evidences point out that the longer junction is in the long ballistic junction limit. In this limit, the junction length L is still much smaller than both normal metal coherence length l_T and elastic scattering length l_e, but greater than the superconducting coherence length: $l_T, l_e \gg L > \xi_0$. In this case, the CPR is described by a completely different expression (see details in Eq. 4.185 from Ref. [248]):

$$I(\phi) = \sum_{\mathbf{k}_{\mathrm{F}}} \frac{e v_{F,x}}{L} \frac{2}{\pi} \sum_{p=1}^{\infty} (-1)^{p+1} e^{-2p\frac{L}{l_e(\mathbf{k}_{\mathrm{F}})}} \frac{L}{l_T(\mathbf{k}_{\mathrm{F}})} \frac{\sin(p\phi)}{\sinh\left(\frac{pL}{l_{\mathrm{T}}(\mathbf{k}_{\mathrm{F}})}\right)} \tag{6.2}$$

with $l_T(\mathbf{k}_{\mathrm{F}}) = \frac{\hbar v_{F,x}}{2\pi k_B T}$ and $l_{\mathrm{e}}(\mathbf{k}_{\mathrm{F}}) = v_{F,x}\tau$. $\mathbf{k}_{\mathrm{F}}$ is Fermi wavevector, $v_{F,x}$ is Fermi velocity, T is the temperature and τ is the scattering time. The subscript x represent different mode. To extract information about the long junction, such as the coherence length ξ_0 and transparency t, a comprehensive modeling and fitting approach is still missing.

Now, we go back to the measurement in Fig. 6.5 again. We found that the maxima of the critical current in the positive branch $I^+_{\mathrm{C,max}}$ have a relative shift with respect to the negative branch $I^-_{\mathrm{C,max}}$. Here, we take the cross sections at position of $I^+_{\mathrm{C,max}}$ and $I^-_{\mathrm{C,max}}$, as shown in Fig. 6.5 (b) by the blue and orange trace. From the orange trace, we extract a critical current at negative bias of $I^-_{\mathrm{C}} = -13.6\,\mathrm{nA}$, while $I^+_{\mathrm{C}} = 12.8\,\mathrm{nA}$ at the positive branch. The fact that $|I^+_{\mathrm{C}}|$ is not equal to $|I^-_{\mathrm{C}}|$, is often described as superconducting diode effect (SDE) [249].

The occurrence of (SDE) necessitates the breaking of both time reversal and inversion symmetry in the system. This can be achieved in Josephson junctions (JJ) where the broken symmetries arises from the material composition of the JJ [249]. In our case, the nonreciprocity can be explained by Ref. [250], where the inversion symmetry is broken the asymmetry in the DC SQUID and time reversal symmetry is broken by the external magnetic field. This mechanism also requires highly transmissive JJs. While SDE in such SQUID configurations has been reported in 2D heterostructures, such as proximitized InAs two-dimensional electron gas [251] or Ge quantum wells [252, 253], we demonstrate here that it can also be realized in a 1D nanowire.

The CPR of a JJ can be expressed as a Fourier series $I_c = \sum_n I_n \sin(n\phi)$ [87], where terms with $n > 2$ represent the higher harmonics. Our observations suggest that Ge/Si JJs are highly transmissive, featuring a significant contribution from the higher harmonics to CPR. In the next section, we will demonstrate that the higher harmonics can even dominate over the first harmonic term at some specific configurations.

6.6. Anomalous current-phase relation

In the course of our experiments, we measured the CPR of the long junction under various gate voltage settings. In most cases, the CPR exhibited a similar pattern, as discussed for in Fig.6.5. However, for certain finely tuned gate values, a notable change in the periodicity of the CPR was observed, as shown in Fig. 6.6. Throughout these experiments, we maintained the values of V_{BG} and V_{SG2} constant, while only adjusting V_{SG1} for the long junction. Intriguingly, the first harmonics is strongly suppressed and the second harmonics becomes the dominating terms in the CPR, for example, at $V_{SG1} = -3.04\,\mathrm{V}$.

A comprehensive map with smaller gate voltage intervals is shown in Fig. S6.3. To further prove that the anomalous CPR originates from the long junction, we show the CPR measurements with $V_{\mathrm{SG1}} = -3.02\,\mathrm{V}$ at different gate voltages applied to the reference junction V_{SG2} in Fig. S6.5. The large second har-

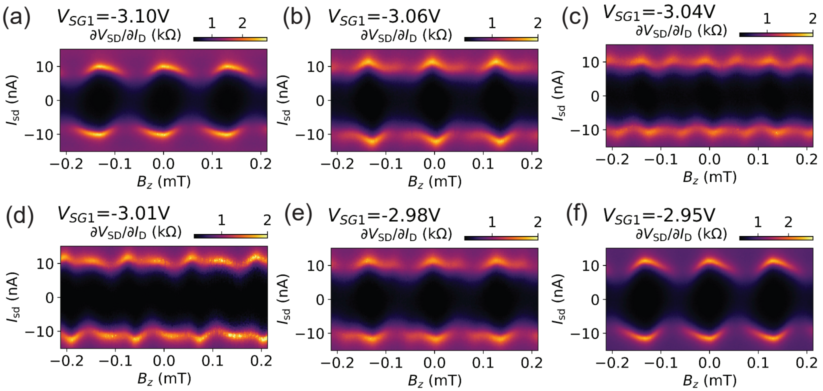

Figure 6.6. Anomalous CPR. (a) to (f) Differential resistance of the DC-SQUID as a function of I_{SD} and B_Z for different gave voltage $V_{SG1} = -3.1\,\text{V}, -3.06\,\text{V}, -3.04\,\text{V}, -3.01\,\text{V}, -2.98\,\text{V}, -2.95\,\text{V}$. The back gate and the other side gate voltage remains fixed at $V_{BG} = -2.5\,\text{V}$ and $V_{SG2} = -7.6\,\text{V}$. The dominant harmonics of CPR went through a transition from 2π periodic to π, and recover back to 2π. A full map is shown in Fig. S6.3.

monics feature remains robust, despite the smearing out of the supercurrent switching at certain gate voltage V_{SG2}.

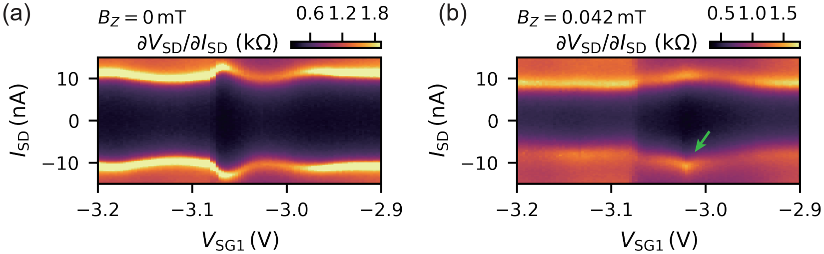

Figure 6.7. Current-bias map as a function of I_{SD} and V_{SG1} at (a) $B_z = 0$ and (b) $B_z = 0.042\,\text{mT}$. The V_{BG} and V_{SG2} is the same as Fig. 6.6. Near the gate voltage where a anomalous CPR is measured, the positive and negative branch becomes highly asymmetric, manifesting as a "bump" as indicated by the green arrow. This bump could appear at zero magnetic field, or finite magnetic filed as shown here.

It is important to note that such anomalous CPR transitions occur within a narrow gate voltage range of approximately $\sim 100\,\mathrm{mV}$. Furthermore, it also brings in another finding: this anomalous CPR does not manifest periodically in gate voltage but rather sporadically and randomly. This observation is supported by the current-bias map when sweeping V_{SG1}, as shown in Fig. 6.7. The appearance of anomalous CPR could introduce a stronger asymmetry in positive and negative branch of current-bias. Hence, the appearance of anomalous CPR always accomplish with a "bump" in the current-bias map that is indicated by the arrow in Fig. 6.7 (b).

In the experiment, we have identified multiple gate configurations where the anomalous CPR can be observed. A second example is presented in Fig. S6.6. All of these configurations exhibit consistent features as discussed above: (1) dominant harmonics transition from $\sin(\phi)$ to $\sin(2\phi)$, and (2) a "bump" in the current-bias map accompanied by the anomalous CPR, and with no periodicity found in nearby gate voltages.

Counter measurement

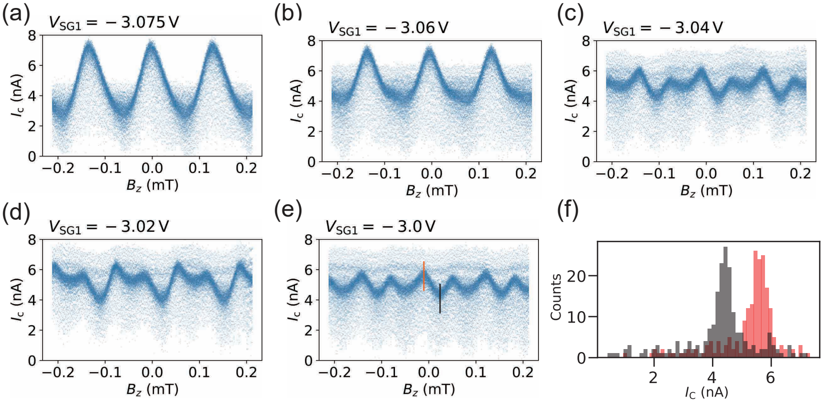

Figure 6.8. Counter measurement of SQUID critical current. (a) to (e) Critical current I_C as a function of B_Z measured at $V_{\mathrm{SG1}} = -3.075, -3.06, -3.04, -3.02 - 3.0\mathrm{V}$, correspondingly ($V_{\mathrm{SG2}} = -8.1\,\mathrm{V}$ and $V_{\mathrm{BG}} = -2.5\,\mathrm{V}$). A whole dataset map is shown in Fig. S6.4. (f) Histograms of I_C at cross sections taken from (e).

The previous measurements were performed using the lock-in techniques, where each data point is recorded with a time constant of 200 ms. However, this quasi-statistic measurement cannot capture the rapid switching dynamics of a JJ, which can occur on much faster timescales, including multivalued CPR [241, 254] or widely distributed switching current values [255–258]. These effects, if present, could lead to a misinterpretation of our experimental data.

To monitor fast-switching events, we employ a dynamic measurement with counter technique. We apply a current-bias using a sawtooth function at a frequency of 77 Hz, resulting in a ramp rate of 1.54 nA/ms. When the JJ switches to its normal state, a voltage drop V_{drop} is measured, which is then forwarded to a counter and compared to a predefined trigger voltage V_{trig}. If V_{drop} exceeds V_{trig}, we record a time t_{meas} relative to the period of the sawtooth function, and subsequently converted to the critical current I_C. We repeat this routine 200 times for each magnetic field, with each field taking less than 3 seconds.

In Fig. 6.8, we present the counter measurements of the SQUID critical current at different V_{SG1} values, which exhibit a similar pattern to the lock-in results. The histogram, as illstrated in Fig. 6.8 (f), does not exhibit a multivalued CPR. We note that the reference junction I_C^{ref} now has a lower value[6], indicating that the SQUID I_C does not accurately capture the CPR of the long junction. We also observe that switching events occur at values different from I_C, which is attributed to noise-induced counter triggering. To the best of our knowledge, this is the first instance where the counter technique has been employed to resolve I_C at the few nA-scale.

6.7. Discussion

Now, let's focus on our most intriguing finding: the anomalous CPR, characterized by a dominant second harmonic in the CPR.

A dominating $\sin(2\phi)$ term in the CPR have been previously reported in various types of junctions. These include superconductor-ferromagnetic-superconductor (SFS) junctions [239, 259], quantum dot Josephson junctions in the Kondo regime [89, 237, 260], superfluid ^{3}He [261–263], 45° twisted d-wave superconductor junctions [264–266]. In addition, we note that SQUIDs with highly transmissive JJs operating in the symmetric regime at π flux bias would also have a dominating $\sin(2\phi)$ term [251–253, 267, 268].

These findings can be categorized into three different mechanisms: (1) The 0-π transition, as observed in quantum dot JJ and SFS junctions. (2) Unique symmetries in the superconducting wave-function, as demonstrated in d-wave superconductor JJ and superfluid ^{3}He. (3) The cancellation of the first harmonics in a SQUID geometry at π flux, due to destructive quantum interference.

---

[6] In the counter measurements, it's crucial to have a relatively sharp transition in the $I-V$ curve to ensure that the supercurrent switching event is distinguishable from noisy background. To achieve this, we must adjust the reference junction voltage V_{SG2} to a less overdamped point.

Cases (2) and (3) clearly do not apply to our scenario, as we are working with standard s-wave superconductors, and our SQUID operates in an asymmetric configuration where the supercurrent in each arm has different amplitudes. In the following discussion, we discuss case (1) and also propose alternative explanations, including spin-orbit interaction, and a cancellation mechanism due to ABSs spectrum in long junction limit.

Quantum dot JJ and Kondo effect

The CPR with a dominating $\sin(2\phi)$ term can occur at the phase transition between 0 and π JJ [237, 260]. This situation is schematically depicted in Fig. 6.9 (c). This means at some phase range it is a 0 JJ, featuring a $\sin(\phi)$ CPR, while at other phase JJ has a π junction ground state with $\sin(\phi + \pi)$ CPR [269]. Therefore, the measured CPR has a combined feature of 0 and π JJ, mimicking the $\sin(2\phi)$ pattern. This effect is named as $0^{'}$ or $\pi^{'}$ junction.

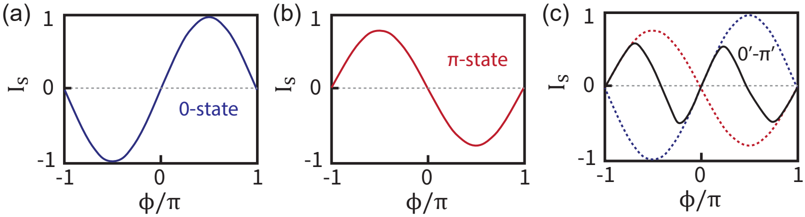

Figure 6.9. Schematic of CPR of a quantum dot JJ.(a) 0 state in a evenly occupied QD (b) π state in an oddly occupied QD. (c) During the phase transition between the 0 and π states, the CPR exhibits a form resembling $\sin(2\phi)$. The dashed lines serve as visual guides, representing the contributions from the 0 and π states. Adapted from Ref.[237].

A π Josephson junctions can arise in quantum dots, where Cooper pair transfer is governed by quantum dot occupancy. In cases of even occupancy, a 0 junction forms, and the supercurrent amplitude aligns with the dot's transmission. Conversely, odd occupancy necessitates fourth-order processes for the first nonzero supercurrent contribution, leading to a reversal in Cooper pair spin ordering [89]. This results in a sign change of the supercurrent and a significant reduction in its amplitude, defining a π junction. In addition, an odd-occupied dot gives rise to the Kondo effect, characterized by a Kondo temperature T_K. When $k_B T_K < \Delta$, superconducting correlations disrupt Kondo screening, leaving the π junction unaffected. However, when $k_B T_K > \Delta$, an unpaired electron's spin forms a Kondo singlet, creating a well-transmitted channel that facilitates Cooper pair transfer. This results in the restoration of a 0 junction [237].

However, this mechanism cannot explain our observations. First, we never observe a π junction in our experiment. It always a transition from dominating $\sin(\phi)$ to $\sin(2\phi)$, and back to $\sin(\phi)$. If this were due to a quantum dot JJ, we would expect the appearance of a π junction during the transition. Secondly, our observed anomalous CPR occurs sporadically and randomly, in contrast to the periodic behavior reported in Ref. [237, 260], since the quantum dot state change periodically from odd to even state with gate voltage.

Moreover, this effect only occurs in the regime that the coupling Γ between NW and superconducting lead is weak enough to have well-define quantum dot. While the coupling Γ increases at higher gate voltage, one always observe a 0 junction. In our SQUID measurement, we heavily doped the NW with global back gate, and therefore expect the junction is in the open regime. Based on these analysis, it appears unlikely that case (1) provides an explanation for the origin of the anomalous CPR.

Spin-orbit interaction

Strong spin-orbit interaction (SOI) is predicted to yield an anomalous CPR with an external magnetic field [78–80], as discussed in Section 2.4.1. Moreover, when an in-plane external magnetic field is applied to the JJ with SOI, a ϕ_0 junction can be observed [97] : $I = I_c \sin(\phi + \phi_0)$. However, our SQUID operates in a relatively weak magnetic field (~mT), which is insufficient to induce this effect.

Nonetheless, we cannot completely exclude the impact of SOI. In Ref. [79], it was predicted that in a two-level quantum dot model, the supercurrent can be drastically modified even without an external magnetic field. Recent experiments [213] also indicates ABSs could split in the absence of magnetic field, which may result in a modified CPR accordingly.

Cancellation of the first harmonics within ABSs

Proposed by Dr. Henry Legg and Prof. Jelena Klinovaja, we have uncovered a new mechanism that offers a potential explanation for our results. Our hypothesis is that the anomalous CPR arises from destructive interference between multiple ABSs in the same NW, as shown in Fig. 6.10.

In the finite length JJ, more than one branch of ABSs could appear. The CPR can be obtain by summing up contribution from each branch:

$$I_s(\phi) = \frac{2e}{\hbar} \sum_x \frac{\partial E_{A,x}(\phi)}{\partial \phi}, \tag{6.3}$$

where x represents the different branches. Let us assume the case where two branches (a and b) mainly contributes to the supercurrent. According to

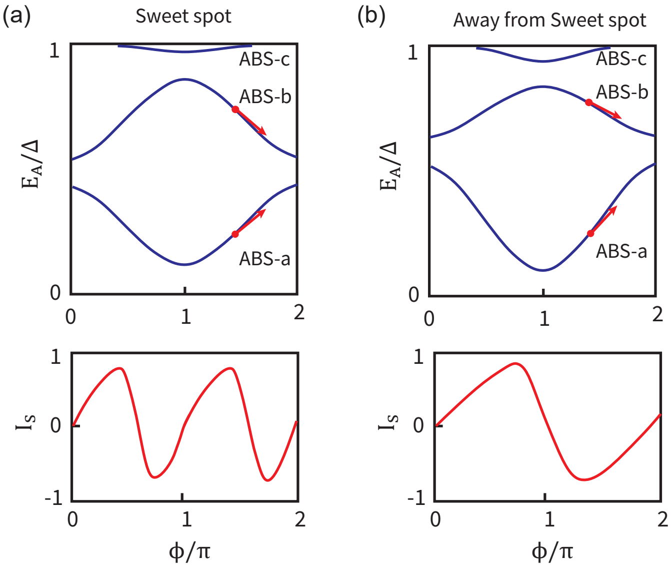

Figure 6.10. Schematic of origin of anomalous CPR. ABSs spectra (top panel) and the corresponding CPR at two different gate voltage for (a) and (b). The schematic is inspired by simulations conducted by Dr. Henry Legg.

Equation 2.14, we can decompose CPR into fourier series:

$$\begin{aligned} I_s(\phi) &= I_{s,a}(\phi) + I_{s,b}(\phi) \\ &= \sum_{n\geqslant 1} I_{n,a}\sin(n\phi) + \sum_{n\geqslant 1} I_{n,b}\sin(n\phi) \\ &= I_{1,a}\sin(\phi) + I_{2,a}\sin(2\phi) + ... + I_{1,b}\sin(\phi) + I_{2,b}\sin(2\phi) + ... \end{aligned} \tag{6.4}$$

Supercurrent contribution $I_s(\phi) \propto dE(\phi)/d\phi$ for two branches could have a different sign, as shown by the red arrow in Fig. 6.10. A scenario could happen that two ABSs have a comparable contribution to the supercurrent, but in a manner that results in the cancellation of the first harmonics ($I_{1,a} = -I_{1,b}$). As a result, the remaining CPR have the 2^{nd} harmonics as the leading term

$$I_s(\phi) = (I_{2,a} + I_{2,b})\sin(2\phi) + ... \tag{6.5}$$

This scenario only happens in certain gate "sweet spot". In addition, this model will only work for JJ that fulfills the following requirements:

- **Highly transmissive channel**: This ensure higher harmonics like $\sin(2\phi)$ emerges.
- **Long junction limit**: At least two branches of ABSs exist.
- **Few transverse modes**: In the case of many modes, such exact cancellation of first harmonics cannot be found.

This model offers an explanation for the sporadic occurrence of the anomalous CPR in gate voltage and the non-occurrence of a π junction. We therefore favor this explanation.

6.8. Conclusion and outlook

In summary, we have embedded two gate-tunable Ge/Si NW JJs into a SQUID geometry. With the side gates, we are able to tune the supercurrent in each individual arm. Using the short junction as a reference junction, we measured the CPR of the long junction, featuring a forward-skewness and non-reciprocal critical current. This demonstrates highly transmissive channels in JJ, thanks to the atomic-sharp and homogeneous Al/Ge interfaces. From tunneling spectroscopy of the ABSs, we conclude that the long junction is in long ballistic limit, and the short junction in the short ballistic limit. Most importantly, we observe the occurrence of an anomalous CPR at selected fine-tuned gate voltage. We tentatively attribute it to the cancellation of first harmonics due to the Andreev level spectrum in the long junction limit.

These results establish Ge/Si core/shell nanowires as a platform to investigate superconductor–semiconductor hybrid physics, paving the way for potential applications like, for example, Andreev spin qubits [142, 143, 213, 270] with enhanced qubit coherence times. Moreover, the π-periodic CPR could be used to build parity protected qubit [268, 271–273]. In a superconducting circuit exhibiting this phase dependence, there are two energy minima in Josephson energy. These minima define the $|0\rangle$ and $|1\rangle$ states of the qubit, with the quantum state protected by the parity of Cooper pairs.

Future work is essential for achieving a comprehensive understanding of this alloyed Al/Ge Josephson junction. Two key directions include: (1) Replacing the reference junction with a SIS tunneling junction featuring a higher I_C, allowing for the investigation of CPR with varying channel lengths L. This approach can provide insights into the emergence of exotic physics across different regimes, including comparisons between the coherence length ξ_0 and the spin-orbit length l_{SO} relative to L. (2) Conducting measurements on the device using a vector magnet. This would involve applying a magnetic field at various directions, enabling a detailed study of the direct Rashba spin-orbit interaction.

Supplemental to Current-Phase Relation of Ge/Si Nanowire Josephson Junctions

Loop inductance

For an ideal CPR measurement, the superconducting phase should only drop over the JJ. However, the presence of finite loop inductance could also result in a phase drop, complicating the measurement and leading to the effect of a multi-valued current-phase relationship (CPR) [241, 254] or a shift of negative and positive branch of $I_C(\phi)$ [274–276]. In the section, we give an estimation of the loop inductance.

The SQUID loop is made from deposited Al with a thickness of 50 nm. Technically, the total inductance (kinetic L_k + geometric L_g) of the Al loop should be negligibly small compared to the Josephson inductance L_J of the NW JJ. A straightforward estimation with $I_C = 10\,\mathrm{nA}$ gives $L_J = \phi_0/(2\pi I_C) = 32.9\,\mathrm{nH}$. However, the Al segment that alloyed in the NW has a nanometer size, which could increase its kinetic inductance. To ensure that our results are not affected by the loop inductance, we estimate the kinetic inductance (L_k) of the Al segment in the NW.

The kinetic inductance L_k of a superconducting nanowire [277, 278] is directly related to its length (l), cross-sectional area (A), and London penetration depth (λ) from the simplified one-dimensional Ginzberg–Landau theory: $L_\mathrm{k} = \left(\mu_0\lambda^2\right)(l/A)$, where μ_0 is the permeability of free space. Given the diameter of the Al section as 15 nm, and $\lambda = 15\,\mathrm{nm}$ for bulk Al, the kinetic inductance L_k is estimated to be $1.6\,\mathrm{pH}/\mu\mathrm{m}$. It's worth noting that λ varies with the critical temperature, normal state resistivity, and operation temperature of the superconducting nanowire. The actual λ of the Al segment could differ from the estimated value. However, the estimated value is five orders of magnitude smaller than the Josephson inductance from the NW JJ. Therefore, the effect of the loop inductance during the CPR measurements should be negligible.

Multiple Andreev reflection

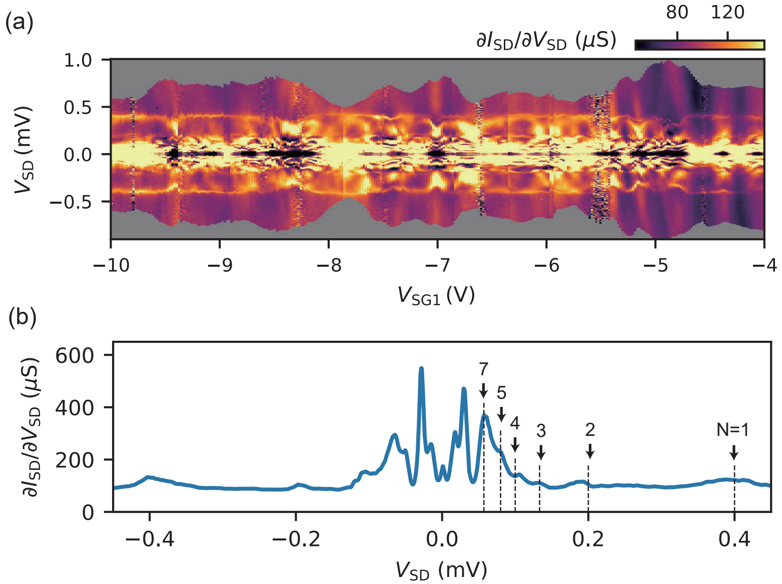

Figure S6.1. Multiple Andreev reflection in the long junction. (a) Numerical differential conductance, $\partial I_{\mathrm{SD}}/\partial V_{\mathrm{SD}}$, plotted against V_{SD} and V_{SG1}. The dataset used is the same as in Fig. 6.2 (b), with I_{SD} converted to V_{SD}. (b) A cross-section at $V_{\mathrm{SG1}} = 6.2\,\mathrm{V}$. Arrows and dashed lines indicate the theoretical Multiple Andreev Reflection (MAR) peak positions at $2\Delta/n \cdot e$, with the corresponding values of n listed.

More data on Anomalous CPR

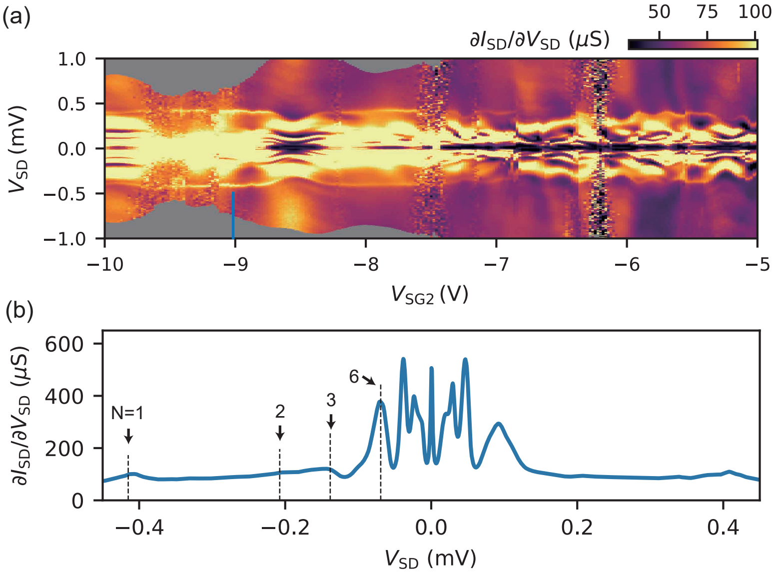

Figure S6.2. Multiple Andreev reflection in the short junction. (a) Numerical differential conductance, $\partial I_{\mathrm{SD}}/\partial V_{\mathrm{SD}}$, plotted against V_{SD} and V_{SG2}. The dataset used is the same as in Fig. 6.2 (b), with I_{SD} converted to V_{SD}. (b) A cross-section at $V_{\mathrm{SG1}} = -9.02\,\mathrm{V}$. Arrows and dashed lines indicate the theoretical Multiple Andreev Reflection (MAR) peak positions at $2\Delta/n \cdot e$, with the corresponding values of n listed.

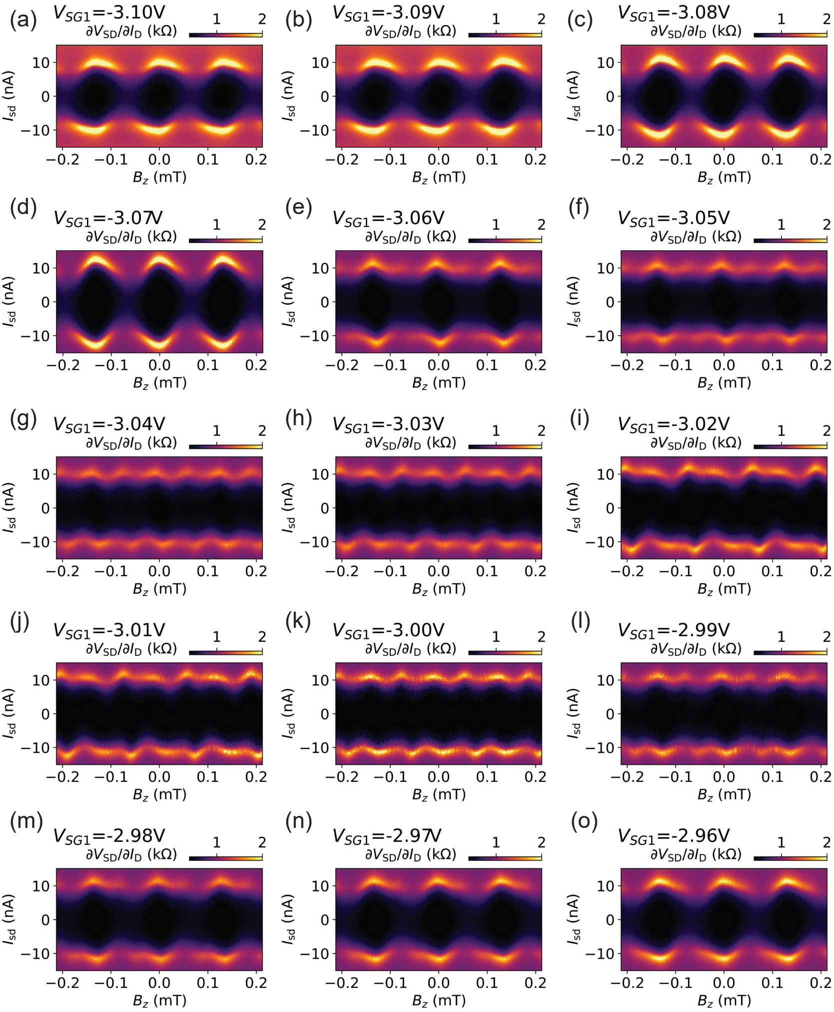

Figure S6.3. Anomalous CPR evolution with V_{SG1}.

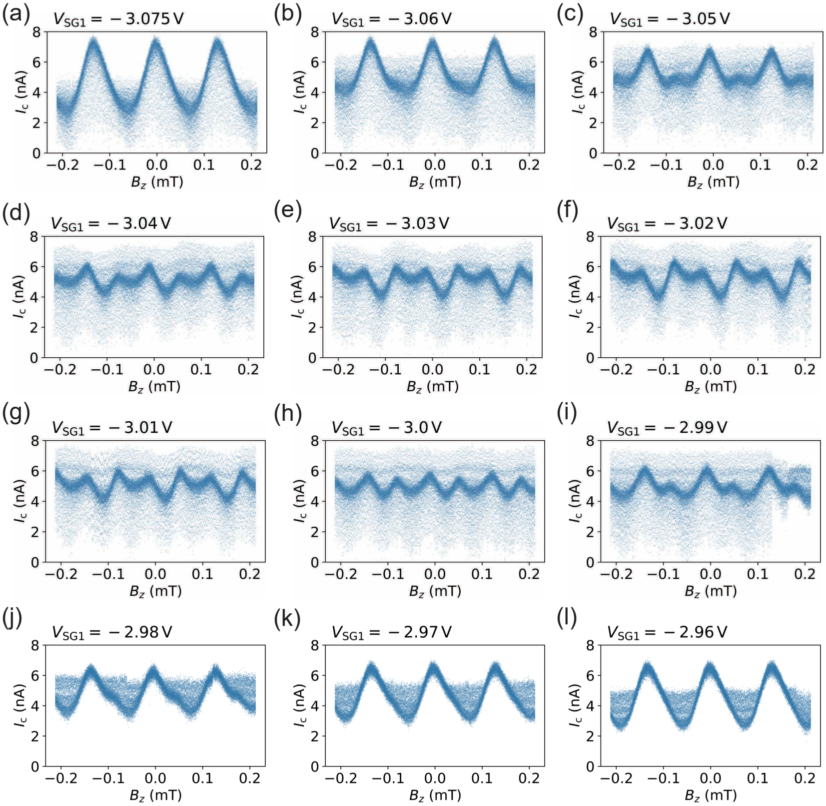

Figure S6.4. Full map of counter measurement of SQUID critical current.

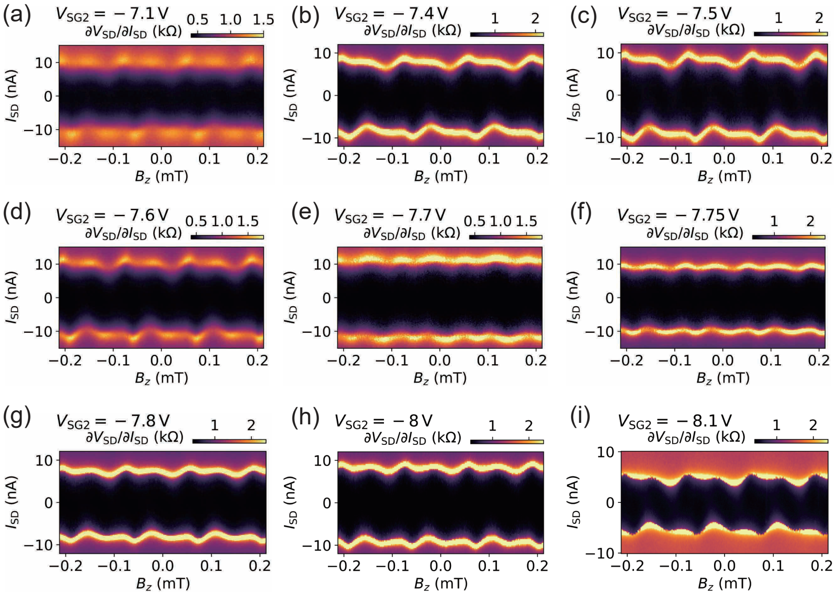

Figure S6.5. Anomalous CPR measurements at different reference junction voltage V_{SG2}.

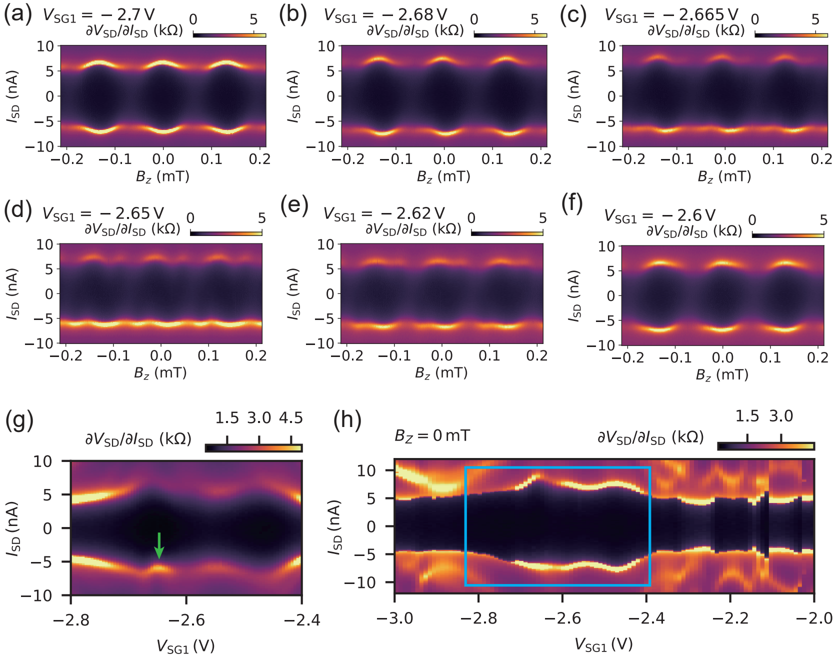

Figure S6.6. Another gate configuration where anomalous CPR is measured, with $V_{\mathrm{BG}} = -3.52$ V, $V_{\mathrm{SG2}} = -8.56$ V. (a) to (f) Current-bias map as a function of magnetic field B_Z, measured at $V_{\mathrm{SG1}} = -2.7, -2.68, -2.665, -2.65 - 2.62, -2.6$V. (g) and (f) Current-bias map as a function of V_{SG1} at $B_Z = 0$ mT. (g) is a zoom-in of (f), with slight different reference junction voltage, a "bump" is indicated with green arrow.

7 Gatemon qubit based on hole-type Ge/Si Nanowire [1] [2]

"Nature isn't classical, dammit, and if you want to make a simulation of nature, you'd better make it quantum mechanical, and by golly it's a wonderful problem, because it doesn't look so easy."
— Richard Feynman

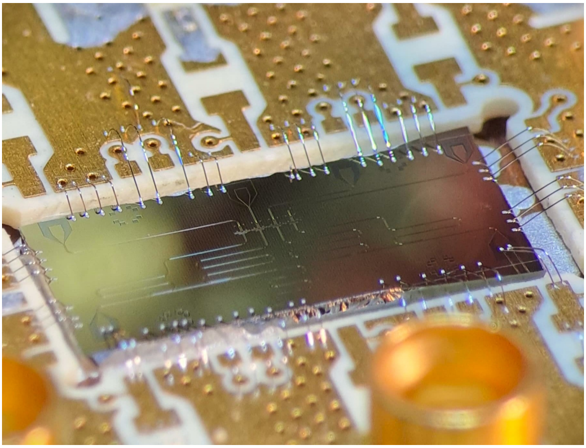

Superconducting "gatemon" qubits are the electrically tunable cousins of "transmon" qubits, with competitive characteristics exclusively from a rather unique material platform. In this work, we demonstrate the full functionality of a gatemon qubit based on hole carriers in a Ge/Si core/shell nanowire (NW), with high-quality Josephson junctions obtained by a simple annealing technique, yielding atomically sharp and highly transparent superconducting interfaces. We demonstrate the gate tunability of the qubit frequency and full

---

[1] The content of this chapter has been submitted in similar form.

[2] This experiment was conducted together with Luk Yi Cheung, a PhD student in Nanoelectronics lab, Nikunj Sangwan, a master thesis student from EPFL.

coherent control in the time domain, with competitive relaxation and dephasing times. By analyzing the anharmonicity of the gatemon spectrum, we find that transport through the NW is dominated by two quantum channels, with transparencies up to unity. This qubit platform is not only CMOS compatible and thus quantum technologically relevant, but will also allow to investigate the impact of fundamental parameters, like a large spin-orbit interaction, or the number and quality of quantum channels.

7.1. Introduction

Quantum computing has become a topic of intense activity due to its potential to revolutionize information processing [279]. Presently, one of the most popular platforms are superconducting circuits in the form of transmon qubits, which are already employed in solving noisy intermediate-scale quantum problems [280–282]. Conventional transmons rely on metallic superconductor-insulator-superconductor (SIS) tunnel junctions, in which tuning the qubit frequency requires a magnetic flux in a SQUID geometry [32]. However, flux cross-talk between qubits and the heat load due to the flux control currents are problematic for scaling up the number of qubits [283].

An alternative to metallic transmons are semiconductor-superconductor (Sm-S) hybrid systems [50], so-called gatemon qubits [267, 284], with a wealth of recently demonstrated related concepts, like parity protected qubits [268], gate-tunable fluxonium qubits [285], gatemons operated with only a few highly transparent quantum channels [136, 286], or Andreev level [137, 287, 288] and Andreev spin qubits [142, 143, 213, 270]. All these devices rely on high-quality crystals with near-perfect Sm-S interfaces. This has limited the material choice mainly to InAs-based systems, like vertically-grown InAs NWs [267, 284, 286, 289, 290], InAs 2D systems [291], or selective-area-grown InAs NWs [292]. However, III/V materials are difficult to integrate in standard CMOS technologies, and hyperfine interactions introduce additional decoherence.

More suitable for CMOS technology would be group IV materials, but only very few gatemon-related experiments have been reported so far: on carbon-nanotubes [293], graphene [294], and large-diameter Ge/Si core/shell NWs [295], with the corresponding qubit coherence times more than an order of magnitude shorter than in III/V materials. However, improvements are expected, especially for the technologically relevant CMOS compatible Si and Ge systems [296, 297]. In particular, Ge is of increasing interest for quantum information processing [21], because hole states in Ge have a p-wave symmetry, inherently reducing hyperfine interactions, with further improvements expected from isotopic purification. Even more promising might be Ge/Si core/shell nanowires with a 1D hole gas strongly confined by the Ge/Si interface [159, 191] and an electrically tunable, very large “direct” Rashba spin-orbit interaction [161, 165].

In this work, we report the full functionality of a gatemon qubit based on narrow Ge/Si core/shell NWs. The key step is the fabrication of highly transparent Josephson junctions (JJs), in an undemanding ex-situ annealing step [298, 299] driving a thermally activated propagation of superconducting aluminum into the Ge NW core [189, 190, 300]. We incorporate such JJs in a gatemon qubit device and explicitly demonstrate the electrical tunability of the qubit frequency and the full coherent control of the qubit in the time domain, with an energy relaxation time on par with III/V systems. Most importantly, these experiments allow us to analyse the qubit anharmonicity, suggesting that the supercurrent through the junction is dominated by two ballistic, virtually Schottky-barrier free conductance channels. This work establishes narrow Ge/Si core/shell NWs as a promising Sm-S hybrid platform for quantum information processing, and opens new avenues to investigate novel effects, for example, in circuit-quantum-electrodynamics (circuit QED) experiments on NWs [31, 301] with ultra-strong spin-orbit interactions.

7.2. Device

Our gatemon qubit can be understood as a non-linear LC oscillator that consists of a gate-tunable Ge/Si core/shell NW JJ as the non-linear inductance, depicted in Fig. 7.1a, and a shunt capacitor $C_{\mathrm{q}b}$ shown in Fig. 7.1b. The NW has a diameter of $\sim 20\,\mathrm{nm}$, and is expected to have minimal strain-induced defects and a high carrier mobility due to the [110] growth direction [159]. Such a NW was transferred to an undoped Si/SiO$_2$ substrate using a micro-manipulator, and contacted by Al using standard lift-off techniques. The crucial step in forming the highly transparent JJ is a thermal annealing step at 200 °C, which drives an inter-diffusion process of Al atoms from the contacts into the Ge core, yielding an Al-Ge-Al junction with an atomically sharp interface [190]. The Si shell remains intact during this process. The bright NW segment in the electron micrograph of Fig. 7.1a has a Ge core, while the Al-filled segments show a darker contrast. The length of the Ge segment can be controlled by the annealing time, and directly read off as 33 nm for this specific device. The interface between Al and Ge turns out to be highly transparent, since it allows for coherent transport of Cooper pairs through the semiconducting Ge, resulting in a JJ [189, 198]. The Josephson energy E_{J} can be tuned by a side gate voltage V_{g}. The gatemon shunt capacitance $C_{\mathrm{q}b}$ (red) is provided by a T-shaped NbTiN island etched into the surrounding ground plane, as shown in Fig. 7.1b. From electromagnetic simulations, we estimate $C_{\mathrm{q}b} \approx 78\,\mathrm{fF}$. The island is galvanically connected to the JJ, forming the non-linear LC-oscillator, with the lowest two oscillator states

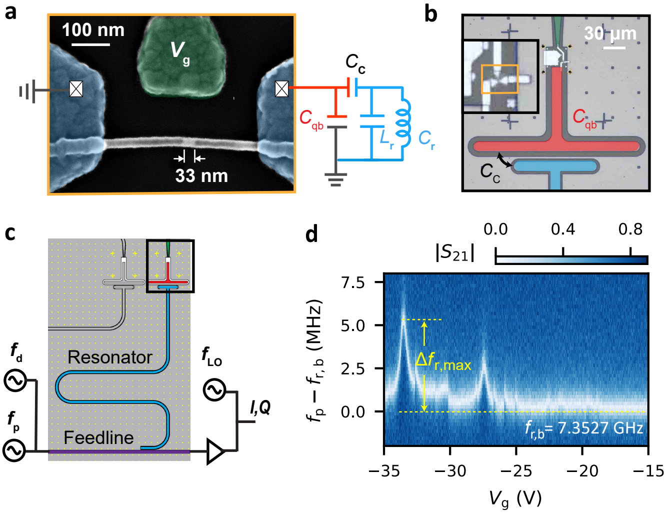

Figure 7.1. Ge/Si core/shell nanowire based gatemon device. a, False-colored SEM image of the Al-Ge-Al junction. The bright segment of the NW has a Ge core, while the dark segments contains Al. The side gate for electrical qubit control is colored in green. The readout resonator is shown as a simplified equivalent circuit on the right. **b**, False-colored optical micrograph of a nanowire Josephson junction shunted by a T-shaped capacitor (red) to the surrounding ground plane and capacitively coupled (C_c) to a superconducting $\lambda/4$ resonator (blue). **c**, Overview of the circuit QED chip and schematic of the readout and control circuit. The $\lambda/4$ resonator is inductively coupled to a feedline for readout. **d**, Transmission amplitude $|S_{21}|$ through the feedline as a function of the gate voltage V_g and the probe frequency f_p, plotted as the difference from the bare resonator frequency $f_{r,b}$. A bright signal signifies the resonator frequency f_r.

forming the qubit states $|0\rangle$ and $|1\rangle$. The corresponding qubit frequency is determined by the gate tunable Josephson energy E_J and the charging energy $E_c = e^2/2C_{qb} \approx h \cdot 248\,\text{MHz}$. The charging energy is fixed and designed to be much smaller than the typical Josephson energy, which significantly reduces the sensitivity to charge noise [135]. In addition, we deposited a 100 nm thick Al layer on the surrounding NbTiN ground plane as a quasiparticle trap (see SI Fig. S7.1).

An overview of the circuit QED chip is shown in Fig. 7.1c. The qubit state is probed via a capacitively coupled $\lambda/4$ coplanar transmission line resonator.

The short end of the microwave resonator with a current anti-node is inductively coupled to the feedline, while the open end with a voltage anti-node is capacitively coupled to the qubit island, forming the qubit-resonator coupling capacitance C_c. This device was measured in a dilution refrigerator with a base temperature of 15 mK, with consistent results in three different cooldowns.

7.3. Measurements

7.3.1. Gate tunable qubit frequency with a two-channel Josephson junction

Readout and manipulation of the gatemon qubit is accomplished using standard circuit QED techniques. When the qubit frequency f_q is strongly detuned from the resonator frequency f_r, the system is in the dispersive regime [302]. The qubit then causes a shift Δf_r of the resonator frequency from its bare value $f_{\mathrm{r},b}$, where $\Delta f_\mathrm{r} = f_\mathrm{r} - f_{\mathrm{r},b} \approx (g/2\pi)^2/(f_{\mathrm{r},b} - f_\mathrm{q})$ is determined by the qubit-resonator coupling strength g. Figure 7.1d shows a measurement of the low power transmission amplitude $|S_{21}|$ plotted as a function of the gate voltage V_g and the probe frequency f_p, plotted as the difference from the bare resonator frequency $f_{\mathrm{r},b}$. The minimum in the transmission signal occurs whenever the probe frequency f_p is resonant with f_r.

The bare resonator frequency $f_{\mathrm{r},b} = 7.3527\,\mathrm{GHz}$ can be directly found at gate voltages $V_\mathrm{g} > -15\,\mathrm{V}$, where the semiconducting part of the NW is close to depletion, so that the Josephson current is negligible and the resonator frequency exhibits no shift. The corresponding internal quality factor of $Q_\mathrm{i} \approx 2.41 \times 10^5$ is found by simultaneously fitting the resonator transmission amplitude and phase in the vicinity of $f_{\mathrm{r},b}$ [303]. At lower gate voltages, the hole density in the Ge segment is increased, resulting in a larger Josephson current on the order of a few tens of nA through the JJ, with a correspondingly larger Josephson energy and an increased qubit frequency. The resonator frequency is Lamb-shifted to higher values accordingly, with a maximum of $\Delta f_{\mathrm{r},max} \approx 6\,\mathrm{MHz}$ found at $V_\mathrm{g} \approx -33\,\mathrm{V}$, pointed out in Fig. 7.1d. The dispersive shift is positive, suggesting a qubit frequency lower than the bare resonator frequency in this gate voltage range. Δf_r does not increase monotonically with gate voltage, possibly due to resonances in the semiconducting NW section [198]. We also find discontinuities in f_r at specific gate voltages, for example at $V_\mathrm{g} \approx 30\,\mathrm{V}$. These, we attribute to a switching of the qubit frequency f_q due to charge traps in the vicinity of the NW. We note that the resonator frequency shift remains highly reproducible, including the switching, within a gate voltage range of a few volts, but becomes less reproducible when subjected to a wider gate sweep, probably due to rearrangements of such localized charges [290].

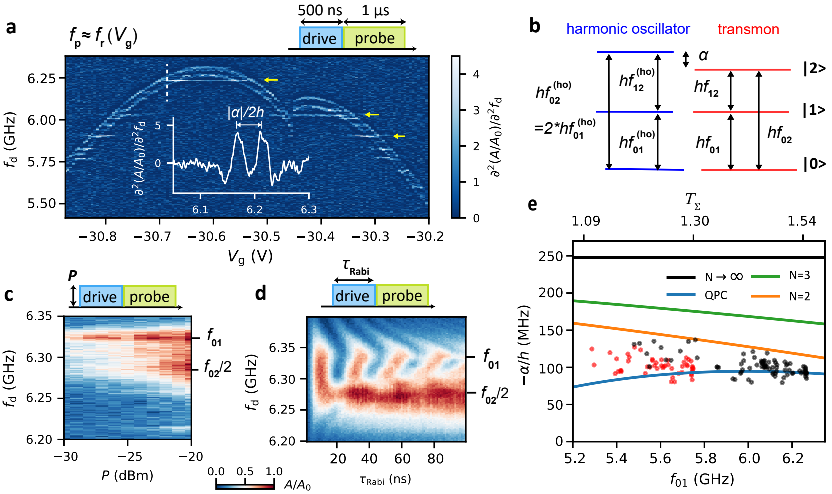

Figure 7.2. Qubit spectroscopy and anharmonicity. **a**, Second derivative of the normalized resonator response A/A_0 with respect to f_d in a two-tone spectroscopy experiment as a function of the f_d and V_g. The pulse sequence is shown schematically on the top right. The drive power P is set to $-20\,\mathrm{dBm}$ and the probe frequency close to the resonator frequency f_r. The inset shows a cross section at $V_\mathrm{g} = -30.7\,\mathrm{V}$, clearly showing two peaks. **b**, Energy diagram of a transmon qubit showing explicitly the anharmonicity α. **c,d**, Normalized resonator response A/A_0 in a two-tone spectroscopy experiment as a function of the drive frequency f_d and the drive power P, and as a function of f_d and the drive pulse duration τ_{Rabi}, respectively. The latter exhibits characteristic Rabi oscillations. **e**, Anharmonicity extracted from two-tone spectroscopy experiments, plotted as a function of the qubit frequency f_{01}. The black data points were extracted from **a**, while the red stem from larger gate voltages (around $V_\mathrm{g} \approx -20V$). The top axis labelled T_Σ is obtained directly from the qubit frequency. The solid lines depict anharmonicity inferred from different models (see main text).

To study the quantised energy levels of the device, we perform pulsed two-tone spectroscopy. We apply a 500 ns drive tone at frequency f_d to the feedline, followed by a $1\,\mu$s probe tone at an optimised frequency of $f_\mathrm{p} \approx f_\mathrm{r}$ to probe the resonator. We note that we obtain similar results when driving via the side gate. The in-phase I and quadrature Q components of the transmitted probe tone are obtained using heterodyne detection techniques. We plot the normalized amplitude A/A_0 of the complex signal, which depends on the state of the qubit. In order to resolve fine features, we plot the numerically calculated second derivative of A/A_0 with respect to f_d, as shown in Fig. 7.2a. The raw data can be found in SI Fig. S7.2. To avoid large charge rearrangement, we focus on the small gate voltage range of $\sim 600\,\mathrm{mV}$ shown in Fig. 7.2a, in which the qubit frequency can be tuned between 5.4 GHz and 6.3 GHz, with a typical qubit-resonator coupling factor of $g \approx 47\,\mathrm{MHz}$. We attribute the reproducible discontinuity in the qubit frequency at $V_\mathrm{g} \approx -30.45\,\mathrm{V}$ to a nearby charge trap. We also find several gate-voltage independent sharp resonances indicated by the yellow arrows in Fig. 7.2a, possibly due to two-level fluctuators more remote from the gate, for example in the $\mathrm{SiO_2}$ substrate, or due to spurious modes in the electromagnetic environment [304].

The main features in Fig. 7.2a are two resonances, moving almost in parallel with changing V_g, clearly visible in the cross section shown in the inset for $V_\mathrm{g} = -30.7\,\mathrm{V}$. Here, the spacing between the two peaks is $\sim 50\,\mathrm{MHz}$. Based on the generic energy diagram for a transmon qubit shown in Fig. 7.2b, we attribute the higher frequency resonance to the qubit transition at frequency f_{01} between state $|0\rangle$ and $|1\rangle$. As we will show, the lower resonance originates from two-photon processes that drive the transition from state $|0\rangle$ to the second excited state $|2\rangle$.

To explicitly identify these two peaks, we perform two-tone spectroscopy as a function of frequency and power of the drive tone, as plotted in Fig. 7.2c. At low powers, only a single resonance is found. For large powers, an additional resonance appears at a slightly lower frequency, consistent with a lower probability for higher order two-photon absorption processes. This transition to the second excited state is also found in the Rabi measurement shown in Fig. 7.2d, where we plot the resonator response as a function of the drive pulse duration $\tau_{\mathrm{R}abi}$ and drive frequency f_d. The drive pulse induces periodic Rabi oscillations between the states $|0\rangle$ and $|1\rangle$, resulting in the characteristic Rabi chevron pattern, with the qubit frequency $f_{01} \approx 6.325\,\mathrm{GHz}$. Again, we find an additional broader feature for longer pulse times at $\sim 6.275\,\mathrm{GHz}$, typically attributed to the $f_{02}/2$ resonance [294, 305]. We point out that the Rabi experiments and the power dependence were not taken at the same gate voltage, because of a slight drift over several weeks of measurements.

This level structure now allows us to directly assess the anharmonicity of the gatemon spectrum $\alpha = 2h(f_{02}/2 - f_{01})$, for different gate voltages. The corresponding data are plotted as black and red points as a function of the gate voltage dependent f_{01} in Fig. 7.2e. We note that for some specific frequencies, spurious resonances hindered us from extracting the peak positions. Details about the data extraction are discussed in the corresponding SI section.

Figure 7.2e is one of our main results, which we now use to estimate the transmission probability and the number of conducting channels in the NW junction. Since the semiconducting NW segment is very short (33 nm) compared to typical superconducting coherence lengths, the JJ is in the short-junction limit. The Josephson potential is then well described by $U(\hat{\phi}) = -\Delta \sum_i \sqrt{1 - T_i \sin^2(\hat{\phi}/2)}$, where Δ, T_i, and $\hat{\phi}$ are the superconducting gap, the individual channel transparencies, and the phase difference between the left and right Al segments [306]. The gatemon Hamiltonian then reads $\hat{H} = 4E_c\hat{n}^2 + U(\hat{\phi})$, which can be expanded to fourth order in $\hat{\phi}$ around the potential minimum at $\hat{\phi} = 0$, with the non-harmonic terms used as a perturbation to the harmonic oscillator solutions [136]. This procedure yields

$$hf_{01} = \sqrt{8E_\mathrm{c}E_\mathrm{J}} - E_\mathrm{c}\left(1 - \frac{3\sum_i T_i^2}{4\sum_i T_i}\right) \tag{7.1}$$

and

$$\alpha = -E_\mathrm{c}\left(1 - \frac{3\sum_i T_i^2}{4\sum_i T_i}\right), \tag{7.2}$$

with the Josephson energy given by the prefactor of the harmonic $\hat{\phi}^2$-term in the Hamiltonian, $E_\mathrm{J} = \frac{\Delta}{4}\sum_i T_i$. Here, we use the gap $\Delta = 210\,\mu\mathrm{eV}$ found in DC transport experiments in a control device (see SI Fig. S7.6). For this device, we estimate $E_\mathrm{J}/E_\mathrm{c} \gtrsim 80$, so that we can approximate $hf_{01} \approx \sqrt{8E_\mathrm{c}E_\mathrm{J}}$. Using the numerically simulated E_c and the measured qubit frequency f_{01}, we obtain the total transmission $T_\Sigma := \sum_i T_i = (hf_{01})^2/(2E_\mathrm{c}\Delta)$, used as the top axis of Fig. 7.2e. The measured quantities hf_{01} and α contain T_Σ and $\sum_i T_i^2$, allowing us to estimate the number of channels and the corresponding transmission probabilities. To do this, we consider two limits [136]. First, we assume N channels of equal transparency $\bar{T} = T_\Sigma/N$, yielding the anharmonicity $\alpha = -E_\mathrm{c}(1 - \frac{3}{4}T_\Sigma/N)$. Figure 7.2e shows the cases $N = 2$, $N = 3$ and $N \to \infty$. This equal-transmission model provides an estimate of the number of active channels, with the case of $N \to \infty$ giving the SIS tunnel junction limit $\alpha = -E_\mathrm{c}$, with many low-transparency channels. All data points lie below the $N = 2$ case, suggesting that at most two channels dominate the JJ transport. The corresponding mean channel transparency is electrically tunable from $\bar{T} \approx 0.55$ to $\bar{T} \approx 0.77$ in this qubit frequency range.

In the second limit, often called the "quantum point contact (QPC) limit", we assume one fully transmitting ($T_\mathrm{I} = 1$) and one partially transmitting channel, with a free parameter T_II. This limit yields the lowest possible $|\alpha|$ for a given T_Σ. The resulting dependence is shown in Fig. 7.2e as the blue solid curve. Since this curve captures our data better than the equal-transparency model, we conclude that the annealed Al-Ge-Al JJ carries one highly transparent channel, consistent with the large values up to $T \approx 0.96$ reported in previous DC transport studies on similar JJs [189, 190], and a second channel with a lower transmission, electrically tuned in the range from $T_\mathrm{II} \approx 0.1$ to $T_\mathrm{II} \approx 0.54$.

7.3.2. Coherent control

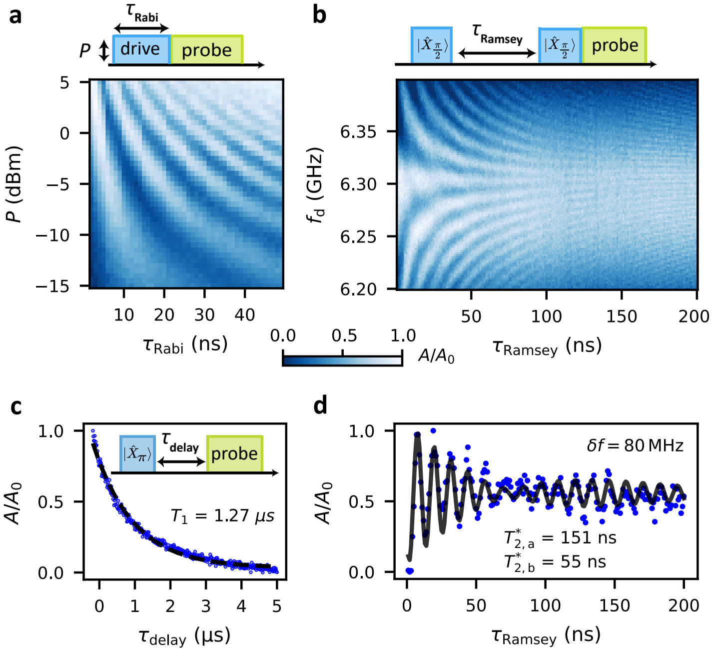

Figure 7.3. Coherent manipulation of the gatemon. **a**, Rabi oscillations as a function of drive power P and pulse duration τ_{Rabi}, measured at $f_{\mathrm{d}} = 6.345\,\mathrm{GHz}$ and $V_{\mathrm{g}} = -30.7\,\mathrm{V}$. **b**, Ramsey fringes as a function of drive frequency f_{d} and time delay t_{Ramsey} measured at $V_{\mathrm{g}} = -30.6\,\mathrm{V}$. Two $X_{\pi/2}$ pulses separated by τ_{Ramsey} are applied prior to the probe tone. **c**, Measurement of the characteristic energy relaxation time T_1 at $V_{\mathrm{g}} = -30.7\,\mathrm{V}$. A 10 ns X_π pulse at $P = -10\,\mathrm{dBm}$ drives the qubit into state $|1\rangle$. After a delay time τ_{delay}, the qubit state is readout. The black dashed line shows a fit of an exponential decay, yielding $T_1 = 1.27\,\mu\mathrm{s}$. **d**, Ramsey experiment measured at $V_{\mathrm{g}} = -30.6\,\mathrm{V}$ at a detuning of 80 MHz. Two dephasing times of $T^*_{2,a}$ and $T^*_{2,b}$ are extracted by fitting to a double sinusoidal functions with different exponential envelopes.

To demonstrate the full functionality of the gatemon qubit, we performed time-domain measurements, namely Rabi oscillations and Ramsey interferometry, and extract the corresponding relaxation and dephasing time. For these measurements, we use a Josephson parametric amplifier (JPA) to enhance the readout signal already at base temperature [307]. In the following experiments, all pulse sequences start with a common initialisation time of $100\,\mu$s to allow the qubit to relax to the ground state $|0\rangle$. We plot the normalized resonator response A/A_0, which essentially represents the occupation of state $|1\rangle$. Each data point is averaged over 10000 identical pulse sequences.

First, we perform Rabi experiments at a fixed gate voltage V_g and drive at the frequency $f_\mathrm{d} \approx f_{01}$. The drive pulse of duration τ_{Rabi} and power P is immediately followed by a $1\,\mu$s probe pulse. The drive pulse induces Rabi oscillations between the states $|0\rangle$ and $|1\rangle$ defining the z-axis of a Bloch sphere. The resulting qubit-state dependent resonator response is plotted in Fig. 7.3a. As expected, the Rabi oscillations become faster for larger drive powers P, which allows for a calibration of the corresponding rotation on the Bloch sphere, around an axis we define as the x-axis. For example, a $X_{\pi/2}$ pulse is obtained as a 5 ns drive pulse at $P = -10\,\mathrm{dBm}$. We note that we perform these experiments at low powers. If the qubit is driven at larger powers, the two-photon processes become more probable, resulting in a deviation from the linear dependence of the Rabi frequency on the drive amplitude for $hf_{Rabi} \gtrsim \alpha$, and a corresponding leakage from the computational space [32], as discussed in SI Fig. S7.3.

Next, we perform Ramsey interferometry, with the corresponding pulse sequence shown schematically in the upper panel of Fig. 7.3b. The qubit state vector is first rotated into the xy-plane of the Bloch sphere using a calibrated $X_{\pi/2}$ pulse with the drive frequency f_d sightly detuned from the qubit frequency by $\delta f = f_\mathrm{d} - f_{01}$. During a subsequent delay time τ_Ramsey, the qubit state precesses around the z-axis of the Bloch sphere, and a phase of $\phi = 2\pi\delta f\tau_\mathrm{Ramsey}$ is accumulated. Then the state vector is again rotated by a $\pi/2$ pulse and the qubit occupation read out as a function of ϕ. This results in the Ramsey fringes shown in Fig. 7.3b, where the resonator response is plotted as a function of f_d and τ_{Ramsey}. The careful timing of these two types of pulses allows one in principle to reach any quantum superposition state on the Bloch sphere.

To quantitatively assess the qubit quality, we now measure the energy relaxation time T_1 and the dephasing time T_2^*. First, to measure T_1, a X_π pulse is applied to bring the qubit to state $|1\rangle$. After a delay time τ_{delay}, the occupation is measured with a probe pulse. Due to the qubit relaxing to the ground state, the probability of finding the qubit in the excited state decays exponentially over a characteristic time scale of $T_1 = 1.27\,\mu$s. Similarly, we extract the dephasing time T_2^* from a Ramsey measurement at a detuning of $\delta f = 80\,\mathrm{MHz}$, see Fig. 7.3d. Instead of the expected single frequency with a dephasing time T_2^*, we find a beating pattern with two slightly different frequencies, similar to the one found in InAs NW gatemons [290] and granular aluminium fluxonium qubits[308]. From a fit to two sinusoidal functions with individual exponential decay times, we obtain the two frequency components

$f_{Ramsey,a} = 80.17\,\text{MHz}$ and $f_{Ramsey,b} = 86.05\,\text{MHz}$. The corresponding time constants are $T^*_{2,\text{a}} = 151\,\text{ns}$ and $T^*_{2,\text{b}} = 55\,\text{ns}$. These two frequencies near f_{01} are also found in the high resolution drive power dependent two tone experiments shown in SI Fig. S7.4. We tentatively attribute the two frequencies to two qubit configurations determined by a nearby low-frequency two-level fluctuator beyond our experimental control. Further qubit characteristics and a discussion of possible physical mechanisms limiting our qubit performance can be found as supplementary information. A comparison between our qubit performance with other gatemons can be found in Fig. S7.5, which illustrates that our device exhibits the significantly longer gatemon coherence times than previously reported for group IV materials, comparable to recent experiments on InAs platforms.

7.4. Summary and outlook

In summary, we have demonstrated a fully functional gatemon qubit based on a narrow Ge/Si core/shell nanowire, with a highly transmissive few-channel Josephson junction fabricated using a simple annealing technique, without resorting to sophisticated epitaxial growth techniques. From a detailed analysis of the gatemon anharmonicity, we conclude that the JJ is dominated by two quantum channels with transmissions up to unity. To demonstrate coherent control in the time domain, we performed Rabi and Ramsey interferometry experiments, yielding a T_1 time on par with gatemons in the more established III/V materials. Since we find $T_2^* \ll 2T_1$, the qubit coherence is not limited by the energy relaxation, but rather by dephasing caused by on-chip noise sources [304, 309], suggesting that these times can still be improved significantly.

Our experiments show that Ge/Si core/shell NW gatemons are a competitive platform for electrically tunable supercondcuting qubits. JJs in the few-channel QPC limit might significantly reduce the charge noise sensitivity as shown in Ref. [310–313], possibly alleviating the requirement for large-footprint capacitors. Ge/Si core/shell NWs also offer additional design parameters not considered for superconducting qubits so far, namely the exceptionally strong and electrically-tunable spin-orbit interaction of the hole carriers, as well as a tunable Landé g-factor [160, 161, 165]. The fabrication techniques and material system employed here are relevant beyond the gatemon qubits. Other platforms, like Andreev spin qubits [142, 143, 213, 270] or Andreev level qubits [137, 287, 288] will benefit even more from the reduced hyperfine interaction of the hole carriers, and from the sharp, homogeneous interfaces to the Ge islands. Our results opens up new avenues to study Andreev bound states and other, more exotic subgap states in large-spin orbit materials.

Methods

The circuit QED chip was fabricated on an undoped silicon substrate with a 100 nm top thermal oxide, using a combination of optical and electron-beam lithography. After cleaning the wafer, a 68 nm NbTiN film was sputter deposited on the wafer, in which the resonator, feed line and gate line were patterned using optical lithography, and further defined using dry etching in an ICP-RIE process with Ar and Cl_2 gas. Next, we fabricated gold markers to later align the nanowire, and we deposited gold islands (size $\sim 500\,\mu\mathrm{m}\cdot 500\,\mu\mathrm{m}$) near the borders of the NbTiN film for better thermalization. The resulting resonator quality factors we obtained in fits shown in SI Fig. S7.7.

The Ge/Si core/shell NWs were then transferred to the circuit QED chip using a micro-manipulator. Source and drain contacts as well as side gates were fabricated using standard electron beam lithography. To remove the native oxide on the Si shell, an 8 s wet etch in buffered HF (buffered oxide etchant 10:1, 4.6% HF) was performed, followed by rinsing in DI water. Next, the chip was immediately loaded into the evaporator where 40 nm of Al was deposited by thermal evaporation. After lift-off, the chip is annealed on a hotplate in ambient at 200°C for 10 min. The NWs were then imaged in a scanning electron microscope to confirm the channel length. Importantly, the annealing and imaging steps can be iterated to obtain the targeted channel length. For each qubit island, we fabricated 3 or 4 annealed junctions, from which we selected the most promising one and connected it to the capacitor and the grounding plane. Ar milling was used to remove the native Al oxide before contacting. The DC and RF wiring of the dilution refrigerator, as well as the measurement setups are discussed in SI Fig. S7.8.

Supplemental to Gatemon qubit based on hole-type Ge/Si Nanowire

Device overview

An optical micrograph of the circuit QED chip is shown in Fig. S7.1. Four qubits are in the center of the image, capacitively coupled to individual readout resonators (not fully shown). As mentioned in the main text, a 100 nm thick Al layer (bright square) was deposited on the NbTiN ground plane (gray background) as quasiparticle trap. Near the borders of the chip, we deposited a several Au islands for better thermalization.

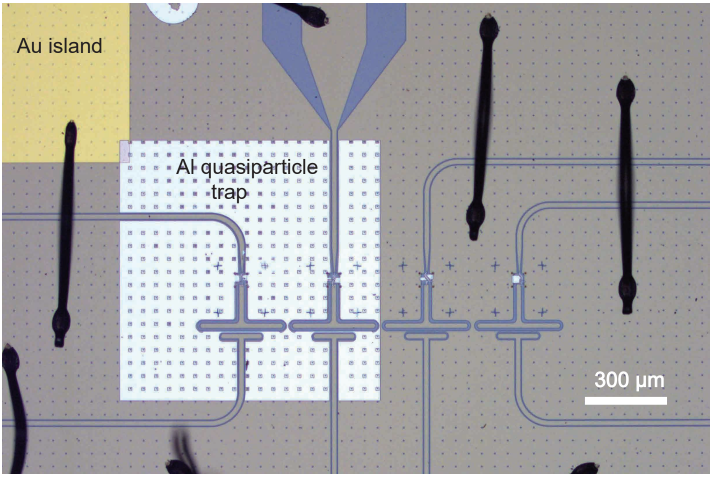

Figure S7.1. Optical micrograph of the circuit QED chip. Four qubits were fabricated on each chip (center), coupled to the readout resonator (not fully shown). Al was deposited on the NbTiN ground plane as a quasiparticle trap and Au islands for better thermalization of the chip.

Peak extraction

In this section, we elucidate how we extracted the peak positions in the two-tone experiments. The raw data of Fig. 7.2 (a) is shown in Fig. S7.2a, with a cross section at $V_g = -30.7\,\mathrm{V}$ in the bottom panel. To better identify the double-peak structure already visible in the raw data, we first applied a moving average with a window size of 10 pixels along the frequency axis, and then took the second derivative. The frequency step size in the raw data is 1 MHz. A cross section of the processed data is displayed alongside the raw data in the lower panel of Fig. S7.2a.

Next, we extract the peak positions as the positions of the maxima in the second derivative of the smoothed raw data. These positions are pointed out by red dots in the two-tone spectroscopy map in Fig. S7.2b. We manually discard peaks close to horizontal resonances that we attribute to gate voltage independent two-level fluctuators. From the difference between the two maxima we extract the anharmonicity, as discussed in the main text. Fig. S7.2c shows additional data and the corresponding second derivative for a different gate voltage range.

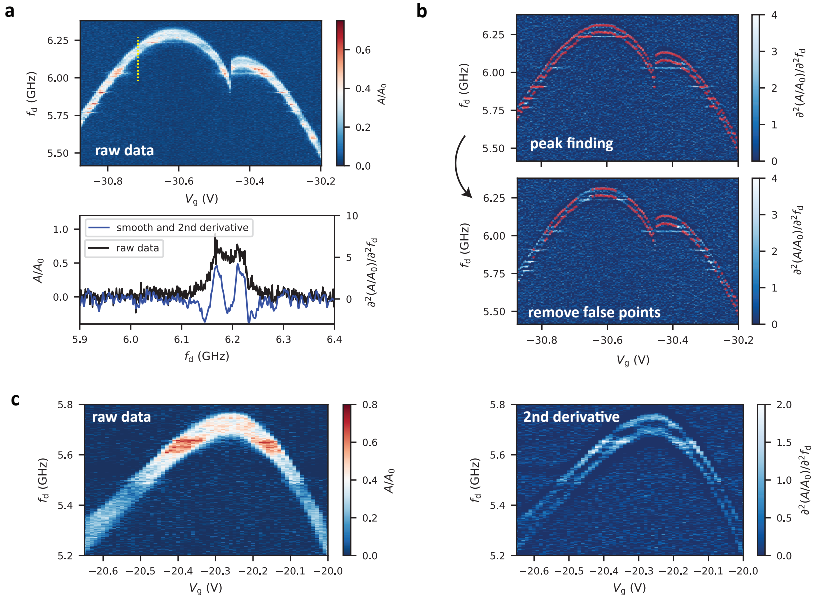

Figure S7.2. Raw data and peak extraction. **a**, Raw data from Fig. 7.2a of the main text, showing the two-tone spectroscopy of the gatemon as a function of the drive frequency f_d and the gate voltage V_g. The indicated cross section (yellow dotted line) of raw data and the corresponding processed data are shown in the bottom panel. **b**, Extracted peak positions (red dots) superimposed on the two-tone spectroscopy map. Due to gate-independent spurious resonances, a subset of the peaks was disregarded. Only the ones shown in the bottom panel were used. **c**, Two-tone spectroscopy in a different gate voltage range used for the additional points in the anharmonicity plot of Fig. 7.2e of the main text. Left panel: raw data, right panel: second derivative of smoothed data.

Power dependence of the Rabi oscillations

In a pure two-level system, the Rabi oscillations are faster for larger power, with a frequency proportional to the drive amplitude, or to the square root of the power. In Fig. S7.3a, we plot three examples of Rabi oscillations for the indicated (constant) powers. We then extract the Rabi frequency $f_{\mathrm{Rab}i}$ by fitting the data points to a sinusoidal function with an exponentially decaying envelope. The resulting $f_{\mathrm{Rab}i}$ is plotted as a function of the relative drive

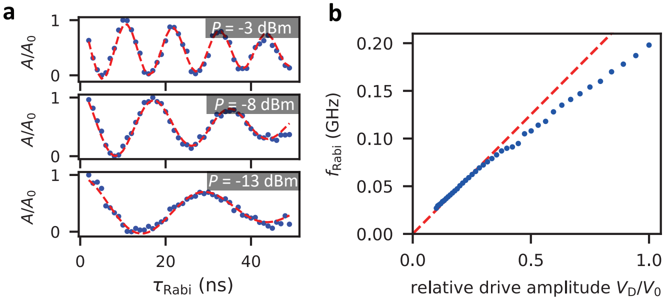

Figure S7.3. Power-dependent Rabi measurements. **a**, Rabi oscillations at different drive powers $P = -3\,\mathrm{dBm}$, $P = -8\,\mathrm{dBm}$ and $P = -13\,\mathrm{dBm}$, as indicated. A sinusoidal function with exponential decay (dashed red line) is fitted to the measured data (blue points) to extract the Rabi frequency $f_{\mathrm{R}abi}$ **b**, $f_{\mathrm{R}abi}$ as a function of the relative drive amplitude V_D/V_0. The red dashed line is a linear fit in the low power range.

amplitude $V_\mathrm{d}/V_0 = \sqrt{P/P_0}$ in Fig. S7.3b. For low amplitudes, $f_{\mathrm{R}abi}$ increases linearly with V_d, as expected. However, for $f_{\mathrm{R}abi}$ larger than $\sim 80\,\mathrm{MHz}$, the observed frequency clearly deviates from the low-amplitude linear dependence. This deviation can be directly attributed to transitions to the second excited state of the gatemon, or in other words, to a leaking out of the computational sub-space. This effect can have two physical origins: 1) a larger power results in a larger occupation of the first excited state and therefore to a larger probability of the two-photon processes that drive the $|0\rangle \rightarrow |2\rangle$ transition. 2) drive pulses of short duration result in a broader frequency spectrum, if assuming a Gaussian broadened pulse shape [32], starting to drive the $|1\rangle \rightarrow |2\rangle$ transition [32]. The deviation from the basic low-power linear dependence occurs around $\sim 80\,\mathrm{MHz}$, consistent with the anharmonicity found in the main text. This discussion directly illustrates how the anharmonicity limits the qubit operation speed.

Beating pattern in Ramsey experiments

In Fig. S7.4, a high-resolution power-dependent two-tone spectroscopy experiment is presented. In addition to the resonances at f_{01} and $f_{02}/2$ discussed in the main text, a third transition at a frequency offset δf above f_{01} is visible, with δf ranging from $5\,\mathrm{MHz}$ to $10\,\mathrm{MHz}$. We tentatively attribute this resonance to a power dependent fast switching between two slightly different values of f_{01}, which leads to the beating pattern observed in our Ramsey measure-

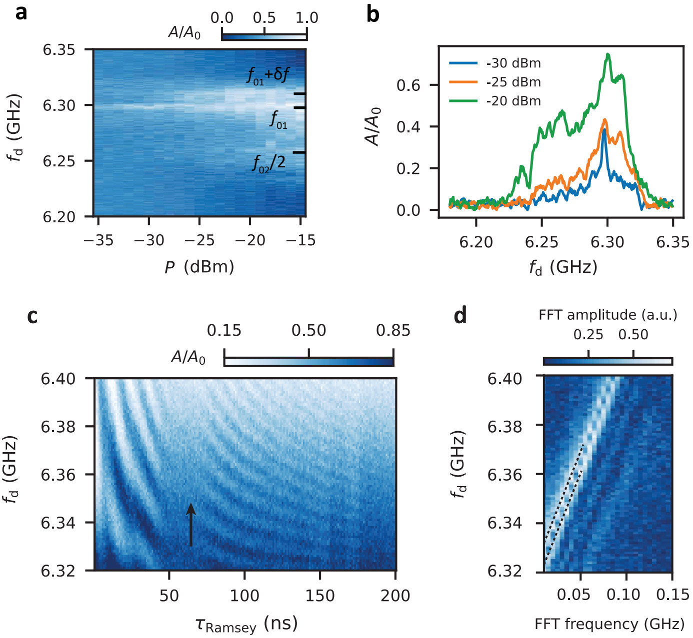

Figure S7.4. Beating pattern in Ramsey measurement. a, Two-tone spectroscopy as a function of drive power P and drive frequency f_d. Specific cross sections at different drive powers are shown in **b**. **c**, Example of a Ramsey type measurement described in the main text. The signal vanishes intermittently around $\tau_{Ramsey} \sim 70\,$ns, pointed out by a black arrow, as discussed in the main text. **d**, Fast Fourier transform of **c** showing two main qubit frequencies, indicated by black dashed lines.

ments. Figure S7.4c shows an example in which the beating is clearly visible. The signal vanishes around a delay time of $\tau_{Ramsey} \sim 70\,$ns, and re-appears for higher values. The Fourier transform of these data is shown in Fig. S7.4d, in which two different frequency components are found close to the main qubit transition f_{01} (dashed lines).

The switching between two qubit frequencies could have various origins. In our case, two possibilities can be excluded: 1) quasiparticle poisoning [314, 315] would block one or more transport channels and therefore change the Josephson energy, and with it the qubit frequency. Since there are only two channels dominating the transport in our JJ (see main text), a poisoning would change the qubit frequency by several GHz, not merely by a few ten

MHz as found in our experiments. 2) fluctuations in the Cooper pair number [135] should occur on the kHz, not on the MHz scale, based on the ratio $E_\mathrm{J}/E_\mathrm{c} \approx 80$. After these consideration, We tentatively attribute the switching frequency to a nearby bi-stable charge fluctuator [290].

Relaxation and dephasing mechanisms

With changes in the gate voltage (and therefore the qubit frequency), T_1 changes seemingly randomly between 0.6 to 1.3 μs. Similar to [267, 291, 294], we cannot find a clear correlation between T_1 and f_{01} or df_{01}/dV_g. Moreover, the obtained T_1 values are much lower than $T_\mathrm{Purcell} = 1/(2\pi\kappa(g/\Delta^2)) \approx 100\mu\mathrm{s}$ ($\kappa = 1.5\,\mathrm{MHz}$ and $\Delta = 1.5\,\mathrm{GHZ}$), suggesting that the qubit relaxation time is not limited by the Purcell decay [316] into the readout resonator. We tentatively attribute the gate dependence of T_1 to two-level fluctuators weakly coupled to the qubit, resulting in various energy-relaxation channels [317]. This is supported by the finding that after leaving the device in ambient conditions for several weeks, the average T_1 dropped by a factor of ~ 2. This suggests that with more impurities adsorbed on the nanowire surface, the qubit energy relaxation time T_1 drops considerably.

Material	Platform	Superconductor	$T_1(\mu s)$	$T_2^*(\mu s)$	$T_{2,echo}(\mu s)$	# channels
III/V	InAs NW (full-shell)[289]	Epitaxy	5.3	3.7	9.5	2 to 3 [136]
III/V	InAs NW (full-shell) [290]	Epitaxy	20	5	30	2
III/V	InAs NW (full-shell) [143]	Epitaxy	0.251	0.141	0.33	
III/V	InAs NW (full-shell) [318]	Epitaxy	0.25	0.18		
III/V	InAs NW (half-shell) [286]	Epitaxy	1.8	0.12		
III/V	InAs NW (half-shell) [319]	Epitaxy	0.218		0.136	
III/V	InAs NW (half-shell) [312]	Epitaxy	0.875	0.079	0.295	
III/V	InAs 2DEG [291]	Epitaxy	1.1	0.4	2.2	many
III/V	InAs SAG NW [292]	Epitaxy	0.74	0.021	1.34	2
IV	Graphene [294]	Surface	0.036	0.055		many
IV	Carbon nanotube [293]	Surface	0.11	(0.01)		1
IV	Ge/Si core/shell thick NW [295]	Al-Ge exchange	0.18	(0.015)		many
IV	Ge/Si core/shell thin NW (our work)	Al-Ge exchange	1.27	0.151		2

Table S7.1. Comparison of gatemon platforms The columns in this table show the material (group III/V or group IV), the exact platform, the types of superconducting contacts, the best reported qubit characteristics times T_1, T_2^*, $T_{2,echo}$, as well as the number of channels active in the JJ. Numbers in brackets indicate that T_2^* was not directly measured in the Ramsey experiment, but deduced from the qubit linewidth. For data points in cyan color, T_2^* were not reported in the experiment, we therefore use T_{Rabi} instead.

In our gatemon, $T_2^* \ll 2T_1$, showing that the qubit coherence is not limited by energy relaxation. In addition, we did not find a significant improvement of T_2^* on and off the gate sweet spots, for example at $V_\mathrm{g} \approx -30.6\,\mathrm{V}$, nor with better filtering on the DC gate-line by replacing the 80 MHz low-pass LC filters

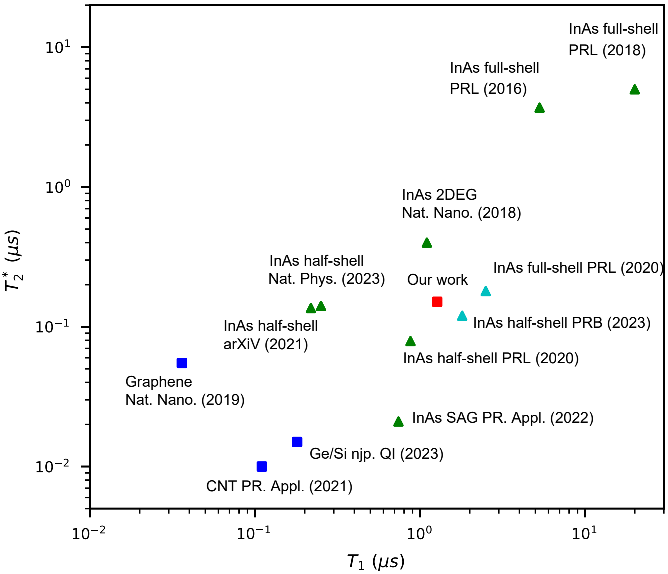

Figure S7.5. Comaprison of transmon coherence times for different material platforms. The plot shows literature values for T_1 and T_2^* times for various experiments in the literature. Squares symbolize group IV devices, green and cyan triangles stand for III/V InAs-based ones. The cyan data points is a subset of group III/V gatemon experiments in which T_2^* was not reported and we substituted it by T_{Rabi}. The data and the corresponding references are listed in Table S7.1

by 100 kHz RC filters. From these findings, we conclude that T_2^* is not limited by gate voltage noise, but rather by on-chip noise originating for example from localized states in the native oxide of the Si shell or in thermal oxide of the substrate, resist residues from fabrication, or from carbon contamination from SEM imaging.

To compare the coherence times of our gatemon to other platforms, we show the results from prior studies in Fig. S7.5 and in Table. S7.1. Our gatemon exhibits the best coherence times of the rather few group IV based platforms to date, on a similar scale as recent InAs based materials with epitaxial Al.

Superconducting gap measurement

The superconducting gap Δ is measured in a control device, shown in Fig. S7.6a. The device is fabricated with the same annealing method, with a Ge channel length of 250 nm. The device was cooled down in the same dilution refrigerator as the circuit QED chip.

When the NW is gate-tuned close to pinch off, the NW channel forms a quantum dot, tunnel coupled to the annealed Al in the NW. In this regime, we can perform tunnel spectroscopy to determine the superconducting gap Δ. For this, we measured the differential conductance $\partial I_{\mathrm{D}}/\partial V_{\mathrm{SD}}$ as a function of source-drain voltage bias V_{SD} and side gate voltage V_{SG}. As shown in Fig. S7.6b, we find Coulomb blockade diamonds with a gap of 2Δ in the transport opened around zero bias. A cross section at the indicated gate voltage is plotted in Fig. S7.6c, where we extract $\Delta \approx 210\,\mu$eV.

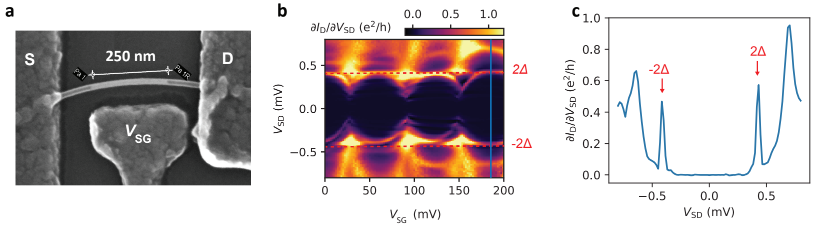

Figure S7.6. Superconducting gap from DC transport. a, SEM image of a Ge/Si core/shell nanowire (NW) JJ fabricated with the same annealing method as in the main text. **b**, DC voltage bias spectroscopy as a function of the gate voltage V_{SG} and the source-drain bias voltage V_{SD}. A cross section at $V_{SG} = 187$ mV is shown in **c**.

Resonator quality factor

We use the python based package “resonator_tools" [303] to extract the quality factors of our readout resonator. The data and fits of the magnitude and phase of the transmission signal S_{21} are shown in Fig. S7.7, yielding the internal and external quality factors listed in the caption of the figure.

Measurement setup

The RF measurements were performed either using a Rohde&Schwarz ZNB-8 vector network analyzer or a Zurich Instrument SHFQA Quantum Analyzer.

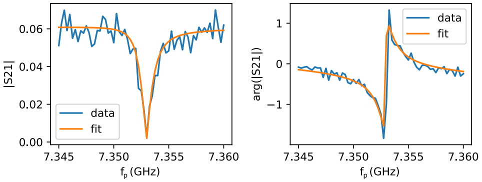

Figure S7.7. The measured magnitude and phase of S_{21} in the vicinity of $f_{r,b}$. A simultaneous fit to both quantities using the model in Ref. [303] results in the internal quality factor $Q_{\mathrm{i}} \approx 2.41 \times 10^5$ and the external quality factor $Q_{\mathrm{c}} \approx 4 \times 10^3$.

The drive and probe signals were heavily attenuated by 66 dB and filtered with home-made Ecosorb filters at low temperature. The output signals were amplified in an amplification chain consisting of a Josephson parametric amplifier (JPA), several circulators, an Ecosorb filter and dual junction isolators, followed by a HEMT amplifier. All components are shown in detail in Fig. S7.8.

The qubit drive tone is generated by a vector signal generator (Agilent E8267D) modulated by an envelope signal from an arbitrary waveform generator (AWG, Tektronix 5014C). The DC flux and gate lines are filtered using Ag epoxy filters at the coldplate and a 3-stage LC-filter with the cutoff frequencies 80 MHz, 225 MHz and 400 MHz. The qubit drive via the gate is achieved by combining a DC and an RF line on the PCB with a RC bias tee using a 1 kΩ resistor and a 15 nF capacitor.

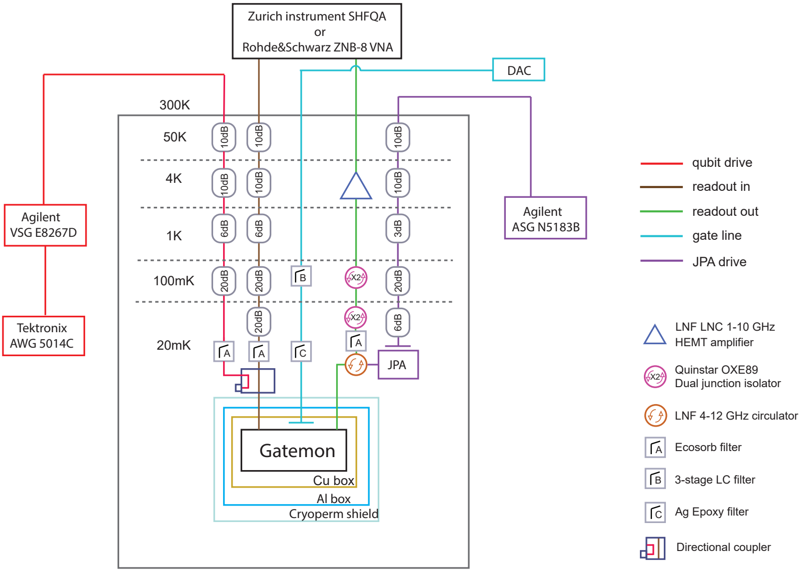

Figure S7.8. Schematic of the dilution refrigerator and measurement setup.

8 Andreev qubit in a Ge/Si Nanowire Josephson Junction [1]

"What I cannot create, I do not understand."
— Richard Feynman

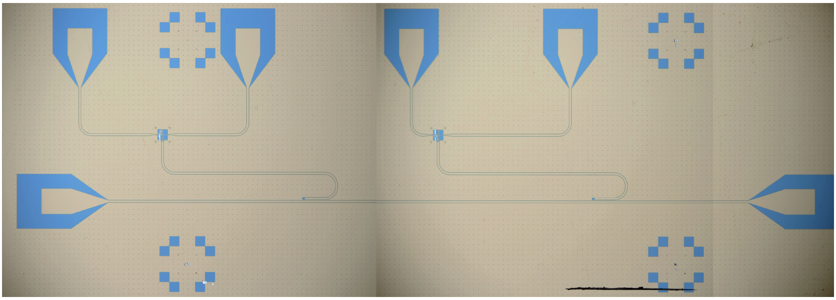

In the previous chapter, we demonstrated a fully-functional gatemon qubit based on a Ge/Si NW JJ and confirmed that the JJ is dominated by at most two quantum channels with high transmission. Furthermore, Ge/Si NWs feature reduced hyperfine interactions [21] and strong, electrically-tunable direct Rashba spin-orbit interactions [160, 161, 165]. Given these compelling features, it is both logical and intriguing to explore the potential of Ge/Si NW JJ in realizing an Andreev (spin) qubit. In the following chapter, we integrated a Ge/Si NW JJ into a RF SQUID, which is inductively coupled to a $\lambda/4$ resonator. We performed both single-tone and two-tone spectroscopy, and demonstrated the gate and flux tunability of the quantum states in Ge/Si NW JJ. Moreover, we are able to achieve coherent control of these quantum states, with T_1 up to 5.1 μs and T_2^* up to 731 ns.

---

[1] The content of this chapter is under preparation for publication.

8.1. Introduction

At present, the two leading platforms in solid-state quantum computing are (1) superconducting qubits [33, 281, 282, 302] that utilize collective electrodynamic modes, and (2) spin qubits [320–323], which involve electrons (or holes) confined within semiconductor quantum dots. Each platform presents a unique set of advantages and challenges. Superconducting qubits offer benefits such as larger coupling [324, 325], thanks to macroscopic quantum state, but they face limitations in operational speed due to small anharmonicity [32] and susceptibility to cross-talk [283] resulting from macroscopic circuit variables like current and flux. In contrast, semiconducting spin qubits leverage individual electron (hole) trapped in microscopic dimensions, showing promise for industry compatibility [326]. Moreover, fast operation is possible owing to substantial level separation. However, spin qubits face challenges in achieving long-distance interconnections [27–31].

The Andreev qubit [137, 138] holds promise by combining the advantages of both platforms. The qubit state is defined within Andreev bound states of a microscopic superconducting weak link, offering a large level spacing for rapid operations. Simultaneously, as a supercurrent-carrying state, the qubit can be easily integrated into circuit quantum electrodynamics (cQED), enabling non-destructive state readout and coherent manipulation. Furthermore, semiconductor/superconductor hybrid nanowires provide a platform for investigating spinful Andreev states [213], with spin degeneracy lifted by spin-orbit interaction. So far, Andreev (spin) qubits have been achieved in superconducting break-junction [287] and InAs NW with epitaxial Al shell [142–144]. Nevertheless, the qubit coherence times remain rather limited, typically on the order of a few tens of nanoseconds. More specifically, Andreev spin qubits in InAs NWs encounter challenges stemming from the spinful nuclear bath, attributed to hyperfine interactions. A promising alternative would be Ge. Ge has several isotopes [327], with the most abundant ones being ^{74}Ge (36.72%), ^{72}Ge (27.31%), ^{70}Ge (20.38%), ^{76}Ge (7.83%), all of which are free of nuclear spin. The only isotope with a spinful nucleus is ^{73}Ge (7.76%). Additionally, Ge exhibits a p-type character in its valence band, further reducing hyperfine interactions [21].

In this work, we report an Andreev qubit in a Ge/Si core/shell NW JJ. The NW JJ is fabricated by annealing the superconducting Al contact into Ge core [189, 190, 300]. The JJ is embedded in an RF SQUID, allowing phase biasing of the NW JJ. The RF SQUID is inductively coupled to a $\lambda/4$ resonator, allowing for readout and coherent manipulation of qubit states. In the time-domain measurements, we have observed an enhanced T_2^* coherence time of up to 700 ns. This value is comparable to what has been reported for hole spin qubits in planar Ge [23–25] and Ge NWs [328, 329], significantly surpassing the coherence times found in any previously reported Andreev qubits by more than one order of magnitude. More importantly, the two-tone spectroscopy reveals a distinct spectrum compared to InAs NW. While the exact nature of this spectrum is still under investigation, we suspect it originates from the interplay between direct-Rashba SOI, heavy-hole light-hole mixing in the Ge hole band, and Coulomb interaction.

8.2. Device

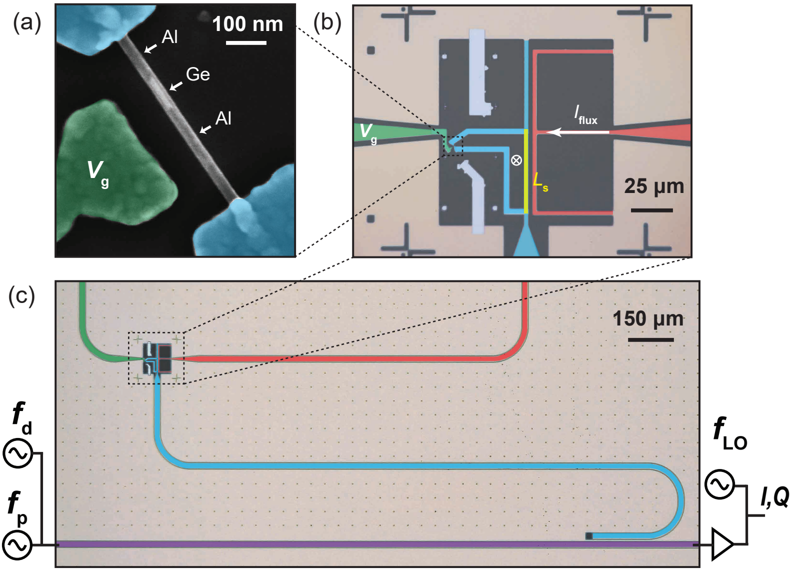

Figure 8.1. Device. (a) False-color SEM image of the Ge/Si NW JJ. The brighter segment of the NW represents the Ge core, while the darker segment is composed of alloyed Al. A side gate, colored green, facilitates the tuning of the Ge segment. **(b)** False-colored optical micrograph of the device's core part. The NW JJ is embedded in an RF SQUID loop (blue) made of Al. This SQUID loop shares a part (yellow) with $\lambda/4$ coplanar waveguide (CPW) resonator, which is fabricated on a NbTiN film. The flux threading through the loop is controlled by a flux-bias current (red) I_{flux}. **(c)** Overview of the cQED chip and a schematic of the readout and control circuit. The $\lambda/4$ resonator is coupled to a feedline in a notch-type design.

The device under investigation is shown in Fig. 8.1. The NW has a Ge core with a diameter of 10 nm, followed by a 2 nm Si shell and native SiO_2.

It is deposited on the cQED chip using a mirco-manipulator, and contacted by evaporated Al using standard lift-off techniques. A side gate (green) is fabricated in the same step, allowing for tuning the Ge section. Next, an annealing step at 200 °C was implement to induce the inter-diffusion of Al atoms into the Ge core. The alloyed Al-Ge-Al NW JJ has a 75 nm long Ge section, as depicted in Fig. 8.1 (a). Subsequently, the NW JJ is embedded in a RF SQUID loop (blue) with a 100 nm thick evaporated Al layer, as shown in Fig. 8.1 (b). To remove the oxide layer prior to making contact, we performed an in-situ Ar milling process before evaporation.

The RF SQUID loop has a shared inductance L_s (yellow) with the $\lambda/4$ resonator at its current antinode, which is fabricated on a 68 nm thick NbTiN film. Notably, the center conductor of the $\lambda/4$ resonator is narrowed down to increase the inductance locally, and therefore enhances the inductive coupling strength to the SQUID. We estimate L_s around 60 pH in this configuration. A flux-bias line (red) is fabricated next to the SQUID, allowing for tuning the flux threading the SQUID loop. The typical NW Josephson inductance is in the order of nH, much larger than the loop inductance, therefore, the superconducting phase drop across the JJ is effectively controlled by the flux current I_{flux}. The optical micrograph of the cQED chip is displayed in Fig. 8.1 (c). The $\lambda/4$ resonator, featuring a notch-type design, is capacitively coupled to the feedline at its open end.

8.3. Spectroscopy measurement

Single-tone spectroscopy

We begin with single-tone spectroscopy measurements using a vector network analyzer (VNA). To this end, a weak microwave probe tone with frequency f_{p} is transmitted through the feedline, and the transmission coefficient $|S_{21}|$ is subsequently measured. Figure 8.2 (a) shows a single-tone spectroscopy map when sweeping the side gate voltage V_{g}. The resonator frequency f_{r}, featuring a dip in $|S_{21}|$, exhibits dispersive shift as a function of V_{g}. The Ge/Si is a hole conductor, therefore pinch-off occurs at at positive gate voltages, around $V_{\text{g}} = 4\,\text{V}$. When the qubit state is gate-tuned close to the resonator frequency $f_{r,b}$, an anti-crossing is observed at around $V_{\text{g}} = -0.8\,\text{V}$, which we will discuss in detail in the following section. In addition, gate jumps are observed at multiple gate voltages, for instance, at around $V_{\text{g}} = -4\,\text{V}$. We note that single-tone spectroscopy measurements are quite reproducible, including the gate jumps, when limited to a smaller gate voltage range of a few volts. However, they become less reproducible during sweeps over a broader gate voltage range. This behavior is akin to what has been seen in gatemon devices and is likely due to the rearrangement of localized charge states. Additionally, we observe a noisy regime in single-tone spectroscopy for gate voltages below $-8\,\text{V}$. This

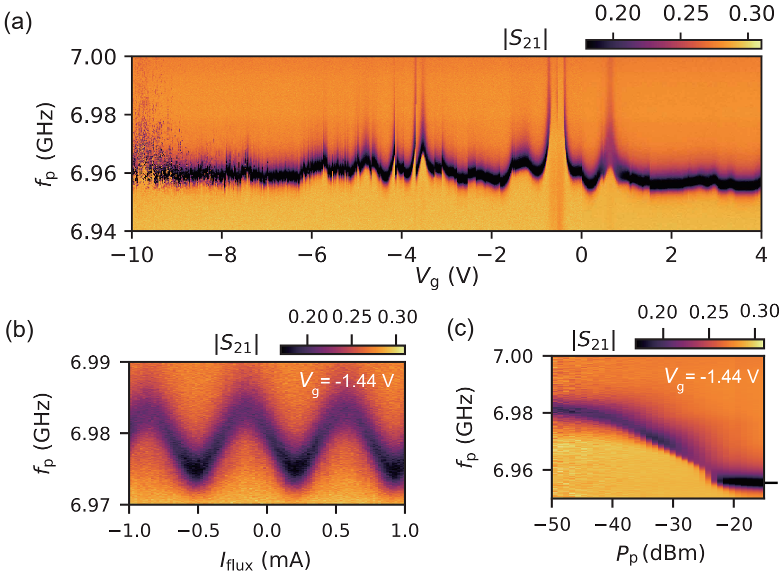

Figure 8.2. Single-tone spectroscopy. (a) Transmission coefficient $|S_{21}|$ as a function of side gate voltage V_g and probe frequency f_p, measured at $P_\mathrm{p} = -30\,\mathrm{dBm}$. The darker color signifies the resonator frequency f_r. **(b)** Transmission coefficient $|S_{21}|$ as a function of flux current I_flux and probe frequency f_p, measured at $V_\mathrm{g} = -1.44\,\mathrm{V}$ and $P_\mathrm{p} = -40\,\mathrm{dBm}$. **(c)** Transmission coefficient $|S_{21}|$ as a function of probe tone power P_p and probe frequency f_p, measured at $V_\mathrm{g} = -1.44\,\mathrm{V}$ and $I_\mathrm{flux} = 0\,\mathrm{mA}$. The bare resonator frequency $f_\mathrm{r,b}$ is found at high probe power.

is not due to gate leakage. But, in this voltage range, the resonator frequency f_r fluctuates between multiple frequencies within the integration time of the VNA for a single trace. The underlying mechanism of this behavior remains unclear and falls outside the scope of this study.

To confirm the flux dependence of the qubit state, we measured the resonance shift as a function of flux current bias I_flux at fixed gate voltage $V_\mathrm{g} = -1.44\,\mathrm{V}$, as shown in Fig. 8.2 (b). A periodic resonance shift is observed, with a minimum at $I_\mathrm{flux} \approx 200\,\mu\mathrm{A}$ and maximum at $I_\mathrm{max} \approx -150\,\mu\mathrm{A}$. The periodic shifts of f_r corresponds to the periodic changes in the superconducting phase drop over the NW JJ. Each period corresponds to a flux quantum, $\Phi/(2e)$, threading through the loop.

Last but not least, we performed a "punch-out" experiment [330] by measuring the resonance frequency as a function of probe tone power P_p, as shown in Fig. 8.2 (c). At low probe power, the photon number in the cavity is low, ensuring the qubit in the ground states. The resonator frequency is measured to be $f_\mathrm{r} = 6.98\,\mathrm{GHz}$. As the probe power increasing, the oscillating current amplitude in the resonator exceeds the critical current of the NW JJ. In this regime, the qubit state is "punched-out" and we obtain the bare resonator frequency $f_\mathrm{r,b} = 6.955\,\mathrm{GHz}$. Importantly, the "punch-out" experiment reaffirms the presence of the qubit which is coupled to the resonator.

Strong coupling regime

Now, our attention shifts to a gate range where the qubit frequency is tuned close to the resonator frequency $f_\mathrm{r,b}$. In this regime, there is a pronounced hybridization of the qubit and resonator states. This hybridization is most evident when the qubit-resonator coupling strength g significantly exceeds both the qubit decay rate (γ) and the resonator decay rate (κ). Under these conditions, two distinct dressed states emerge, indicative of the strong coupling regime [33].

Figure 8.3 (a) shows such single-tone spectroscopy data in the strong coupling regime, measured at $I_\mathrm{flux} = -150\,\mu\mathrm{A}$. Interestingly, we find three pairs of dressed states as indicated by the colored dashed lines[2]. The bare resonator frequency $f_\mathrm{r,b}$ is plotted as the white dashed line. From this, we can track three clear anti-crossing features. The coupling strength is extracted to be $g \approx 70.2\,\mathrm{MHz}$. In addition, a tiny anti-crossing feature is observed at $f = 7.05\,\mathrm{GHz}$, as indicated by the white arrow, which we attribute to either a two-level fluctuator or a spurious electromagnetic mode in the environment. Next, we measured the single-tone spectroscopy at $I_\mathrm{flux} = 200\,\mu\mathrm{A}$, as shown in Fig. 8.3 (b). The anti-crossing features persist, but we can now observe only two pairs of dressed states instead of the three as discussed above.

Additionally, we performed flux-dependent single-tone spectroscopy measurement in this strong coupling regime, with a fixed gate voltage of $V_\mathrm{g} = -1.01\,\mathrm{V}$, as illustrated in Fig. 8.3 (c). Notably, all the dressed states exhibit dispersion with respect to flux. However, it is noteworthy that different states display distinct flux-dependent dispersion. A magnified view of the upper and lower sections of the spectrum is presented in the right panel of Fig. 8.3 (c). The state marked with a green dashed line exhibits a slightly larger frequency range of dispersion compared to the other two states. Additionally, the states marked in cyan and blue appear to be degenerate at $I_\mathrm{flux} = -50\,\mu\mathrm{A}$ and $I_\mathrm{flux} = -200\,\mu\mathrm{A}$, and they display opposite dispersion with respect to flux.

In summary, our observations reveal a complex spectrum in the strong coupling regime, characterized by multiple pairs of dressed states. This behavior is

---

[2] We tentatively attribute these states to different colors as shown. However, they could be assigned differently.

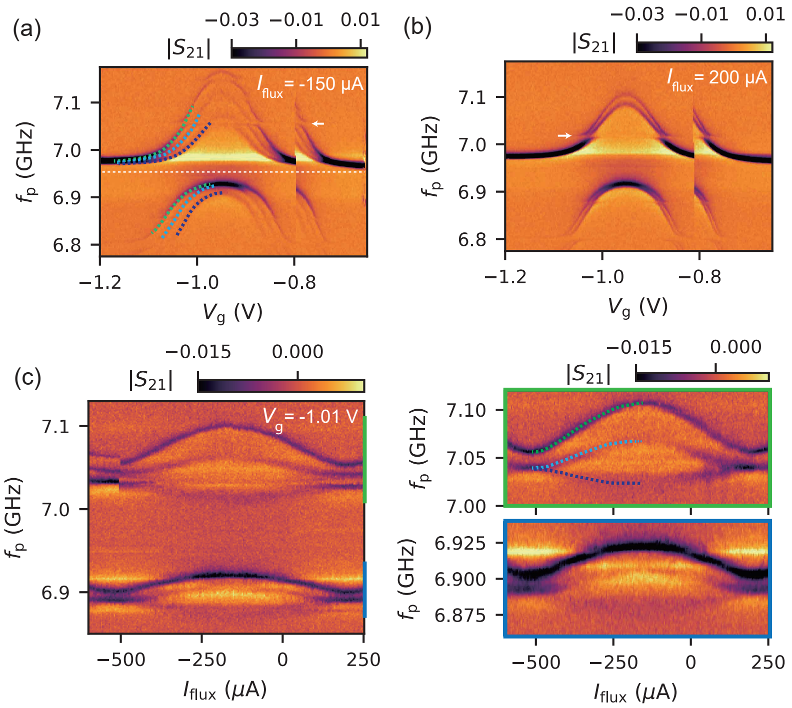

Figure 8.3. Single-tone spectroscopy in strong coupling regime. Resonator transmission spectra as a function of V_g, measured at **(a)** $I_{\text{flux}} = -150\,\mu\text{A}$ and **(b)** $I_{\text{flux}} = 200\,\mu\text{A}$. The white dashed line indicates the bare resonator frequency $f_{\text{r,b}}$. Three pairs of dressed states are indicated with the green, cycan and blue dashed lines. **(c)** Resonator transmission spectrum as a function of flux current I_{flux} at fixed gate voltage $V_g = -1.01\,\text{V}$. The right panel displays a higher resolution measurements of the upper and lower sections of the spectrum. To improve visibility, we removed the background by subtracting the moving average along the horizontal axis for all the figures here.

notably different from what has been reported in InAs Andreev qubit devices. Remarkably, the linewidth of the dressed states remains narrow, unaffected by the decay of the qubit. This observation is indicative of a decent qubit coherence time.

Two-tone spectroscopy

To directly probe the qubit states, we conducted pulsed two-tone spectroscopy measurements, as shown in Fig. 8.4 (a). An 8 μs saturating pulse at frequency f_d was applied, either through the gate or feedline, addressing the qubit state. Next, a 2 μs probe pulse at frequency $f_\mathrm{p} \approx f_\mathrm{r}$ was immediately applied to probe the resonator. Using heterodyne detection techniques, we obtained the two quadrature components I and Q of the transmitted probe signal. We note that 15 μs after the first probe pulse, a second probe pulse (not shown in the schematic in Fig. 8.4 (a)) was applied to probe the resonator when the qubit relaxed to the ground state. We plot the normalized change A/A_0 of the quadrature components between two probe signals, where A represents either I or Q depending on which is stronger[3]. For each point, we averaged for about 300 ms.

Firstly, we investigate the gate tunability of the qubit states. Fig. 8.4(a) shows the resonator response A/A_0, as a function of gate voltage V_g and drive frequency f_d, measured at a flux current of $I_\mathrm{flux} = 0.16\,\mathrm{mA}$. Interestingly, 3 states are observed, dispersing parallel with each other as a function of V_g. Moreover, avoided crossing features are observed in the two-tone spectroscopy, as indicated by the white arrows in Fig. 8.4. This is attributed to the coupling with two-level fluctuator (TLFs) [317]. The strength of coupling varies for different TLFs, which can be seen from the magnitude of splitting.

Next, we examine the flux tunability of the qubit states at $V_\mathrm{g} = 1.0\,\mathrm{V}$, as shown in Fig. 8.4 (c). A periodic pattern is found as a function of I_flux. Again, three distinct states can be resolved, exhibiting behaviors closely analogous to that observed in Fig. 8.3 (c). These states disperse in a small frequency range of $\sim 150\,\mathrm{MHz}$, in contrast to $\sim$GHz dispersion in V_g.

Moreover, we measured the power-dependent two-tone spectroscopy as shown in Fig. 8.4 (d). At $I_\mathrm{flux} = -0.16\,\mathrm{mA}$, the states at higher frequency exhibit a stronger magnitude comparing to the lower two. However, at $I_\mathrm{flux} \approx 200\,\mathrm{mA}$ where the lower two states seem to be degenerate, the magnitude of two peaks is comparable (not shown). While Fig. 8.4 (c) and (d) are measured via the gate drive, we have performed the same measurements with feedline drive as shown in SI Fig. S8.2, and the resulting pattern is nearly identical. However, the gate drive requires approximately 15 dBm more power to achieve the same two-tone signal magnitude. We note these two RF lines are designed to have same attenuation when reaching the PCB, but the power difference could originate from different coupling mechanism between gate and feedline drive. The gate drive engages with the charge degree of freedom in the NW, whereas the feedline drive directly couples with the current in the loop. However, another trivial explanation would be that more signal is reflected from the gate drive

---

[3] In fact, we could adjust the f_p to maximize the signal of one component while the other component being around zero.

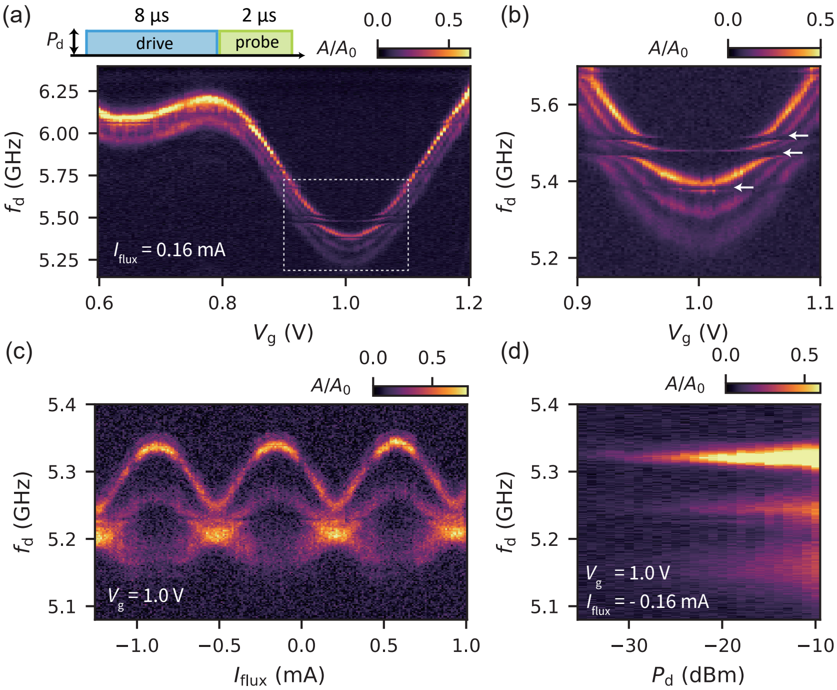

Figure 8.4. Two-tone spectroscopy. **(a)** Resonator response A/A_0 as a function of V_g and drive frequency f_d. **(b)** Zoom-in view of (a), white arrows indicated two-level fluctuators (TLFs). **(c)** Resonator response A/A_0 as a function of flux current I_{flux} and drive frequency f_d, measured at $V_g = 1.0\,\text{V}$. **(d)** Power dependent two-tone spectroscopy measured at $V_g = 1.0\,\text{V}$ and $I_{\text{flux}} = 0.15\,\text{mA}$.

due to non-ideal impedance matching.

We note we cannot performed single-shot readout of qubit states with the current setup. One possible reason is that the JPA is not functioning properly, and the resonator quality factor is not good enough $Q_i \approx 5,000$ and $Q_c \approx 4,000$.

With higher drive power

Last but not the least, We note that Fig. 8.4 only reports states measured with relative low drive power P_d. With a higher P_d, we observed a zoo of states across a much broader frequency range up to 20 GHz. These measurements are shown in SI Fig. S8.3 and Fig. S8.4.

However, we stress that the observed states here have a very different characteristic comparing to what has been reported in InAs NWs, as discussed in Section. 2.7. For Andreev spectrum in InAs NWs, even-parity transition have a large dispersion in phase with a frequency range of around a few GHz. For odd states, a “spider” structure is expected due to the spin-orbit splitting. In our experiments, we observed that the dispersion of states in phase spans a relatively narrow range, on the order of a few hundred MHz, and we do not observed the “spider” structure. We note that the SOI length l_{so} in this NW is comparable or much shorter than channel length L [165]. With such a strong SOI, combined with heavy-hole light-hole band mixing, a different physics picture could emerge.

The physics behind this spectrum is still currently under investigation, in collaboration with Prof. Alfredo Levy Yeyati and Francisco Jesus Matute-cañadas from Universidad Autónoma de Madrid. Also, we notice an unpublished theoretical work on Andreev spin qubit in Ge-based JJ [331].

8.4. Qubit measurements

Now, we discuss the time domain measurements. In the following section, we focus on the dominant states observed in the spectrum, as shown in Fig. 8.4, to perform the qubit measurements. During the measurements, we fix the gate voltage and set the flux current to $I_{\mathrm{flux}} = -160\,\mu\mathrm{A}$, where the states are most widely separated in frequency.

Rabi measurement

To coherently manipulate the qubit state, we apply a square pulse with a frequency of f_{d} and a pulse duration of τ_{Rabi} to the feedline. The pulse sequences are shown in Fig. 8.5 (a). This drive tone induces an effective current oscillation at the current anti-node of the $\lambda/4$ resonator, thereby addressing the qubit state. Subsequently, a 2 μs probe tone near the resonator frequency, f_{r}, is applied to measure the resonator's response. A second probe tone is then applied 15 μs later to measure the resonator after the qubit has decayed to its ground state. The normalized change of the resonator response A/A_0 is depicted in Fig. 8.5 (a), as a function of τ_{Rabi} and f_{d}. The drive pulse with $P_{\mathrm{d}} = -12\,\mathrm{dBm}$ induces a coherent oscillation of the qubit state between $|0\rangle$ and $|1\rangle$, resulting in the characteristic Rabi chevron pattern. The qubit frequency $f_{\mathrm{q}} = 5.77\,\mathrm{GHz}$ is found at the center of the Rabi chevron pattern.

Next, we perform the same measurement but with a stronger drive power $P_{\mathrm{d}} = -5\,\mathrm{dBm}$, as shown in Fig. 8.5 (b). We observed that the Rabi chevron pattern becomes distorted, which could originate from the interaction between the qubit and TLFs. We speculate two Rabi frequencies could co-exist due to this interaction, as we will discuss later. Additionally, we were able to resolve two more states below the qubit frequency f_q, exhibiting Rabi oscillations but with a much slower Rabi frequency. We tentatively attribute them to the two lower-frequency states that were measured previously in two-tone spectroscopy. More time domain measurements of this lower states can be found in SI Fig. S8.5. However, for the scope of this study, we mainly focus on the main qubit with frequency f_q in the following time domain measurements.

Furthermore, we fixed the drive frequency to the main qubit frequency f_q, and measured the Rabi oscillation as a function of pulse duration τ_Rabi and drive power P_d, as shown in Fig. 8.5 (c). As expected, the Rabi oscillations become faster with increasing drive power. But, we observe discontinuities at $P_\mathrm{d} \approx -3\,\mathrm{dBm}$ and -7 dBm, which we tentatively attribute as previously to the interaction between qubit and TLFs. Next, we determined the Rabi frequency, f_Rabi, by fitting the Rabi oscillations to an exponentially decaying sinusoidal function. Figure 8.5 (d) show a representative fit at fixed drive power. In Fig. 8.5 (e), we plotted the f_Rabi as a function of relative drive amplitude V_d/V_0, where drive amplitude is converted from drive power with $V_d = \sqrt{10^{P_\mathrm{d}/10}}$. The Rabi frequency is linear with the drive amplitude across a broad range, from 34 to 129 MHz, as demonstrated by the red dashed line's linear fit. However, we note that the fit has a slight offset with respect to the origin, which we do not fully understand. This might be due to an offset of output power of the signal generator.

Now, we discuss the switching of main qubit freqency f_q between two values. As illustrated above, the Rabi chevron pattern is distorted at higher power, and discontinuity is seen in power dependent Rabi measurement, indicating that the f_q could have two different values. Fig. 8.6 shows two Rabi oscillations measured up to a longer pulse duration $\tau_\mathrm{Rabi} = 800\,\mathrm{ns}$. In Fig. 8.6 (a), the Rabi oscillations were fitted using a single sinusoidal function with an exponentially decaying envelope. It was observed that the fitting does not adequately represent the data at longer τ_Rabi values, where an increase in the amplitude of the Rabi oscillations occurs, as indicated by the black arrow. To capture this beating feature, we fit the data to a double sinusoidal function with a different exponentially decaying envelope, as shown in Fig. 8.6 (b). From the fitting, we extracted two Rabi frequencies $f_\mathrm{Rabi,a} = 16.14\,\mathrm{MHz}$ and $f_\mathrm{Rabi,a} = 16.92\,\mathrm{MHz}$, with exponential decay time $T_\mathrm{Rabi,a} = 725\,\mathrm{ns}$ and $T_\mathrm{Rabi,b} = 723\,\mathrm{ns}$. This suggests that the main qubit could have a second frequency value $f_\mathrm{q} + \delta f$ which is slightly detuned. When driving at fixed frequency $f_\mathrm{d} = f_\mathrm{q}$, the second frequency value $f_\mathrm{q} + \delta f$ results in a slightly detuned $f_\mathrm{Rabi,b}$. We attribute the double valued f_q to the coupling bewteen the qubit and a bi-state charge trap nearby the NW [290], or the existence of another excitation in the ABS spectrum. Furthermore, we observe that the Rabi oscillations persist for at least

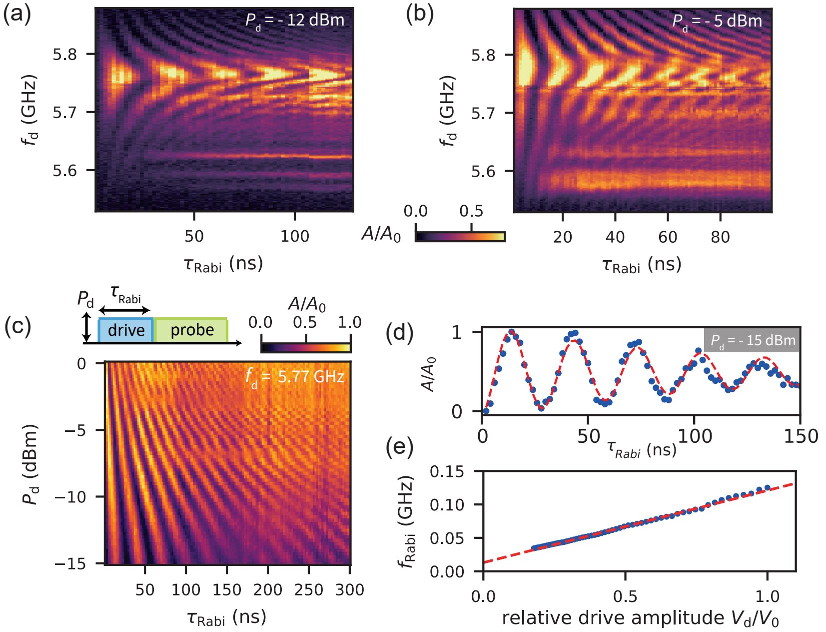

Figure 8.5. Coherent control of the qubit. Rabi oscillations as a function of drive frequency f_d and pulse duration τ_{Rabi}, with drive power **(a)** $P_d = -12\,\mathrm{dBm}$ and **(b)** $-5\,\mathrm{dBm}$ respectively, measured at $V_g = 1.064\,\mathrm{V}$. **(c)** Rabi oscillations measured as a function of drive power P_d and pule duration τ_{Rabi}, at a fixed frequency $f_d = 5.77\,\mathrm{GHz}$. **(d)** A cross section of (c) at $P_d = -15\,\mathrm{dBm}$. A sinusoidal function with an exponentially decaying envelope was fitted to the data, and from the fit, a Rabi frequency $f_{\mathrm{Rabi}} = 33.48\,\mathrm{MHz}$ was extracted. **(e)** The extracted Rabi frequency f_{Rabi} as a function of relative drive amplitude V_d/V_0, the red dashed line is a linear fit.

25 full periods, which further corroborates the qubit's considerable coherence: The Rabi quality factor, denoted as $Q = T_{\mathrm{Rabi}} f_{\mathrm{Rabi}}$, is estimated to be at least 20.

Ramsey measurement

The Rabi measurements discussed above demonstrate the coherent manipulation of qubit state along one axis of the Bloch sphere (x). The coherent manipulation along the z axis can be addressed by a Ramsey interferometry

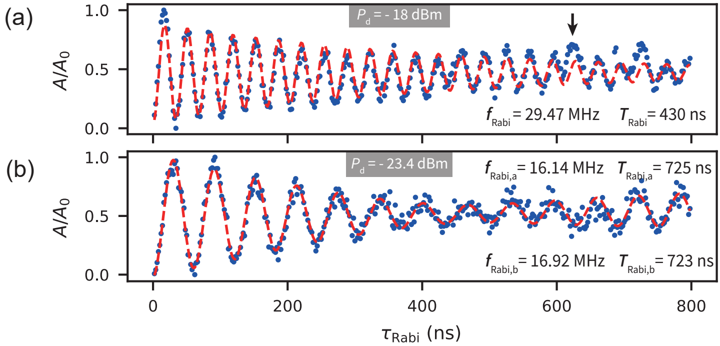

Figure 8.6. Beating pattern in Rabi oscillation. Rabi oscillations measured with drive power **(a)** $P_\mathrm{d} = -18\,\mathrm{dBm}$ and **(b)** $P_\mathrm{d} = -23.4\,\mathrm{dBm}$, measured at $V_\mathrm{g} = 0.75\,\mathrm{V}$, where $f_\mathrm{q} = 6.26\,\mathrm{GHz}$. In **(a)**, the data is fitted with a single sinusoidal function with an exponentially decaying envelope. The fit fails to capture the data at longer pulse times, as indicated by the black arrow. In **(b)**, a double sinusoidal function with different exponential envelops was fitted. Two slightly different Rabi frequency $f_\mathrm{Rabi,a} = 16.14\,\mathrm{MHz}$ and $f_\mathrm{Rabi,b} = 16.92\,\mathrm{MHz}$ are extracted, with characteristic decay time $T_\mathrm{Rabi,a} = 725\,\mathrm{ns}$ and $T_\mathrm{Rabi,b} = 723\,\mathrm{ns}$.

experiment. To this end, we applied two $X_{\pi/2}$ pulses separated with a waiting time τ_Ramsey. The first $X_{\pi/2}$ pulse brings the qubit state vector to the equator of the Bloch sphere. During the waiting time, the qubit state vector precesses along the z axis, accumulating a phase of $\phi = 2\pi\delta f\tau_{Ramsey}$ at finite detuning δf. Next, the second $X_{\pi/2}$ pulse rotates the qubit vector again, and the qubit occupation is readout immediately by a probe tone.

Figure 8.7 (a) shows the Ramsey measurements as a function of f_d and τ_Ramsey, displaying the expected Ramsey fringes. However, we observe the signal getting dimmer at $\tau_\mathrm{Ramsey} \approx 120\,\mathrm{ns}$. We preformed discrete-time Fourier transform of the Ramsey fringes, see Fig. 8.7 (b). Two frequency components, separated by approximately 5 MHz, are clearly visible near δf. This is in good agreement with the results discussed in Fig. 8.6. Moreover, we note that we do not observe a third frequency component as shown in Fig. S7.4 for the gatemon device, and in Ref. [294]. This demonstrates that the qubit represents a more effective two-level system compared to the gatemon, which exhibits small anharmonicity. To extract the dephasing time, we fit the Ramsey pattern with a double sinusoidal function with a different exponentially decaying envelope, as shown in Fig. 8.7 (c). From this fit, we extracte two dephasing times $T^*_{2,a} = 731\,\mathrm{ns}$ and $T^*_{2,b} = 341\,\mathrm{ns}$. These values are more than an order of

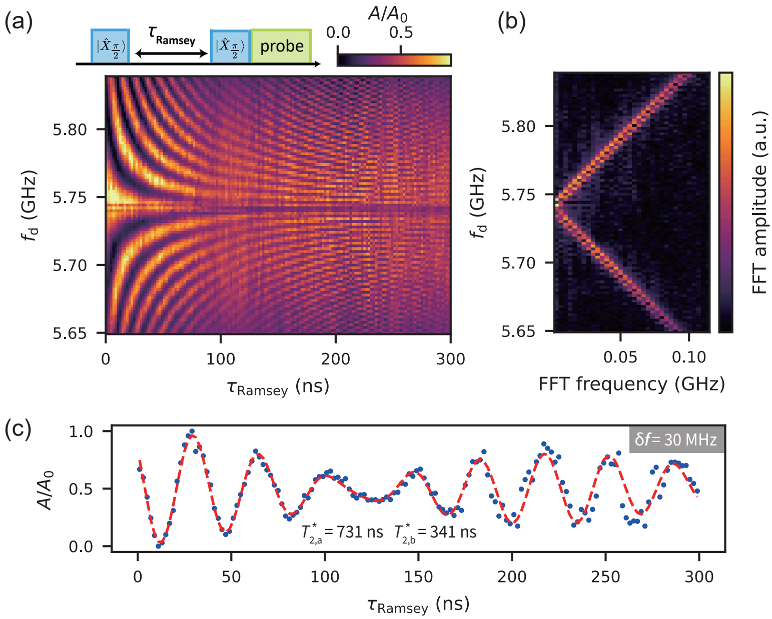

Figure 8.7. Ramsey experiment and qubit's dephasing time. (a) Ramsey fringes measured as a function of waiting time τ_{Ramsey} and drive frequency f_d. (b) Discrete time Fourier transform of (a), two frequency component can be observed. (c) A horizontal cross section of (a) at $\delta f = 30\,\mathrm{MHz}$ from f_q. Two dephasing times $T^*_{2,a} = 731\,\mathrm{ns}$ and $T^*_{2,b} = 341\,\mathrm{ns}$ were extracted from a double sinusoidal fitting with decay.

magnitude longer than previously reported coherence time for both Andreev level qubit [144, 287], and Andreev spin qubits [142, 143].

Coherence times characterization

In this section, we will present a detailed discussion of the qubit's coherence times, including the factors that limit qubit performance.

Firstly, we characterize the energy relaxation time T_1 of the qubit. A X_π pulse is applied to drive the qubit to excited state $|1\rangle$, and after a delay time τ_{delay}, the qubit state population is read out. Figure 8.8 (a) shows such a measurement with extracted $T_1 = 5.11\,\mu\mathrm{s}$. We performed the energy relaxation measurement at different gate voltage V_g (and therefore qubit frequency f_q). The extracted T_1 varies randomly bewteen 5 μs and 0.8 μs at different V_g (f_q),

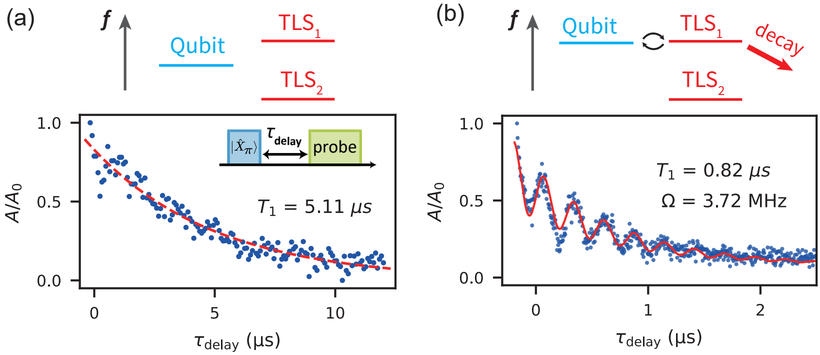

Figure 8.8. Qubit's energy relaxation time. (a) The population of qubit measured as a function of delay time τ_{delay} after a X_π pulse at $V_g = 0.87\,\text{V}$. A characteristic energy ralaxtion time $T_1 = 5.11\,\mu\text{s}$ is extracted from exponential decay envelop. **(b)** Energy ralaxtion time measure at a different gate voltage $V_g = 1.73\,\text{V}$, where a much shorter T_1 of $0.82\,\mu\text{s}$ is found. An oscillatory pattern occurs during the qubit's decay.

showing no discernible pattern. We do not find a correlation between T_1 and df_q/dV_g, indicating that gate noise is not limiting the qubit's T_1.

We hypothesize that the energy relaxation of the qubit is limited due to its coupling with two-level fluctuators (TLFs) in the environment. This is supported by the measurement shown in Fig. 8.8 (b). T_1 was measured with the same pulse sequence as in Fig. 8.8 (a). However, instead of measuring a free decay, we found the qubit state undergoes decaying oscillations. Moreover, the qubit population decay much faster compared to Fig. 8.8 (a). We fit the qubit population with function $a \cdot [1 - \sin(2\pi\Omega t)] \cdot e^{-t/T_1}$, and obtain $T_1 = 0.82\,\mu\text{s}$ and $\Omega = 3.72\,\text{MHz}$. The observed oscillation pattern may stem from vacuum Rabi oscillations between the measured qubit and either a TLF [332] or a second qubit [333]. In this context, Ω represents the vacuum Rabi oscillation frequency between two states. This type of oscillation pattern in T_1 measurements occurs only at specific gate voltages, where the qubit frequency f_q is closely tuned to the frequency of a TLFs. Consequently, we conclude that the coupling with TLFs acts as an energy relaxation channel [317], becoming the limiting factor of the qubit's T_1. Nevertheless, we note T_1 could still be limited by other factors related to our experimental setup[4] (noise in the dilution refrigerator, pulse shaping, and shielding of the sample).

---

[4] We have benchmarked the dilution refrigerator by measuring a transmon chip fabricated in Siddiqi's lab, where an averge $T_1 \approx 5\,\mu\text{s}$ is obtained. Credit to Lukyi Cheung.

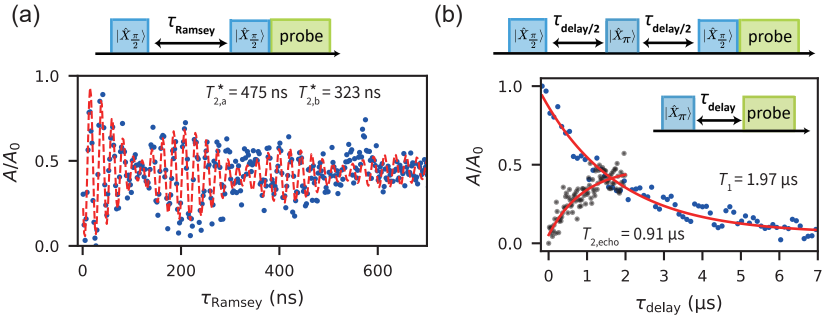

Figure 8.9. Coherence time of the qubit (a) Ramsey interferometry and extracted dephasing times. (b) Enengy relaxation time measurement and Hahn echo experiment. The pulse sequences for different measurements are shown schematically. These data set were measured at the same gate voltage, $V_{\mathrm{g}} = 1.21\,\mathrm{V}$.

To investigate the decoherence of the qubit, we measured a full set of coherence times at same gate voltage, including T_1, T_2^* and $T_{2,\text{echo}}$, as shown in Fig. 8.9. The $T_1 = 1.97\,\mu$s, $T_{2,a}^* = 475\,$ns and $T_{2,b}^* = 323\,$ns were extracted with the same methods as discussed above. $T_2^* \ll 2T_1$, indicating that the qubit's coherence is limited by dephasing. The dephasing time could be enhanced by a Hahn echo pulse sequence, where the inhomogeneous dephasing due to low-frequency noise is canceled out. To this end, a refocusing X_π pulse between two $X_{\pi/2}$ pulses is applied with a delay time $\tau_{delay/2}$, as shown schematically in the Fig. 8.9 (b). With an exponential fit, we obtain $T_{2,\text{echo}} = 0.91\,\mu$s. The echo pulse thus increases the measured coherence time by a factor of 2 to 3, and we conclude that the decoherence is predominantly influenced by low-frequency noise, originating either from the gate line or the surrounding environment, such as defects in the SiO$_2$ on the NW surface or residuals from the fabrication process.

8.5. Discussion and Summary

In summary, we have successfully fabricated a device with a Ge/Si NW JJ embedded in an RF SQUID loop, and conducted both single-tone and two-tone spectroscopy measurements on this device. The spectrum distinctly different from what has been reported on InAs/Al NWs, as discussed in Section 2.7, but nature of this spectrum is still under investigation.

In addition, we have performed time-domain measurements on the qubit states. Our results reveal cpmpelling qubit coherence times, with T_1 up to 5 μs and T_2^* up to 700 ns. This number is much higher compared to our Ge/Si NW gatemon as discuss in Chapter 7, and previously reported Andreev (spin) qubits. These results suggest that Ge nanowire hybrids can be a competitive platform for quantum information processing.

Supplemental to Andreev qubit in a Ge/Si Nanowire Josephson Junction

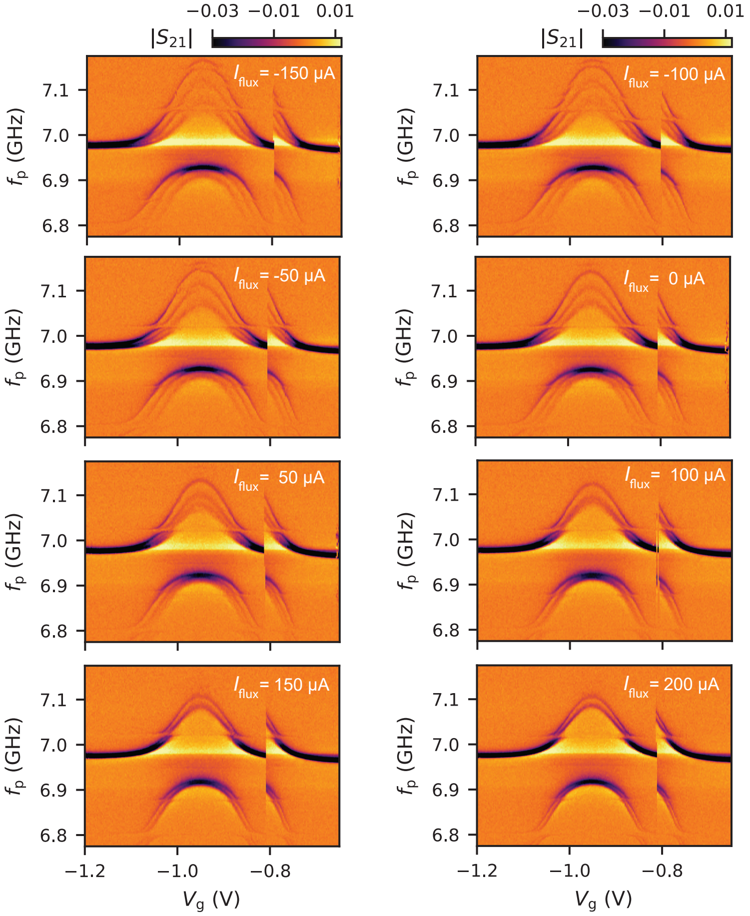

Figure S8.1. Single-tone spectroscopy in strong coupling regime

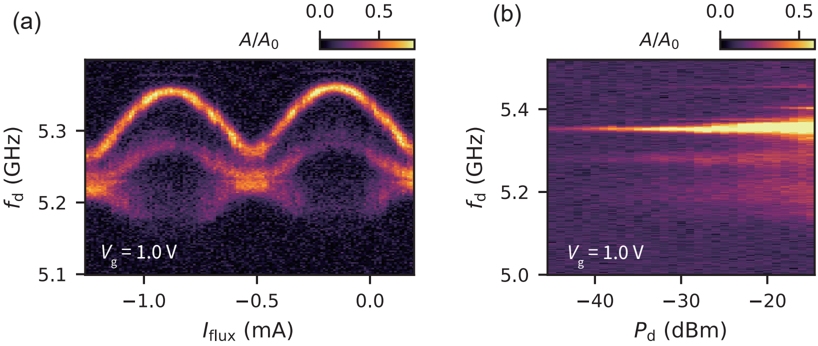

Figure S8.2. Two-tone spectroscopy via feedline drive. Measurements were conducted under the same settings as in Fig. 8.4 (c) and (d), with the only difference being that the drive tone was applied through the feedline.

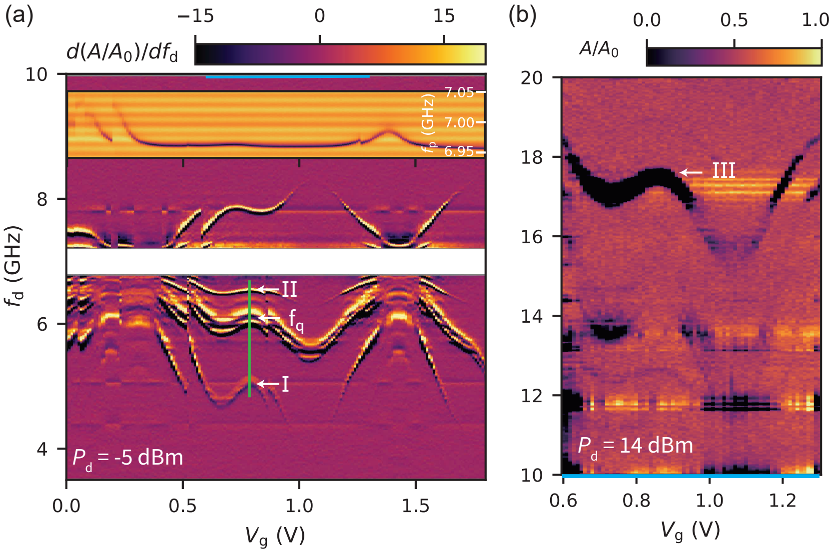

Figure S8.3. Two-tone spectroscopy measured with higher power (a) Resonator response measured between 3.5 GHz to 10 GHz, $P_d = -5\,\text{dBm}$. To better resolve features, a differential is implemented. We observed at least 5 branches of states dispersing in this range, three of them are below the f_r, and the other two above f_r. A few horizontal lines originate from the JPA modes. Moreover, we found that the drive line has a cut-off in frequency ranging from 0.5 GHz to 3.5 GHz, therefore no signals can be measured in this range. In addition, the inset shows a single-tone measurement of the resonator frequency. **(b)** Resonator response measured between 10 GHz to 20 GHz, $P_d = 14\,\text{dBm}$. Note that the V_g axis has a different range than (a), indicated by the blue line. Again, we could identify at least 2 to 3 states dispersing with V_g. This dataset is measured driving via feedline.

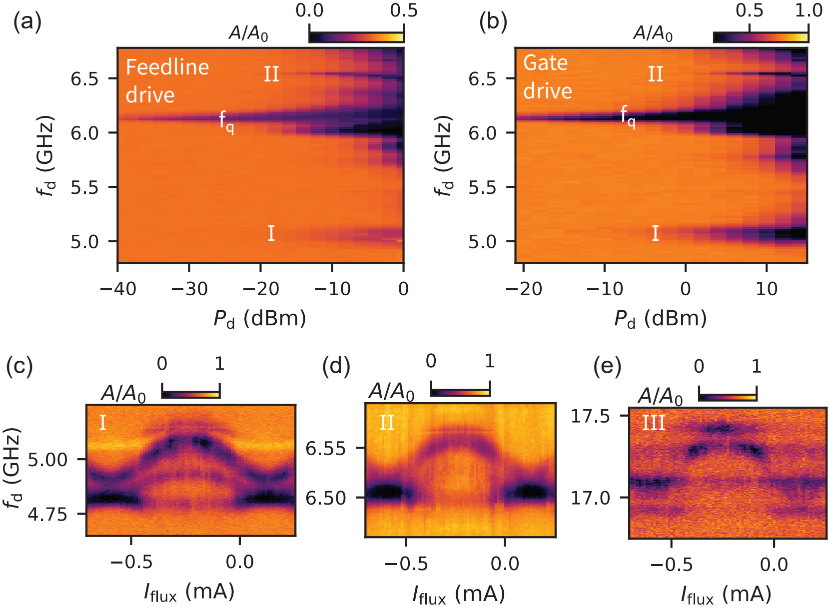

Figure S8.4. Power-dependence and phase-dependence of the states noted in Fig. S8.3. (a) to (b) Power-dependent two-tone map measured at the cross-section marked by the green line in Fig. S8.3 (a), for feedline drive and gate drive respectively. **(c) to (e)** Phase-dependence of the states. The dispersion spans exhibit variation among different states, ranging from 50 MHz to 500 MHz.

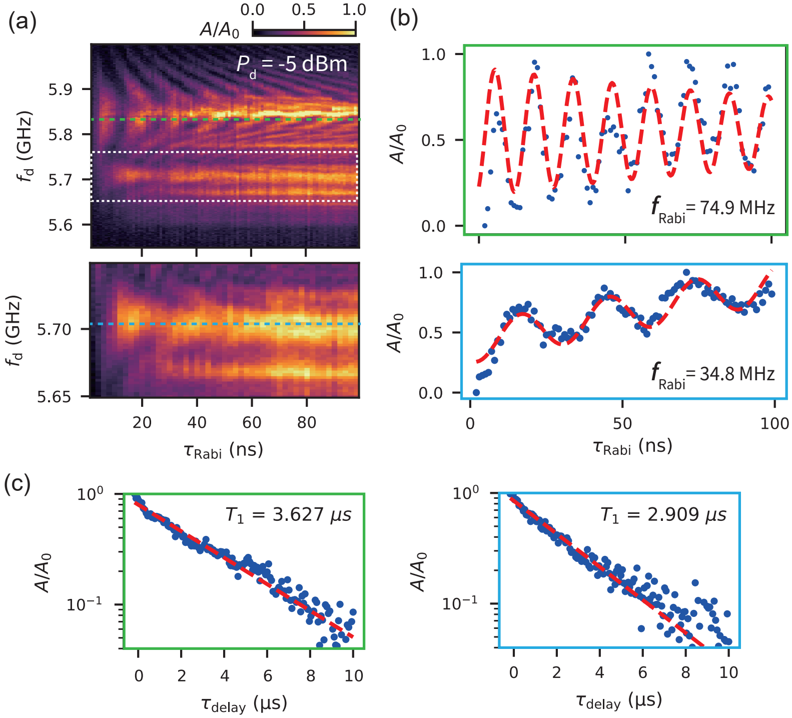

Figure S8.5. Time domain measurement at $V_g = 1.08\,\text{V}$. (a) Rabi oscillations with a relatively high drive power $P_d = -5\,\text{dBm}$. Below the main qubit frequency, another state exhibiting Rabi patterns was observed, as detailed in a higher-resolution measurement in the lower panel. **(b)** Cross sections taken from (a), where the Rabi frequencies of the two states were extracted from fits. The state at the lower frequency demonstrates a slower f_{Rabi} compared to the main qubit state. Intriguingly, the Rabi oscillation of this lower-frequency state is asymmetric relative to its mean value, showing oscillation on top of a linear increase. This behavior is not yet fully understood. For the fitting process, a linear term was incorporated to account for this observed trend. **(c)** Energy relaxation time T_1 measured for the two states.

9 Conclusion and Outlook

"Somewhere, something incredible is waiting to be known."
— Carl Sagan

The main objective of this thesis is to explore the potential of superconducting quantum devices with the Ge/Si core/shell NWs as platforms for quantum information processing. In pursuit of this goal, our exploration spans multiple directions.

First of all, a reproducible recipe to making superconducting contact to NWs is the basis toward developing more complicated device design. Besides the existing Al/Ge inter-diffusion recipe, we established two new contacting techniques using TMAH etching and a Pd interlayer (Chapter 4). Our measurements on S-NW-S devices revealed a full multitude of Andreev bound states (ABSs) in the proximitized NWs, from weak to strong coupling, from short to long junctions. This enhances our understanding of the sub-gap states in Ge hybrid NWs, which is crucial for the applications outlined below. We further investigated devices with local finger gates, and reported ABSs in a double quantum dot (QD) configuration, and the formation of a long QD ($\sim 450\,\mathrm{nm}$) confirms that the high quality of these NWs. We concluded these NWs are not yet optimal for probing the exotic Majorana bound states, due to small g factor and lower critical magnetic field and soft gap from evaporated Al. Finally, we revisited and optimized the inter-diffusion recipe. We significantly improved the device yield by optimizing annealing temperatures and device design, enabling the integration of NW JJs into more complex devices. Moreover, our measurements revealed a high critical magnetic field (>1 T) of the alloyed Al contacts, presenting opportunities to explore superconductor-Ge hybrid devices in high magnetic field environments. (Chapter 5).

Subsequently, we embedded two Ge/Si NW Josephson junctions into a DC SQUID loop and, for the first time, reported the current-phase relation (CPR) of the NW JJ. The skewed CPR indicates highly transmissive channels, which is originated from the atomic-sharp interfaces formed in the inter-diffusion process. More interestingly, we found an anomalous CPR with a dominating $\sin(2\phi)$ term at fine-tuned gate voltages. This anomalous CPR was verified with both low-frequency lock-in measurements and dynamical counter measurements. We tentatively attributed this effect to the interference of at least two ABSs with opposite sign in the long-junction limit, leading to the cancellation of the first order Fourier terms in CPR. In addition, we performed tunneling spectroscopy of ABSs using the sharp interfaces when NWs is close to pinch-off (Chapter 6).

Next, we built a gatemon qubit based on Ge/Si NW JJ. We demonstrated the gate-tunability of the qubit frequency and analyze its anharmonicity, revealing that the Ge/Si NW JJ is dominated by at most two quantum channels with high transparency. Furthermore, we conducted time-domain measurements on the qubit, demonstrating the longest qubit coherence times in group IV materials to-date, comparable to recently reported coherence times in InAs-based gatemons (Chapter 7).

Last but not the least, we integrated a Ge/Si NW JJ into an RF SQUID loop coupled to a $\lambda/4$ CPW resonator, aiming to build an Andreev (spin) qubit. We observed gate and flux tunable states in both single-tone and two-tone spectroscopy. Notably, we reported a rich spectrum which is distinct from previously reported ABSs in InAs NWs. Next, we performed time-domain measurements of the qubit, and obtained qubit coherence times with T_1 up to 5 μs and T_2^* up to 700 ns. The T_2^* is an order of magnitude longer than in previous Andreev (spin) qubits, also much longer than in the gatemon. While the exact nature of the quantum states is still under investigation, our findings are encouraging and highlight Ge's significant potential in quantum computing (Chapter 8).

Outlook

Based on the research presented in this thesis, we have successfully established superconductor-Ge NWs hybrid devices as a competitive platform for quantum information processing. We investigate the ABSs formed in hybrid NWs, realize the integration of Ge NWs in circuit-QED architecture, and demonstrate two prototype qubits based on these NWs. These results significantly expand the scope of Ge's applications in quantum computing.

From a physics point of view, the one-dimensional hole gas in Ge/Si core/shell NWs hosts a wealth of unexplored phenomena. Many **open questions** still lie ahead of us: To what extent that SOI in these NWs can be tuned using electric fields and how could this tuning benefit quantum computing applications? How can we leverage JJ in various limits to more effectively engineer quantum information and achieve better coherence times? How can we establish coupling between our two prototype qubits and qubits in other platforms, such as semiconductor spin qubits? Is it feasible to further engineer the device structure and material properties to enable the exploration of exotic Majorana bound states?

From an engineering standpoint, the CMOS compatibility of the materials employed in this research (Si, Ge, Al) facilitates their integration into industrial semiconductor manufacturing [326]. Such compatibility is vital for the development of scalable quantum processors.

Yet, several challenges must be addressed before Ge NWs can be effectively used to build scalable quantum processors. Overcoming these issues is crucial for the practical implementation of Ge-hybrid-based quantum computing technologies.

- **Material quality**: Although high-quality, defect-free NWs with high mobility have been achieved in the [110] direction [159], this conclusion is limited to the Ge core and the Ge/Si interface. The impact of native SiO_2 on the surface of the NWs has often been overlooked. Our findings, along with results from spin qubit research using similar wires [165], indicate the presence of two-level fluctuators (TLFs) and charge traps in the vicinity of the NWs. The ultra-thin diameter of these NWs result in a large surface-to-volume ratio, amplifying the detrimental effects of surface defects.

  However, as this issue is material-related, improvements are anticipated. Here, we suggest several potential solutions: (1) Growing a thermal SiO_2 layer before removing the NWs from the growth chamber, which could replace the native SiO_2 with a more stable thermal SiO_2. (2) Utilizing a thicker Si shell to further separate the NW surface from the Ge core[1]. (3) Employing surface passivation with alternative materials or through chemical treatments.

- **Yield of the annealing contacts**: In this thesis, we have improved the yield of Al/Ge inter-diffusion contact methods. However, the asymmetry in alloyed Al length is often observed in actual devices, due to variations in the annealing start time [199, 201]. We attribute this asymmetry to variations in the NW/metal interface condition, which may arise from factors such as wet etching, fabrication residues, or the granularity of evaporated Al.

  Nevertheless, based on both our experience and findings in the literature [190], there is potential to further increase the yield and uniformity of these devices. We suggest following directions: (1) Employing rapid thermal processing to induce inter-diffusion. (2) Improving the interface uniformity by growing an in-situ epitaxial Al shell.

- **Scalability**: These NWs, grown vertically on a growth chip, must be transferred to the device chip using a micro-manipulator. This bottom-up approach is evidently not feasible for large-scale fabrication. However, there have been efforts made in top-down growth using the Selective Area

---

[1] The strain effect needs to be re-evaluated in this case. Nevertheless, growing Si_xGe_{1-x} shells could be another way to engineer strain.

Growth (SAG) techniques [334]. An alternative approach involves the use of 2D Ge heterostructures [154, 242, 335].

- **Difficulty of fabrication** We have not extensively discussed the difficulty of handling these ultra-thin NWs during fabrication, though challenges exist. In practice, it is common to observe multiple wires growing from a single nucleation site, and these wires often do not grow vertically [37, 159]. Additionally, the coexistence of three growth directions requires experience and additional lab work to select suitable wires. This issue may be resolved through the previously mentioned SAG technique, which allows for the epitaxial growth of Ge NWs in pre-patterned structures and along designed crystal orientations.

- **Availability of material** The NWs utilized in this thesis were grown in 2015. To our knowledge, only a few groups worldwide worked or are currently working with these NWs, in contrast to the larger community focused on InAs and InSb NWs or 2DEGs. The limited availability of high quality materials, combined with a comparatively small research community, has resulted in a slower pace of research advancement. We hope that the findings presented in this thesis will spark interest across a broad community.

Beyond applications in quantum computing, the high-quality semiconductor-metal contacts discussed here also hold potential for use in the classical semiconductor industry, in the fabrication of Ge transistors [298, 336–338].

All in all, the future is bright. As the title quotation in Chapter 1 says: "the best way to predict the future is to invent it." Ge was the foundational material that initiated the information age for mankind. Now, standing at the forefront once more in the second quantum revolution, it is time to reignite its glory: "Make Germanium Great Again" (MGGA)!

Bibliography

[1] F. Bellaiche, "Complexity and quantum computing," `https://www.quantum-bits.org/?p=1988` (2024), accessed: 2024-01-14.

[2] K. He, X. Zhang, S. Ren, and J. Sun, 2016 IEEE Conference on Computer Vision and Pattern Recognition (CVPR) , 770 (2016).

[3] A. Krizhevsky, I. Sutskever, and G. E. Hinton, Communications of the ACM **60**, 84 (2012).

[4] Y. LeCun, Y. Bengio, and G. Hinton, nature **521**, 436 (2015).

[5] Y. LeCun, L. Bottou, Y. Bengio, and P. Haffner, Proceedings of the IEEE **86**, 2278 (1998).

[6] D. E. Rumelhart, G. E. Hinton, and R. J. Williams, Nature **323**, 533 (1986).

[7] K. Gurney, *An introduction to neural networks* (CRC press, 2018).

[8] M. Riordan, L. Hoddeson, and C. Herring, Reviews of Modern Physics **71**, S336 (1999).

[9] J. S. C. Kilby, ChemPhysChem **2**, 482 (2001).

[10] J. S. Kilby, Proceedings of the IEEE **88**, 109 (2000).

[11] T. Cross, The Economist (2016).

[12] P. Benioff, Journal of statistical physics **22**, 563 (1980).

[13] R. P. Feynman *et al.*, Int. j. Theor. phys **21** (2018).

[14] P. W. Shor, in *Proceedings 35th annual symposium on foundations of computer science* (Ieee, 1994) pp. 124–134.

[15] P. W. Shor, SIAM review **41**, 303 (1999).

[16] D. Castelvecchi, Nature **624**, 238 (2023).

[17] D. Bluvstein, S. J. Evered, A. A. Geim, S. H. Li, H. Zhou, T. Manovitz, S. Ebadi, M. Cain, M. Kalinowski, D. Hangleiter, *et al.*, Nature , 1 (2023).

[18] M. T. Mądzik, S. Asaad, A. Youssry, B. Joecker, K. M. Rudinger, E. Nielsen, K. C. Young, T. J. Proctor, A. D. Baczewski, A. Laucht, *et al.*, Nature **601**, 348 (2022).

[19] A. Noiri, K. Takeda, T. Nakajima, T. Kobayashi, A. Sammak, G. Scappucci, and S. Tarucha, Nature **601**, 338 (2022).

[20] X. Xue, M. Russ, N. Samkharadze, B. Undseth, A. Sammak, G. Scappucci, and L. M. Vandersypen, Nature **601**, 343 (2022).

[21] G. Scappucci, C. Kloeffel, F. A. Zwanenburg, D. Loss, M. Myronov, J.-J. Zhang, S. De Franceschi, G. Katsaros, and M. Veldhorst, Nature Reviews Materials **6**, 926 (2021).

[22] R. Pillarisetty, Nature **479**, 324 (2011).

[23] N. Hendrickx, W. Lawrie, L. Petit, A. Sammak, G. Scappucci, and M. Veldhorst, Nature communications **11**, 3478 (2020).

[24] N. Hendrickx, D. Franke, A. Sammak, G. Scappucci, and M. Veldhorst, Nature **577**, 487 (2020).

[25] N. W. Hendrickx, W. I. Lawrie, M. Russ, F. van Riggelen, S. L. de Snoo, R. N. Schouten, A. Sammak, G. Scappucci, and M. Veldhorst, Nature **591**, 580 (2021).

[26] F. Borsoi, N. W. Hendrickx, V. John, M. Meyer, S. Motz, F. van Riggelen, A. Sammak, S. L. de Snoo, G. Scappucci, and M. Veldhorst, Nature Nanotechnology , 1 (2023).

[27] X. Mi, M. Benito, S. Putz, D. M. Zajac, J. M. Taylor, G. Burkard, and J. R. Petta, Nature **555**, 599 (2018).

[28] N. Samkharadze, G. Zheng, N. Kalhor, D. Brousse, A. Sammak, U. Mendes, A. Blais, G. Scappucci, and L. Vandersypen, Science **359**, 1123 (2018).

[29] A. J. Landig, J. V. Koski, P. Scarlino, U. Mendes, A. Blais, C. Reichl, W. Wegscheider, A. Wallraff, K. Ensslin, and T. Ihn, Nature **560**, 179 (2018).

[30] P. Harvey-Collard, J. Dijkema, G. Zheng, A. Sammak, G. Scappucci, and L. M. Vandersypen, Physical Review X **12**, 021026 (2022).

[31] K. D. Petersson, L. W. McFaul, M. D. Schroer, M. Jung, J. M. Taylor, A. A. Houck, and J. R. Petta, Nature **490**, 380 (2012).

[32] P. Krantz, M. Kjaergaard, F. Yan, T. P. Orlando, S. Gustavsson, and W. D. Oliver, Applied physics reviews **6** (2019).

[33] A. Blais, A. L. Grimsmo, S. M. Girvin, and A. Wallraff, Reviews of Modern Physics **93**, 025005 (2021).

[34] T. Ihn, *Semiconductor Nanostructures* (Oxford University Press, 2009).

[35] J. Gramich, *Andreev and Spin Transport in Carbon Nanotube Quantum Dot Hybrid Devices*, Ph.D. thesis, University of Basel (2016).

[36] J. Schindele, *Observation of Cooper Pair Splitting and Andreev Bound States in Carbon Nanotubes*, Ph.D. thesis, University of Basel (2014).

[37] J. Ridderbos, *Quantum dots and superconductivity in Ge - Si nanowires*, Ph.D. thesis, University of Twente (2018).

[38] C. H. Jünger, *Transport Spectroscopy of Semiconductor Superconductor Nanowire Hybrid Devices*, Ph.D. thesis, University of Basel (2019).

[39] A. Hertel, *Development of superconducting gatemon qubits based on selective-area-grown semiconductors*, Ph.D. thesis, University of Copenhagen (2021).

[40] A. Pally, *Crystal-phase defined nanowire quantum dots as a platform for qubits*, Ph.D. thesis, University of Basel.

[41] M. A. Endres, *WTe2: Candidate for topological superconductivity*, Ph.D. thesis, University of Basel.

[42] C. Metzger, *Spin charge effects in Andreev Bound States*, Ph.D. thesis, University of Paris-Saclay.

[43] H. K. Onnes, Leiden Communication **120b,122b** (1911).

[44] W. Meissner and R. Ochsenfeld, Naturwissenschaften **21**, 787 (1933).

[45] F. London and H. London, Proceedings of the Royal Society of London. Series A-Mathematical and Physical Sciences **149**, 71 (1935).

[46] M. N. Chernodub, in *Strongly Interacting Matter in Magnetic Fields* (Springer, 2013) pp. 143–180.

[47] J. Bardeen, L. N. Cooper, and J. R. Schrieffer, Physical review **108**, 1175 (1957).

[48] J. Bardeen, L. N. Cooper, and J. R. Schrieffer, Physical Review **106**, 162 (1957).

[49] M. Tinkham, *Introduction to superconductivity* (Courier Corporation, 2004).

[50] S. De Franceschi, L. Kouwenhoven, C. Schönenberger, and W. Wernsdorfer, Nature nanotechnology **5**, 703 (2010).

[51] J. Pillet, C. Quay, P. Morfin, C. Bena, A. L. Yeyati, and P. Joyez, Nature Physics **6**, 965 (2010).

[52] A. Andreev, Soviet Physics JETP **19**, 1823 (1964).

[53] C. Beenakker, "Andreev reflection note," Lecture notes for Andreev reflection (2012), lecture conducted at NATO Advanced Study Institute in Ankara.

[54] G. Blonder, m. M. Tinkham, and k. T. Klapwijk, Physical Review B **25**, 4515 (1982).

[55] T. T. Heikkilä, *The physics of nanoelectronics: transport and fluctuation phenomena at low temperatures*, Vol. 21 (Oxford University Press, USA, 2013).

[56] W. Lu, J. Xiang, B. P. Timko, Y. Wu, and C. M. Lieber, Proceedings of the National Academy of Sciences **102**, 10046 (2005).

[57] L. Y. Cheung, *Semiconducting nanowire-based Josephson junctions for qubits*, Ph.D. thesis, University of Basel (2023).

[58] P. F. Bagwell, Physical Review B **46**, 12573 (1992).

[59] E. Prada, P. San-Jose, M. W. de Moor, A. Geresdi, E. J. Lee, J. Klinovaja, D. Loss, J. Nygård, R. Aguado, and L. P. Kouwenhoven, Nature Reviews Physics **2**, 575 (2020).

[60] C. Caroli, P. De Gennes, and J. Matricon, Physics Letters **9**, 307 (1964).

[61] L. Yu, Acta Physica Sinica **21**, 75 (1965).

[62] H. Shiba, Progress of Theoretical Physics **40**, 435 (1968).

[63] A. Rusinov, Soviet Physics JETP **9**, 85 (1969).

[64] I. Kulik, Soviet Journal of Experimental and Theoretical Physics **30**, 944 (1969).

[65] I. O. Kulik, Soviet Physics JETP **30**, 944 (1970).

[66] C. W. J. Beenakker and H. van Houten, Physical Review Letters **66**, 3056 (1991).

[67] A. Furusaki and M. Tsukada, Solid State Communications **78**, 299 (1991).

[68] F. Nichele, E. Portolés, A. Fornieri, A. M. Whiticar, A. C. Drachmann, S. Gronin, T. Wang, G. Gardner, C. Thomas, A. Hatke, *et al.*, Physical review letters **124**, 226801 (2020).

[69] B. D. Josephson, Physics letters **1**, 251 (1962).

[70] V. Ambegaokar and A. Baratoff, Physical Review Letters **10**, 486 (1963).

[71] M. Della Rocca, M. Chauvin, B. Huard, H. Pothier, D. Esteve, and C. Urbina, Physical review letters **99**, 127005 (2007).

[72] E. M. Spanton, M. Deng, S. Vaitiekėnas, P. Krogstrup, J. Nygård, C. M. Marcus, and K. A. Moler, Nature Physics **13**, 1177 (2017).

[73] C. English, D. Hamilton, C. Chialvo, I. Moraru, N. Mason, and D. Van Harlingen, Physical Review B **94**, 115435 (2016).

[74] G. Nanda, J. L. Aguilera-Servin, P. Rakyta, A. Kormányos, R. Kleiner, D. Koelle, K. Watanabe, T. Taniguchi, L. M. Vandersypen, and S. Goswami, Nano Letters **17**, 3396 (2017).

[75] A. Lipman, R. Mints, R. Kleiner, D. Koelle, and E. Goldobin, Physical Review B **90**, 184502 (2014).

[76] G.-H. Park, W. Lee, S. Park, K. Watanabe, T. Taniguchi, G. Y. Cho, and G.-H. Lee, arXiv preprint arXiv:2312.02640 (2023).

[77] I. Borzenets, F. Amet, C. Ke, A. Draelos, M. Wei, A. Seredinski, K. Watanabe, T. Taniguchi, Y. Bomze, M. Yamamoto, *et al.*, Physical review letters **117**, 237002 (2016).

[78] A. Zazunov, R. Egger, T. Jonckheere, and T. Martin, Physical review letters **103**, 147004 (2009).

[79] L. Dell'Anna, A. Zazunov, R. Egger, and T. Martin, Physical Review B **75**, 085305 (2007).

[80] T. Yokoyama, M. Eto, and Y. V. Nazarov, Physical Review B **89**, 195407 (2014).

[81] J. Arjoranta and T. T. Heikkilä, Physical Review B **93**, 024522 (2016).

[82] M. Cheng and R. M. Lutchyn, Physical Review B **86**, 134522 (2012).

[83] O. A. Awoga, J. Cayao, and A. M. Black-Schaffer, Physical Review Letters **123**, 117001 (2019).

[84] F. Matute-Cañadas, C. Metzger, S. Park, L. Tosi, P. Krogstrup, J. Nygård, M. Goffman, C. Urbina, H. Pothier, and A. L. Yeyati, Physical Review Letters **128**, 197702 (2022).

[85] S. Hart, Z. Cui, G. Ménard, M. Deng, A. E. Antipov, R. M. Lutchyn, P. Krogstrup, C. M. Marcus, and K. A. Moler, Physical Review B **100**, 064523 (2019).

[86] T. Yokoyama, M. Eto, and Y. V. Nazarov, Journal of the Physical Society of Japan **82**, 054703 (2013).

[87] A. A. Golubov, M. Y. Kupriyanov, and E. Il'Ichev, Reviews of modern physics **76**, 411 (2004).

[88] L. Bulaevskii, V. Kuzii, and A. Sobyanin, JETP lett **25**, 290 (1977).

[89] J. A. Van Dam, Y. V. Nazarov, E. P. Bakkers, S. De Franceschi, and L. P. Kouwenhoven, Nature **442**, 667 (2006).

[90] J.-P. Cleuziou, W. Wernsdorfer, V. Bouchiat, T. Ondarçuhu, and M. Monthioux, **1**, 53.

[91] V. Ryazanov, V. Oboznov, A. Y. Rusanov, A. Veretennikov, A. A. Golubov, and J. Aarts, Physical review letters **86**, 2427 (2001).

[92] V. B. Geshkenbein, A. I. Larkin, and A. Barone, Physical Review B **36**, 235 (1987).

[93] D. J. Van Harlingen, Reviews of Modern Physics **67**, 515 (1995).

[94] J. Baselmans, A. Morpurgo, B. Van Wees, and T. Klapwijk, Nature **397**, 43 (1999).

[95] A. Buzdin and A. Koshelev, Physical Review B **67**, 220504 (2003).

[96] H. Sickinger, A. Lipman, M. Weides, R. Mints, H. Kohlstedt, D. Koelle, R. Kleiner, and E. Goldobin, Physical review letters **109**, 107002 (2012).

[97] D. Szombati, S. Nadj-Perge, D. Car, S. Plissard, E. Bakkers, and L. Kouwenhoven, Nature Physics **12**, 568 (2016).

[98] E. Terzioglu and M. Beasley, IEEE Transactions on applied superconductivity **8**, 48 (1998).

[99] L. B. Ioffe, V. B. Geshkenbein, M. V. Feigel'Man, A. L. Fauchere, and G. Blatter, Nature **398**, 679 (1999).

[100] A. Blais and A. M. Zagoskin, Physical Review A **61**, 042308 (2000).

[101] F. Thomas, *Deterministic Tunnel Barriers in 1D Quantum Electronic Systems*, Thesis, University of Basel (2020).

[102] A. Bordoloi, *Spin Projection and Correlation Experiments in Nanoelectronic Devices*, Thesis, University of Basel (2021).

[103] L. P. Kouwenhoven, D. Austing, and S. Tarucha, Reports on progress in physics **64**, 701 (2001).

[104] B. Trauzettel, D. V. Bulaev, D. Loss, and G. Burkard, Nature Physics **3**, 192 (2007).

[105] S. Schnez, F. Molitor, C. Stampfer, J. Güttinger, I. Shorubalko, T. Ihn, and K. Ensslin, Applied Physics Letters **94** (2009).

[106] M. Eich, R. Pisoni, A. Pally, H. Overweg, A. Kurzmann, Y. Lee, P. Rickhaus, K. Watanabe, T. Taniguchi, K. Ensslin, *et al.*, Nano letters **18**, 5042 (2018).

[107] P. Jarillo-Herrero, S. Sapmaz, C. Dekker, L. P. Kouwenhoven, and H. S. Van Der Zant, Nature **429**, 389 (2004).

[108] E. A. Laird, F. Kuemmeth, G. A. Steele, K. Grove-Rasmussen, J. Nygård, K. Flensberg, and L. P. Kouwenhoven, Reviews of Modern Physics **87**, 703 (2015).

[109] M. Jung, J. Schindele, S. Nau, M. Weiss, A. Baumgartner, and C. Schonenberger, Nano letters **13**, 4522 (2013).

[110] K. Ono, D. Austing, Y. Tokura, and S. Tarucha, Science **297**, 1313 (2002).

[111] J. Elzerman, R. Hanson, L. Willems van Beveren, B. Witkamp, L. Vandersypen, and L. P. Kouwenhoven, nature **430**, 431 (2004).

[112] S. De Franceschi, L. Kouwenhoven, C. Schönenberger, and W. Wernsdorfer, Nature Nanotechnology **5**, 703 (2010).

[113] L. Aslamazov and M. Fistul, Sov. Phys.-JETP (Engl. Transl.);(United States) **56** (1982).

[114] E. J. Lee, X. Jiang, M. Houzet, R. Aguado, C. M. Lieber, and S. De Franceschi, Nature nanotechnology **9**, 79 (2014).

[115] N. Claughton, M. Leadbeater, and C. Lambert, Journal of Physics: Condensed Matter **7**, 8757 (1995).

[116] T. Meng, S. Florens, and P. Simon, Phys. Rev. B **79**, 224521 (2009).

[117] J. Bauer, A. Oguri, and A. Hewson, J. Phys.: Condens. Matter **19**, 486211 (2007).

[118] A. Braggio, M. Governale, M. G. Pala, and J. Konig, Solid State Commun. **151**, 155 (2011).

[119] Y. Tanaka, N. Kawakami, and A. Oguri, Journal of the Physical Society of Japan **76**, 074701 (2007).

[120] J. Schindele, A. Baumgartner, R. Maurand, M. Weiss, and C. Schönenberger, Physical Review B **89**, 045422 (2014).

[121] J.-D. Pillet, P. Joyez, M. Goffman, *et al.*, Physical Review B **88**, 045101 (2013).

[122] A. Jellinggaard, K. Grove-Rasmussen, M. H. Madsen, and J. Nygård, Physical Review B **94**, 064520 (2016).

[123] C. Jünger, A. Baumgartner, R. Delagrange, D. Chevallier, S. Lehmann, M. Nilsson, K. A. Dick, C. Thelander, and C. Schönenberger, Communications Physics **2**, 76 (2019).

[124] Z. Scherübl, G. Fülöp, C. P. Moca, J. Gramich, A. Baumgartner, P. Makk, T. Elalaily, C. Schönenberger, J. Nygård, G. Zaránd, *et al.*, Nature communications **11**, 1834 (2020).

[125] F. Hassani, M. Peruzzo, L. Kapoor, A. Trioni, M. Zemlicka, and J. M. Fink, Nature Communications **14**, 3968 (2023).

[126] Y. Makhlin, G. Schön, and A. Shnirman, Reviews of modern physics **73**, 357 (2001).

[127] V. Bouchiat, D. Vion, P. Joyez, D. Esteve, and M. Devoret, Physica Scripta **1998**, 165 (1998).

[128] Y. Nakamura, Y. A. Pashkin, and J. Tsai, nature **398**, 786 (1999).

[129] J. R. Friedman, V. Patel, W. Chen, S. Tolpygo, and J. E. Lukens, nature **406**, 43 (2000).

[130] C. H. Van Der Wal, A. Ter Haar, F. Wilhelm, R. Schouten, C. Harmans, T. Orlando, S. Lloyd, and J. Mooij, Science **290**, 773 (2000).

[131] J. M. Martinis, S. Nam, J. Aumentado, and C. Urbina, Physical review letters **89**, 117901 (2002).

[132] G. Wendin, Reports on Progress in Physics **80**, 106001 (2017).

[133] M. H. Devoret, B. Huard, R. Schoelkopf, and L. F. Cugliandolo, *Quantum machines: measurement and control of engineered quantum systems*, Vol. 96 (Oxford University Press, USA, 2014).

[134] U. Vool and M. Devoret, International Journal of Circuit Theory and Applications **45**, 897 (2017).

[135] J. Koch, M. Y. Terri, J. Gambetta, A. A. Houck, D. I. Schuster, J. Majer, A. Blais, M. H. Devoret, S. M. Girvin, and R. J. Schoelkopf, Physical Review A **76**, 042319 (2007).

[136] A. Kringhøj, L. Casparis, M. Hell, T. W. Larsen, F. Kuemmeth, M. Leijnse, K. Flensberg, P. Krogstrup, J. Nygård, K. D. Petersson, *et al.*, Physical Review B **97**, 060508 (2018).

[137] A. Zazunov, V. Shumeiko, E. Bratus, J. Lantz, and G. Wendin, Physical review letters **90**, 087003 (2003).

[138] N. M. Chtchelkatchev and Y. V. Nazarov, Physical review letters **90**, 226806 (2003).

[139] C. Padurariu and Y. V. Nazarov, Physical Review B **81**, 144519 (2010).

[140] A. A. Reynoso, G. Usaj, C. Balseiro, D. Feinberg, and M. Avignon, Physical Review B **86**, 214519 (2012).

[141] S. Park and A. L. Yeyati, Physical Review B **96**, 125416 (2017).

[142] M. Hays, V. Fatemi, D. Bouman, J. Cerrillo, S. Diamond, K. Serniak, T. Connolly, P. Krogstrup, J. Nygård, A. Levy Yeyati, *et al.*, Science **373**, 430 (2021).

[143] M. Pita-Vidal, A. Bargerbos, R. Žitko, L. J. Splitthoff, L. Grünhaupt, J. J. Wesdorp, Y. Liu, L. P. Kouwenhoven, R. Aguado, B. van Heck, *et al.*, Nature Physics , 1 (2023).

[144] M. Hays, G. De Lange, K. Serniak, D. Van Woerkom, D. Bouman, P. Krogstrup, J. Nygård, A. Geresdi, and M. Devoret, Physical review letters **121**, 047001 (2018).

[145] L. R. Bernstein, Geochimica et Cosmochimica Acta **49**, 2409 (1985).

[146] J. Feng, Y. Liu, P. B. Griffin, and J. D. Plummer, IEEE Electron Device Letters **27**, 911 (2006).

[147] Y. Xie, D. Monroe, E. Fitzgerald, P. Silverman, F. Thiel, and G. Watson, Applied physics letters **63**, 2263 (1993).

[148] M. Currie, S. Samavedam, T. Langdo, C. Leitz, and E. Fitzgerald, Applied physics letters **72**, 1718 (1998).

[149] D. Kuzum, A. J. Pethe, T. Krishnamohan, and K. C. Saraswat, IEEE transactions on electron devices **56**, 648 (2009).

[150] R. Pillarisetty, B. Chu-Kung, S. Corcoran, G. Dewey, J. Kavalieros, H. Kennel, R. Kotlyar, V. Le, D. Lionberger, M. Metz, *et al.*, in *2010 International Electron Devices Meeting* (IEEE, 2010) pp. 6–7.

[151] R. Zhang, P. Huang, N. Taoka, M. Takenaka, and S. Takagi, in *2012 Symposium on VLSI Technology (VLSIT)* (IEEE, 2012) pp. 161–162.

[152] B. S. Meyerson, Scientific American **270**, 62 (1994).

[153] P. S. Goley and M. K. Hudait, Materials **7**, 2301 (2014).

[154] A. Sammak, D. Sabbagh, N. W. Hendrickx, M. Lodari, B. Paquelet Wuetz, A. Tosato, L. Yeoh, M. Bollani, M. Virgilio, M. A. Schubert, *et al.*, Advanced Functional Materials **29**, 1807613 (2019).

[155] L. Yang, R. N. Musin, X.-Q. Wang, and M. Chou, Physical Review B **77**, 195325 (2008).

[156] S. Zhang, F. J. Lopez, J. K. Hyun, and L. J. Lauhon, Nano letters **10**, 4483 (2010).

[157] F. Froning, *Hole Spin Qubits in Ge/Si Core/Shell Nanowires*, Ph.D. thesis, University of Basel.

[158] A. Nduwimana, R. Musin, A. Smith, and X.-Q. Wang, Nano letters **8**, 3341 (2008).

[159] S. Conesa-Boj, A. Li, S. Koelling, M. Brauns, J. Ridderbos, T. T. Nguyen, M. A. Verheijen, P. M. Koenraad, F. A. Zwanenburg, and E. P. Bakkers, Nano letters **17**, 2259 (2017).

[160] C. Kloeffel, M. Trif, and D. Loss, Physical Review B **84**, 195314 (2011).

[161] C. Kloeffel, M. J. Rančić, and D. Loss, Physical Review B **97**, 235422 (2018).

[162] X.-J. Hao, T. Tu, G. Cao, C. Zhou, H.-O. Li, G.-C. Guo, W. Y. Fung, Z. Ji, G.-P. Guo, and W. Lu, Nano letters **10**, 2956 (2010).

[163] A. P. Higginbotham, F. Kuemmeth, T. W. Larsen, M. Fitzpatrick, J. Yao, H. Yan, C. M. Lieber, and C. Marcus, Physical Review Letters **112**, 216806 (2014).

[164] F. Froning, M. Rančić, B. Hetényi, S. Bosco, M. Rehmann, A. Li, E. P. Bakkers, F. A. Zwanenburg, D. Loss, D. Zumbühl, *et al.*, Physical Review Research **3**, 013081 (2021).

[165] F. N. Froning, L. C. Camenzind, O. A. van der Molen, A. Li, E. P. Bakkers, D. M. Zumbühl, and F. R. Braakman, Nature Nanotechnology **16**, 308 (2021).

[166] R. Wang, R. S. Deacon, J. Yao, C. M. Lieber, and K. Ishibashi, **32**, 094002.

[167] A. Hansen, M. Björk, C. Fasth, C. Thelander, and L. Samuelson, Physical Review B **71** (2005).

[168] P. Roulleau, T. Choi, S. Riedi, T. Heinzel, I. Shorubalko, T. Ihn, and K. Ensslin, Physical Review B **81** (2010).

[169] D. Liang and X. Gao, Nano Letters **12**, 3263 (2012).

[170] Z. Scherübl, G. Fülöp, M. Madsen, J. Nygård, and S. Csonka, Physical Review B **94** (2016).

[171] I. van Weperen, B. Tarasinski, D. Eeltink, V. Pribiag, S. Plissard, E. Bakkers, L. Kouwenhoven, and M. Wimmer, Physical Review B **91** (2015).

[172] L. J. Lauhon, M. S. Gudiksen, D. Wang, and C. M. Lieber, nature **420**, 57 (2002).

[173] I. A. Goldthorpe, A. F. Marshall, and P. C. McIntyre, Nano letters **8**, 4081 (2008).

[174] J. Nah, D. C. Dillen, K. M. Varahramyan, S. K. Banerjee, and E. Tutuc, Nano letters **12**, 108 (2012).

[175] S. A. Dayeh, J. Wang, N. Li, J. Y. Huang, A. V. Gin, and S. T. Picraux, Nano letters **11**, 4200 (2011).

[176] D. C. Dillen, K. Kim, E.-S. Liu, and E. Tutuc, Nature nanotechnology **9**, 116 (2014).

[177] K. Varahramyan, D. Ferrer, E. Tutuc, and S. Banerjee, Applied physics letters **95** (2009).

[178] J. Xiang, W. Lu, Y. Hu, Y. Wu, H. Yan, and C. M. Lieber, nature **441**, 489 (2006).

[179] H. Yan, H. S. Choe, S. Nam, Y. Hu, S. Das, J. F. Klemic, J. C. Ellenbogen, and C. M. Lieber, Nature **470**, 240 (2011).

[180] Y. Hu, J. Xiang, G. Liang, H. Yan, and C. M. Lieber, Nano letters **8**, 925 (2008).

[181] G. Liang, J. Xiang, N. Kharche, G. Klimeck, C. M. Lieber, and M. Lundstrom, Nano letters **7**, 642 (2007).

[182] Y. Hu, H. O. Churchill, D. J. Reilly, J. Xiang, C. M. Lieber, and C. M. Marcus, Nature nanotechnology **2**, 622 (2007).

[183] S. Roddaro, A. Fuhrer, P. Brusheim, C. Fasth, H. Xu, L. Samuelson, J. Xiang, and C. Lieber, Physical review letters **101**, 186802 (2008).

[184] M. Brauns, J. Ridderbos, A. Li, E. P. Bakkers, and F. A. Zwanenburg, Physical Review B **93**, 121408 (2016).

[185] M. Brauns, J. Ridderbos, A. Li, E. P. Bakkers, W. G. Van Der Wiel, and F. A. Zwanenburg, Physical Review B **94**, 041411 (2016).

[186] F. Froning, M. Rehmann, J. Ridderbos, M. Brauns, F. Zwanenburg, A. Li, E. Bakkers, D. Zumbühl, and F. Braakman, Applied physics letters **113** (2018).

[187] M. Brauns, J. Ridderbos, A. Li, W. G. Van Der Wiel, E. P. Bakkers, and F. A. Zwanenburg, Applied physics letters **109** (2016).

[188] A. Zarassi, Z. Su, J. Danon, J. Schwenderling, M. Hocevar, B.-M. Nguyen, J. Yoo, S. A. Dayeh, and S. M. Frolov, Physical Review B **95**, 155416 (2017).

[189] J. Ridderbos, M. Brauns, J. Shen, F. K. de Vries, A. Li, E. P. Bakkers, A. Brinkman, and F. A. Zwanenburg, Advanced materials **30**, 1802257 (2018).

[190] M. Sistani, J. Delaforce, R. B. Kramer, N. Roch, M. A. Luong, M. I. den Hertog, E. Robin, J. Smoliner, J. Yao, C. M. Lieber, *et al.*, ACS nano **13**, 14145 (2019).

[191] J. Xiang, A. Vidan, M. Tinkham, R. M. Westervelt, and C. M. Lieber, Nature nanotechnology **1**, 208 (2006).

[192] Z. Su, A. Zarassi, B.-M. Nguyen, J. Yoo, S. A. Dayeh, and S. M. Frolov, arXiv preprint arXiv:1610.03010 (2016).

[193] Y. Hu, F. Kuemmeth, C. M. Lieber, and C. M. Marcus, Nature nanotechnology **7**, 47 (2012).

[194] A. P. Higginbotham, T. Larsen, J. Yao, H. Yan, C. Lieber, C. Marcus, and F. Kuemmeth, Nano letters **14**, 3582 (2014).

[195] a. R. Wagner and s. W. Ellis, Applied physics letters **4**, 89 (1964).

[196] B.-M. Nguyen, Y. Taur, S. T. Picraux, and S. A. Dayeh, Nano letters **14**, 585 (2014).

[197] R. Haller, *Probing the Microwave Response of Novel Josephson Elements*, Ph.D. thesis, University of Basel (2021).

[198] J. Ridderbos, M. Brauns, F. K. de Vries, J. Shen, A. Li, S. Kolling, M. A. Verheijen, A. Brinkman, W. G. van der Wiel, E. P. Bakkers, *et al.*, Nano letters **20**, 122 (2019).

[199] S. Kral, C. Zeiner, M. Stoger-Pollach, E. Bertagnolli, M. Den Hertog, M. Lopez-Haro, E. Robin, K. El Hajraoui, and A. Lugstein, Nano letters **15**, 4783 (2015).

[200] W. M. Weber, L. Geelhaar, A. P. Graham, E. Unger, G. S. Duesberg, M. Liebau, W. Pamler, C. Chèze, H. Riechert, P. Lugli, *et al.*, Nano letters **6**, 2660 (2006).

[201] K. El Hajraoui, M. A. Luong, E. Robin, F. Brunbauer, C. Zeiner, A. Lugstein, P. Gentile, J.-L. Rouvière, and M. Den Hertog, Nano letters **19**, 2897 (2019).

[202] J. C. Wheatley, O. Vilches, and W. Abel, Physics Physique Fizika **4**, 1 (1968).

[203] H. Zu, W. Dai, and A. De Waele, Cryogenics **121**, 103390 (2022).

[204] C. Jünger, S. Lehmann, K. A. Dick, C. Thelander, C. Schönenberger, and A. Baumgartner, Communications Physics **6**, 190 (2023).

[205] W. Chang, V. E. Manucharyan, T. S. Jespersen, J. Nygård, and C. M. Marcus, Physical Review Letters **110**, 217005 (2013).

[206] M. T. Deng *et al.*, Science **354**, 1557 (2016).

[207] E. J. H. Lee *et al.*, Physical Review B **95**, 180502 (2017).

[208] M. Buitelaar, T. Nussbaumer, and C. Schönenberger, Physical Review Letters **89**, 256801 (2002).

[209] T. Sand-Jespersen *et al.*, Physical Review Letters **99**, 126603 (2007).

[210] R. Zitko, J. S. Lim, R. López, and R. Aguado, Physical Review B **91**, 045441 (2015).

[211] D. J. Van Woerkom, A. Proutski, B. Van Heck, D. Bouman, J. I. Väyrynen, L. I. Glazman, P. Krogstrup, J. Nygård, L. P. Kouwenhoven, and A. Geresdi, Nature Physics **13**, 876 (2017).

[212] A. Bargerbos, M. Pita-Vidal, L. J. Splitthoff, L. Grünhaupt, J. J. Wesdorp, Y. Liu, L. P. Kouwenhoven, R. Aguado, C. K. Andersen, A. Kou, *et al.*, Physical Review Letters **131**, 097001 (2023).

[213] L. Tosi, C. Metzger, M. Goffman, C. Urbina, H. Pothier, S. Park, A. L. Yeyati, J. Nygård, and P. Krogstrup, Physical Review X **9**, 011010 (2019).

[214] V. Mourik, K. Zuo, S. M. Frolov, S. Plissard, E. P. Bakkers, and L. P. Kouwenhoven, Science **336**, 1003 (2012).

[215] D. I. Pikulin, B. van Heck, T. Karzig, E. A. Martinez, B. Nijholt, T. Laeven, G. W. Winkler, J. D. Watson, S. Heedt, M. Temurhan, *et al.*, arXiv preprint arXiv:2103.12217 (2021).

[216] M. Aghaee, A. Akkala, Z. Alam, R. Ali, A. A. Ramirez, M. Andrzejczuk, A. E. Antipov, P. Aseev, M. Astafev, B. Bauer, *et al.*, Physical Review B **107**, 245423 (2023).

[217] R. Hess, H. F. Legg, D. Loss, and J. Klinovaja, Physical Review B **104**, 075405 (2021).

[218] A. Y. Kitaev, Physics-uspekhi **44**, 131 (2001).

[219] F. Maier, J. Klinovaja, and D. Loss, Physical Review B **90**, 195421 (2014).

[220] F. K. De Vries, J. Shen, R. J. Skolasinski, M. P. Nowak, D. Varjas, L. Wang, M. Wimmer, J. Ridderbos, F. A. Zwanenburg, A. Li, *et al.*, Nano letters **18**, 6483 (2018).

[221] R. T. Tung, Applied Physics Reviews **1** (2014).

[222] R. S. Muller and T. I. Kamins, *Device electronics for integrated circuits* (John Wiley & Sons, 2002).

[223] F. Gao, J.-H. Wang, H. Watzinger, H. Hu, M. J. Rančić, J.-Y. Zhang, T. Wang, Y. Yao, G.-L. Wang, J. Kukučka, *et al.*, Advanced Materials **32**, 1906523 (2020).

[224] J. Gramich, A. Baumgartner, and C. Schönenberger, Physical Review B **96**, 195418 (2017).

[225] J. Thong, W. Choi, and C. Chong, Sensors and Actuators A: Physical **63**, 243 (1997).

[226] K. Yao, *Silicon And Silicon-germanium Epitaxy For Quantum Dot Device Fabrications Towards An Electron Spin-Based Quantum Computer*, Ph.D. thesis, Princeton University.

[227] W. Li, P. Anantha, S. Bao, K. H. Lee, X. Guo, T. Hu, L. Zhang, H. Wang, R. Soref, and C. S. Tan, Applied physics letters **109** (2016).

[228] O. Faist, *Andreev bound states in semiconducting double nanowires*, Ph.D. thesis, University of Basel.

[229] C. Adelsberger, S. Bosco, J. Klinovaja, and D. Loss, Physical Review B **106**, 235408 (2022).

[230] T. Dvir, G. Wang, N. van Loo, C.-X. Liu, G. P. Mazur, A. Bordin, S. L. Ten Haaf, J.-Y. Wang, D. van Driel, F. Zatelli, *et al.*, Nature **614**, 445 (2023).

[231] A. Bordin, G. Wang, C.-X. Liu, S. L. Ten Haaf, N. Van Loo, G. P. Mazur, D. Xu, D. Van Driel, F. Zatelli, S. Gazibegovic, *et al.*, Physical Review X **13**, 031031 (2023).

[232] G. Wang, T. Dvir, G. P. Mazur, C.-X. Liu, N. van Loo, S. L. Ten Haaf, A. Bordin, S. Gazibegovic, G. Badawy, E. P. Bakkers, *et al.*, Nature **612**, 448 (2022).

[233] D. Wollman, D. Van Harlingen, W. Lee, D. Ginsberg, and A. Leggett, Physical Review Letters **71**, 2134 (1993).

[234] A. Kononov, G. Abulizi, K. Qu, J. Yan, D. Mandrus, K. Watanabe, T. Taniguchi, and C. Schonenberger, Nano letters **20**, 4228 (2020).

[235] H. I. Jørgensen, T. Novotný, K. Grove-Rasmussen, K. Flensberg, and P. E. Lindelof, **7**, 2441.

[236] R. Maurand, T. Meng, E. Bonet, S. Florens, L. Marty, and W. Wernsdorfer, **2**, 011009.

[237] R. Delagrange, R. Weil, A. Kasumov, M. Ferrier, H. Bouchiat, and R. Deblock, Physical Review B **93**, 195437 (2016).

[238] M. Weides, M. Kemmler, H. Kohlstedt, R. Waser, D. Koelle, R. Kleiner, and E. Goldobin, Physical review letters **97**, 247001 (2006).

[239] M. Stoutimore, A. Rossolenko, V. Bolginov, V. Oboznov, A. Rusanov, D. Baranov, N. Pugach, S. Frolov, V. Ryazanov, and D. Van Harlingen, Physical review letters **121**, 177702 (2018).

[240] A. Murani, A. Kasumov, S. Sengupta, Y. A. Kasumov, V. Volkov, I. Khodos, F. Brisset, R. Delagrange, A. Chepelianskii, R. Deblock, *et al.*, Nature Communications **8**, 15941 (2017).

[241] M. Endres, A. Kononov, H. S. Arachchige, J. Yan, D. Mandrus, K. Watanabe, T. Taniguchi, and C. Schonenberger, Nano Letters (2023).

[242] F. Vigneau, R. Mizokuchi, D. C. Zanuz, X. Huang, S. Tan, R. Maurand, S. Frolov, A. Sammak, G. Scappucci, F. Lefloch, *et al.*, Nano letters **19**, 1023 (2019).

[243] K. Aggarwal, A. Hofmann, D. Jirovec, I. Prieto, A. Sammak, M. Botifoll, S. Martí-Sánchez, M. Veldhorst, J. Arbiol, G. Scappucci, *et al.*, Physical Review Research **3**, L022005 (2021).

[244] K. Likharev, Reviews of Modern Physics **51**, 101 (1979).

[245] O. Kurtossy, Z. Scherubl, G. Fulop, I. E. Lukács, T. Kanne, J. Nygård, P. Makk, and S. Csonka, Nano Letters **21**, 7929 (2021).

[246] A. Fornieri, A. M. Whiticar, F. Setiawan, E. Portolés, A. C. Drachmann, A. Keselman, S. Gronin, C. Thomas, T. Wang, R. Kallaher, *et al.*, Nature **569**, 89 (2019).

[247] C. Jünger, R. Delagrange, D. Chevallier, S. Lehmann, K. A. Dick, C. Thelander, J. Klinovaja, D. Loss, A. Baumgartner, and C. Schönenberger, Physical Review Letters **125**, 017701 (2020).

[248] A. M. Zagoskin, *Quantum theory of many-body systems*, Vol. 174 (Springer, 1998).

[249] M. Nadeem, M. S. Fuhrer, and X. Wang, Nature Reviews Physics , 1 (2023).

[250] R. S. Souto, M. Leijnse, and C. Schrade, Physical Review Letters **129**, 267702 (2022).

[251] C. Ciaccia, R. Haller, A. C. Drachmann, C. Schrade, T. Lindemann, M. J. Manfra, and C. Schönenberger, arXiv preprint arXiv:2304.00484 (2023).

[252] A. Leblanc, C. Tangchingchai, Z. S. Momtaz, E. Kiyooka, J.-M. Hartmann, G. T. Fernandez-Bada, B. Brun-Barriere, V. Schmitt, S. Zihlmann, R. Maurand, *et al.*, arXiv preprint arXiv:2311.15371 (2023).

[253] M. Valentini, O. Sagi, L. Baghumyan, T. de Gijsel, J. Jung, S. Calcaterra, A. Ballabio, J. A. Servin, K. Aggarwal, M. Janik, *et al.*, arXiv preprint arXiv:2306.07109 (2023).

[254] H. Dausy, L. Nulens, B. Raes, M. J. Van Bael, and J. Van de Vondel, Physical Review Applied **16**, 024013 (2021).

[255] D. Z. Haxell, E. Cheah, F. Křížek, R. Schott, M. F. Ritter, M. Hinderling, W. Belzig, C. Bruder, W. Wegscheider, H. Riel, *et al.*, Physical Review Letters **130**, 087002 (2023).

[256] A. Murphy, P. Weinberg, T. Aref, U. Coskun, V. Vakaryuk, A. Levchenko, and A. Bezryadin, Physical review letters **110**, 247001 (2013).

[257] V. Krasnov, T. Bauch, S. Intiso, E. Hürfeld, T. Akazaki, H. Takayanagi, and P. Delsing, Physical review letters **95**, 157002 (2005).

[258] G.-H. Lee, D. Jeong, J.-H. Choi, Y.-J. Doh, and H.-J. Lee, Physical review letters **107**, 146605 (2011).

[259] H. Sellier, C. Baraduc, F. Lefloch, and R. Calemczuk, Physical review letters **92**, 257005 (2004).

[260] R. Maurand, T. Meng, E. Bonet, S. Florens, L. Marty, and W. Wernsdorfer, Physical Review X **2**, 011009 (2012).

[261] S. Backhaus, S. Pereverzev, A. Loshak, J. Davis, and R. Packard, Science **278**, 1435 (1997).

[262] A. Marchenkov, R. Simmonds, S. Backhaus, A. Loshak, J. Davis, and R. Packard, Physical review letters **83**, 3860 (1999).

[263] S.-K. Yip, Physical review letters **83**, 3864 (1999).

[264] M. Fogelström, S. Yip, and J. Kurkijärvi, Physica C: Superconductivity **294**, 289 (1998).

[265] Y. Zhu, M. Liao, Q. Zhang, H.-Y. Xie, F. Meng, Y. Liu, Z. Bai, S. Ji, J. Zhang, K. Jiang, *et al.*, Physical Review X **11**, 031011 (2021).

[266] M. Fogelström and S.-K. Yip, Physical Review B **57**, R14060 (1998).

[267] G. De Lange, B. Van Heck, A. Bruno, D. Van Woerkom, A. Geresdi, S. Plissard, E. Bakkers, A. Akhmerov, and L. DiCarlo, Physical review letters **115**, 127002 (2015).

[268] T. W. Larsen, M. E. Gershenson, L. Casparis, A. Kringhøj, N. J. Pearson, R. P. McNeil, F. Kuemmeth, P. Krogstrup, K. D. Petersson, and C. M. Marcus, Physical review letters **125**, 056801 (2020).

[269] A. Martín-Rodero and A. Levy Yeyati, Advances in Physics **60**, 899 (2011).

[270] M. Hays, V. Fatemi, K. Serniak, D. Bouman, S. Diamond, G. de Lange, P. Krogstrup, J. Nygård, A. Geresdi, and M. Devoret, Nature Physics **16**, 1103 (2020).

[271] A. Kitaev, arXiv preprint cond-mat/0609441 (2006).

[272] M. T. Bell, J. Paramanandam, L. B. Ioffe, and M. E. Gershenson, Physical review letters **112**, 167001 (2014).

[273] A. Gyenis, P. S. Mundada, A. Di Paolo, T. M. Hazard, X. You, D. I. Schuster, J. Koch, A. Blais, and A. A. Houck, PRX Quantum **2**, 010339 (2021).

[274] J. Clarke and A. I. Braginski, *The SQUID Handbook: Fundamentals and Technology of SQUIDs and SQUID Systems*, Vol. 1 (Wiley-Vch, 2004).

[275] M. D. Thompson, M. Ben Shalom, A. Geim, A. Matthews, J. White, Z. Melhem, Y. A. Pashkin, R. P. Haley, and J. R. Prance, Applied Physics Letters **110** (2017).

[276] E. Portolés, S. Iwakiri, G. Zheng, P. Rickhaus, T. Taniguchi, K. Watanabe, T. Ihn, K. Ensslin, and F. K. de Vries, Nature Nanotechnology **17**, 1159 (2022).

[277] C. M. Natarajan, M. G. Tanner, and R. H. Hadfield, Superconductor science and technology **25**, 063001 (2012).

[278] A. J. Annunziata, D. F. Santavicca, L. Frunzio, G. Catelani, M. J. Rooks, A. Frydman, and D. E. Prober, Nanotechnology **21**, 445202 (2010).

[279] M. Brooks, Nature **617**, S1 (2023).

[280] J. Preskill, Quantum **2**, 79 (2018).

[281] F. Arute, K. Arya, R. Babbush, D. Bacon, J. C. Bardin, R. Barends, R. Biswas, S. Boixo, F. G. Brandao, D. A. Buell, *et al.*, Nature **574**, 505 (2019).

[282] M. Kjaergaard, M. E. Schwartz, J. Braumüller, P. Krantz, J. I.-J. Wang, S. Gustavsson, and W. D. Oliver, Annual Review of Condensed Matter Physics **11**, 369 (2020).

[283] S. Krinner, S. Storz, P. Kurpiers, P. Magnard, J. Heinsoo, R. Keller, J. Luetolf, C. Eichler, and A. Wallraff, EPJ Quantum Technology **6**, 2 (2019).

[284] T. W. Larsen, K. D. Petersson, F. Kuemmeth, T. S. Jespersen, P. Krogstrup, J. Nygård, and C. M. Marcus, Physical review letters **115**, 127001 (2015).

[285] M. Pita-Vidal, A. Bargerbos, C.-K. Yang, D. J. Van Woerkom, W. Pfaff, N. Haider, P. Krogstrup, L. P. Kouwenhoven, G. De Lange, and A. Kou, Physical Review Applied **14**, 064038 (2020).

[286] A. Danilenko, D. Sabonis, G. W. Winkler, O. Erlandsson, P. Krogstrup, and C. M. Marcus, Physical Review B **108**, L020505 (2023).

[287] C. Janvier, L. Tosi, L. Bretheau, Ç. Girit, M. Stern, P. Bertet, P. Joyez, D. Vion, D. Esteve, M. Goffman, *et al.*, Science **349**, 1199 (2015).

[288] L. Cheung, R. Haller, A. Kononov, C. Ciaccia, J. Ungerer, T. Kanne, J. Nygård, P. Winkel, T. Reisinger, I. Pop, *et al.*, arXiv preprint arXiv:2310.15995 (2023).

[289] L. Casparis, T. Larsen, M. Olsen, F. Kuemmeth, P. Krogstrup, J. Nygård, K. Petersson, and C. Marcus, Physical review letters **116**, 150505 (2016).

[290] F. Luthi, T. Stavenga, O. Enzing, A. Bruno, C. Dickel, N. Langford, M. A. Rol, T. S. Jespersen, J. Nygård, P. Krogstrup, *et al.*, Physical review letters **120**, 100502 (2018).

[291] L. Casparis, M. R. Connolly, M. Kjaergaard, N. J. Pearson, A. Kringhøj, T. W. Larsen, F. Kuemmeth, T. Wang, C. Thomas, S. Gronin, *et al.*, Nature nanotechnology **13**, 915 (2018).

[292] A. Hertel, M. Eichinger, L. O. Andersen, D. M. van Zanten, S. Kallatt, P. Scarlino, A. Kringhøj, J. M. Chavez-Garcia, G. C. Gardner, S. Gronin, *et al.*, Physical Review Applied **18**, 034042 (2022).

[293] M. Mergenthaler, A. Nersisyan, A. Patterson, M. Esposito, A. Baumgartner, C. Schönenberger, G. A. D. Briggs, E. A. Laird, and P. J. Leek, Physical Review Applied **15**, 064050 (2021).

[294] J. I.-J. Wang, D. Rodan-Legrain, L. Bretheau, D. L. Campbell, B. Kannan, D. Kim, M. Kjaergaard, P. Krantz, G. O. Samach, F. Yan, *et al.*, Nature nanotechnology **14**, 120 (2019).

[295] E. Zhuo, Z. Lyu, X. Sun, A. Li, B. Li, Z. Ji, J. Fan, E. Bakkers, X. Han, X. Song, *et al.*, npj Quantum Information **9**, 51 (2023).

[296] L. C. Gunn III, G. Capellini, M. J. Rattier, and T. J. Pinguet, "Methods of incorporating germanium within cmos process," (2005), uS Patent 6,887,773.

[297] M. Veldhorst, H. Eenink, C.-H. Yang, and A. S. Dzurak, Nature communications **8**, 1766 (2017).

[298] W. M. Weber and T. Mikolajick, Reports on Progress in Physics **80**, 066502 (2017).

[299] A. Heinzig, S. Slesazeck, F. Kreupl, T. Mikolajick, and W. M. Weber, Nano letters **12**, 119 (2012).

[300] J. Delaforce, M. Sistani, R. B. Kramer, M. A. Luong, N. Roch, W. M. Weber, M. I. den Hertog, E. Robin, C. Naud, A. Lugstein, *et al.*, Advanced Materials **33**, 2101989 (2021).

[301] S. Nadj-Perge, S. Frolov, E. Bakkers, and L. P. Kouwenhoven, Nature **468**, 1084 (2010).

[302] A. Blais, R.-S. Huang, A. Wallraff, S. M. Girvin, and R. J. Schoelkopf, Physical Review A **69**, 062320 (2004).

[303] S. Probst, F. Song, P. A. Bushev, A. V. Ustinov, and M. Weides, Review of Scientific Instruments **86** (2015).

[304] J. Lisenfeld, A. Bilmes, A. Megrant, R. Barends, J. Kelly, P. Klimov, G. Weiss, J. M. Martinis, and A. V. Ustinov, npj Quantum Information **5**, 105 (2019).

[305] A. Antony, M. V. Gustafsson, G. J. Ribeill, M. Ware, A. Rajendran, L. C. Govia, T. A. Ohki, T. Taniguchi, K. Watanabe, J. Hone, *et al.*, Nano letters **21**, 10122 (2021).

[306] C. Beenakker, Physical review letters **67**, 3836 (1991).

[307] P. Winkel, I. Takmakov, D. Rieger, L. Planat, W. Hasch-Guichard, L. Grünhaupt, N. Maleeva, F. Foroughi, F. Henriques, K. Borisov, *et al.*, Physical Review Applied **13**, 024015 (2020).

[308] D. Rieger, S. Günzler, M. Spiecker, P. Paluch, P. Winkel, L. Hahn, J. Hohmann, A. Bacher, W. Wernsdorfer, and I. Pop, Nature Materials **22**, 194 (2023).

[309] A. P. Vepsäläinen, A. H. Karamlou, J. L. Orrell, A. S. Dogra, B. Loer, F. Vasconcelos, D. K. Kim, A. J. Melville, B. M. Niedzielski, J. L. Yoder, *et al.*, Nature **584**, 551 (2020).

[310] M. Reznikov, M. Heiblum, H. Shtrikman, and D. Mahalu, Physical Review Letters **75**, 3340 (1995).

[311] A. Kringhøj, B. Van Heck, T. Larsen, O. Erlandsson, D. Sabonis, P. Krogstrup, L. Casparis, K. Petersson, and C. Marcus, Physical Review Letters **124**, 246803 (2020).

[312] A. Bargerbos, W. Uilhoorn, C.-K. Yang, P. Krogstrup, L. P. Kouwenhoven, G. De Lange, B. Van Heck, and A. Kou, Physical review letters **124**, 246802 (2020).

[313] D. Willsch, D. Rieger, P. Winkel, M. Willsch, C. Dickel, J. Krause, Y. Ando, R. Lescanne, Z. Leghtas, N. T. Bronn, *et al.*, arXiv preprint arXiv:2302.09192 (2023).

[314] X. Pan, Y. Zhou, H. Yuan, L. Nie, W. Wei, L. Zhang, J. Li, S. Liu, Z. H. Jiang, G. Catelani, *et al.*, Nature Communications **13**, 7196 (2022).

[315] J. Aumentado, G. Catelani, and K. Serniak, Physics Today **76**, 34 (2023).

[316] A. Houck, J. Schreier, B. Johnson, J. Chow, J. Koch, J. Gambetta, D. Schuster, L. Frunzio, M. Devoret, S. Girvin, *et al.*, Physical review letters **101**, 080502 (2008).

[317] P. Klimov, J. Kelly, Z. Chen, M. Neeley, A. Megrant, B. Burkett, R. Barends, K. Arya, B. Chiaro, Y. Chen, *et al.*, Physical review letters **121**, 090502 (2018).

[318] D. Sabonis, O. Erlandsson, A. Kringhøj, B. Van Heck, T. W. Larsen, I. Petkovic, P. Krogstrup, K. D. Petersson, and C. M. Marcus, Physical Review Letters **125**, 156804 (2020).

[319] W. Uilhoorn, J. G. Kroll, A. Bargerbos, S. D. Nabi, C.-K. Yang, P. Krogstrup, L. P. Kouwenhoven, A. Kou, and G. de Lange, arXiv preprint arXiv:2105.11038 (2021).

[320] D. Loss and D. P. DiVincenzo, Physical Review A **57**, 120 (1998).

[321] J. J. Pla, K. Y. Tan, J. P. Dehollain, W. H. Lim, J. J. Morton, D. N. Jamieson, A. S. Dzurak, and A. Morello, Nature **489**, 541 (2012).

[322] R. Maurand, X. Jehl, D. Kotekar-Patil, A. Corna, H. Bohuslavskyi, R. Laviéville, L. Hutin, S. Barraud, M. Vinet, M. Sanquer, *et al.*, Nature communications **7**, 13575 (2016).

[323] G. Burkard, T. D. Ladd, A. Pan, J. M. Nichol, and J. R. Petta, Reviews of Modern Physics **95**, 025003 (2023).

[324] J. Majer, J. Chow, J. Gambetta, J. Koch, B. Johnson, J. Schreier, L. Frunzio, D. Schuster, A. A. Houck, A. Wallraff, *et al.*, Nature **449**, 443 (2007).

[325] A. Wallraff, D. I. Schuster, A. Blais, L. Frunzio, R.-S. Huang, J. Majer, S. Kumar, S. M. Girvin, and R. J. Schoelkopf, Nature **431**, 162 (2004).

[326] A. Zwerver, T. Krähenmann, T. Watson, L. Lampert, H. C. George, R. Pillarisetty, S. Bojarski, P. Amin, S. Amitonov, J. Boter, *et al.*, Nature Electronics **5**, 184 (2022).

[327] J. R. De Laeter, J. K. Böhlke, P. De Bievre, H. Hidaka, H. Peiser, K. Rosman, and P. Taylor, Pure and applied chemistry **75**, 683 (2003).

[328] H. Watzinger, J. Kukučka, L. Vukušić, F. Gao, T. Wang, F. Schäffler, J.-J. Zhang, and G. Katsaros, Nature communications **9**, 3902 (2018).

[329] K. Wang, G. Xu, F. Gao, H. Liu, R.-L. Ma, X. Zhang, Z. Wang, G. Cao, T. Wang, J.-J. Zhang, *et al.*, Nature Communications **13**, 206 (2022).

[330] M. Naghiloo, arXiv preprint arXiv:1904.09291 (2019).

[331] S. Hoffman and C. Tahan, Bulletin of the American Physical Society (2024).

[332] M. Spiecker, A. I. Pavlov, A. Shnirman, and I. M. Pop, arXiv preprint arXiv:2307.06900 (2023).

[333] M. Mirhosseini, E. Kim, X. Zhang, A. Sipahigil, P. B. Dieterle, A. J. Keller, A. Asenjo-Garcia, D. E. Chang, and O. Painter, Nature **569**, 692 (2019).

[334] S. P. Ramanandan, P. Tomic, N. P. Morgan, A. Giunto, A. Rudra, K. Ensslin, T. Ihn, and A. Fontcuberta i Morral, Nano Letters **22**, 4269 (2022).

[335] N. Hendrickx, D. Franke, A. Sammak, M. Kouwenhoven, D. Sabbagh, L. Yeoh, R. Li, M. Tagliaferri, M. Virgilio, G. Capellini, *et al.*, Nature communications **9**, 2835 (2018).

[336] S. Thomas, Nat Electron **4**, 452 (2021).

[337] J. Trommer, A. Heinzig, U. Muhle, M. Loffler, A. Winzer, P. M. Jordan, J. Beister, T. Baldauf, M. Geidel, B. Adolphi, *et al.*, ACS nano **11**, 1704 (2017).

[338] J. N. Quijada, T. Baldauf, S. Rai, A. Heinzig, A. Kumar, W. M. Weber, T. Mikolajick, and J. Trommer, IEEE transactions on nanotechnology **21**, 728 (2022).

A Fabrication Recipes

The fabrication techniques used in this work can be found in 4. This appendix shows the detailed fabrication recipes.

A. Fabrication of Ge-Si core-shell NW Devices

A.1. Wafer Characteristics

- **Substrate Material:** Highly doped Silicon
- **Dopant:** Boron (p-doped)
- **Resistivity:** $0.003 - 0.005\,\Omega\mathrm{m}$
- **Capping Layer:** 100 or 300 nm thick thermally grown SiO_2

A.2. Wafer Cleaning

1. Dice the wafer into 2.5 cm x 2.5 cm pieces.
2. Sonicate in acetone for $\sim$ 10 min.
3. Sonicate in IPA for $\sim$ 10 min.
4. Sonicate in DI water for $\sim$ 10 min.
5. Blow dry with pressurized air or N_2
6. Clean with Ozone plasma for 5 min

A.3. Optical Lithography, Development and Lift-off

- **Instrument:** Heidelberg instrument μMLA direct laser
- **Pre-baking:** 125°C on a hotplate for 90 s.
- **Resist:** Microposit S1805 optical resist

- **Spin Coating:** 4500 RPM for 40 s with 3 s ramp resulting in a thickness of ∼ 500 nm.

- **Baking:** 125°C on a hotplate for 120 s.

- **Patterning parameters:** 10 mW, 48 % power, -6 focus

- **Development:** Microposit MF-319 developer for 50 s, followed by a dip in DI-water and blow dry with pressurized air or N_2.

- **Lift off:** 20 mins or longer in 65°C warm Remover AR300-76.

A.4. E-beam Lithography, Development(Cold) and Lift-off

- **Resist:** PMMA 950K dissolved in Anisole.

- **Spin Coating:** 4000 RPM for 45 s resulting in a thickness of ∼ 230 nm.

- **Baking:** 180°C on a hotplate for 3 mins.

- **Area Dose:** 1700 µC/cm^2 at 30 kV for big structure ($\sim \mu$m). 2300 µC/cm^2 at 30 kV for small structure (∼ 100 nm).

- **Development:** 3:1 Isopropyl alcohol (IPA) / Methylisobutyl ketone (MIBK) for 33 s at -20°C, followed by a dip in IPA for 30 s at -20°C and blow dry with pressurized air or N_2.

- **Liftoff:** 30 mins or longer in 65°C warm Remover AR300-76.

A.5. E-beam Lithography, Development(warm) and Lift-off

- **Resist:** PMMA 950K dissolved in Anisole.

- **Spin Coating:** 4000 RPM for 45 s resulting in a thickness of ∼ 230 nm.

- **Baking:** 180°C on a hotplate for 5 mins.

- **Area Dose:** 250 µC/cm^2 at 17 kV.

- **Development:** 3:1 Isopropyl alcohol (IPA) / Methylisobutyl ketone (MIBK) for 60 s at room temperature, followed by a dip in IPA for 10 s and blow dry with pressurized air or N_2.

- **Liftoff:** 30 mins or longer in 50°C warm acetone.

A.6. Reactive ion etching - O_2 Plasma Etching

To remove residue with PMMA resist only.

- **Parameters:**
  - **O_2 Flow:** 16 %
  - **RF Power:** 30 W
  - **Process Pressure:** 250 mTorr
  - **Time:** 60 s,
- **Etch Rates:**
  - **SiO_2:** negligible
  - **PMMA:** ~20 nm/min

B. Etching of the Ge-Si core-shell NW before metallization

To remove the native SiO_2 of Si shell before contacting.

1. Open the etching window for the contact area using standard E-beam lithography.
2. Perform 15 s O_2 plasma cleaning.
3. Etch for 8 s in Buffered-Hydrogen Fluoride (Buffered oxide etchant 10:1, 4.6 %)
4. Rinse for 30 s in DI water
5. Blow dry with pressurized air or N_2 and immediately load the sample in vacuum.

To remove both the native SiO_2 and Si shell before contacting.

1. Open the etching window for the contact area using standard E-beam lithography.
2. Perform 15 s O_2 plasma cleaning.
3. Etch for 8 s in Buffered-Hydrogen Fluoride (Buffered oxide etchant 10:1, 4.6 %)
4. Etch for 15 s in Tetramethylammonium hydroxide (TMAH)
5. Etch for 3 s in Buffered-Hydrogen Fluoride (Buffered oxide etchant 10:1, 4.6 %)

6. Rinse for 30 s in DI water
7. Blow dry with pressurized air or N_2 and immediately load the sample in vacuum.

C. Metal deposition

C.1. Ti/Pd

Used for base structures and normal metal gates.

1. **Type:** E-beam evaporation in Balzers.
2. Pump to a base pressure of $\sim 2e^{-6}$ mbar.
3. Align sample stage with metal sources
4. Evaporate 1 nm of Ti (0.5 Å per second).
5. Evaporate 20 nm of Pd (1 Å per second).

C.2. Pd/Al contacts

Used for superconducting Al contacts to Ge-Si NW, side gates.

1. **Type:** E-beam evaporation in Balzers.
2. Pump to a base pressure of $\sim 2e^{-6}$ mbar.
3. Align sample stage with metal sources
4. Optional: Cool sample stage to -20 °C with liquid nitrogen.
5. Evaporate 2.5 nm of Pd (1 Å per second).
6. Evaporate 40 nm of Al (1.5 Å per second).

C.3. Al contacts

Used for annealed superconducting Al contacts to Ge-Si NW, side gates, and contacts to NbTiN.

1. **Type:** E-beam evaporation in Balzers.
2. Pump to a base pressure of $\sim 2e^{-6}$ mbar.
3. For contact to NbTiN: Align sample stage with ion gun and perform a 27 s in-situ Ar-mill.

4. Align sample stage with metal sources
5. Optional: Cool sample stage to −20 °C with liquid nitrogen.
6. Evaporate 45 nm of Al (1.5 Å per second). For NbTiN: Evaporate 110 nm of Al

Curriculum Vitae

Han Zheng
Born on 15th July 1995 in Shiyan (China)

Education

2/2024–1/2020	**PhD in Experimental Physics at the University of Basel, Switzerland** - Dissertation in the group of Prof. Dr. C. Schönenberger *“Superconducting quantum devices with germanium nanowires”*
9/2017–11/2019	**Masters of Science in Physics at ETH Zürich, Switzerland** - Master thesis in the group of Prof. Dr. K. Ensslin *“Investigation of the equilibrium properties of quantum Hall edge states in confined geometries”*
2017–2013	**Bachelors of Science in Physics at the Sun Yat-sen Universiy, China** - Bachlor thesis in the group of Prof. Dr. Y. Zheng *“Investigation of localized surface plasmon resonance spectrum based on nanosphere lithography technique”*
2010–2013	**Shiyan No.1 High School, Shiyan, China**

Positions

2/2020–	*Teaching assistant for physics at the University of Basel*
7/2016–8/2016	*Research assistant at Department of Quantum Matter Physics, University of Geneva, Switzerland*
6/2015–9/2015	*Research assistant at the CERN, Geneva, Switzerland*

Publications

- *“Coherent control of a few-channel hole type gatemon qubit”*
  H. Zheng, L. Y. Cheung, N. Sangwan, A. Kononov, R. Haller, J. Ridderbos, C. Ciaccia, J. H. Ungerer, A. Li, E.P.A.M. Bakkers, A. Baumgartner, C. Schönenberger
  Nano Letters 2024 24 (24), 7173-7179

- *“Anomalous current-phase relations in Ge/Si nanowire Josephson junctions”*
  H. Zheng, T. Jenniskens, A. Kononov, R. Haller, H. Legg, J. Klinovaja, E.P.A.M. Bakkers, A. Baumgartner, C. Schönenberger
  in preparation

- *“Andreev qubit in Ge/Si nanowire Josephson junctions”*
  H. Zheng, A. Kononov, L. Y. Cheung, E.P.A.M. Bakkers, A. Baumgartner, C. Schönenberger
  in preparation

Talks

- *Current-phase relation of hole-type Ge/Si core/shell nanowire Josephson junctions*
  Les rencontres de Moriond, La Thuile (Italy), March 2023

- *Current-phase relation of hole-type Ge/Si core/shell nanowire Josephson junctions*
  QCQT Research Seminar, Basel (Switzerland), May 2023

- *Coherent manipulation of a Ge/Si core-shell nanowire based gatemon*
  Joint Annual Meeting of SPS and ÖPG, Basel (Switzerland), September 2023

- *A group IV gatemon*
  QCQT Research Seminar, Basel (Switzerland), November 2023

- *Gatemon qubit in a narrow Ge/Si core/shell nanowire*
  APS march meeting, Minneapolis (USA), March 2024

Poster Contributions

- *"Ge/Si Core-shell Nanowires coupled to superconductor"*
  QSIT General Meeting, Arosa (Switzerland), February 2022
- *"Ge/Si Core-shell Nanowires coupled to superconductor"*
  QSIT Junior Meeting, Flumserberg (Switzerland), June 2022
- *"Andreev bound states in Ge/Si Core-shell Nanowires coupled to superconducting contacts"*
  Mauterndorf Winter School, Mauterndorf (Austria), February 2023

Acknowledgements

Over the past four years, my journey pursuing a Ph.D. in the Quantum Nanoelectronics group must have been the most challenging yet profoundly rewarding experience of my life. There were moments of blood and tears during the failure of nano-fabrication, experiments showing negative results and countless hours spending on troubleshooting every error message flashed across the screen. Yet, amidst the challenges, there were *eureka* moments: witnessing the SQUID oscillation aligned seamlessly with the predictions of quantum mechanics, achieving a coherence manipulation of qubits in an entirely new platform, or even simply observing the occurrence of supercurrent in the experiments. It's these moments that makes you feel all the efforts worth it.

It goes without saying that this remarkable journey would not have been possible without the invaluable guidance, support, and collaborative efforts of the excellent people around me. Here, I want to express my genuine gratitude and give credit to those who played a meaningful role in this journey.

First of all, I would like to thank my advisor Prof. Dr. Christian Schönenberger. Thanks you for giving me the opportunity to conduct the research presented in this thesis. I am impressed by your unwavering enthusiasm and passion for physics, which has truly motivated me to going forwards and digging deeper. It's very rare that a group can cover so many research topics like in Quantum Nanoelectronics group. You are able to keep a track on every project and provide valuable guidance with your profound expertise. You consistently offered praise, even for small steps forward. There were times when things weren't going well, and I found myself in deep depression. Your encouragement kept me pushing forward. Not long after, when I presented the double quantum dot ABSs data to you, you remarked, "Now I see the smile on your face." A few months later, when I presented the SQUID results to you, you said again, "Your smile is even bigger now." These words truly lifted my spirit up. I am especially thankful for the many group excursions and events we had the last four years. Biking in the mountain in Italy and climbing up via ferrata in Pontresina certainly were highlights of our group activities. All these events allowed for a relaxed and enjoyable working environment, which I very much appreciate.

I want to express my thanks to Prof. Dr. Christian Anderson, Dr. Lucas Casparis, and my second supervisor, Prof. Dr. Jelena Klinovaja, for kindly agreeing to be part of the doctoral committee. It means a lot that you took the time to evaluate my thesis, and I am truly honored by your involvement in this journey.

I am sincerely grateful to Dr. Andreas Baumgartner. This thesis would not be possible without your immense contribution and unwavering support. After Joost left, there was a time when I felt puzzled, unsure of how to push the projects forward. It was at this critical juncture that you appeared, stepping in as my supervisor. I cannot recall the number of long discussions we had in front of the LMCK and Bluefors. The toughest phase of my PhD study was the time trying to measuring Majorana states in Ge/Si NWs. The goal was ambitious, but I even struggled in establishing proper superconducting contacts to these nanowires. Your guidance and assistance during this time were precious. Although we are not able to observe Majorana, we still manage to measure and understand ABSs physics in sinlge and double quantum dot configuration. Beyond experimental challenges, you imparted numerous research skills, including optimizing measurement setups, understanding the electronics of instruments, scientific writing, etc. As a PI, you spent quite some times in lab, one-to-one coaching us how to do things properly. Thanks so much for everything, and there are still so many interesting physics ahead of us for exploration.

I'd also like to extend my heartfelt gratitude to those who dedicated their time to proofreading parts of my thesis: Dr. Andreas Baumgartner, Dr. Artem Kononov, Dr. Alessia Pally, Prof. Dr. Joost Ridderbos, Prof. Dr. Christian Schönenberger, and Dr. Paritosh Karnatak.

I am thankful to the colleagues whom I collaborate closed with. The exchange of ideas, endless discussions, and mutual support have played a crucial role in the development of this thesis.

Dr. Luk Yi Cheung: I still remember in the very beginning of my PhD, we discussed the exciting possibility of integrating Ge/Si core/shell nanowires into RF experiments, potentially creating a qubit. After four years of dedicated effort, we have not only achieved success but exceeded expectations with not just one, but two qubits! Your significant contributions to establishing the qubit measurement infrastructure were pivotal, as without them, the qubit experiments would not have been possible. During my transition from DC to RF experiments, I gained invaluable insights from you, including knowledge about microwave setup, RF chip design, and fabrication.

Dr. Artem Kononov: I am grateful for your extensive laboratory experience, sharp critical thinking, and valuable inputs you brought to to the project. Your always-ready-to-help attitude, including those late-night quick responses, was truly helpful. Your adept troubleshooting skills and helps with the measurements when I began writing my thesis saved me a significant amount of time. Progressing with the project would not have been possible for me without your invaluable support.

Prof. Dr. Joost Ridderbos: You served as my initial supervisor at the beginning of my PhD, and I want to express my gratitude for your exceptional guidance. You did a good job teaching me everything about micro and nano fabrication, particularly in handling these ultra-thin Ge/Si NWs. Moreover, you are also a excellent programmer. The EBL automation script you wrote saved me considerable time by eliminating manual alignment (although the script sometimes is not working properly and I have to redo the patterning). Thanks for your efforts in setting up Qcodes and assistance in debugging measurement scripts. The *tessierplot* is such a useful tool to visualize the measurement. Moreover, I would like to highlight that I rely extensively on *tessierplot* for generating figures.

Dr. Roy Haller: In our RF subgroup, you've been like a big brother to me, probably since you are the most senior PhD in the subgroup when I join. I really appreciate all the help you gave me during the CPR experiments. Not just that, I've learned so much about RF, electronics, and wiring of a dilution fridge from you. You're not only great with the scientific stuff but also super easy-going and a fantastic organizer. You've taught me how to work effectively with a plan. Thanks for being such a great colleague and mentor!

Dr. Alessia Pally: We worked together on the selective area growth Ge nanowires. Even though the project do not work out in the end, I really have to say how much I valued your reliability and teamwork. Working with you on HF etching and your commitment to maintaining the Balzers was awesome. Also, your thoughts on nano-fabrication issues were super helpful and really appreciated. Thanks for being such a great partner in this project!

Tom Jenniskens: I am grateful that you chose to undertake a semester project with me. Your significant contributions to optimizing the annealing recipe were instrumental and proved to be crucial for the subsequent qubit project. Your reliability and quick learning ability were noteworthy, making our collaboration enjoyable and productive. I truly appreciated our time working together.

Dr. Martin Endres: Thank you for your assistance in setting up the counter measurement for the SQUID experiment. Additionally, I gained valuable insights from you on how to measure and interpret the CPR data. You are very supportive, and I appreciate the knowledge and expertise you shared with me.

I would like to thank all the people involving TOPSQUAD project: Zhen Wu, Simon Svab, Dr. Richard Hess, Oliver Sag, Orson van der Molen, Dr. Marco Valentini, Prof. Dr. Georgios Katsaros, Prof. Dr. Erik Bakker Prof, Dr. Dominik Zumbühl, Prof. Dr. Daniel Loss, Prof. Dr. Floris Zwanenburg, Prof. Dr. Alexander Brinkman, Prof. Dr. Chuan li, Dr. Parisa Fallahi.

Getting through PhD is not a easy journey, but it's made so much better with awesome colleagues and fun moments like BBQs, short breaks to the corner shop, and sports like sola-run, ping-pong, or via ferrata. Big thanks to all the current and past MESO group members—I've enjoyed hanging out with you all these years! Cheers to Dr. Jann Hinnerk Ungerer, Dr. Paritosh Karnatak, Dr. Prasanta Kumbhakar, Dr. Ian Correa Sampaio, Dr. Zarina Mingazheva, Dr. Blessonsam Varghese, Dr. Arunav Bordoloi, Dr. Olivier Faist, Dr. David Indolese, Dr. Mehdi Ramenzani, Dr. Frederick Thomas, Dr. Lujun Wang, Dr. Libin Wang, Dr. Christian Jünger, Rounak Jha, Matthijs Hermans, Carlo Ciaccia, Deepankar Sarmah, Jibin N Sunil and all the colleagues and former colleagues mentioned above. Good times, great memories!

Special thanks also go to many people at the Physics Department. I want to thank Barbara Kammermann, Astrid Kalt and Christian Wölfle for the administrative works and cheerful chats in the corridors. I would like to thanks the people in the electronics workshop and the mechanical workshop. Michael Steinacher, thanks for sharing your expertise in electronics and for the time you spent on reducing the noise level at output of differential amplifier. The latter make counter measurement possible. Sascha Linder, thank you for soldering SME on the PCB for us. I would also like to thank Dominik Sifrig for the supply of helium even I forgot to order, Gerard Diez, Arnold Lücke and Laurent Marot for the help with the cleanroom.

Finally, I must express my deepest gratitude to my family and friends. Your unwavering love and support were the pillars that sustained me through this journey. To my parents, I am especially grateful for your nurturing and unconditional support, especially when I decided to study abroad. I also want to extend a heartfelt thank you to my friends, both near and far. We've shared so many great moments together, hiking in the mountains, snowboarding down the slopes, or even sharing a beer over Zoom: Xiangzhou Zhu, Zhou Yang, Minhao Li, Dr. Ruocheng Han, Qianqian Qiao, Weigutian Ou, Zhiyin Chen, Dr. Jingwei Tang, Nan Li, Xinjie Chen....Finally, a special thanks to my wife, Dr. Shen Yan, for her constant love and enduring me. Thank you for being my steadfast partner in every aspect of life.

Without all these people I would not be where I am today.